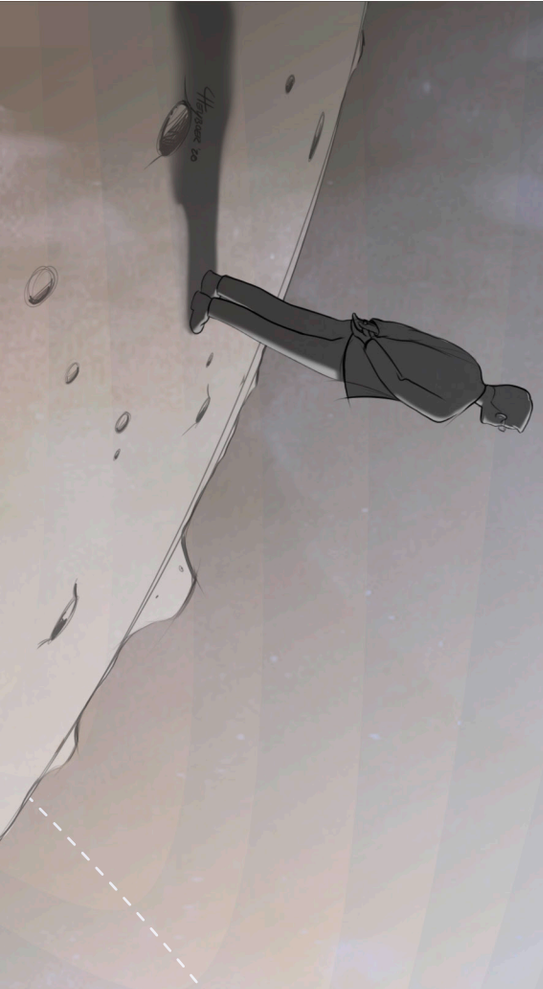

A Nonlinear Future - Félix Simon Carlier

A NONLINEAR FUTURE

Measurements and corrections of nonlinear beam dynamics using forced transverse oscillations

Félix Simon Carlier

A NONLINEAR FUTURE

MEASUREMENTS AND CORRECTIONS OF NONLINEAR BEAM DYNAMICS USING FORCED TRANSVERSE OSCILLATIONS

Félix Simon Carlier

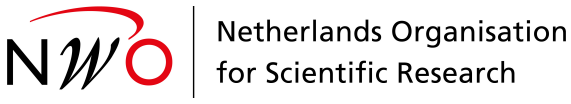

This work is part of the research programme of the Dutch Research Council (NWO). The work is carried out at the European Organization for Nuclear Research (CERN) in Geneva, Switzerland, and the National Institute for Subatomic Physics (Nikhef) in Amsterdam, The Netherlands.

ISBN 978-94-640-2214-8

Printed by Gildeprint

A NONLINEAR FUTURE

MEASUREMENTS AND CORRECTIONS OF NONLINEAR BEAM DYNAMICS USING FORCED TRANSVERSE OSCILLATIONS

ACADEMISCH PROEFSCHRIFT

ter verkrijging van de graad van doctor
aan de Universiteit van Amsterdam
op gezag van de Rector Magnificus
prof. dr. ir. K.I.J. Maex
ten overstaan van een door het College voor Promoties
ingestelde commissie, in het openbaar te verdedigen
op vrijdag 8 mei 2020, te 12:00 uur

door

Félix Simon Carlier

geboren te Toulouse.

Promotiecommissie:

Promotores:	Prof. dr. F.L. Linde	Universiteit van Amsterdam
	dr. R. Tomás	European Organization for Nuclear Research (CERN)
Overige Leden:	Prof. dr. S.C.M. Bentvelsen	Universiteit van Amsterdam
	Prof. dr. S. Brandenburg	Rijksuniversiteit Groningen
	Prof. dr. A.P. Colijn	Universiteit van Amsterdam/ Universiteit Utrecht
	Prof. dr. M.P. Decowski	Universiteit van Amsterdam
	dr. W. Fischer	Brookhaven National Laboratory
	Prof. dr. ir. P.J. de Jong	Universiteit van Amsterdam
	Prof. dr. S.J. de Jong	Radboud Universiteit
	dr. M. Vreeswijk	Universiteit van Amsterdam

Faculteit der Natuurwetenschappen, Wiskunde en Informatica

PUBLICATIONS

Chapter 4

F.S. Carlier, R. Tomás , *Forced resonance driving terms*, Physical Review Accelerators and Beams, Submitted 25 November 2019 [1].

The development of the theoretical derivations was performed by F.S. Carlier under supervision of R. Tomás. The simulations and analysis were performed by F.S. Carlier. The text and images were produced by F.S. Carlier.

Chapter 5

F.S. Carlier, R. Tomás, and E.H. Maclean , *Measurement and correction of resonance driving terms in the Large Hadron Collider*, Physical Review Accelerators and Beams, Submitted 22 January 2020 [2].

All authors contributed to the data acquisition, and provided valuable insight in discussions. The analysis of the measurements, as well as the simulations were performed by F.S. Carlier. The text and images were produced by F.S. Carlier, with corrections provided by R. Tomás. All authors contributed to the review of the manuscript.

Chapter 6

F.S. Carlier, R. Tomás, E.H. Maclean, and T.H.B. Persson , *First experimental demonstration of forced dynamic aperture measurements with LHC ac dipoles*, Physical Review Accelerators and Beams 22, 031002, Published 13 March 2019 [3].

The data acquisition was performed by all authors. The analysis of the data and the simulations were performed by F.S. Carlier. The text and images were produced by F.S. Carlier. All authors contributed to the review of the manuscript, providing valuable contributions.

F.S. Carlier, M. Giovannozzi, R. Tomás, E.H. Maclean, T.H.B. Persson, and R. Tomás, , *Probing the forced dynamic aperture in the LHC at top energy using ac dipoles*, Proceedings of 9th International Particle Accelerator Conference (IPAC'18), Vancouver, Canada, MOPMF0033, Published July 2018 [4].

The data acquisition was performed by F.S. Carlier, R. Tomás, E.H. Maclean, T.H.B. Persson, and R. Tomás. The analysis of the data and the simulations were performed by F.S. Carlier. The text and images were produced by F.S. Carlier. All authors contributed to valuable discussions, and to the review of the article.

Chapter 7

F.S. Carlier, R. Tomás, and X. Buffat, *First measurement of resonance driving terms from head-on beam-beam interaction in the LHC*, Physical Review Accelerators and Beams, Submitted 15 October 2019 [5].

All authors contributed to the measurements. The analytical derivations, simulations and analysis of the measurements was performed by F.S. Carlier with close collaboration of R. Tomás. The text and images were produced by F.S. Carlier, and reviewed by all authors before submission.

ACKNOWLEDGMENTS

Four years of work have finally been summarized in this little book you now hold in your hands. It is with great pleasure that I would like to take the time to thank the people that have contributed to this work and supported me along the way. It has been an incredible few years and these few lines do not do it justice.

There is no better way to start these acknowledgments than by thanking Dr. Rogelio Tomás for the good humored, enthusiastic and engaging supervision of my thesis. I am ever thankful for the freedom and trust I received to follow my own interests and explore different topics. I believe this has produced some truly exciting work that would not have been achievable without your support and guidance. I could not have wished for a better supervisor.

I would also like to thank Prof. Frank Linde for the supervision of my thesis at Nikhef. I thank you for taking on the challenge of supervising an accelerator physics thesis. I have been very lucky to receive all the support from Nikhef to attend conferences and workshops abroad, as well as having to opportunity to work a fourth year at Nikhef. It has been a pleasure staying at Nikhef for that last year, and the fruits of this extra effort are presented in Chapter 4.

A special thanks goes to Dr. Wolfram Fischer for the opportunity to work at the Brookhaven National Laboratory (BNL) before my PhD, and for the invitation to attempt measurements of the beam-beam interaction in RHIC during my PhD. It is a pleasure working with you and the rest of the staff at BNL. Although the goal of the stay was not achieved at BNL, it has motivated me to pursue this in the LHC which lead to the success of Chapter 7.

Of the many colleagues I have had the pleasure of working with at CERN, some merit a special mention. It is with great pleasure that I thank Ewen Maclean for all the support and fruitful discussions on nonlinear beam dynamics, and Tobias Persson for his valuable insights along the way. Particular thanks also goes to Xavier Buffat for our collaboration on studies of the beam-beam interaction. Furthermore, this thesis would not have been possible without the incredible support from the LHC operations team to perform all the measurements presented in this thesis. Last but definitely not least, I want to thank the OMC team for all the valuable contributions to this thesis and sleepless nights in the control room.

Looking back on my time at CERN, it would be inconceivable without one con-

stant factor. I am ever thankful to the residents of 6/R-006 and fellow members of the CBJ; Drs. Fabien Plassard, Michael Schenk and Lee Carver, for blurring the lines of the work-life balance. It is with great honor and humility that I may finally join my fellow members of the CBJ in their doctorhood.

I am ever thankful to Xavi and Megan for their incredible kindness and friendship. I also want to thank Debora, Kristel, Stephen, Gesu, Alessandro, Malek and Pierre for all the good times I had in Geneva. I would also like extend a special thanks to Jaime and Elena for the memorable "movie nights" in R4, l'Usine and La Graviere.

It is also with great pleasure that I thank my friends and colleagues at Nikhef that have accepted this stranger from the field of accelerator physics and given him a home. It has been an enormous pleasure to stay at Nikhef and be included so readily into the life at Nikhef.

To my friends back home and abroad, Floris, Imre, Christophe, Olivier, Stefan, Jan, Philip and all the others, I thank you for the continuous support and incredible friendship that has lasted despite my absence. It has been fantastic to be back in the Netherlands for a while to be closer to you. To Stefan, thank you for all your efforts in converting my imagination into graphic reality. Your willingness to help others out is always inspiring.

Je profite aussi de l'occasion pour remercier Les Relous pour tous les moments de détente et de rires. Le mardi soir était devenu le moment le plus attendu de la semaine. Continuez comme ça, et *Relous un jour, relus toujours!*

Finalement, je voudrais remercier les personnes qui me sont les plus proches. Tout d'abord Franka qui a vécu toutes les facettes de ma vie de doctorant. Tu as toujours été une source continue de soutien et d'inspiration. Merci pour ces dernières années merveilleuses.

Pour finir, j'aimerais remercier Maman, Papa, Antoine, Louis et Lise pour votre soutien continu, naturel et sans fin. Je vous souhaite tout le bonheur possible. Cette thèse vous est dédiée.

CONTENTS

1

INTRODUCTION

Particle accelerators and colliders are established as one of the major driving forces in fundamental particle physics research. Particle colliders have over the past decades led to the discovery of nearly all the particles in the Standard Model [6–20], with the exception of the electron neutrino that was discovered using the neutrino flux of a nuclear reactor [21], and the muon that was discovered from studies of cosmic rays [22]. It is in the continuation of this success that the Large Hadron Collider (LHC) [23] was built. The primary objective of the LHC, together with the incorporated particle detectors (ATLAS [24], CMS [25], LHCb [26], and ALICE [27]), is to provide experimental evidence to study the fundamental structure of the universe. This eventually led to the recent discovery of the Higgs boson [19, 20], which forms the keystone of the Standard Model. The Standard Model of particle physics has been instrumental at predicting new particles, and has proven to be a reliable guide to predict the particle properties and interactions [28–30]. While it is widely tested and benchmarked in a wide range of experiments, it does by no means form the final answer in fundamental physics. Many currently open and unanswered questions in fundamental physics lie beyond the Standard Model. With the discovery of all the particles in the Standard Model, efforts now shift towards the study of potential discrepancies between the Standard Model and experimental measurements, as well as the discovery of new physical phenomena that lie beyond the Standard Model.

There are currently two key areas that can improve the chances of new discoveries in particle physics using circular colliders. The first is known as the high-energy frontier, where the aim is to increase the center-of-mass energy of the collisions to allow the detection of particles and processes whose energies lie beyond the current reach of the LHC. Such experiments pushing the energy frontier are the focus of the proposed Future Circular Collider (FCC) [31]. The second field of study that can lead to new discoveries is called the intensity frontier, and aims to increase the generated luminosity in the detectors to improve statistics and allow the detection of extremely rare processes and events. This has been the continuous effort of the LHC and lies at the core of the High Luminosity LHC upgrade [32]. The luminosity

upgrade aims to achieve a ten times higher integrated luminosity over its lifespan by increasing the bunch intensity and reducing the beam size at the collision points in the detectors.

In the search for higher luminosities, the design of the LHC pushes the particle dynamics to ever more challenging regimes. Linear dynamics have been studied in great detail since the emergence of synchrotrons providing a strong and well established basis [33–36]. In the LHC continuous improvements and developments of correction strategies have pushed the control of linear optics well beyond the established design parameters of the LHC [37–39]. This success has allowed the study of more challenging sources of perturbations. More recently, the nonlinear dynamics in the LHC have been a limiting factor for both operation as well as performance. Nonlinear magnetic errors arising from the magnetic field errors, magnet misalignments, magnet rotations, or other possible sources, can greatly perturb the particle motion in the collider, by causing particle orbits to become unstable, reducing the dynamic aperture, and causing resonances in the beam motion, all of which can critically reduce the luminosity. The correction of these magnetic errors has been an integral part of the LHC commissioning in Run II, and is seen as a priority for Run III. Furthermore, the design parameters for the High Luminosity LHC upgrade are predicted to be unachievable by controlling the linear beam optics only. It will be the first hadron collider where the accurate understanding and control of the transverse nonlinear beam dynamics is necessary to operate the machine at the design parameters. The measurement and correction of nonlinear magnetic sources is thus critical to achieve the performance of future colliders.

Measurements of transverse beam dynamics in the Large Hadron Collider

Measurements of beam optics and of nonlinear dynamics are done by generating a large transverse beam oscillation that is typically much larger than the natural beam size. The transverse beam position is measured at each turn at specific locations in the accelerator using Beam Position Monitors (BPM) [40, 41]. The spectral content of this turn-by-turn position read out provides valuable insights in all the modes contained in the particle motion at each BPM location. A few criteria can be put forward that are important for good and accurate measurements of the beam dynamics. Large oscillation amplitudes are necessary to provide clear signal-to-noise ratios in the BPMs, as well as to increase the amplitudes of secondary modes in the turn-by-turn data. Secondly, long lasting oscillations are beneficial to the

spectral analysis of the turn-by-turn data as they increase the spectral resolution and reduce the noise floor. Finally, the measurement technique should preferably be non-destructive to the beam, i.e. the measurements can be repeated without changing the state of the beam, such that it does not require injecting fresh beams. The latter is especially true for the LHC, where destructive measurements at top energy require a ramp down and ramp up cycle, taking up valuable LHC time.

The conventional method to excite the bunches in accelerator is to use a single kick. This single kick changes the beam's momentum and creates a free oscillation of the beam. Such types of kicks are widely used in synchrotrons, but are not possible for the LHC at top energy. A single kick can create large transverse displacements in a single turn, which is much too fast for machine protection feedback systems in the LHC. As such, the kicker magnet in the LHC is only allowed to be used at injection energy. Furthermore, such excitations are destructive in nature, as the momentum distribution of the particles in a bunch will cause the particles to decohere, resulting in incoherent oscillating particles. This not only makes the bunch unrecoverable, but it also greatly impacts the BPM measurements, as the measured centre of charge will gradually go to zero, as shown in Fig. 1.1.

The ac dipole was proposed for the first time in the AGS [42] to create large transverse oscillations. The ac dipole, as the name suggests, consists of a dipole with an oscillating field. By choosing this oscillation frequency to be close to the natural

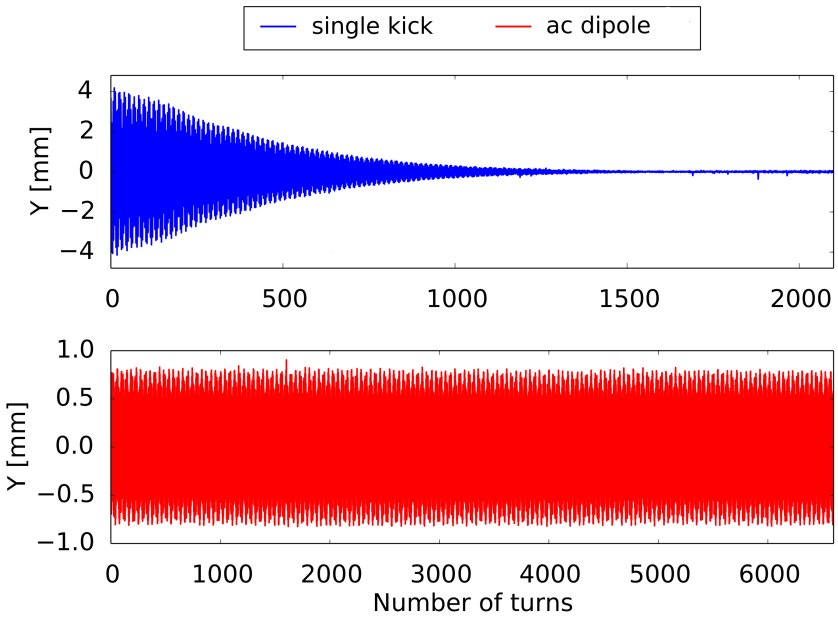

Figure 1.1: *Comparison between turn-by-turn data obtained from a single free kick (blue) and an ac dipole excitation (red) at injection energy.*

tune of the accelerator the beams can be excited in the transverse planes. The ac dipole field strength is ramped up adiabatically [43] to large beam oscillation amplitudes. Once large amplitudes are reached the ac dipole strength is held constant, allowing for a long lasting coherent oscillation, also known as forced oscillations. A typical ac dipole excitation is also shown in Fig. 1.1. The ac dipole strength can be adiabatically ramped down during which the beam oscillation amplitude will reduce to zero. This technique not only provides large amplitude oscillations, it also manages to provide a long lasting coherent oscillation that is non-destructive in nature.

These properties have turned the ac dipole into the single most critical measurement tool for beam dynamics in the LHC. All linear, as well as nonlinear beam dynamics measurement methods now make use of the ac dipoles. The nonlinear forced motion can be used as a valuable observable to understand and control the machine nonlinearities by probing different states of the accelerator and comparing to particle tracking simulations.

The aim of this thesis is to develop the understanding of the nonlinear particle motion under forced transverse oscillations with ac dipoles, especially of resonance driving terms, in order to measure and correct nonlinear errors in the LHC. Furthermore, the LHC is used as a test-bench for experiments to validate the methods, and to continue towards the implementation of measurements and corrections of nonlinear sources in the LHC in view of the High Luminosity LHC.

THESIS OUTLINE

This thesis starts by introducing the linear beam dynamics and the theoretical structure for the analysis of resonance driving terms in the case of free transverse oscillations in Chapter 2. The forced linear motion under the influence of ac dipoles is subsequently introduced in Chapter 3.

Chapter 4 presents the study of forced resonance driving terms, by exploring the normal form transformations in the forced parameters space. It further introduces a new parametrization of the forced resonance driving terms, as well as the perturbative second order cross-term between the ac dipoles and the resonance driving terms.

Measurements and corrections of forced resonance driving terms are presented in Chapter 5. The measurement methods are detailed, and a review of the measured resonance driving terms is presented. The first ever measurement of resonance

driving terms of decapolar order are presented. Lastly the first correction of skew octupolar errors using forced resonance driving terms is presented.

Chapter 6 explores the effect of ac dipoles on the available dynamic aperture. A new observable is introduced as the forced dynamic aperture. This new observable can be used to study machine nonlinearities by comparing measurements to simulations. The first measurements of forced dynamic aperture in the LHC are also presented and compared to particle tracking simulations.

Lastly the beam-beam perturbation is studied in Chapter 7. Derivations for free and forced resonance driving terms as generated by the head-on beam-beam interaction are presented. A method is proposed to measure resonance driving terms by characterizing the spectral line amplitudes as a function of the beam oscillation amplitudes. The first measurement of beam-beam generated resonance driving terms as well as the first measurements of resonance driving terms of dodecapolar order are presented.

THE CERN ACCELERATOR COMPLEX AND THE LARGE HADRON COLLIDER

The CERN accelerator complex consists of multiple linear and circular particle accelerators serving a large variety of different experiments, as shown in Fig. 1.2. Particles go through a chain of different particle accelerators before reaching their final experimental destination. For protons, this starts at LINAC 4, a linear particle accelerator that accelerates the protons to a kinetic energy of 160 MeV. The protons are then injected into the Proton Synchrotron Booster (PSB), where the protons are accelerated further to an energy of 1.4 GeV. The next stage is the Proton Synchrotron (PS). There the protons reach an energy of 25 GeV before being injected into the Super Proton Synchrotron (SPS). In the SPS the protons can be accelerated up to 450 GeV, the energy required for the injection into the LHC.

The accelerator chain for heavy ions shares much of the proton chain, with the exception of LINAC 2 and the PSB. Heavy ions are first accelerated in LINAC 3, another linear accelerator, before being injected in the Low Energy Ion Ring (LEIR), that prepares the heavy ion beams for injection into the PS. At each accelerator in the injection chain, protons and heavy ions can be extracted for other experiments. This provides a large range of particles with different kinetic energies that feed into a wide selection of physics experiments.

At the core of the CERN scientific program lies the LHC, currently the largest hadron collider in the world. The LHC is a synchrotron type accelerator accelerating two different beams in opposite directions. A schematic representation of the

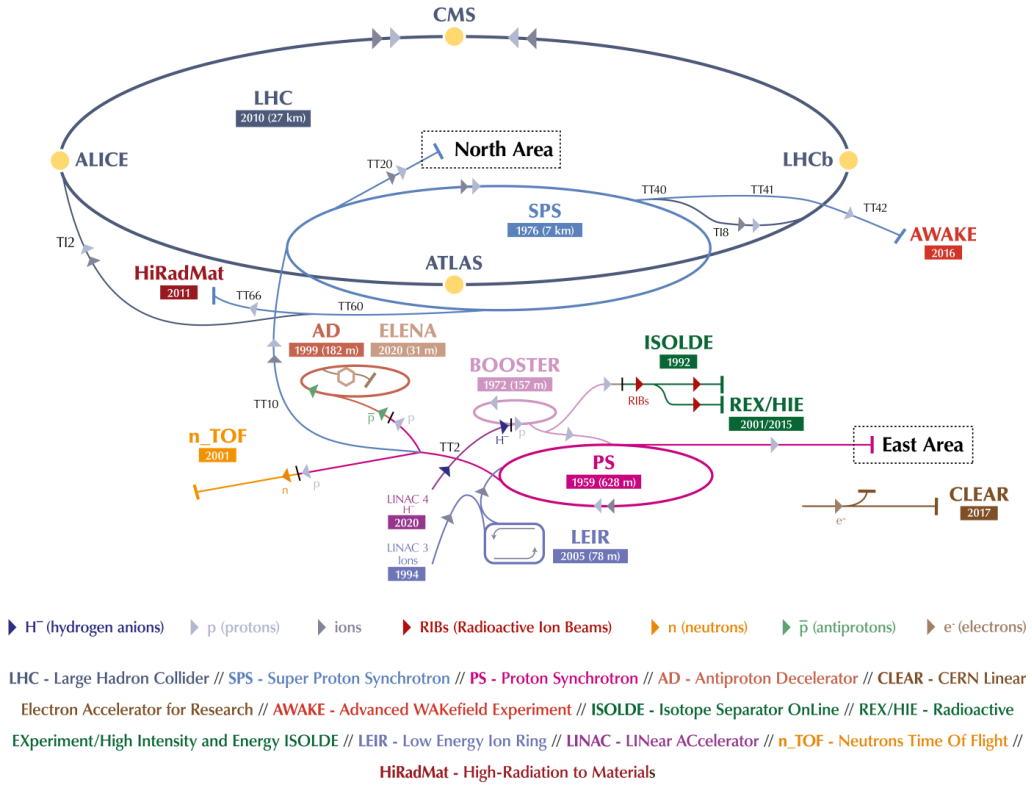

Figure 1.2: *Schematic representation of the CERN accelerator complex [44].*

LHC layout is presented in Fig. 1.3. Particles injected in the LHC propagate through the arcs, where superconducting dipoles bend the trajectories of the charged particles, and long straight sections, known as the insertion regions (IR). The succession of arcs and IRs form an almost eight-fold symmetric synchrotron. The IRs contain most of the dedicated beam diagnostics, such as cleaning sections, instrumentation, radio-frequency cavities, and the dump, as well as the experiments. The beams travel through different apertures in most of the accelerator. At four locations in the ring the beams share the same aperture and their trajectories intersect, resulting in high-energy particle collisions. Dedicated particle detectors are built at these interaction points (IPs). The LHC contains two all-purpose particle detectors, ATLAS [24] that is located at IP1, and CMS [25] that is located at IP5. Two more detectors are located at IPs with lower luminosities. The LHCb [26] detector that is located in IP8 studies the possible asymmetries between matter and anti-matter, while the ALICE [27] detector is located in IP2 and studies the quark-gluon plasmas from heavy ion collisions.

The LHC receives the proton beams from the SPS at an energy of 450 GeV and further accelerates them to an energy of 6.5 TeV for collisions with a total center-of-mass energy of 13 TeV. Run III of the LHC will see the beam kinetic energy be

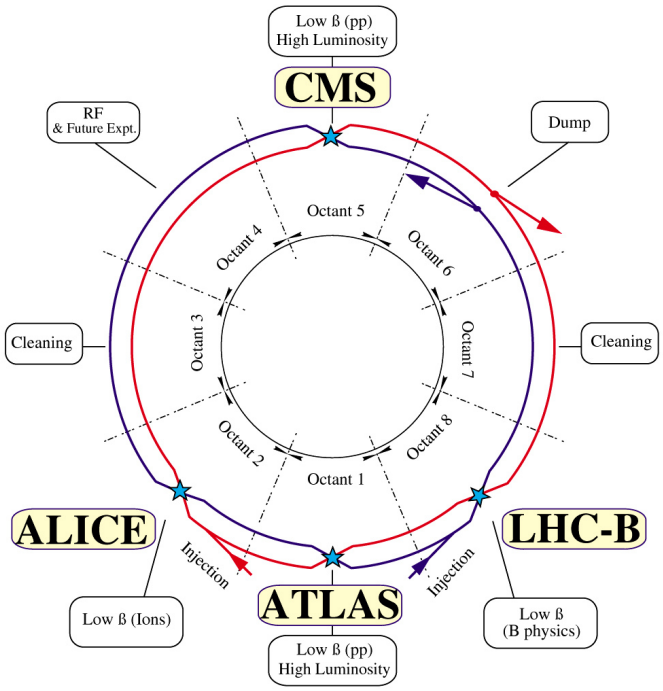

Figure 1.3: *Schematic representation of the layout of the LHC as viewed from above. Beam 1, shown in red, travels in the clockwise direction, while beam 2 is shown in blue and travels in the anti-clockwise direction. The apertures are separate, except at the IPs were the beams cross and collide [45].*

increased to the design energy of 7 TeV. At top energy, the beam sizes at the collision points are reduced to increase the local particle density. The separation between the two beams is then reduced until the collision of the beams is obtained. The luminosity is optimized by achieving the best possible overlap of the two beams.

Although the ultimate aim of the LHC is to provide sufficient luminosity to the experiments, a lot of the commissioning and developments done in the LHC are performed with different machine setups. Beam manipulations with a fully filled LHC are considered delicate and potentially dangerous for the machine. As such, measurements of transverse beam dynamics as presented in this thesis are done with a single low intensity bunch. This allows for the large transverse beam excitations needed to measure resonance driving terms and other nonlinear effects, while operating at safe conditions. However, as the nonlinear effects studied in this thesis are independent of the intensities of the probed bunch, the used experimental setup offers a good representation of operational conditions.

2

THEORETICAL CONSIDERATIONS

This chapter starts by introducing the linear and nonlinear single particle beam dynamics in the free parameter space. It derives the turn-by-turn motion by introducing the formulation of transfer maps for each element, and is followed by the normal form transformation to obtain the nonlinear motion. This forms but a concise introduction to the field of single particle dynamics in synchrotrons. For a more complete treatment of relevant accelerator physics the reader is best referred to textbooks by A. Wolski [33] as well as those of S.Y. Lee [34] and H. Wiedemann [35]. Relevant lectures on nonlinear beam dynamics are given by A. Chao [46].

This introduction is followed by the description of the forced linear motion under the influence of ac dipoles in Chapter 3. It is an essential step to better frame the following derivations presented in Chapter 4 for the forced motion.

INTRODUCTION TO TRANSFER MAPS

Single particle dynamics in circular accelerators are described with respect to a reference orbit. For synchrotrons this reference orbit usually refers to the closed orbit. The closed orbit is defined as the trajectory along an accelerator for which a particle with design energy p_0 will return to its initial location with the same conditions, and is determined by the bending of the main dipoles. All descriptions of positions and momenta in the following work describe the motion around this moving reference frame. Figure 2.1 shows the moving reference frame, also known as the Frenet-Serret coordinate system, where the horizontal and vertical coordinates are denoted by x and y respectively, and s is the longitudinal coordinate in the direction of travel. When discussing the transverse dynamics, the longitudinal coordinates (s, p_s) are usually neglected, and so the particle state is fully determined by its horizontal and vertical physical coordinates $\mathbf{z} = \{x, p_x, y, p_y\}$, where p_x and p_y are the derivatives of x and y with respect to the path length s.

A particle travelling on the closed orbit at location s_0 with coordinates $\mathbf{z}_{CO}(s_0)$, will end up with the same position and momenta after a full revolution of the

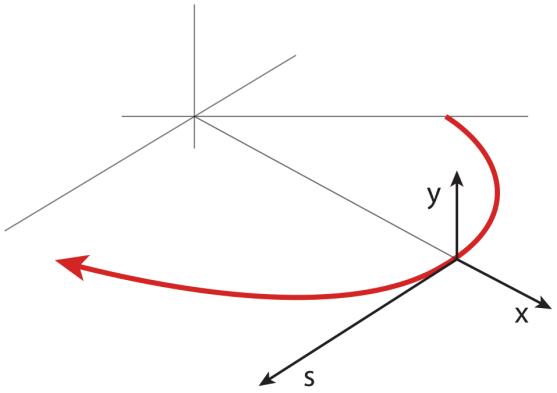

Figure 2.1: *Frenet-Serret coordinate system where the transverse coordinates are given by x and y for the horizontal and vertical planes respectively. The coordinate system moves along the propagation direction given by s.*

accelerator with circumference C,

$$\mathbf{z}_{CO}(s_0 + C) = \mathbf{z}_{CO}(s_0) \ . \tag{2.1}$$

As a particle travels through the accelerator it will encounter various magnetic elements and each of these magnets will change the particle's coordinates and thus affect its trajectory. The effect of the elements can be mathematically expressed as maps. A map M_i of element i transforms the coordinates before the element ($\mathbf{z_1}$) to those after the element ($\mathbf{z_2}$),

$$\mathbf{z_2} = M_i \mathbf{z_1} \ . \tag{2.2}$$

The most common maps are the maps of linear elements. Figure 2.2 shows a schematic representation of a dipole and a quadrupole, both linear elements, as well as a sextupole. The magnetic field of a sextupole changes quadratically in the transverse coordinates, and thus forms the lowest order of nonlinear elements. For linear elements the transfer maps take the form of simple matrices. To introduce the practicality of maps, only the linear maps of drifts, dipoles and quadrupoles are considered for now, as these form the fundamental building blocks of synchrotrons. The transfer maps of drift spaces and dipoles are given by,

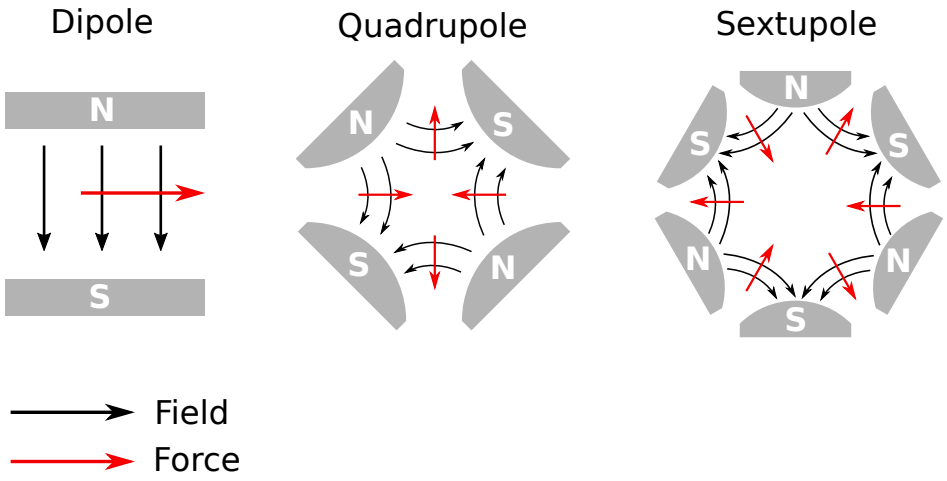

Figure 2.2: *Schematic representation of a dipole (left), a focussing quadrupole (middle), and a sextupole (right), with corresponding field lines and forces on a positively charged particle moving into the paper. Both dipoles and quadrupoles are linear elements, while sextupoles are the lowest order nonlinear elements.*

$$\text{Drift space}: \quad \begin{pmatrix} z \\ p_z \end{pmatrix}_{L+s_0} = \begin{pmatrix} 1 & L \\ 0 & 1 \end{pmatrix} \begin{pmatrix} z \\ p_z \end{pmatrix}_{s_0}, \tag{2.3}$$

$$\text{Dipoles}: \quad \begin{pmatrix} x \\ p_x \end{pmatrix}_{L+s_0} = \begin{pmatrix} \cos(L/\rho) & \rho \sin(L/\rho) \\ -\frac{1}{\rho}\sin(L/\rho) & \cos(L/\rho) \end{pmatrix} \begin{pmatrix} x \\ p_x \end{pmatrix}_{s_0}, \tag{2.4}$$

where s_0 indicates the longitudinal position in the accelerator at the start of the element, L is the length of the element, ρ is the radius of curvature of the orbit, and $z \in \{x, y\}$ can either denote the coordinates of the horizontal (x) or vertical (y) plane, and does not represent a third coordinate. Notice that only the x coordinate is given for the dipole, indicating a horizontally bending dipole. Quadrupoles have a focussing field in one plane and a defocussing field in the perpendicular plane. The convention is to name a quadrupole with a focussing field in the horizontal plane as a focussing quadrupole. A polarity change will turn it into a defocussing quadrupole. For a focussing quadrupole, the transfer matrix for the focussing horizontal plane is given by,

$$\begin{pmatrix} x \\ p_x \end{pmatrix}_{L+s_0} = \begin{pmatrix} \cos\sqrt{K_1}L & \frac{1}{\sqrt{K_1}}\sin\sqrt{K_1}L \\ -\sqrt{K_1}\sin\sqrt{K_1}L & \cos\sqrt{K_1}L \end{pmatrix} \begin{pmatrix} x \\ p_x \end{pmatrix}_{s_0} , \tag{2.5}$$

and for the defocussing vertical plane by,

$$\begin{pmatrix} y \\ p_y \end{pmatrix}_{L+s_0} = \begin{pmatrix} \cosh\sqrt{K_1}L & \frac{1}{\sqrt{K_1}}\sinh\sqrt{K_1}L \\ \sqrt{K_1}\sinh\sqrt{K_1}L & \cosh\sqrt{K_1}L \end{pmatrix} \begin{pmatrix} y \\ p_y \end{pmatrix}_{s_0} , \tag{2.6}$$

where K_1 is the normalized gradient of a quadrupole that generates a linear field that vanishes at the reference orbit, and is defined as,

$$K_1 = \frac{1}{B_0\rho}\frac{\partial B_y}{\partial x} , \tag{2.7}$$

where B_y is the vertical component of the magnetic field, and where the magnetic rigidity $B_0\rho$ is defined using the charge of the particle q and the reference energy p_0 as,

$$B_0\rho = \frac{p_0}{q} . \tag{2.8}$$

It is sometimes useful to approximate elements as thin lenses, where $L \to 0$ and $K_1 L \to constant$. In this case the transfer map for the focussing plane of a quadrupole in the thin lens approximation becomes,

$$\begin{pmatrix} x \\ p_x \end{pmatrix}_{L+s_0} = \begin{pmatrix} 1 & 0 \\ -K_1 L & 1 \end{pmatrix} \begin{pmatrix} x \\ p_x \end{pmatrix}_{s_0} . \tag{2.9}$$

One-turn map

As accelerators consist of thousands of elements, the interest lies not in the effect of a single map, but in the combined effect of all these elements. Figure 2.3 shows a schematic representation of an accelerator with linear elements interleaved by drift spaces. All elements and drift spaces are represented by their corresponding linear map M_i. The maps of linear elements are matrices and so can be easily combined

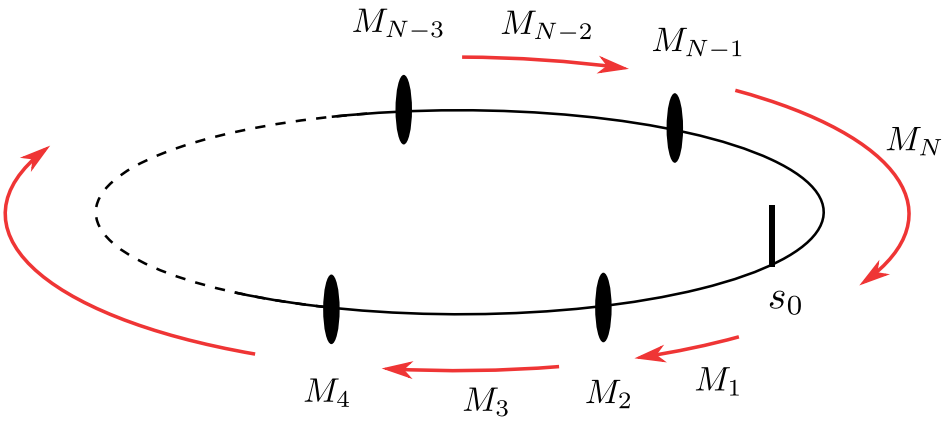

Figure 2.3: *Simplified layout of circular accelerator with linear elements. Magnets are portrayed as black blocks with drift spaces in between. All parts have a corresponding linear map M_i attributed to it.*

to obtain the coordinates after a full revolution of the machine through matrix multiplications,

$$\begin{aligned} \mathbf{z}(s_0 + C) &= M_N \cdot M_{N-1} \cdot \ldots \cdot M_2 \cdot M_1 \cdot \mathbf{z}(s_0) \\ &= \mathbf{M}_{\mathrm{OTM}} \cdot \mathbf{z}(s_0) \, . \end{aligned} \tag{2.10}$$

This special map $\mathbf{M}_{\mathrm{OTM}}$ is called the one-turn map (OTM) and fully describes the linear evolution of the coordinates of particles over one revolution of the accelerator.

Courant-Snyder parameters

Synchrotrons and synchrotron type colliders are specifically built with cells of alternating focussing and defocussing quadrupoles. Such a cell consists of a focussing quadrupole, a drift space followed by a defocussing quadrupole with a drift space. This type of cell is called a FODO cell. A series of such cells forms a periodic lattice as shown in Fig. 2.4. Synchrotrons are often built by combining FODO cells into a periodic lattice. Such periodic lattices can be set up to enforce periodicity in the beam optics. Indeed, even though the individual particles' dynamics do not have the same periodicity as the lattice, the envelope of oscillation amplitudes does show this periodicity.

The phase space $\{z, p_z\}$ at a specific location in the lattice is described by an ellipse, as shown in Fig. 2.5. The shape of the phase space ellipse will change as a function of the longitudinal position in the lattice. For FODO cells, the phase-space

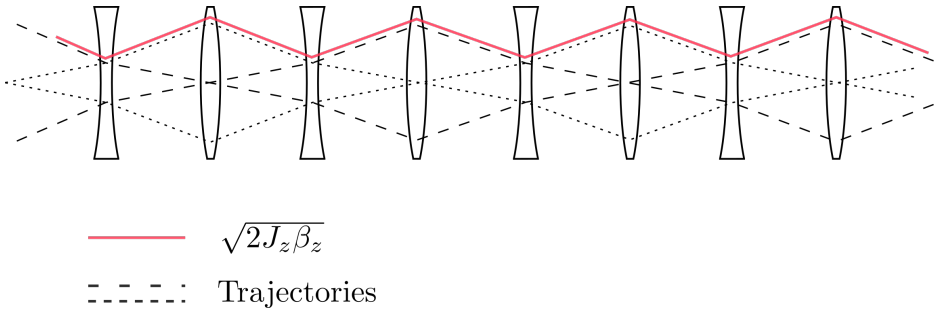

Figure 2.4: *Illustrative graphic of four FODO cells consisting of alternating focussing and defocussing quadrupoles. Sample particle trajectories are shown as dotted lines. The oscillation amplitude of the particles is determined by the β-function $\beta_z(s)$, and the invariant J_z that is introduced in Eq. (2.11), as shown in red.*

ellipse will be the same at each focussing quadrupole and defocussing quadrupole respectively. This ellipse is fully described by the Courant-Snyder parameters $\alpha_z(s)$, $\beta_z(s)$, and $\gamma_z(s)$, also known as Twiss parameters [47] or the optics functions. The ellipse equation that defines the phase-space is given by,

$$J_z = \frac{1}{2}(\gamma_z z^2 + 2\alpha_z z p_z + \beta_z p_z^2) \,, \tag{2.11}$$

where the quantity J_z is the action variable and can be shown to be an invariant of the motion for single particles when the reference energy p_0 is constant. This

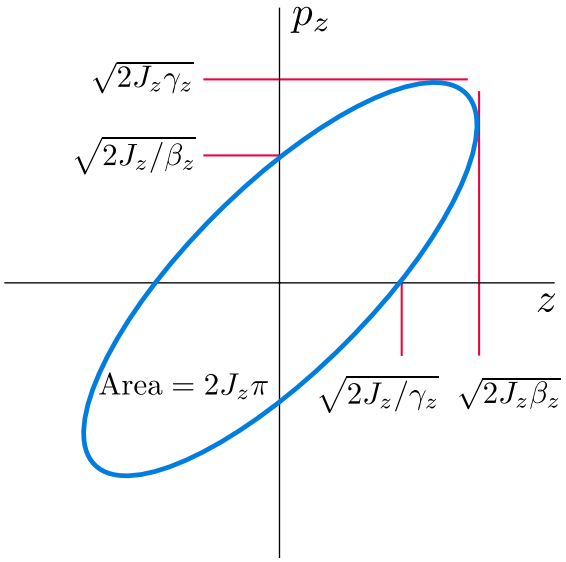

Figure 2.5: *Courant-Snyder ellipse showing the phase-space in physical coordinates and the characteristics of the ellipse as defined by the Courant-Snyder parameters α_z, β_z, γ_z, and action J_z.*

means that as the particles' phase-space coordinates change along the beam line, the Courant-Snyder parameters will change as well to yield an invariant action J_z. Note that the explicit s dependence of the optics functions is left out for clarity of the notation.

The state of particles in phase-space can be fully described by the action variable J_z and a corresponding phase variable ϕ. The phase variable can be defined as,

$$\tan(\phi_z) = -\beta_z \frac{p_z}{z} - \alpha_z \, . \tag{2.12}$$

The inverse of Eqs. (2.11) and (2.12) yield very useful expressions for the phase-space coordinates in terms of action-angle variables,

$$\begin{aligned} z &= \sqrt{2J_z\beta_z}\cos(\phi_z) \, , \\ p_z &= -\sqrt{\frac{2J_z}{\beta_z}}[\sin(\phi_z) + \alpha_z\cos(\phi_z)] \, . \end{aligned} \tag{2.13}$$

The position z in Eq. (2.13) describes a harmonic oscillation, with an oscillation energy that is represented by the action J_z. The parameter β_z, referred to as the β-function or betatron function, describes the envelope of local oscillation amplitude of a particle at a given location due to the changing focussing and defocussing strengths of the quadrupoles. This harmonic oscillation is a solution of Hill's equations for uncoupled linear motion [48],

$$\frac{d^2z}{ds^2} + K_1(s)z = 0 \tag{2.14}$$

where $K_1(s)$ is the quadrupolar focussing at each point along the accelerator and a periodic function.

As a particle moves through a periodic lattice, its oscillation characteristics will vary with the same periodicity as the lattice, due to the fact that the Courant-Snyder parameters follow the lattice periodicity. The α-function (α_z) and the evolution of the phase can be obtained from Eq. (2.13), by taking the derivative of the position coordinate to s,

$$\frac{dz}{ds} = \frac{1}{2}\sqrt{\frac{2J_z}{\beta_z}}\cos(\phi_z)\frac{d\beta_z}{ds} - \sqrt{2\beta_z J_z}\sin(\phi_z)\frac{d\phi_z}{ds} \, . \tag{2.15}$$

By equating Eq. 2.15 to p_z in Eq. 2.13 a few properties are found. Firstly, while the β-function describes the envelope of oscillation around the accelerator, the parameter α_z describes the change of β_z with s, as given by,

$$\alpha_z = -\frac{1}{2}\frac{d\beta_z}{ds} \quad . \tag{2.16}$$

Secondly, the rate of change of the angle variable over longitudinal distances is inversely proportional to the β-function as,

$$\frac{d\phi_z}{ds} = \frac{1}{\beta_z} \, . \tag{2.17}$$

This naturally leads to the definition of the tune as the total number of betatron oscillations during a full turn around the circumference of the accelerator.

$$Q_z = \frac{1}{2\pi} \oint \frac{1}{\beta_z(s)} ds \, . \tag{2.18}$$

The tune is the single most important design parameter in synchrotrons. The tune can greatly affect the excitation of resonances, creation of instabilities, and critically reduce the performance of the machine, or in some cases make machine operation impossible. At the beginning of Run II, the tunes at injection in the LHC were $Q_x = 64.28$ and $Q_y = 59.31$, which indicates that the beam performed 64 full horizontal betatron oscillations. However, the more important part is the fractional tune, as that determines the proximity to resonances, as will be shown later. In the LHC, the fractional tunes at injection are $Q_x = 0.28$ and $Q_y = 0.31$, and currently at collision the tunes are $Q_x = 0.27$ and $Q_y = 0.295$. During most of Run II, the tunes at collision were $Q_x = 0.31$ and $Q_y = 0.32$, which is the more common working point used in the measurements presented in this thesis.

Another valuable beam parameter for particle bunches can be obtained from these functions. The emittance can be defined as the mean of all the individual actions of the particles in the bunch as,

$$\epsilon_z = \langle J_z \rangle \, . \tag{2.19}$$

The emittance is a measure of the area in phase-space that the particles in the beam occupy, and it naturally follows from Eq. 2.19 that the emittance is invariant. The beam size σ_z at a given location is related to the emittance and the local β-functions as given by,

$$\sigma_z(s) = \sqrt{\epsilon_z \beta_z(s)} \, . \tag{2.20}$$

Normalized coordinates

In physical coordinates (z, p_z), the linear one-turn map can be expressed in terms of the Courant-Snyder parameters and the tune as [33],

$$\mathbf{M}_{OTM} = \begin{pmatrix} \cos(2\pi Q_z) + \alpha_z \sin(2\pi Q_z) & \beta_z \sin(2\pi Q_z) \\ -\gamma_z \sin(2\pi Q_z) & \cos(2\pi Q_z) - \alpha_z \sin(2\pi Q_z) \end{pmatrix} . \quad (2.21)$$

This transfer map describes the change of coordinates over a full revolution as a function of the Courant-Snyder parameters at that specific location and the tune of the machine. This is a rather elegant result, in which the tune is sufficient and the optics functions around the rest of the machine are no longer needed. However, the dependencies on the optics functions at the location of observation still complicate calculations.

To further simplify the description of linear motion in a periodic lattice, a coordinate transformation can be applied to obtain the linearly normalized coordinates $\hat{z}$, $\hat{p_z}$, also known as the Courant-Snyder coordinates,

$$\begin{pmatrix} \hat{z} \\ \hat{p_z} \end{pmatrix} = \begin{pmatrix} \frac{1}{\sqrt{\beta_z}} & 0 \\ \frac{\alpha_z}{\sqrt{\beta_z}} & \sqrt{\beta_z} \end{pmatrix} \begin{pmatrix} z \\ p_z \end{pmatrix} , \quad (2.22)$$

where the normalized phase-space coordinates are given by,

$$\begin{aligned} \hat{z} &= \sqrt{2J_z}\cos(\phi_z) , \\ \hat{p}_z &= -\sqrt{2J_z}\sin(\phi_z) . \end{aligned} \quad (2.23)$$

The major benefit of moving to this new coordinate space is that the linear transformations from linear elements reduce to simple rotations. This difference between the two coordinate spaces is shown in Fig. 2.6. A transformation to normalized coordinates generates a circular phase-space, as shown in Fig. 2.6b. The linear one-turn map then reduces to a rotation in phase-space with the tune that is given by,

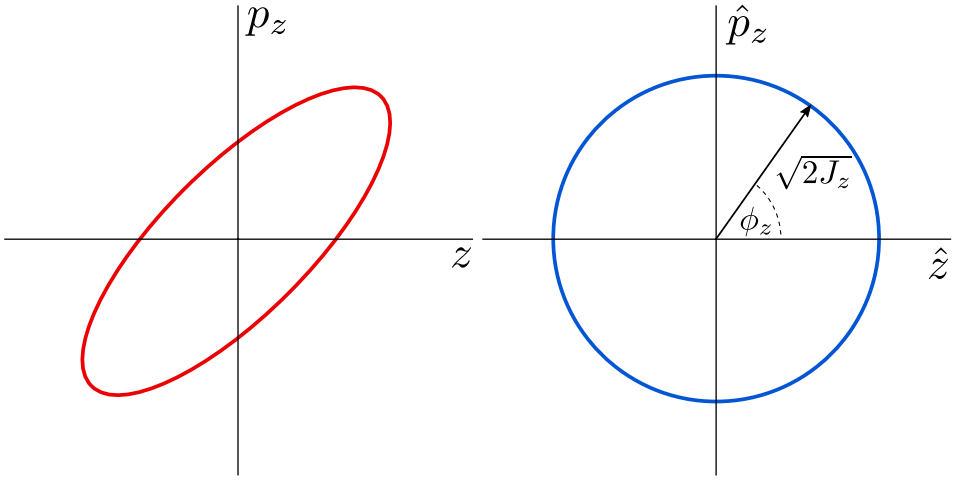

(a) *Physical coordinates* ***(b)*** *Normalized coordinates*

Figure 2.6: *Illustrative representation of phase-space in physical coordinates (left) and normalized coordinates (right) for an accelerator with linear elements only. The Courant-Snyder transformation transforms the elliptical phase-space into a much simpler circular phase-space where the motion is described by simple rotations.*

$$\hat{\mathbf{M}}_{OTM} = \begin{pmatrix} \cos(2\pi Q_z) & \sin(2\pi Q_z) \\ -\sin(2\pi Q_z) & \cos(2\pi Q_z) \end{pmatrix} . \tag{2.24}$$

NONLINEAR LATTICE

The previous section described the linear motion with the approach of linear maps, and concluded with the introduction to the Courant-Snyder coordinates. In this section, this approach is extended to the nonlinear regime and the transformation to normal form coordinates will be introduced. The difficulty is that nonlinear maps cannot be described in simple matrix form. Nonlinear magnetic elements have magnetic fields that do not depend linearly on the transverse position coordinates inside the magnet.

The magnetic field of a sextupole, for example, increases quadratically with the transverse coordinates, thereby making the sextupole the lowest order nonlinear element. To simplify the transfer maps, multipoles are often assumed to be thin in the longitudinal coordinate when the length of the element is small compared to the focal length. In this thin lens approximation the transfer map of a sextupole is

given by,

$$\begin{pmatrix} x \\ p_x \\ y \\ p_y \end{pmatrix}_{s_1} = \begin{pmatrix} x \\ p_x \\ y \\ p_y \end{pmatrix}_{s_0} - \frac{1}{2} L K_2 \begin{pmatrix} 0 \\ x^2 - y^2 \\ 0 \\ -2xy \end{pmatrix} , \tag{2.25}$$

where L is the length of the sextupole, K_2 is the strength of the sextupole, and the coordinates of Eq. (2.25) are shown schematically with respect to the sextupole in Fig. 2.7. The change of coordinates is now no longer linear, and a different approach is needed to derive the particle dynamics.

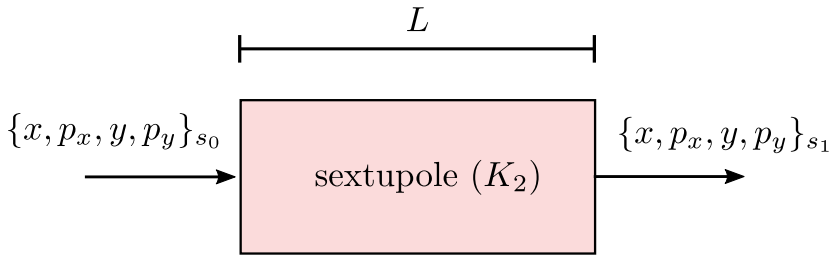

Figure 2.7: *Illustrative representation of coordinates through a sextupole with length L and strength K_2. The transfer map is defined in Eq.* (2.25).

Hamiltonian of electromagnetic elements

To start, the Hamiltonian of a relativistic particle inside an electromagnetic field can be given by,

$$\mathcal{H}(\vec{z}, \vec{p}_z, t) = c\sqrt{(\vec{p} - q\vec{A}(\vec{z}, t))^2 + m_0^2 c^2} + q\Phi(\vec{z}, t) , \tag{2.26}$$

where $\vec{z}$ are the Cartesian positions, $\vec{p}_z$ are the conjugate momenta, $\vec{A}$ is the magnetic vector potential, and Φ is the electric scalar potential. Several approximations and canonical transformations can be used to simplify the Hamiltonian. The coordinate system can be changed to the Frenet-Sernet system of Fig. 2.1, and the independent time variable t can be changed to the path length s. Furthermore, the electric field can be set to zero, and only static transverse magnetic fields can be considered as the effect of longitudinal fields are negligibly small in the LHC. This constraints the vector potential to only have a single component in the direction of

the path length s as $\vec{A} = (0, 0, A_s)$. Lastly, the momentum can be rescaled and the origin can be moved to the closed orbit. The resulting Hamiltonian is then given by,

$$\mathcal{H}(x, p_x, y, p_y, \delta_p) = -\left(1 + \frac{x}{\rho}\right) \cdot \sqrt{(1+\delta_p)^2 - p_x^2 - p_y^2} + \frac{x}{\rho} + \frac{x^2}{2\rho^2} - \frac{A_s(x,y)}{B_0\rho} \,, \tag{2.27}$$

where $\delta_p = (p_s - p_0)/p_s$ is the relative momentum deviation, and A_s is the vector potential in the direction of the path length s, as only transverse magnetic fields are considered. Lastly, the transverse momenta can be assumed to be small, and the horizontal coordinate to be much smaller than the bending radius $x \ll \rho$. In that case the square root can be expanded. Furthermore, as only on momentum particles are considered that are on the closed orbit, δ_p can be set to zero, and the dipolar term $\frac{x^2}{2\rho^2}$ can be ignored. The Hamiltonian is then obtained as,

$$\mathcal{H} = \frac{1}{2}(p_x^2 + p_y^2) - \frac{A_s(x,y)}{B_0\rho} \,. \tag{2.28}$$

It is thus fully dependent on the kinematic part given in terms of p_x^2 and p_y^2, and the vector potential $A_s(x, y)$. All elements act through the vector potential. By knowing the magnetic field of an element, the Hamiltonian of that element can thus be constructed.

Multipolar expansion and multipolar maps

The transverse magnetic field of multipoles can be constrained by a few conditions. In a region of space that is free of currents and charges, as in the vacuum of the beam-pipe of the LHC, the magnetic field must satisfy,

$$\nabla \cdot \mathbf{B} = 0 \,, \tag{2.29}$$

$$\nabla \times \mathbf{B} = 0 \,. \tag{2.30}$$

These equations result in two more constraints on the magnetic field. First, Eq. (2.29) implies that there exists a vector potential that satisfies,

$$\mathbf{B} = \nabla \times \mathbf{A} \,. \tag{2.31}$$

Secondly, Eq. (2.30) implies that the magnetic field can be written as the gradient of a scalar potential V as,

$$\mathbf{B} = -\nabla V \, . \tag{2.32}$$

The relations between field components and potentials are obtained from the previous equations as,

$$B_x = -\frac{\partial V}{\partial x} = \frac{\partial A_s}{\partial y} \, , \quad B_y = -\frac{\partial V}{\partial y} = -\frac{\partial A_s}{\partial x} \, . \tag{2.33}$$

Equations (2.33) are the Cauchy-Riemann conditions for the real and imaginary parts of an analytic function. From this, a complex potential function can be defined as,

$$\begin{aligned} \mathcal{A}(x+iy) &= A_s(x,y) + iV(x,y) \, , & (2.34) \\ &= \sum_{n=1}^{\infty} C_n (x+iy)^n \, , & (2.35) \end{aligned}$$

where the coefficients C_n are complex numbers. The magnetic field of a multipole can then be expressed as an expansion of $\mathcal{A}$ using the complex notation for the transverse position $x+iy$, and taking the derivative with respect to the horizontal coordinate. The multipolar field expansions is then obtained as,

$$\begin{aligned} B_y(x,y,s) + iB_x(x,y,s) &= -\frac{\partial}{\partial x}\mathcal{A}(x+iy) \, , & (2.36) \\ &= \sum_{n=1}^{\infty} [K_{n-1}(s) + iJ_{n-1}(s)](x+iy)^{n-1} \, , & (2.37) \end{aligned}$$

where the coefficients K_{n-1} and J_{n-1} are defined as,

$$K_{n-1}(s) = \frac{1}{B_0\rho}\frac{\partial^{n-1}B_y}{\partial x^{n-1}}\bigg|_{(0,0;s)} \, , \quad J_{n-1}(s) = \frac{1}{B_0\rho}\frac{\partial^{n-1}B_x}{\partial x^{n-1}}\bigg|_{(0,0;s)} \, , \tag{2.38}$$

where n indicates the order of the component with $2n$ poles. The coefficients K_{n-1} and J_{n-1} represent the strengths of normal and skew multipoles respectively. Non-linear fields correspond to orders where $n \geq 3$. So $n = 3$ and $n = 4$ describe sextupoles and octupoles respectively. A skew multipole is the same as a normal

multipole but with a rotation over the longitudinal axis with half its geometric symmetry angle, or $\frac{1}{2}\frac{\pi}{n}$, as shown in Fig. 2.8. Note that rotational errors can create normal and skew field errors in any multipole.

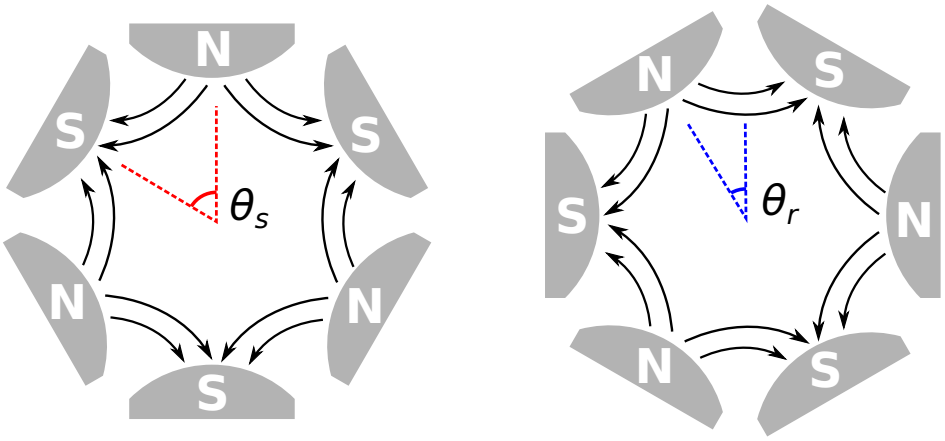

Figure 2.8: *Schematic graphic of a normal sextupole (left) and a skew sextupole (right). A skew element is obtained by rotating a normal element with θ_r that is half the geometric symmetry angle θ_s.*

Since $\vec{B} = \nabla \times \vec{A}$, the Hamiltonian of magnetic elements can be derived from Eq. (2.37). The explicit expression for the kick Hamiltonian and appropriate elements is obtained by taking the real part of the primitive of Eq. (2.37),

$$H = \Re\left[\sum_{n>1}(K_{n-1} + iJ_{n-1})\frac{(x+iy)^n}{n!}\right] = \sum_{n>1} H^{(n)} \quad . \tag{2.39}$$

As an example, the kick Hamiltonian for a normal sextupole can be expressed as,

$$H^{(3)} = \frac{1}{6}K_2(s)[x^3 - 3xy^2] \, , \tag{2.40}$$

and the kick Hamiltonian for a normal quadrupole is given by,

$$H^{(2)} = \frac{1}{2}K_1(s)[x^2 - y^2] \, . \tag{2.41}$$

The full Hamiltonians can be obtained by adding the kinematic part of the Hamiltonian of Eq. (2.28).

Nonlinear transfer maps

Now that the Hamiltonian of a nonlinear element is found, it can be used to define a nonlinear transfer map for that element. For any function g of canonical variables (x, p_x, y, p_y) that is not explicitly dependent on s, the change of g over the distance Δs can be expressed in the form of a Taylor series as in,

$$g|_{s=s_0+\Delta s} = g|_{s=s_0} + \Delta s \frac{dg}{ds}\bigg|_{s=s_0} + \frac{\Delta s^2}{2}\frac{d^2g}{ds^2}\bigg|_{s=s_0} + \dots , \tag{2.42}$$

$$= \sum_{k=0}^{\infty} \frac{\Delta s^k}{k!}\frac{d^k g}{ds^k}\bigg|_{s=s_0} , \tag{2.43}$$

$$= e^{\Delta s \frac{d}{ds}} g|_{s=s_0} . \tag{2.44}$$

This series of polynomial functions describes the final state of a function $g|_{s=s_0+\Delta s}$, as a function of its initial state $g|_{s=s_0}$. This relation can be solved by rewriting the derivative of g to a function of the local Hamiltonian using Hamilton's equations,

$$\frac{dg}{ds} = \frac{dx}{ds}\frac{\partial g}{\partial x} + \frac{dp_x}{ds}\frac{\partial g}{\partial p_x} + \frac{dy}{ds}\frac{\partial g}{\partial y} + \frac{dp_y}{ds}\frac{\partial g}{\partial p_y} , \tag{2.45}$$

$$= \frac{\partial H}{\partial p_x}\frac{\partial g}{\partial x} - \frac{\partial H}{\partial x}\frac{\partial g}{\partial p_x} + \frac{\partial H}{\partial p_y}\frac{\partial g}{\partial y} - \frac{\partial H}{\partial y}\frac{\partial g}{\partial p_y} . \tag{2.46}$$

This expression can be rewritten in a useful way with the introduction of Lie operators. The Lie operator is defined as,

$$: f := \sum_{z=x,y} \frac{\partial f}{\partial z}\frac{\partial}{\partial p_z} - \frac{\partial f}{\partial p_z}\frac{\partial}{\partial z} , \tag{2.47}$$

where the operator $: f :$ has no explicit dependence on s. The Lie operator can be expressed with two different notations, so for an operator f acting on g the following equivalence holds,

$$: f : g \equiv [f, g] . \tag{2.48}$$

The square brackets are also referred to as the Poisson brackets. In the case where the Hamiltonian (H) of an element has no explicit dependence on s either, the

derivative $\frac{dg}{ds}$ of Eq. (2.45) can be rewritten as,

$$\frac{dg}{ds} = - : H : g \,, \tag{2.49}$$

where $: H :$ is the new Lie operator. Using this, Eq. (2.42) is rewritten as,

$$g|_{s=s_0+\Delta s} \;=\; e^{-\Delta s : H :} g|_{s=s_0} \,. \tag{2.50}$$

This equation describes the evolution of a function $g(x, p_x, y, p_y)$ through an element with the local Hamiltonian H. As the function g can be any function of the phase-space variables, it naturally follows to choose g to be the phase-space variables themselves. So, as an example, the final coordinates at s_1 after passing through a thin sextupole with Hamiltonian $H^{(3)}$ and length L, can be obtained as a function of the initial coordinates at s_0,

$$\begin{pmatrix} x \\ p_x \\ y \\ p_y \end{pmatrix}_{s_1} \;=\; e^{-L:H^{(3)}:} \begin{pmatrix} x \\ p_x \\ y \\ p_y \end{pmatrix}_{s_0} = e^{-L:\frac{1}{6}K_2(s)[x^3-3xy^2]:} \begin{pmatrix} x \\ p_x \\ y \\ p_y \end{pmatrix}_{s_0} \,. \tag{2.51}$$

Solving the derivatives of the Lie operator of Eq. (2.47) to first order yields,

$$\begin{pmatrix} x \\ p_x \\ y \\ p_y \end{pmatrix}_{s_1} = \begin{pmatrix} x \\ p_x \\ y \\ p_y \end{pmatrix}_{s_0} - \frac{1}{2} L K_2 \begin{pmatrix} 0 \\ x^2 - y^2 \\ 0 \\ -2xy \end{pmatrix} \,. \tag{2.52}$$

This is the same transfer map as presented in Eq. (2.25). An illustrative representation of the coordinates in Eq. (2.51) is shown in Fig. 2.9. For further illustration, the transfer map of the focussing plane of a thin quadrupole can also be derived,

$$\begin{pmatrix} x \\ p_x \end{pmatrix}_{s_1} \;=\; e^{-L:H^{(2)}:} \begin{pmatrix} x \\ p_x \end{pmatrix}_{s_0} = e^{-L:\frac{1}{2}K_1(s)[x^2-y^2]:} \begin{pmatrix} x \\ p_x \end{pmatrix}_{s_0} \,. \tag{2.53}$$

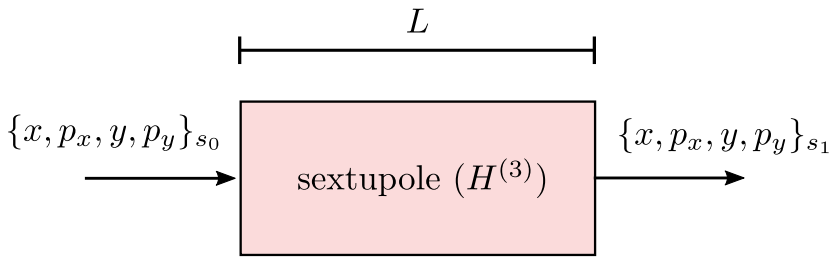

Figure 2.9: *Illustrative representation of coordinates through a sextupole with length L and strength K_2. The transfer map is now determined by the Hamiltonian $H^{(3)}$ as shown in Eq.* (2.51).

This can be solved to obtain,

$$\begin{pmatrix} x \\ p_x \end{pmatrix}_{s_1} = \begin{pmatrix} x \\ p_x \end{pmatrix}_{s_0} - K_1 L \begin{pmatrix} 0 \\ x \end{pmatrix} = \begin{pmatrix} 1 & 0 \\ -K_1 L & 1 \end{pmatrix} \begin{pmatrix} x \\ p_x \end{pmatrix}_{s_0} . \tag{2.54}$$

which is the same as the thin lens approximation shown in Eq. (2.9) for a focussing quadrupole. Both the quadrupolar and sextupolar thin lens approximations are reproduced by solving their respective Hamiltonian Lie operator to first order. However, the order is not limited. A more precise calculation of transfer maps is possible by deriving further orders in the Lie operator. Furthermore, deriving the evolution of particles through thick elements is possible when the kinematic term of the Hamiltonian $\frac{1}{2}(p_x^2 + p_y^2)$ is included.

The nonlinear maps of multipoles can thus be expressed as maps in Lie operator format by their Hamiltonians and their lengths. Using the multipolar expansion of Eq. (2.39), the transformation of variables through any nonlinear element can be calculated, and due to the expression of nonlinear transfer maps as Lie operators, the combined effect of multiple nonlinear sources can be easily calculated.

COMBINING NONLINEAR MAPS

The derived normalized coordinates can be rewritten into a more usable form in the form of the complex normalized coordinates using,

$$\xi_{z,\pm} = \hat{z} \pm i\hat{p}_z \, , \tag{2.55}$$

which yields a 4D complex coordinate space,

$$\boldsymbol{\xi} = \begin{pmatrix} \xi_{x,+} \\ \xi_{x,-} \\ \xi_{y,+} \\ \xi_{y,-} \end{pmatrix} = \begin{pmatrix} \sqrt{2J_x}e^{-i(\phi_x+\phi_{x,0})} \\ \sqrt{2J_x}e^{i(\phi_x+\phi_{x,0})} \\ \sqrt{2J_y}e^{-i(\phi_y+\phi_{y,0})} \\ \sqrt{2J_y}e^{i(\phi_y+\phi_{y,0})} \end{pmatrix} . \tag{2.56}$$

In this notation, the linear evolution of the coordinates takes an even simpler form. The evolution through the linear lattice is described by rotations with the phases. For a particle going from point s_0 to s_1, where the phase advance is given by $\Delta\phi_z = \phi_z(s_1) - \phi_z(s_0)$, the complex coordinates at s_1 are expressed in terms of the coordinates at s_0 as,

$$\xi_{z,\pm}(s_1) = e^{\mp i\Delta\phi_z}\xi_{z,\pm}(s_0) . \tag{2.57}$$

The one-turn map can similarly be defined as a rotation operator R. In the case of the horizontal complex coordinate $\xi_{x,+}$ the evolution over one turn is now expressed as,

$$\begin{aligned} \xi_{x,+}(s_0 + C) &= R\xi_{x,+}(s_0) && (2.58) \\ &= e^{-i2\pi Q_x}\xi_{x,+}(s_0) . && (2.59) \end{aligned}$$

Figure 2.10 shows a schematic representation of an accelerator lattice with nonlinear elements shown as black blocks with corresponding nonlinear maps H_w, and linear sections with corresponding linear maps M_w interleaved between the nonlinear elements. The nonlinear elements can represent known nonlinear magnets such as sextupoles and octupoles, but can also represent nonlinear errors arising in linear elements due to limitations in manufacturing processes, misalignments, and rotations. Analog to the linear case the composition of all successive linear and nonlinear maps yield a one-turn map that relates the initial coordinate of a particle to the final coordinates after a full revolution of the accelerator. The full nonlinear one-turn map at location s_0 is given by,

$$\mathcal{M} = M_{W+1}\prod_{w=1}^{W} e^{:H_w:}M_w . \tag{2.60}$$

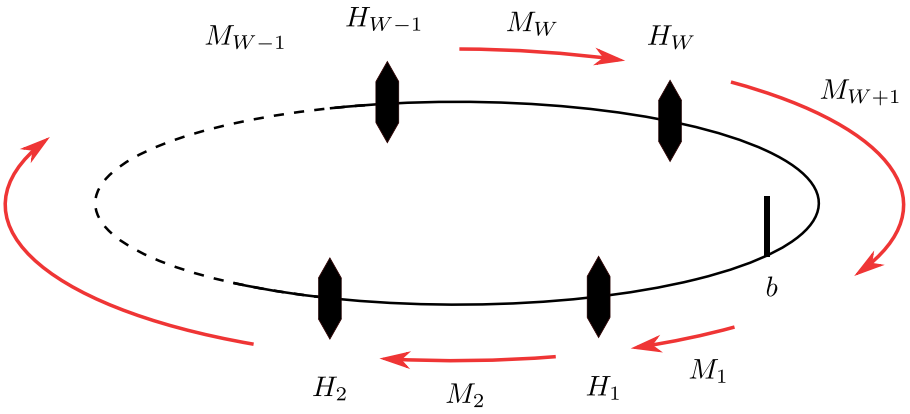

Figure 2.10: *Simplified representation of an accelerator lattice with linear elements (M_w) and nonlinear elements (H_w). The nonlinear elements are shown as black blocks, while the space in between contains all linear elements in between the nonlinear counterparts.*

Here, $\mathcal{M}$ is the nonlinear one-turn map, M_w are the linear maps of the linear elements at location w, $e^{:H_w:}$ are the nonlinear maps of the nonlinear elements at location w, and M_{W+1} is the final linear map closing the loop. A transformation to normalized coordinates as presented in Sec. 2.1 reduces the linear maps to phase-space rotations. It can be shown that in this normalized phase-space the nonlinear one-turn map then reduces to [49],

$$\tilde{\mathcal{M}} = \prod_{w=1}^{W} e^{:\tilde{H}_w:} R \,, \tag{2.61}$$

where R is the linear rotational matrix describing the linear motion over one turn, and the new Hamiltonians $\tilde{H}_w$ are expressed as a function of the normalized coordinates at the location of observation b propagated by the linear map between that location and the location w. The normalized coordinates propagated from the location w are given by,

$$\boldsymbol{\xi_{bw}} = \tilde{M}_b \cdot \tilde{M}_{b+1} \ldots \tilde{M}_w \, \boldsymbol{\xi_w} \,, \tag{2.62}$$

where $\tilde{M}_i$ are the linear maps normalized by Eq. (2.22) and have the form of rotations in phase-space. Using the fact that this is in normalized space, the composition of linear maps also becomes a simple rotation. As such, the propagated coordinates are just the initial coordinates propagated by the phase advance between the initial location and location w,

$$\xi_{bw,z,\pm} = \xi_{w,z,\pm} e^{\mp i \Delta\phi_{bw,z}} \ , \tag{2.63}$$

where $\Delta\phi_{bw,z}$ is the phase advance between the initial location b and the location of the source w. The Hamiltonians of Eq. (2.61) are thus expressed as,

$$\tilde{H}_w = H_w(\boldsymbol{\xi_{bw}}) \ . \tag{2.64}$$

The properties of Lie operators can be used to solve the product of Eq. (2.61). The Campbell-Baker-Hausdorf theorem [50] expresses the concatenation of multiple exponential Lie operators into a single new exponential Lie operator,

$$e^{:f_1:} e^{:f_2:} = e^{:f:} \ , \tag{2.65}$$

where,

$$f = f_1 + f_2 + \frac{1}{2}[f_1, f_2] + \dots \ . \tag{2.66}$$

Generally, for cases where the generators f_1 and f_2 are small enough such that the series converges quickly, only the first two terms of Eq. (2.66) are used. Assuming that the nonlinear perturbations are small compared to the linear motion, the one-turn map is expressed as a single exponential Lie operator using the Campbell-Baker-Hausdorf theorem,

$$\tilde{\mathcal{M}} = e^{:\tilde{H}:} R \ , \tag{2.67}$$

where $\tilde{\mathcal{M}}$ is the one-turn map to first order in the nonlinear perturbation, and the concatenated Hamiltonian is given by,

$$\tilde{H} \approx \sum_{w=1}^{W} \tilde{H}_w \ . \tag{2.68}$$

Note that this results in a single Hamiltonian describing the nonlinear evolution of the coordinates over one turn at a single location, as a sum of all the sources in the accelerator. The sum can then be expanded in terms of the eigencoordinates of

Eq. (2.56) as,

$$\tilde{H} = \sum_{w=1}^{W} \sum_{jklm} h_{w,jklm} e^{i[(j-k)\Delta\phi_{w,x}+(l-m)\Delta\phi_{w,y}]} \xi_{w,x,+}^{j} \xi_{w,x,-}^{k} \xi_{w,y,+}^{l} \xi_{w,y,-}^{m} \ , \tag{2.69}$$

where the multipolar order is given by $n = j + k + l + m$, $\xi_{w,z,\pm}$ are the Courant-Snyder complex coordinates at the specific nonlinear magnet w, and $\Delta\phi_{w,z}$ is the phase advance from the reference point to the specific magnet. The Hamiltonian coefficients $h_{w,jklm}$ are obtained by rewriting x and y of Eq. (2.39) in terms of the complex coordinates as,

$$x = \frac{1}{2}\sqrt{\beta_x}(\xi_{x,+} + \xi_{x,-}) \tag{2.70}$$

$$y = \frac{1}{2}\sqrt{\beta_y}(\xi_{y,+} + \xi_{y,-}) \ . \tag{2.71}$$

By invoking the binomial theorem to expand the coordinates, the Hamiltonian coefficients can finally be obtained as [51],

$$h_{w,jklm} = -\frac{[K_{w,n-1}\Omega(l+m) + iJ_{w,n-1}\Omega(l+m+1)]}{j!\ k!\ l!\ m!\ 2^{j+k+l+m}}\ i^{l+m} \beta_{x,w}^{\frac{(j+k)}{2}} \beta_{y,w}^{\frac{(l+m)}{2}} \ , \tag{2.72}$$

where $\Omega(i)$ does the job of selecting either the normal (K_w) or the skew (J_w) multipoles,

$$\Omega(i) = 1 \quad \text{if } i \text{ is even} \tag{2.73}$$

$$\Omega(i) = 0 \quad \text{if } i \text{ is odd} \ . \tag{2.74}$$

The magnitude of the Hamiltonian terms are directly proportional to the strength of the sources with K_w and J_w and are proportional with the β-functions with $\beta_{x,w}^{\frac{(j+k)}{2}} \beta_{y,w}^{\frac{(l+m)}{2}}$. This indicates that the larger the β-function is at the location of a nonlinear source, the more sensitive it becomes to the nonlinear error. Not surprisingly this becomes important in the LHC, where the β-functions in the final focus sections of the experimental insertion regions can become very large.

NORMAL FORM FORMALISM

Although a one-turn map is found in normalized space for the nonlinear motion, it turns out to be complicated to use. The phase-space is distorted by the nonlinear perturbations losing its invariance, and calculations of the turn-by-turn motion become difficult. An analogous transformation to the linear Courant-Snyder transformation can be found in the nonlinear case to simplify the form of the one-turn map. This Normal Form transformation yields a new coordinate system with circular phase-space, which represents an amplitude dependent rotation that is easier to handle. Figure 2.11 shows an illustrative representation of the phase-space through the two coordinate transformations. Figure 2.11a shows the initial phase-space in physical coordinates (z, p_z). The Courant-Snyder transformation of Eq. (2.22) to normalized coordinates $(\hat{z}, \hat{p}_z)$ transforms the phase-space to Fig. 2.11b. However, this transformation does not account for all the nonlinear contributions of multipolar fields. For this, the final normal form transformation is used to obtain a circular phase-space in terms of new normal form complex coordinates $(\zeta_{z,\pm})$, as shown in Fig. 2.11c.

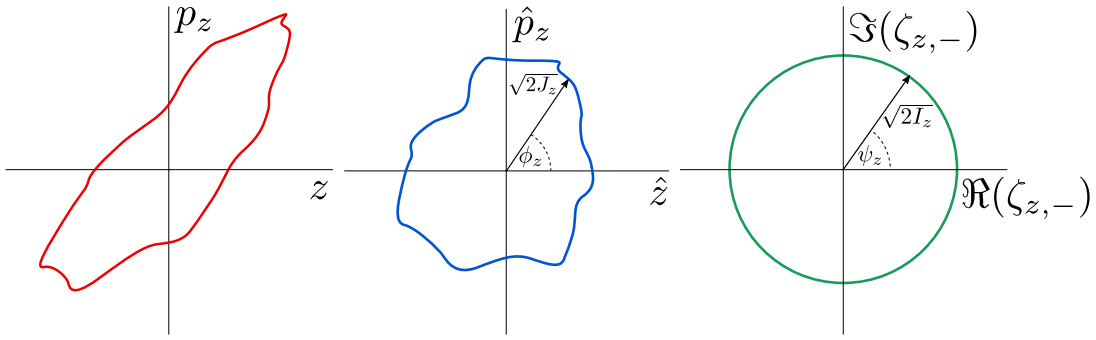

(a) *Physical coordinates* ***(b)*** *Normalized coordinates* ***(c)*** *Normal form coordinates*

Figure 2.11: *Phase-space representations in the three different coordinate systems. The first shows the phase-space in physical coordinates, the second in normalized coordinates after the Courant-Snyder transformation, while the last shows the phase-space in normal form coordinates after the normal form transformation. This is an exaggerated schematic representation for illustrative purposes.*

A transformation exists that transforms the one-turn map into the simplest form of an amplitude dependent rotation. The generating function of this transformation is found by a similarity transformation,

$$e^{-:F:}\tilde{\mathcal{M}}e^{:F:} = e^{:H(I):}R \ , \tag{2.75}$$

where F is the generating function of the normal form transformation, $H(I)$ describes the average of H over the phase variables, and I is the new invariant in the normal form space. Using the definition of the one-turn map from Eq. (2.67), and the properties of exponential Lie operators, the transformation can be rewritten as,

$$e^{-:F:}e^{:\tilde{H}:}e^{:RF:}R = e^{:H(I):}R \ . \tag{2.76}$$

Solving the transformation up to first order using the Campbell-Baker-Hausdorf theorem, the following is obtained,

$$(R-1)F + \tilde{H} = H(I) \ . \tag{2.77}$$

Finally, the generating function is found by solving Eq. (2.77) for F,

$$F = \frac{1}{1-R}(\tilde{H} - H(I)) \ . \tag{2.78}$$

Figure 2.12 presents a practical scheme that shows the different transformations and changes to the one-turn map. To calculate the evolution of the normalized coordinates one can directly solve the problem in Courant-Snyder coordinates by applying the map $\tilde{\mathcal{M}}$. However, this approach is complicated and difficult to solve. It is far easier to transform to normal form coordinates ($\boldsymbol{\zeta}$) first, using the calculated generating function F, apply the amplitude dependent rotation R, and lastly transform back to the normalized coordinates ($\boldsymbol{\xi}$). All nonlinearities of the motion are included in the transformation F, which simplifies the calculations.

$$\begin{array}{ccc} \boldsymbol{\xi}_N & \xrightarrow{\quad\tilde{\mathcal{M}}\quad} & \boldsymbol{\xi}_{N+1} \\ \Big\downarrow e^{:-F:} & & \Big\uparrow e^{:F:} \\ \boldsymbol{\zeta}_N & \xrightarrow[\mathrm{R} = e^{:\mathrm{H}:}R]{} & \boldsymbol{\zeta}_{N+1} \end{array}$$

Figure 2.12: *Scheme representing the coordinate transformations and change of the one-turn map, where N is the turn number. Solving the one-turn map for the next turn is best done by performing a transformation to normal form coordinates ($\boldsymbol{\zeta}$), apply the amplitude dependent rotation map (*R*), and transform back to normalized coordinates ($\boldsymbol{\xi}$).*

First the new normal form coordinates are defined as,

$$\zeta_{z,\pm} = \sqrt{2I_z} e^{(\mp i(\psi_z + \psi_{z0}))} \ , \tag{2.79}$$

where I_z is the new motion invariant and ψ_z and ψ_{z0} are the new phases and initial conditions respectively. The generating function F is now given by,

$$F = \sum_{jklm} f_{jklm} \zeta_{x,+}^{j} \zeta_{x,-}^{k} \zeta_{y,+}^{l} \zeta_{y,-}^{m} \ , \tag{2.80}$$

where f_{jklm} are the resonance driving terms (RDTs). The resonance driving terms f_{jklm} are related to the Hamiltonian terms h_{jklm} by,

$$f_{jklm} = \frac{h_{jklm}}{1 - e^{i2\pi[(j-k)Q_x + (l-m)Q_y]}} \ , \tag{2.81}$$

where the Hamiltonian coefficients are obtained from Eq. (2.72) to be,

$$h_{jklm} = \sum_{w} h_{w,jklm} e^{i[(j-k)\Delta\phi_x + (l-m)\Delta\phi_y]} \ . \tag{2.82}$$

In normal form coordinates, the one-turn map describes an amplitude dependent rotation. Using this and the definition of the normal form coordinates of Eq. (2.79) the turn-by-turn motion of in the normal form basis as a function of turn number N is easily given by,

$$\zeta_{z,\pm}(N) = \sqrt{2I_z} e^{(\mp i(2\pi Q_z N + \psi_{z0}))} \ , \tag{2.83}$$

where N is the number of turns and Q_z is the tune of the accelerator. Note that in normal form the tunes Q_z are now amplitude dependent due to the amplitude dependent rotation of the normal form one-turn map. The turn-by-turn motion in normalized coordinates can be constructed by transforming back to Courant-Snyder coordinates using the generating function,

$$\xi_{z,\pm}(N) = e^{:F:} \zeta_{z,\pm}(N) \ . \tag{2.84}$$

As an example, the turn evolution of the normalized horizontal coordinate $\xi_{x,-}(N)$ can be written as a function of the number of turns as,

$$\begin{aligned}\xi_{x,-}(N) &= \sqrt{2I_x}e^{i(2\pi Q_x N+\psi_{x0})} \\ &\quad -2i\sum_{jklm} j f_{jklm}(2I_x)^{\frac{j+k-1}{2}}(2I_y)^{\frac{l+m}{2}} \\ &\quad \times e^{i[(1-j+k)(2\pi Q_x N+\psi_{x0})+(m-l)(2\pi Q_y N+\psi_{y0})]}\,. \end{aligned} \tag{2.85}$$

This expression describes the full nonlinear motion in normalized coordinates for free transverse oscillations. The first part describes the linear motion, while the nonlinear contributions are expressed in the summation over the resonance driving terms f_{jklm}. This expression may be viewed as a spectral decomposition of the motion, where the linear part drives a mode with the tune frequency Q_x, while the specific resonance driving terms drive specific frequencies of $(k-j+1)Q_x+(m-l)Q_y$. The spectral analysis of the transverse position at a location in the accelerator can thus reveal all the nonlinear modes that perturb the linear motion at that location.

The denominator of Eq. (2.81) specifies the resonance conditions as a function of the tunes Q_x and Q_y. The resonance driving terms will drive different resonances dependent on the multipolar order of the sources and the repartitioning of the indices j,k,l and m. The appropriate choice of tunes is critical to avoid resonances from nonlinear elements. Figure 2.13 shows a resonance diagram with all the resonances up to decapolar order. Each line represents a resonance that satisfies the condition,

$$(j-k)Q_x+(l-m)Q_y = \mathrm{q}, \tag{2.86}$$

where q is an integer. The red dot in Fig. 2.13 represents the tunes at injection energy as used in the LHC.

The nonlinear modes are also dependent on the invariants I_x and I_y. It shows that the secondary mode content of the signal can be enhanced by increasing the amplitude of oscillation. This is the reason why large transverse oscillations of the beams are necessary to measure resonance driving terms and to probe nonlinearities in the machine.

In all, the resonance driving terms represent a measure for the nonlinearity of the machine. This can be directly due to nonlinear elements, but also due to nonlinear errors arising in quadrupoles and dipoles from the manufacturing process or from misalignments and rotations of the magnets. These nonlinear sources can be modelled exactly as a nonlinear magnet. Measurements of resonance driving terms can

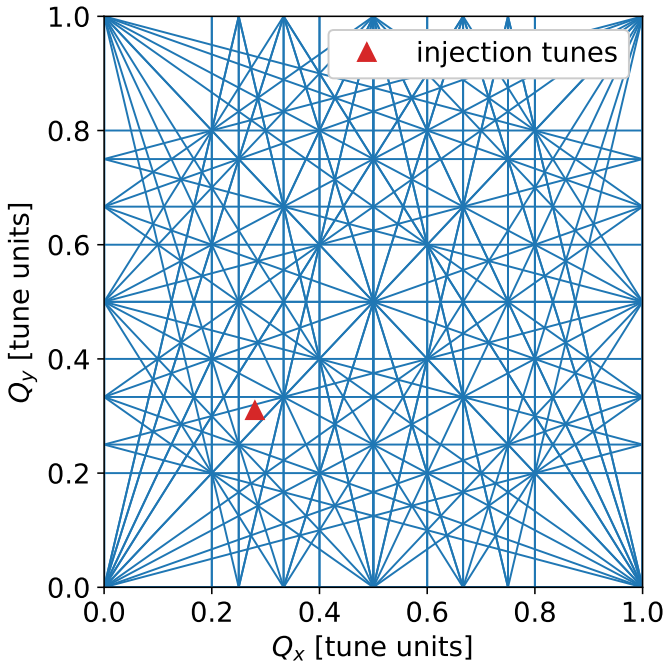

Figure 2.13: *Resonance diagram showing all resonances up to decapolar order. The tunes Q_x and Q_y are chosen in an area where resonances are scarce. At injection energy in the LHC, the tunes are $Q_x = 0.28$ and $Q_y = 0.31$.*

thus be used to measure and identify specific sources of nonlinearities in the machine. By comparing this to simulations, specific corrections can be implemented in the machine to correct for these nonlinear perturbations.

MEASUREMENTS OF RESONANCE DRIVING TERMS

The derivations presented so far are limited to free transverse oscillations. Measurements of resonance driving terms are generally done by exciting the beam in the transverse plane with a single kick. In the LHC this can be done using the aperture kicker [52]. The transverse position of the beam is recorded at each turn using Beam Position Monitors (BPMs) at around 550 locations around the accelerator. The turn-by-turn data obtained from the BPMs provides a discrete oscillation signal of the beam at a single location that is described by Eq. (2.85). Spectral analysis of this signal reveals all the secondary spectral modes that are related to the resonance driving terms.

Unfortunately, the aperture kicker cannot be used at top energy in the LHC. From a point of view of machine protection considerations, the aperture kicker is too powerful and can potentially cause significant losses of the beams in a few

turns, which is too fast for current safety feedback systems to act upon. Secondly, a beam that is excited by a single kick will decohere. In Eq. (2.75) it is shown that the remaining rotation term is amplitude dependent. In other words, particles with different amplitudes will have different total phase advances over one turn, or different tunes. Due to the distribution of the bunch, over time, the bunch will decohere. The decrease of amplitude observed in Fig. 1.1 for a kicked beam is not due to damping of the beam, but purely due to the decoherence of the beam. As the beam decoheres, the centroid of charge of the beam will gradually decrease to zero. What is left is a bunch that is blown up, and that is not reusable for further measurements. Measurements with single kicks therefore would require a dump and reinject scheme that would be far too time consuming.

In practice, almost all optics measurements in the LHC are performed using the ac dipoles. The ac dipoles adiabatically drive a coherent transverse oscillation of the beam, and can adiabatically damp the oscillation. The forced motion with ac dipoles creates a long lasting coherent oscillation between the ramping up and ramping down of the ac dipole current. Forced beam excitations with ac dipoles are non-destructive, as the state of the beam is recovered after ramping down the ac dipole. Therefore multiple measurements can be taken in series, in a scheme that does not require reinjections of fresh beams. All following chapters pertain to the forced motion with ac dipoles. The derivations of the free resonance driving terms in this chapter serve as an introduction to the forced resonance driving terms presented in Chapter 4.

3

LINEAR FORCED MOTION WITH AC DIPOLES

The ac dipoles are the single most important tool for optics measurements in the LHC. A good understanding of the motion of particles under forced oscillations with ac dipoles is thus critical. The linear forced motion was first parametrized in [53]. This section will summarize the derivations of forced linear motion of [53], and introduce an ensuing parametrization [54]. Although the final parametrization could be given straight away, the steps in the derivation offer an insight in the studies of Chapter 4, where a new nonlinear parametrization of the forced motion is given. First, the linear Courant-Snyder complex coordinate of the free motion is used,

$$\xi_{z,\pm} = \sqrt{2J_z} e^{\mp i(\phi_z + \phi_{z0})} \quad , \tag{3.1}$$

and the turn evolution is given by,

$$\xi_{z,\pm}(t+1) = R\xi_{z,\pm}(t) \quad , \tag{3.2}$$

where t is the turn number, and $R = e^{\mp i2\pi Q_z}$ describes the rotation of the coordinate with the natural tune. Equations (3.1) and (3.2) describe the evolution of a particle under free motion. At the location of the ac dipole, this particle will receive a kick from the ac dipole. The kick from the ac dipole is defined as

$$\begin{aligned} \Delta\xi_{z,\pm}(t) &= \delta\sqrt{\beta_{\mathrm{acd},z}}\cos(2\pi Q_{\mathrm{d},z}t + \chi_0) & (3.3)\\ &= \frac{\delta\sqrt{\beta_{\mathrm{acd},z}}}{2}[e^{i(2\pi Q_{\mathrm{d},z}t+\chi_0)} + e^{-i(2\pi Q_{\mathrm{d},z}t+\chi_0)}] \quad , & (3.4) \end{aligned}$$

where $\delta = \frac{BL}{(B_0\rho)}$, BL is the integrated field amplitude of the ac dipole, $\sqrt{\beta_{\mathrm{acd},z}}$ is the free β-function at the location of the ac dipole, $Q_{\mathrm{d},z}$ is the drive tune of the ac dipole and χ_0 is the initial phase of the ac dipole.

At a location just before the ac dipole, a particle with initial coordinate $\xi_{z,\pm}(0)$

is defined. It will first experience the kick of the ac dipole of Eq. (3.3), followed by the the one-turn evolution described by (3.2). Over the course of several turns the particle will feel a kick at every turn and then propagate with the free tune. For simplicity and clarity of notation the coordinate at turn t is written as ξ_t, and the kick at turn t is written as $\Delta\xi_t$. The coordinate after τ turns is then given by,

$$\xi_\tau = R^\tau \xi_0 + R^\tau \Delta\xi_0 + R^{\tau-1}\Delta\xi_1 + R^{\tau-2}\Delta\xi_2 + ... + R^2\Delta\xi_{\tau-2} + R\Delta\xi_{\tau-1} \quad . \tag{3.5}$$

By substituting Eq. (3.4) in Eq. (3.5) this is rewritten to,

$$\xi_\tau = R^\tau \xi_0 + \frac{1}{2}\delta e^{i\chi_0} R^\tau \sum_{t=0}^{\tau-1} \mathrm{p}_-^t + \frac{1}{2}\delta e^{-i\chi_0} R^\tau \sum_{t=0}^{\tau-1} \mathrm{p}_+^t \quad , \tag{3.6}$$

where,

$$\mathrm{p}_\pm = e^{-i2\pi(Q_z \mp Q_{\mathrm{d},z})} \quad . \tag{3.7}$$

The following identity can be used to obtain the general solution for the linear motion,

$$\sum_{t=0}^{\tau-1} \mathrm{p}^t = \frac{\mathrm{p}^\tau - 1}{\mathrm{p} - 1} \quad . \tag{3.8}$$

The solution for the linear motion under influence of an ac dipole is then given after some algebra by,

$$\xi_{z,\pm}(\tau) = \sqrt{2J_z} e^{\mp i(2\pi Q_z \tau + \phi_{z,0})} + \delta_{z,-} e^{\mp i2\pi Q_{\mathrm{d},z}\tau} - \delta_{z,+} e^{\pm i2\pi Q_{\mathrm{d},z}\tau} \quad , \tag{3.9}$$

where,

$$\delta_{z,-} = \frac{\delta}{4} \frac{e^{-i[\pi(Q_{\mathrm{d},z} - Q_z) - \chi_0]}}{\sin[\pi(Q_{\mathrm{d},z} - Q_z)]} \tag{3.10}$$

$$\delta_{z,+} = \frac{\delta}{4} \frac{e^{i[\pi(Q_{\mathrm{d},z} + Q_z) - \chi_0]}}{\sin[\pi(Q_{\mathrm{d},z} + Q_z)]} \quad . \tag{3.11}$$

Equation (3.9) describes three linear modes that together form the forced linear motion. The first mode is the free mode, describing the linear motion of a particle in the absence of ac dipoles. The second two modes are the forced modes. The first

of the forced modes arises from the difference resonance between the ac dipole tune and the natural tune $(Q_{d,z} - Q_z)$, as shown in Eq. (3.10). The second forced mode is related to the sum resonance between the forced tune and natural tune $(Q_{d,z} + Q_z)$, as shown in Eq. (3.11). In general the ac dipole tunes are chosen in such a way that the difference resonance is excited, such that $|\delta_{z,-}| \gg |\delta_{z,+}|$. A parameter λ_z is defined as the ratio of amplitudes between the second mode and the main mode of the ac dipole as,

$$\lambda_z = \frac{\delta_{z,+}}{\delta_{z,-}} \tag{3.12}$$

$$= \frac{\sin[\pi(Q_{d,z} - Q_z)]}{\sin[\pi(Q_{d,z} + Q_z)]} \,. \tag{3.13}$$

By choosing the ac dipole tunes to be close to the natural tunes the parameter λ_z is minimized. Generally, during optics measurements in the LHC, the parameter will be of the order of a few percent.

COMBINED AC DIPOLE MODES

The parametrization of linear forced motion was further developed in [54], where the two forced modes of the ac dipoles are combined to a single mode. The price paid for this simplification is the introduction of new perturbed optics functions $(\alpha_{d,z}, \beta_{d,z}, \gamma_{d,z})$, referred to as the forced optics functions or forced Courant-Snyder parameters. An analogy is later made between the forced optics functions and optics functions perturbed by a quadrupolar error. This analogy will prove to be very useful in Chapter 4.

Ignoring the free part of the motion of Eq. (3.9) the transverse position of a particle can be expressed as,

$$\begin{aligned} z_d(\tau C + \Delta s) = & \frac{\theta_{d,z}\sqrt{\beta_{acd,z}}}{4\sin[\pi(Q_{d,z} - Q_z)]}\sqrt{\beta_z(\Delta s)} \\ & \times \cos(2\pi Q_{d,z}\tau + \phi_z(\Delta s) + \pi(Q_{d,z} - Q_z) + \chi_d) \\ & + \frac{\theta_{d,z}\sqrt{\beta_{acd,z}}}{4\sin[\pi(Q_{d,z} + Q_z)]}\sqrt{\beta_z(\Delta s)} \\ & \times \cos(-2\pi Q_{d,z}\tau + \phi_z(\Delta s) + \pi(Q_{d,z} + Q_z) - \chi_d) \,, \end{aligned} \tag{3.14}$$

where $\theta_{d,z}$ is the maximum kick angle. The two terms in Eq. (3.14) can be combined

into a compact form with new forced optics functions that are continuous in s [54],

$$z_{\mathrm{d}}(s) \;=\; \sqrt{2A_{\mathrm{d},z}\beta_{\mathrm{d},z}(s)}\cos(\phi_{\mathrm{d},z}(s)+\chi_{\mathrm{d}})\;, \tag{3.15}$$

where the new constant of motion $A_{\mathrm{d},z}$ is defined as,

$$A_{\mathrm{d},z} = \frac{\theta_{\mathrm{d},z}}{4\sin(\pi[Q_{\mathrm{d},z}-Q_z)]}\sqrt{(1-\lambda_z^2)\beta_{\mathrm{acd},z}} \quad , \tag{3.16}$$

and where the forced β-function is defined as,

$$\beta_{\mathrm{d},z}(s) = \frac{1+\lambda_z^2-2\lambda_z\cos(2\phi_z(s)-2\pi Q_z)}{1-\lambda_z^2}\beta_z(s)\;. \tag{3.17}$$

This new forced β-function, $\beta_{\mathrm{d},z}(s)$, describes a beating over $\beta_z(s)$ with a deviation of the order of λ_z. It should be noted that as the ac dipole tunes approach the natural tunes, $\beta_{\mathrm{d},z}(s)$ will converge to $\beta_z(s)$.

The new forced phase $\phi_{\mathrm{d},z}(s)$ is defined as,

$$\begin{aligned}\tan[\phi_{\mathrm{d},z}(s)-\pi Q_{\mathrm{d},z}] &= \frac{1+\lambda_{\mathrm{d},z}}{1-\lambda_{\mathrm{d},z}}\tan[\phi_z(s)-\pi Q_z] \\ &= \frac{\tan(\pi Q_{\mathrm{d},z})}{\tan(\pi Q_z)}\tan[\phi_z(s)-\pi Q_z] \quad .\end{aligned} \tag{3.18}$$

All the forced optics functions ($\alpha_{\mathrm{d},z}$, $\beta_{\mathrm{d},z}$, $\gamma_{\mathrm{d},z}$) behave in the same way as their free counterpart (α_z, β_z, γ_z) and describe a phase-space ellipse. The only difference being that this forced parameter ellipse has a slightly different shape compared to the free parameter ellipse.

FORCED OPTICS AS GRADIENT ERROR

The benefit of this new parametrization of the forced motion is that the forced optics functions closely resemble the optics functions under the influence of a single quadrupolar error. A quadrupolar error creates a deformation of the phase-space that is analogous to that of the forced parameters. It is remarkable that the effect of an oscillating dipole field yields the same effect on the phase-space as a gradient error. This analogy allows to easily calculate the forced optics functions by inserting a quadrupole in the nominal lattice. The strength of this quadrupole will be determined by the the forced and free tunes as well as the free β-function at the

location of the ac dipole. The strength q_{acd} of a quadrupole at the location of the ac dipole is given by,

$$\begin{aligned} q_{\mathrm{acd}} &= \frac{\theta_{\mathrm{d},z}}{A_{\mathrm{d},z}\sqrt{\beta_{\mathrm{d},z}(0)}} \\ &= 2\frac{\cos(2\pi Q_z) - \cos(2\pi Q_{\mathrm{d},z})}{\beta_{\mathrm{acd},z}\sin(2\pi Q_z)} \quad . \end{aligned} \tag{3.19}$$

This does not mean that the ac dipole acts like a true quadrupole on the optics, but it merely states that the phase-space is modified in a way that is analogous to a quadrupole error. In practice, forced optics functions are calculated in simulations by inserting a quadrupole with its strength as defined by Eq. (3.19) at the location of the ac dipole and calculating the free optics functions. The free optics functions calculated with this fictive quadrupole reflect the forced optics functions observed from forced oscillation with ac dipoles, as shown in Fig.3.1.

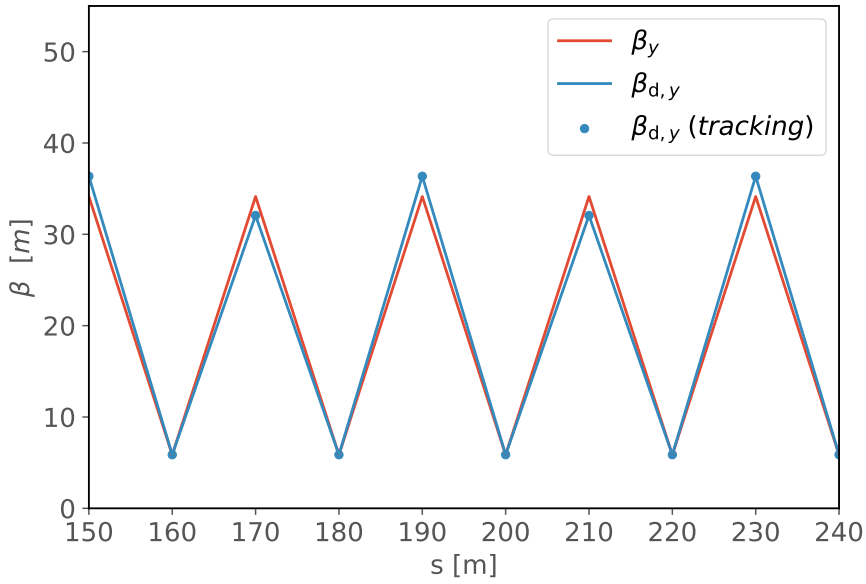

Figure 3.1: *Results from β-functions calculations for a FODO lattice with the free lattice and with the forced lattice, compared to the results obtained from tracking simulations.*

4

FORCED RESONANCE DRIVING TERMS

Resonance driving terms promise to be a valuable observable for the measurement and correction of nonlinear magnetic errors in the LHC. Measurements of resonance driving terms can be performed by exciting the beam with a single kick using the aperture kicker. Unfortunately, this method is not deemed safe at top energy in the LHC, as it poses the risk of causing large losses that are too fast for current safety feedback systems to act upon.

Currently, resonance driving terms can only be measured at top-energy by using the ac dipole for transverse beam excitations. Chapter 3 presented how the forced motion with ac dipoles changes the linear motion of particles. However, these changes are not limited to the linear motion. The nonlinear beam dynamics are also perturbed by the use of the ac dipole, which infers a change in the description of the resonance driving terms.

A first parametrization of resonance driving terms under the influence of forced oscillations from ac dipoles, also known as forced resonance driving terms, was presented in [49]. This derived the forced resonance driving terms in the free Courant-Snyder parameter space in one dimension and under the assumption that the main mode of the ac dipole is much larger that the secondary mode, i.e. $|\delta_{z,-}| \gg |\delta_{z,+}|$. An extension of this approach in two dimensions including the effect of the second mode is presented in Appendix A, where it is shown that serious complications arise in the parametrization of forced resonance driving terms when these additional requirements are taken into account. Spectral lines are now no longer driven by a single resonance driving term, but by multiple driving terms of the same order with different strengths. This stands in stark contrast to the resonance driving terms of the free motion as presented in Sec. 2.4 where each resonance driving term drives a single spectral line.

The studies presented in this chapter reflect a continuation of Chapters 2 and 3 as well as the studies presented in [49]. This chapter offers a parametrization of forced resonance driving terms in the forced Courant-Snyder parameter space of Chapter 3 using the forced optics parameters $\alpha_{\mathrm{d},z}$, $\beta_{\mathrm{d},z}$, and $\gamma_{\mathrm{d},z}$. It shows that significant simplifications arise by moving to the forced Courant-Snyder space. Sec-

ondly, this chapter explores for the first time a second order contribution from the ac dipole to the resonance driving terms.

FORCED RESONANCE DRIVING TERMS

F.S. Carlier, R. Tomás

Physical Review Accelerators and Beams
Submitted 25 November 2019

ABSTRACT

This paper presents the derivation of resonance driving terms under forced oscillations with ac dipoles in the forced Courant-Snyder parameter space. Forced resonance driving terms take a simple form when analysed in forced parameter space. A new parametrization of forced resonance driving terms is presented that more accurately reproduces results from tracking simulations in forced parameter space. Furthermore, a new contribution from ac dipoles to resonance driving terms is observed. An analytical description of this perturbation cross-term between ac dipole and resonance driving terms is presented and validated in simulations.

INTRODUCTION

Forced oscillations from ac dipoles are widely used as a diagnostics tool for optics measurements in synchrotrons [37, 38, 42, 53–63]. Recently the forced motion has become increasingly important to measure nonlinear beam dynamics as well [3, 5, 43, 49, 53, 64–67]. A good understanding of nonlinear forced motion is thus crucial for measurements of nonlinear dynamics in synchrotrons.

Forced oscillations change the direct observables in the transverse turn-by-turn motion. Next to the free motion, two other modes are introduced to the linear motion by the ac dipoles. One mode relates to the difference resonance between the free motion and the ac dipole, while the other relates to the sum resonance. The oscillation amplitudes and phases are perturbed by these two ac dipole modes [54]. The analysis of the nonlinear motion, specifically of resonance driving terms, of forced oscillations has until now relied on the normal form description of the forced motion in free parameter space [49]. This analysis features complexity by staying in the free optics parameters, as the free phase and β-functions need to be calculated separately.

In [54] it is shown that the parametrization of the linear forced motion when combining the two ac dipole modes closely resembles that of the free motion. New forced optics functions (α_d, β_d, γ_d) arise to describe the forced motion. Simulations in this paper show that the analysis of resonance driving terms in this forced parameter space is simpler than in the free parameter space. An important finding is that the forced resonance driving terms have a constant amplitude between nonlinear sources, while current theoretical predictions expect amplitude beating due to mixing of modes. Furthermore, moving to the forced parameter space better reflects the direct observables from BPM turn-by-turn data.

It is useful at this point to illustrate the main difference between forced resonance driving terms analysed in the free parameter space and those analysed in the forced parameter space. A single particle tracking simulation of a FODO lattice with a closed skew sextupole bump is used. The sextupoles are positioned at π phase advance of each other to form a closed resonance driving term bump, and the ac dipole is placed at $s = 0$. Further details of tracking procedures are best left in the simulations section in Sec. 4.5.

Figure 4.1 shows the normalized phase-space using turn-by-turn data from ac dipole excitations. In red the normalized phase-space using the free Courant-Snyder parameters is shown, while the normalized phase-space with forced parameters is shown in blue. The normalized phase-space is expected to have a constant ampli-

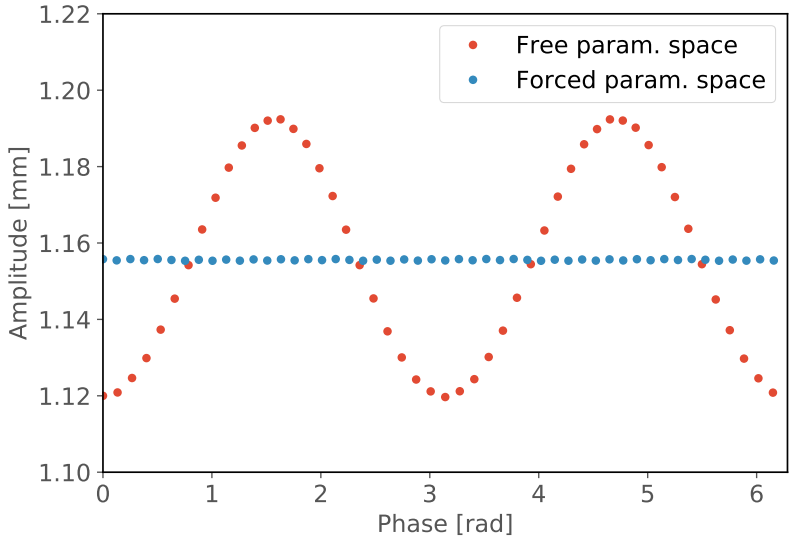

Figure 4.1: *Phase-space obtained from the complex signal reconstruction of two BPMs using free (blue) and forced (orange) Courant-Snyder parameters.*

tude over phases, i.e. a circular phase-space. This is clearly reflected in the obtained results using the forced parameters. Using free Courant-Snyder parameters to normalize the phase-space of forced oscillations introduces a beating that eventually propagates to the resonance driving terms.

The resonance driving terms from tracking simulations when analysed in the free parameter space as opposed to the forced parameter space are shown in Figure 4.2. A significant amplitude beating is observed when the analysis is performed in the free parameter space. This beating arises from deformed phase-space of the forced motion that is not accounted for in the free optics parameters, and further motivates the analysis of forced resonance driving in the forced parameter space.

This paper presents the challenges encountered when deriving the resonance driving terms following the normal form approach established in the free parameter space and extending it to the forced parameter space. A new description of the forced resonance driving terms that more closely matches the direct observables is proposed. The results present an elegant parametrization of the nonlinear forced motion, where the resonance driving term amplitudes are constant between sources.

Furthermore, it is observed for the first time that the amplitude and phase of resonance driving terms are perturbed at the location of the ac dipole. The second order effects of the ac dipoles have until now never been considered. However, a second order cross-term between the ac dipole and the resonance driving terms

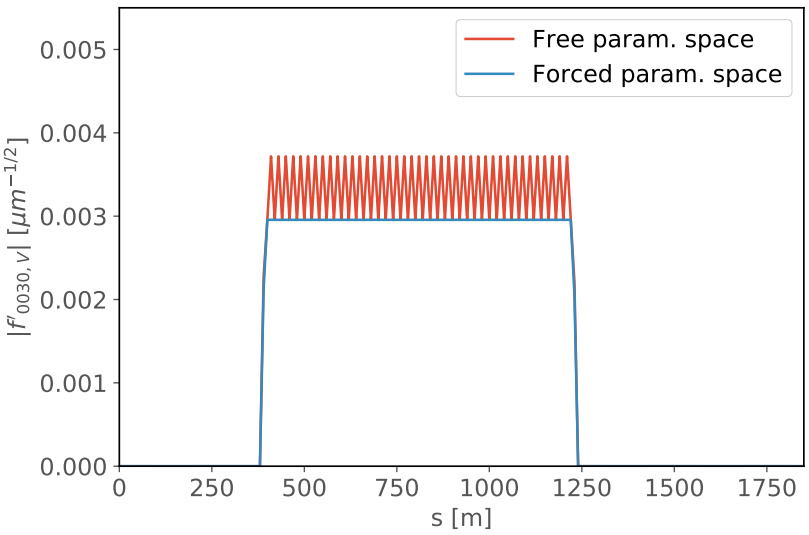

Figure 4.2: *Amplitude of f_{0030} resonance driving term obtained from the analysis in free parameter space (red) and in forced parameter space (blue). A significant amplitude beating is found in the free parameter space.*

becomes relevant for the calculation of resonance driving terms. Such perturbations further show the complexity of the forced motion and highlight the need for improved understanding of nonlinear forced motion.

This paper proceeds by presenting the derivations of the linear complex normalized coordinates as well as a first derivation of the normal form in forced parameter space in Sec. 4.2. An approximation is made following observations and a resulting parametrization of the forced parameter space is presented in Sec. 4.3. This is followed by an analytical derivation of second order perturbations of ac dipoles is presented in Sec. 4.4. Simulations with a closed skew sextupole resonance driving terms bump will be shown throughout the derivations to illustrate specific observations and offer motivation for certain derivations. Finally Sec. 4.5 compares the analytical parametrization of forced resonance driving terms to single particle tracking simulations for various test cases.

FORCED THEORY

The theoretical framework for the derivation of resonance driving terms is presented in this section. First a full parametrization of the forced motion is needed in the forced parameter space before an extension into the nonlinear domain is

presented.

Linear forced motion

Under forced motion with an ac dipole the parametrization of the transverse motion along the longitudinal position s can be defined in the parameter space of the free motion as in [43, 49, 53, 54] by,

$$\begin{aligned} x(\tau C + \Delta s) &= \sqrt{2J_x\beta_x(\Delta s)}\cos(2\pi Q_x\tau + \phi_x(\Delta s) + \phi_0) \\ &+ \frac{\theta_{\mathrm{d},x}\sqrt{\beta_{\mathrm{acd},x}}}{4\sin(\pi Q_{x,-})}\sqrt{\beta_x(\Delta s)}\cos(2\pi Q_{\mathrm{d},x}\tau + \phi_x(\Delta s) + \pi Q_{x,-} + \chi_\mathrm{d}) \\ &+ \frac{\theta_{\mathrm{d},x}\sqrt{\beta_{\mathrm{acd},x}}}{4\sin(\pi Q_{x,+})}\sqrt{\beta_x(\Delta s)}\cos(-2\pi Q_{\mathrm{d},x}\tau + \phi_x(\Delta s) + \pi Q_{x,+} - \chi_\mathrm{d})\ . \end{aligned} \tag{4.1}$$

Here J_x is the invariant of the free motion, ϕ_x and β_x are the free phase and β-functions around the accelerator, $\theta_{\mathrm{d},x}$ is the maximum kick angle from the ac dipole, $\beta_{\mathrm{acd},x}$ is the free β-function at the location of the ac dipole, Q_x and $Q_{\mathrm{d},x}$ are respectively the free and forced tunes, $Q_{x,\pm}$ is defined as $Q_{x,\pm} = Q_{\mathrm{d},x} \pm Q_x$, χ_d is the initial phase of the ac dipole, while ϕ_0 is the initial free phase, τ is the number of turns, and lastly C is the circumference of the accelerator.

Note that in this description the longitudinal position is determined by Δs and not of s, where $0 \leq \Delta s < C$. A discontinuity arises at the location of the ac dipole ($s = 0$) [54]. This discontinuity, as well as the presence of two ac dipole modes greatly complicates the calculation of resonance driving terms [49].

The two modes of the ac dipole related to the difference and sum resonances are described in the two last summands of Eq. (4.1) respectively. In [54] it is shown that the two ac dipole modes can be combined into a single forced mode that is continuous in s, accompanied by new forced optics functions α_d, β_d and γ_d, as well as new amplitude and phase variables A_d and ϕ_d. The complete linear parametrization then becomes,

$$\begin{aligned} x(s) &= \sqrt{2J_x\beta_x(s)}\cos(\phi_x(s) + \phi_0) \\ &+ \sqrt{2A_{\mathrm{d},x}\beta_{\mathrm{d},x}(s)}\cos(\phi_{\mathrm{d},x}(s) + \chi_\mathrm{d})\ , \end{aligned} \tag{4.2}$$

where $A_{\mathrm{d},x}$ and $\phi_{\mathrm{d},x}$ are the new amplitude and phase parameters of forced motion, and $\beta_{\mathrm{d},x}$ is the forced β-function. The forced phase $\phi_{\mathrm{d},x}$ is defined as [54],

$$\tan[\phi_{\mathrm{d},x}(s) - \pi Q_{\mathrm{d},x}] = \frac{1+\lambda_x}{1-\lambda_x}\tan[\phi_x(s) - \pi Q_x] \tag{4.3}$$

while the forced β-function $\beta_{\mathrm{d},x}$ is defined by,

$$\beta_{\mathrm{d},x}(s) = \frac{1+\lambda_x^2 - 2\lambda_x\cos(2\phi_x(s) - 2\pi Q_x)}{1-\lambda_x^2}\beta_x(s)\ . \tag{4.4}$$

The parameter λ_x is the ratio of amplitudes between the second mode and the main mode of the ac dipole, and it is defined by,

$$\lambda_x = \frac{\sin[\pi(Q_{x,-})]}{\sin[\pi(Q_{x,+})]}\ . \tag{4.5}$$

In general, the ac dipole tunes are chosen close to the natural tunes such that the difference resonance is enhanced as opposed to the sum resonance. The parameter λ_x is thus generally very small, of the order of a few percent.

The transverse momentum is obtained from the derivative of the position coordinate over the longitudinal variable and is defined as,

$$\begin{aligned} p_x(s) \;=\; & -\alpha_x\sqrt{\frac{2J_x}{\beta_x(s)}}\cos(\phi_x(s)+\phi_0) \\ & -\sqrt{\frac{2J_x}{\beta_x(s)}}\sin(\phi_x(s)+\phi_0) \\ & -\alpha_{\mathrm{d},x}\sqrt{\frac{2A_{\mathrm{d},x}}{\beta_{\mathrm{d},x}(s)}}\cos(\phi_{\mathrm{d},x}(s)+\chi_{\mathrm{d}}) \\ & -\sqrt{\frac{2A_{\mathrm{d},x}}{\beta_{\mathrm{d},x}(s)}}\sin(\phi_{\mathrm{d},x}(s)+\chi_{\mathrm{d}})\ , \end{aligned} \tag{4.6}$$

where α_x and $\alpha_{\mathrm{d},x}$ are the Courant-Snyder α-functions for the free and forced components. The forced $\alpha_{\mathrm{d},x}$ parameter is defined analogously to the free motion as,

$$\alpha_{\mathrm{d},x} = -\frac{1}{2}\frac{d\beta_{\mathrm{d},x}(s)}{ds} \tag{4.7}$$

Traditionally the linear normalization to Courant-Snyder coordinates is performed

using the free parameters. In this case, however, the normalization will be performed using the forced parameters. This will lead to great simplifications in subsequent normal form derivations. The normalized coordinates are found with the Courant-Snyder transformation using the forced parameters,

$$\begin{pmatrix} \hat{x} \\ \hat{p}_x \end{pmatrix} = \begin{pmatrix} \frac{1}{\sqrt{\beta_{\mathrm{d},x}}} & 0 \\ \frac{\alpha_{\mathrm{d},x}}{\sqrt{\beta_{\mathrm{d},x}}} & \sqrt{\beta_{\mathrm{d},x}} \end{pmatrix} \begin{pmatrix} x \\ p_x \end{pmatrix} , \tag{4.8}$$

where $\hat{x}$ and $\hat{p}_x$ indicate the linearly normalized coordinates and are defined by,

$$\begin{aligned} \hat{x}(s) &= \sqrt{\frac{2J_x}{r_{\beta,x}}} \cos(\phi_x(s) + \phi_0) + \sqrt{2A_{\mathrm{d},x}} \cos(\phi_{\mathrm{d},x}(s) + \chi_{\mathrm{d}}) \\ \hat{p}_x(s) &= \sqrt{2J_x} \left(\frac{\alpha_{\mathrm{d},x}}{\sqrt{r_{\beta,x}}} - \alpha_x \sqrt{r_{\beta,x}} \right) \cos(\phi_x(s) + \phi_0) \\ &\quad - \sqrt{2J_x r_{\beta,x}} \sin(\phi_x(s) + \phi_0) \\ &\quad - \sqrt{2A_{\mathrm{d},x}} \sin(\phi_{\mathrm{d},x}(s) + \chi_{\mathrm{d}}) \, . \end{aligned} \tag{4.9}$$

The parameter $r_{\beta,x}$ is the ratio of the forced over free β-functions $\frac{\beta_{\mathrm{d},x}(s)}{\beta_x(s)}$. The linearly normalized complex coordinate $\xi_{x,\pm}$ is then defined as,

$$\xi_{x,\pm}(s) = \hat{x}(s) \pm i\hat{p}_x(s) \, . \tag{4.10}$$

Specifically the coordinate $\xi_{x,-}(s)$ is given by,

$$\begin{aligned} \xi_{x,-}(s) &= \sqrt{2A_{\mathrm{d},x}} e^{i(\phi_{\mathrm{d},x}(s) + \chi_{\mathrm{d}})} + \sqrt{\frac{2J_x}{r_{\beta,x}}} \Big(\cos(\phi_x(s) + \phi_0) \\ &\quad - i \Big[(\alpha_{\mathrm{d},x} - \alpha_x r_{\beta,x}) \cos(\phi_x(s) + \phi_0) \\ &\quad - r_{\beta,x} \sin(\phi_x(s) + \phi_0) \Big] \Big) \, . \end{aligned} \tag{4.11}$$

The free part is written in the form of complex exponentials as,

$$\sqrt{\frac{2J_x}{r_{\beta,x}}}\Big(\cos(\phi_x(s)+\phi_0) - i\Big[(\alpha_{\mathrm{d},x}-\alpha_x r_{\beta,x})\cos(\phi_x(s)+\phi_0) - r_{\beta,x}\sin(\phi_x(s)+\phi_0)\Big]\Big)$$
$$= \sqrt{\frac{2J_x}{1-\lambda_x^2}}e^{i[\phi_d(s)-\pi Q_{x,-}]}e^{i\phi_0} + \lambda_x\sqrt{\frac{2J_x}{1-\lambda_x^2}}e^{i[\phi_d(s)-\pi Q_{x,+}]}e^{-i\phi_0}\,. \tag{4.12}$$

Here the amplitudes of the two exponential modes are found by expanding all the cosines and sines in exponential form and solving the equation, while the phase terms are obtained numerically. Equation (4.12) is only valid for s in the range $[0, C)$. Finally, combining these results, the complex linear coordinate is given by,

$$\begin{aligned}\xi_{x,-} &= \sqrt{2A_{\mathrm{d},x}}e^{i(2\pi Q_{\mathrm{d},x}\tau+\chi_{\mathrm{d}})} \\ &\quad +\sqrt{2J'_x}e^{i(\phi_x-\pi Q_{x,-}+\phi_0)} \\ &\quad +\lambda_x\sqrt{2J'_x}e^{-i(\phi_x+\pi Q_{x,+}+\phi_0)}\,.\end{aligned} \tag{4.13}$$

where the canonical variable ϕ_x is written out explicitly, $J'_x = \frac{J_x}{1-\lambda_x^2}$, and the s dependence is extracted such that the coordinate at a specific location is given by,

$$\xi_{x,-}(s) = e^{i\phi_{\mathrm{d},x}(s)}\xi_{x,-} \tag{4.14}$$

Equation (4.14) shows that between two locations in the lattice the phase advance is given by $\Delta\phi_{\mathrm{d},x}$ for both the forced and the free modes. Furthermore, the turn-like motion can be expressed as a function of turn T as,

$$\begin{aligned}(R_x R_\tau)^T\xi_{x,-} &= (R_x R_\tau)^T\Big[\sqrt{2A_{\mathrm{d},x}}e^{i(2\pi Q_{\mathrm{d},x}\tau+\chi_{\mathrm{d}})} \\ &\quad +\sqrt{2J'_x}e^{i(\phi_x-\pi Q_{x,-}+\phi_0)} \\ &\quad +\lambda_x\sqrt{2J'_x}e^{-i(\phi_x+\pi Q_{x,+}+\phi_0)}\Big]\,.\end{aligned} \tag{4.15}$$

where the rotation operators R_τ and R_x are defined as $R_\tau\tau = \tau + 1$ and $R_x\phi_x = \phi_x + 2\pi Q_x$.

Nonlinear one-turn-map

The nonlinear one-turn-map is given as a function of the initial coordinates by,

$$\mathcal{M} = \left(\prod_{n=1}^{N} M_n e^{:h_n:} \right) M_{N+1} \tag{4.16}$$

where M_n are the linear maps between nonlinear elements, and h_n are the Hamiltonians of the nonlinear elements. The last linear map M_{N+1} is needed to close the turn to the starting location. From Eq. (4.15) the propagation of the coordinates along s are shown to be dependent on the forced phase only, hence the linear maps M_n will describe a rotation with the forced phase between the nonlinear elements.

The linear maps in the nonlinear one-turn-map can be concatenated to obtain,

$$\mathcal{M} = \left(\prod_{n=1}^{N} e^{:\tilde{h}_n:} \right) \tilde{M}_{N+1} \tag{4.17}$$

where $\tilde{h}_n$ is the Hamiltonian of the n^{th} element expressed as a function of the coordinates at the location of observation, and $\tilde{M}_{N+1}$ is the product of all the individual linear maps M_n. In the forced parameter space obtained with the normalization of Eq. (4.8) the linear map $\tilde{M}_{N+1}$ is a rotation with the forced tune, where the rotation is defined as,

$$\tilde{M}_{N+1}\xi_{z,\pm} = e^{\mp i 2\pi Q_{\mathrm{d},z}}\xi_{z,\pm} \quad . \tag{4.18}$$

However, this map is not the one-turn-map, it represents the map from just after the ac dipole till just before the ac dipole. It does not reproduce the turn-by-turn motion obtained in Eq. (4.15), as this map is only dependent on the forced tunes. The correct turn-by-turn motion is generally retrieved by implementing a tune jump at the location of the ac dipole as in [49], and replacing the map $\tilde{M}_{N+1}$ by the rotation operators $R_{x,y}R_{\tau}$. New coordinates are then defined before and after the ac dipole as,

$$\begin{aligned}\xi^{<}_{x,-} &= e^{i\phi_{\mathrm{d},x}(s)}\Big[\sqrt{2A_{\mathrm{d},x}}e^{i(2\pi Q_{\mathrm{d},x}\tau+\chi_{\mathrm{d}})} \\ &\quad +\sqrt{2J'_x}e^{i(\phi_x-\pi Q_{x,-}+\phi_0)} \\ &\quad +\lambda_x\sqrt{2J'_x}e^{-i(\phi_x+\pi Q_{x,+}+\phi_0)}\Big] \quad . \end{aligned} \tag{4.19}$$

$$\begin{aligned}\xi^{>}_{x,-} &= e^{i\phi_{\mathrm{d},x}(s)}\Big[\sqrt{2A_{\mathrm{d},x}}e^{i(2\pi Q_{\mathrm{d},x}\tau+\chi_{\mathrm{d}})} \\ &\quad +\sqrt{2J'_x}e^{i(\phi_x-\pi Q_{x,-}+\phi_0)}e^{-i2\pi Q_{x,-}} \\ &\quad +\lambda_x\sqrt{2J'_x}e^{-i(\phi_x+\pi Q_{x,+}+\phi_0)}e^{-i2\pi Q_{x,+}}\Big] \quad . \end{aligned} \tag{4.20}$$

where $\xi^{<}_{x,-}$ is the coordinate between the point of observation and the ac dipole and $\xi^{>}_{x,-}$ is the coordinate after the ac dipole till the point of observation.

Using the Campbell-Baker-Hausdorff theorem the exponential nonlinear maps of Eq. (4.17) can be combined into a single map. To first order in the nonlinear perturbations the new nonlinear Hamiltonian is given by,

$$\tilde{H} = \sum_{n=1}^{N} \tilde{h}_n \tag{4.21}$$

and the resulting one-turn-map is then obtained as,

$$\mathcal{M} = e^{:\tilde{H}:}R_{x,y}R_{\tau} \quad . \tag{4.22}$$

The Hamiltonian $\tilde{H}$ can be expanded in terms of the eigencoordinates as,

$$\begin{aligned}\tilde{H} &= \sum_{jklm} h^{<}_{jklm}\xi^{<,j}_{x,+}\xi^{<,k}_{x,-}\xi^{<,l}_{y,+}\xi^{<,m}_{y,-} \\ &\quad + \sum_{jklm} h^{>}_{jklm}\xi^{>,j}_{x,+}\xi^{>,k}_{x,-}\xi^{>,l}_{y,+}\xi^{>,m}_{y,-} \end{aligned} \tag{4.23}$$

where the Hamiltonian terms $h^{<}_{jklm}$ are the contributions from sources before the ac dipole, while $h^{>}_{jklm}$ contains the contributions from sources after the ac dipole and are given by,

$$h^{>/<}_{jklm} = \sum_n h^{>/<}_{n,jklm}e^{i[(j-k)\Delta\phi_{\mathrm{d},n,x}+(l-m)\Delta\phi_{\mathrm{d},n,y}]} \tag{4.24}$$

where $\Delta\phi_{\mathrm{d},n,z}$ are the phase advances from the reference point to the specific nonlin-

ear element n. In this case $h^{<}_{jklm}$ will be the sum over all sources n that are between the reference point and the ac dipole, as $\Delta\phi_{\mathrm{d},n,z} < \Delta\phi_{\mathrm{d,acd},z}$. While $h^{<}_{jklm}$ is the sum over all sources that are between the ac dipole and the reference point, for $\Delta\phi_{\mathrm{d},n,z} > \Delta\phi_{\mathrm{d,acd},z}$. The Hamiltonian coefficients $h_{n,jklm}$ are given by

$$\begin{aligned} h_{n,jklm} &= -\frac{[K_{n,q-1}\Omega(l+m) + iJ_{n,q-1}\Omega(l+m+1)]}{j!\ k!\ l!\ m!\ 2^{j+k+l+m}} \\ &\quad \times i^{l+m}\beta_{\mathrm{d},x,w}^{\frac{(j+k)}{2}}\beta_{\mathrm{d},y,w}^{\frac{(l+m)}{2}} \quad , \end{aligned} \tag{4.25}$$

where the multipolar order is given by $q = j + k + l + m$, and where $\Omega(i) = 1$ does the job of selecting either the normal (K) or the skew multipoles (J) as,

$$\Omega(i) = 1 \quad \text{if } i \text{ is even} \tag{4.26}$$

$$\Omega(i) = 0 \quad \text{if } i \text{ is odd} \quad . \tag{4.27}$$

Note that the description of the Hamiltonian terms h_{jklm} relies on forced parameters only, and is analogous to the free motion treatment in free parameter space.

Normal form

The normal form method [49, 68–70] is the preferred approach to derive the nonlinear motion in accelerators. The detailed derivations of the normal form approach applied in the forced parameter space are presented in Appendix 4.7. The resulting nonlinear coordinate is given by,

$$\begin{aligned} \xi_{x,-} &= \sqrt{2A_{\mathrm{d},x}}e^{i2\pi(Q_{\mathrm{d},x}\tau+\chi_{\mathrm{d},x})} \\ &\quad -2i\sum_{jklm} f_{jklm}(2A_{\mathrm{d},x})^{\frac{j+k-1}{2}}(2A_{\mathrm{d},y})^{\frac{m+l}{2}}e^{i2\pi[(k-j+1)(Q_{\mathrm{d},x}\tau+\chi_{\mathrm{d},x})+(m-l)(Q_{\mathrm{d},y}\tau+\chi_{\mathrm{d},y})]} \end{aligned} \tag{4.28}$$

where the forced resonance driving terms f_{jklm} are given by,

$$
\begin{aligned}
f_{jklm} \;=\; & \frac{1}{1-\lambda_x^2}\Bigg[j\frac{h^{<}_{jklm} + h^{>}_{jklm} e^{i2\pi Q_{x,-}}}{1-e^{i2\pi[-Q_x+(k-j+1)Q_{\mathrm{d},x}+(m-l)Q_{\mathrm{d},y}]}} \\
& -j\lambda_x^2 \frac{h^{<}_{jklm} + h^{>}_{jklm} e^{i2\pi Q_{x,+}}}{1-e^{i2\pi[Q_x+(k-j+1)Q_{\mathrm{d},x}+(m-l)Q_{\mathrm{d},y}]}} \\
& -k\lambda_x e^{-i2\pi Q_{\mathrm{d},x}} \frac{h^{<}_{j-1,k+1,lm} + h^{>}_{j-1,k+1,lm} e^{-i2\pi Q_{x,-}}}{1-e^{i2\pi[Q_x+(k-j+1)Q_{\mathrm{d},x}+(m-l)Q_{\mathrm{d},y}]}} \\
& +k\lambda_x e^{-i2\pi Q_{\mathrm{d},x}} \frac{h^{<}_{j-1,k+1,lm} + h^{>}_{j-1,k+1,lm} e^{-i2\pi Q_{x,+}}}{1-e^{i2\pi[-Q_x+(k-j+1)Q_{\mathrm{d},x}+(m-l)Q_{\mathrm{d},y}]}} \Bigg]
\end{aligned}
\tag{4.29}
$$

Equation (4.29) shows that there are four contributions to resonance driving terms from solving the normal form to first order. There is a main mode that does not depend on λ in the numerator, one that depends on λ_x^2, and two modes that depend on λ_x. Interestingly, the two nonlinear modes that depend on λ_x also have an extra phase factor that depends on the forced tune. These four contributions cannot be simplified into a single contribution due to the different resonance denominators, as a result of the two rotation operators of Eq. (4.22). The results of Eq. (4.28) show that multiple Hamiltonian terms will contribute to the same spectral line with different orders in λ_x. As the Hamiltonian terms that contribute to the same line will not oscillate with the same phase, a beating of the resonance driving terms is predicted.

Figure 4.3 shows the amplitude of f_{0030} from tracking simulations and from the predictions of Eq. (4.28) for a model with a closed sextupole driving term bump, and illustrates the main discrepancy between the predictions and tracking results. The first important observation is that forced resonance driving terms as analysed in forced parameter space have constant amplitudes between sources. This result clearly contradicts the predictions of Eq. (4.29) where a superposition of four modes of different orders in λ_x is expected. This superposition leads to amplitude beating of the resonance driving terms, due to the different Hamiltonian terms and resonance denominators. This discrepancy is not understood and is bypassed with an approximation shown in the following section.

APPROXIMATION OF THE NONLINEAR MOTION

Unfortunately the development of forced resonance driving terms as presented above offers contradicting results with simulations and significantly increases the

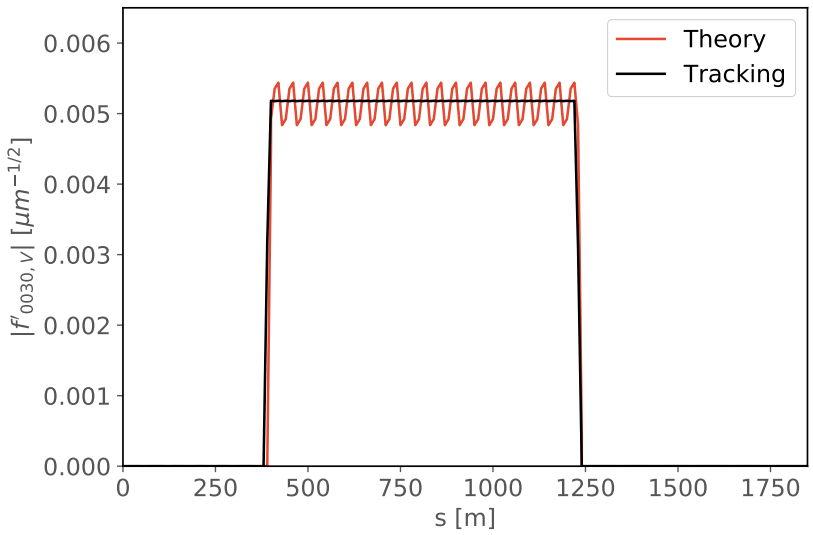

Figure 4.3: *Amplitude of f_{0030} for a closed skew sextupole bump, with $Q_y = 0.31$ and $Q_{d,y} = 0.315$. The prediction from Eq. (4.28) is shown in red, while the result from single particle tracking simulation is shown in black. An amplitude beating is predicted in theory, but not observed in the result from tracking simulations.*

complexity of calculations. An approximation is presented in this section based on observations of forced resonance driving terms in tracking simulations.

One possible way to retrieve the property that forced resonance driving terms have constant amplitudes between sources is to have the same resonance denominators for each of the four modes in order to have cancellation. The one-turn rotation is thus approximated as directly obtained from the concatenation of the linear maps as described by Eq. (4.17). The tune jump at the location of the ac dipole is neglected, and the coordinates before and after the ac dipole are the same as defined in Eq. (4.15). The one-turn-map now becomes,

$$\mathcal{M} = e^{:\tilde{H}:} R_{d,z} \quad , \tag{4.30}$$

where $R_{d,z} = \tilde{M}_{N+1}$ and $\tilde{M}_{N+1}$ is defined in Eq. (4.18). Neglecting the tune jump at the ac dipole has the further benefit of simplifying the expansion of the Hamiltonian yielding,

$$\tilde{H} = \sum_{jklm} h_{jklm} \xi_{x,+}^{j} \xi_{x,-}^{k} \xi_{y,+}^{l} \xi_{y,-}^{m} \tag{4.31}$$

where the Hamiltonian terms are just given by

$$h_{jklm} = \sum_n h_{n,jklm} e^{i[(j-k)\Delta\phi_{\mathrm{d},n,x}+(l-m)\Delta\phi_{\mathrm{d},n,y}]} \quad . \tag{4.32}$$

Equation (4.32) is identical to Eq. (4.24) except that no distinction between terms before and after the ac dipole is made. The detailed derivation to derive the parametrization of the forced motion are detailed in Appendix 4.8. The resulting linearly normalized complex coordinate including all contributions from nonlinear sources is now given by,

$$\begin{aligned} \xi_{x,-} \approx & \sqrt{2A_{\mathrm{d},x}} e^{i2\pi(Q_{\mathrm{d},x}\tau+\chi_{\mathrm{d},x})} \\ & -2i \sum_{jklm} j f_{jklm} (2A_{\mathrm{d},x})^{\frac{j-1+k}{2}} (2A_{\mathrm{d},y})^{\frac{l+m}{2}} \\ & \times e^{i2\pi[(k-j+1)(Q_{\mathrm{d},x}\tau+\chi_{\mathrm{d},x})+(m-l)(Q_{\mathrm{d},y}\tau+\chi_{\mathrm{d},y})]} \end{aligned} \tag{4.33}$$

where f_{jklm} are the resonance driving terms and are defined as,

$$f_{jklm} = \frac{h_{jklm}}{1 - e^{i2\pi[(k-j)Q_{\mathrm{d},x}+(m-l)Q_{\mathrm{d},y}]}} \, . \tag{4.34}$$

The same derivation can be performed for the vertical motion, which gives the following result for the evolution of the vertical coordinate,

$$\begin{aligned} \xi_{y,-} \approx & \sqrt{2A_{\mathrm{d},y}} e^{i2\pi(Q_{\mathrm{d},y}\tau+\chi_{\mathrm{d},y})} \\ & -2i \sum_{jklm} l f_{jklm} (2A_{\mathrm{d},x})^{\frac{j+k}{2}} (2A_{\mathrm{d},y})^{\frac{l-1+m}{2}} \\ & \times e^{i2\pi[(k-j)(Q_{\mathrm{d},x}\tau+\chi_{\mathrm{d},x})+(m-l+1)(Q_{\mathrm{d},y}\tau+\chi_{\mathrm{d},y})]} \end{aligned} \tag{4.35}$$

This result is the forced motion equivalent to the free motion resonance driving terms from [70]. Two distinctions can be made between this new parametrization of the nonlinear motion and that of Eq. (4.28). Firstly, only a single nonlinear mode is obtained from this derivation, which means that the resonance driving terms amplitude is constant between sources. Secondly, a resonance denominator is obtained that is only dependent on the forced tunes. The lack of the free tune in the

resonance denominator is problematic, as forced resonances should be dependent on both free and forced tunes. However, the proper resonance behaviour is recovered in the next section by introducing the cross-term between the ac dipole and resonance driving terms.

DERIVATION OF SECOND ORDER CROSS-TERMS FROM AC DIPOLE

All previous derivations assume linear motion at the location of the ac dipole. However a significant perturbation can be expected at the location of the ac dipole when the phase-space is deformed due to the machine driving terms. Second order cross-terms between resonance driving terms and the ac dipole can perturb the resonance driving terms around the machine.

To illustrate this, tracking simulations are performed with a closed skew sextupole bump. One simulation is done with the ac dipole outside the bump at $s = 0$ m, while the second simulation is done with the ac dipole inside the bump at $s = 830$ m. Figure 4.4 shows the amplitude of f_{0030} for the two simulations. When the ac dipole is located in a region with non-zero f_{0030} it shows a clear perturbation at the location of the ac dipole. A jump in amplitude is observed as well as the non-closure of the skew sextupolar resonance driving term bump.

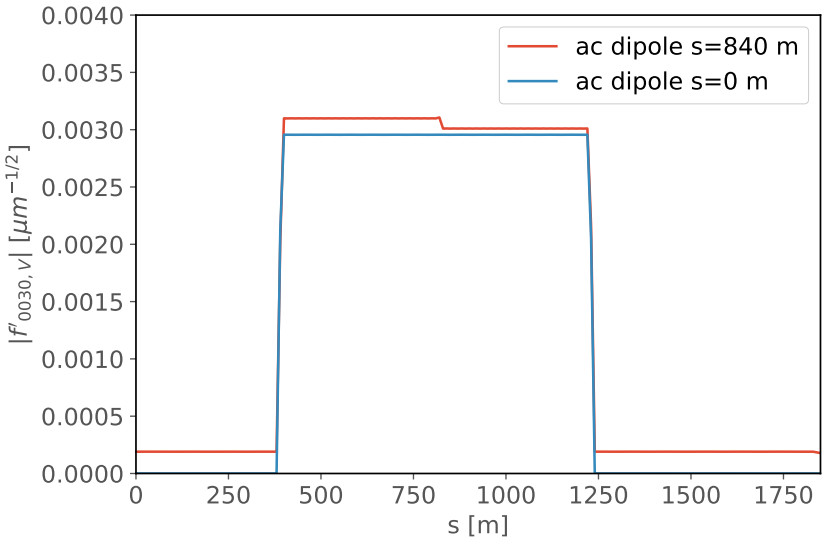

Figure 4.4: *Amplitude of f_{0030} resonance driving term from tracking simulations with the ac dipole located at $s = 0$ m (blue), and for a simulation with the ac dipole at $s = 830$ m (red). The perturbation from the ac dipole prevents the resonance bump from closing, and creates a jump in amplitude at the location of the ac dipole.*

A possible approach to derive this second order contribution from the ac dipole is to find the second order generating function and solve the normal form approach to second order. A derivation of the generating function to second order is found in [71]. The cross-term is derived in an illustrative way by calculating an effective Hamiltonian term at the location of the ac dipole.

First the kick of the ac dipole in physical space is defined as,

$$\Delta z' = \frac{BL}{B_0\rho}\cos(2\pi Q_{\mathrm{d},z}\tau) \tag{4.36}$$

The normalized complex coordinate including the ac dipole kick term $\zeta^\dagger$ is then defined as

$$\begin{aligned} \zeta^\dagger_{z,\pm} &= \zeta_{z,\pm} \pm i\sqrt{\beta_{\mathrm{d},z}}\Delta z' \\ &= \zeta_{z,\pm} \pm i\delta_z\cos(2\pi Q_{\mathrm{d},z}\tau) \end{aligned} \tag{4.37}$$

where $\delta_y = \sqrt{\beta_{\mathrm{acd},y}}\frac{BL}{B_0\rho}$. So far, the kick has only been accounted for in relation with the linear motion which led to the linear coordinate of Eq. (4.1). This is sufficient in the assumption that the phase-space at the location of the ac dipole is circular. However, nonlinearities will distort the phase-space around the accelerator as well as at the location of the ac dipole. The kicks acting on this distorted phase-space will result in cross-terms between resonance driving terms and the ac dipole. To calculate these cross-terms it is necessary to move to the normal form space.

The approach is to evaluate the modified normalized complex coordinates of Eq. (4.37) in the normal form basis, and subtract the evaluation of the original linear normalized complex coordinate. A residual is obtained for each turn in the motion. This can be summed over the total number of turns, taking into account the turn-by-turn rotation $R = e^{-i2\pi Q_z}$, to obtain,

$$r = -\frac{1}{2}\sum_{\tau=0}^{N-1} R^{N-\tau}\left([F,h]\Big|_{h=\zeta^\dagger} - [F,h]\Big|_{h=\zeta}\right) \quad . \tag{4.38}$$

The factor $\frac{1}{2}$ in Eq. (5.14) results from the derivations of the second order generating function in [71]. For the vertical motion the residual cross-term $r_{jklm,V}$, arising from the interaction between the resonance driving term f_{jklm} and the ac dipole, will take the form of,

$$
\begin{aligned}
r_{jklm,V} &= i \times l f_{jklm} \sum_{\tau=0}^{N-1} R^{N-\tau} \\
&\quad \times \Big((\xi_{x,+}^{\dagger})^j (\xi_{x,-}^{\dagger})^k (\xi_{y,+}^{\dagger})^{l-1} (\xi_{y,-}^{\dagger})^m \\
&\quad - \xi_{x,+}^{j} \xi_{x,-}^{k} \xi_{y,+}^{l-1} \xi_{y,-}^{m} \Big) \quad . \qquad (4.39)
\end{aligned}
$$

Note that a distinction is now made between the planes of motion by the addition of V in the indices. This is needed to account for the fact that R acts on the two planes differently. Furthermore, the calculated residual from Eq. (4.39) will yield multiple contributions per resonance driving term. The resonance driving terms of the same order will all contribute, i.e. f_{0030} will be perturbed by $r_{0030,V}$, $r_{0021,V}$, and $r_{0012,V}$. In fact this approach bears resemblance to the second order normal form development in [71]. The summation of the kicks over turns is an operation analogous to a normal form transformation.

Cross-term for $f_{0030,V}$

In view of the simulations done in Sec. 4.5 the contribution to $f_{0030,V}$ is calculated as an example in this section. The residual $r_{0030,V}$ is calculated as follows,

$$
\begin{aligned}
r_{0030,V} &= i \times 3 f_{0030} \sum_{\tau=0}^{N-1} R^{N-\tau} \left[(\xi_{y,+}^{\dagger})^2 - \xi_{y,+}^{2} \right] \\
&= i \times 3 f_{0030} \sum_{\tau=0}^{N-1} R^{N-\tau} \left[\left(-\frac{\delta_y^2}{2} + i\sqrt{2A_{\mathrm{d},y}}\delta_y \right) \right. \\
&\quad + \left(-\frac{\delta_y^2}{4} + i\sqrt{2A_{\mathrm{d},y}}\delta_y \right) e^{-i2\pi[2Q_{\mathrm{d},y}]\tau} \\
&\quad \left. + \left(-\frac{\delta_y^2}{4} \right) e^{i2\pi[2Q_{\mathrm{d},y}]\tau} \right] \quad .
\end{aligned}
$$

Only the terms with $\pm 2Q_{\mathrm{d},y}$ will contribute to the skew sextupolar resonance driving terms. The first term of the summand can thus be neglected to obtain,

$$
\begin{aligned}
r_{0030,V} &= i \times 3 f_{0030} \sum_{\tau=0}^{N-1} R^{N-\tau} \\
&\times \left[\left(-\frac{\delta_y^2}{4} + i\sqrt{2A_{\mathrm{d},y}}\delta_y \right) e^{-i2\pi[2Q_{\mathrm{d},y}]\tau} \right. \\
&\left. + \left(-\frac{\delta_y^2}{4} \right) e^{i2\pi[2Q_{\mathrm{d},y}]\tau} \right] \quad .
\end{aligned}
\tag{4.40}
$$

The summation can be solved by using the identity,

$$
1 + p + p^2 + \ldots + p^{N-1} = \frac{p^N - 1}{p - 1} \quad , \tag{4.41}
$$

and observing that $p = e^{i2\pi[-Q_y \pm 2Q_{\mathrm{d},y}]}$. Solving the summation while neglecting the terms that oscillate with Q_y only, and rewriting the new resonance denominator in the familiar form of $1 - p$, the residual contribution is given by,

$$
\begin{aligned}
r_{0030,V} &= -i \times 3 f_{0030} \left[\left(-\frac{\delta_y^2}{4} \right) \frac{e^{i2\pi[2Q_{\mathrm{d},y}]N}}{1 - e^{i2\pi[-Q_y + 2Q_{\mathrm{d},y}]}} \right. \\
&\left. + \left(-\frac{\delta_y^2}{4} + i\sqrt{2A_{\mathrm{d},y}}\delta_y \right) \frac{e^{i2\pi[-2Q_{\mathrm{d},y}]N}}{1 - e^{i2\pi[-Q_y - 2Q_{\mathrm{d},y}]}} \right] \quad .
\end{aligned}
\tag{4.42}
$$

This can be further simplified by expressing the kick strength δ_y in terms of $A_{\mathrm{d},y}$ using,

$$
\delta_y = \Lambda_y \sqrt{2A_{\mathrm{d},y}} \quad , \tag{4.43}
$$

with,

$$
\Lambda_y = \frac{4 \sin(\pi(Q_{\mathrm{d},y} - Q_y))}{\sqrt{1 - \lambda_y^2}} \quad . \tag{4.44}
$$

Equation (4.42) then reduces to,

$$\begin{aligned} r_{0030,V} &= -i \times 3 f_{0030}(2A_{\mathrm{d},y}) \\ &\quad \times \left[\left(-\frac{\Lambda_y^2}{4} \right) \frac{e^{i2\pi[2Q_{\mathrm{d},y}]N}}{1 - e^{i2\pi[-Q_y+2Q_{\mathrm{d},y}]}} \right. \\ &\quad \left. + \left(-\frac{\Lambda_y^2}{4} + i\Lambda_y \right) \frac{e^{i2\pi[-2Q_{\mathrm{d},y}]N}}{1 - e^{i2\pi[-Q_y-2Q_{\mathrm{d},y}]}} \right] \quad . \end{aligned} \tag{4.45}$$

This result is very similar in form to Eq. (4.35) for skew sextupolar resonance driving terms. By imposing the form of Eq. (4.35) on to the acquired result a correctional Hamiltonian term at the location of the ac dipole $h^{\mathrm{ac}}_{jklm,V}$ can be defined and substituted into the result as,

$$\begin{aligned} r_{0030,V} &= -2i \frac{h^{\mathrm{ac}}_{0012,V}}{1 - e^{i2\pi[Q_{\mathrm{d},y}]}} (2A_{\mathrm{d},y}) e^{i2\pi[2Q_{\mathrm{d},y}]N} \\ &\quad -2i \frac{3h^{\mathrm{ac}}_{0030,V}}{1 - e^{i2\pi[-3Q_{\mathrm{d},y}]}} (2A_{\mathrm{d},y}) e^{i2\pi[-2Q_{\mathrm{d},y}]N} \quad , \end{aligned} \tag{4.46}$$

where the Hamiltonian terms for the contributions at the AC dipole are,

$$\begin{aligned} h^{\mathrm{ac}}_{0012,V} &= -\frac{3}{2} f_{0030} \frac{\Lambda_y^2}{4} \frac{1 - e^{i2\pi[Q_{\mathrm{d},y}]}}{1 - e^{i2\pi[-Q_y+2Q_{\mathrm{d},y}]}} \\ h^{\mathrm{ac}}_{0030,V} &= -\frac{1}{2} f_{0030} \left(\frac{\Lambda_y^2}{4} - i\Lambda_y \right) \frac{1 - e^{i2\pi[-3Q_{\mathrm{d},y}]}}{1 - e^{i2\pi[-Q_y-2Q_{\mathrm{d},y}]}} \, . \end{aligned} \tag{4.47}$$

The resonant behaviour near the true forced motion resonances $-Q_x + mQ_{\mathrm{d},x} + nQ_{\mathrm{d},y}$, where $m, n \in Z$, that was lost in Eq. (4.34) is now recovered by this contribution at the location of the ac dipole. The same derivations can be done for the other skew sextupolar resonance driving terms $f_{0012,V}$ and $f_{0021,V}$, as both terms will contribute to $h^{\mathrm{ac}}_{0030,V}$. Combining the contributions from all three resonance driving terms and explicitly writing out the factor $\frac{1}{2}$ from the second order generating function, the final contribution at the location of the ac dipole is obtained and given by,

$$h^{\mathrm{ac}}_{0030,V} = \frac{1}{2}\Bigg[-f_{0030}\left(\frac{\Lambda_y^2}{4} - i\Lambda_y\right) - \frac{1}{3}f_{0012}\frac{\Lambda_y^2}{4} + \frac{2}{3}f_{0021}\left(\frac{\Lambda_y^2}{4} - \frac{i}{2}\Lambda_y\right)\Bigg] \times \left[\frac{1 - e^{i2\pi[-3Q_{\mathrm{d},y}]}}{1 - e^{i2\pi[-Q_y - 2Q_{\mathrm{d},y}]}}\right] . \tag{4.48}$$

Calculation of resonance driving terms

The procedure to calculate the resonance driving terms now becomes apparent. First a model is made of the forced motion by modelling the linear optics perturbations as a quadrupolar kick, as shown in [54]. The forced optics parameters obtained from this model are used to calculate the resonance driving terms from Eqs. (4.32) and (4.34). The forced resonance driving terms obtained at the location of the ac dipole are used to calculate the cross-term at the same location using Eq. (4.48).

The Hamiltonian terms of Eq. (4.32) can then be re-expressed as,

$$h_{jklm,H/V} = \sum_n h_{n,jklm} e^{i[(j-k)\Delta\phi_{\mathrm{d},n,x} + (l-m)\Delta\phi_{\mathrm{d},n,y}]} + h^{\mathrm{ac}}_{jklm,H/V} e^{i[(j-k)\Delta\phi_{\mathrm{d,ac},x} + (l-m)\Delta\phi_{\mathrm{d,ac},y}]} . \tag{4.49}$$

The forced resonance driving terms are now calculated using,

$$f_{jklm,H/V} = \frac{h_{jklm,H/V}}{1 - e^{i2\pi[(k-j)Q_{\mathrm{d},x} + (m-l)Q_{\mathrm{d},y}]}} . \tag{4.50}$$

where the index H/V specifies the plane in which the resonance driving terms are observed.

COMPARISON OF THEORY TO PARTICLE TRACKING SIMULATIONS

Single particle tracking simulations are done in MAD-X [72] to verify the analytical development of resonance driving terms with forced oscillations. A simple FODO

lattice is used as the model for the tracking simulations with natural tunes $Q_x = Q_y = 0.25$. A vertical ac dipole is installed at the beginning of the lattice, at location $s = 0$ m. The ac dipole starts with a ramp-up time of 2000 turns, and has a flattop excitations of 6000 turns before ramping down again. Only the turn-by-turn data of the flattop excitation is used for the spectral analysis. Skew sextupoles are added to the model to create various different test cases that are detailed in the following sections. For illustrative purposes all results are shown for the skew sextupolar resonance driving term $f_{0030,V}$, but it reflects the results found for other driving terms.

Closed resonance driving term bump

First an idealised test case is used in the form of a closed resonance driving term bump. Two skew sextupolar sources are introduced at π phase advance from each other to form a closed driving term bump. This closed bump is specifically chosen such that the resonance driving term at the location of the ac dipole is zero, thus mitigating any second order contribution from the ac dipole. The comparison between the theoretical derivations of Eq. (4.34) and the results from tracking simulations are shown in Fig. 4.5 for the amplitude of the $f_{0030,V}$ driving term. A very good agreement is observed between the two results.

Figure 4.6 shows the relative amplitude deviation and phase deviation between the theoretical predictions and the results from tracking simulations for the closed bump case. The deviation inside the closed bump is negligibly small and shows an almost exact agreement between theory and simulations.

Non-closed resonance driving term sources

The closed driving term bump is a special case of course, for which the ac dipole is located in a region where the driving terms are zero. Furthermore, by construction the closed bump does not show resonant behaviour as it functions similarly to a single pass of the lattice. A second test case is used to probe the effect of the ac dipole on the resonance driving terms as well as the resonance behaviour close to resonances. The second skew sextupole in the lattice is removed leaving a single skew sextupole in the lattice. The same single particle tracking simulations are repeated.

The results from tracking simulations and from the analytical predictions of Eq. (4.34) with and without the contribution of Eq. (4.48) are presented in Fig. 4.7.

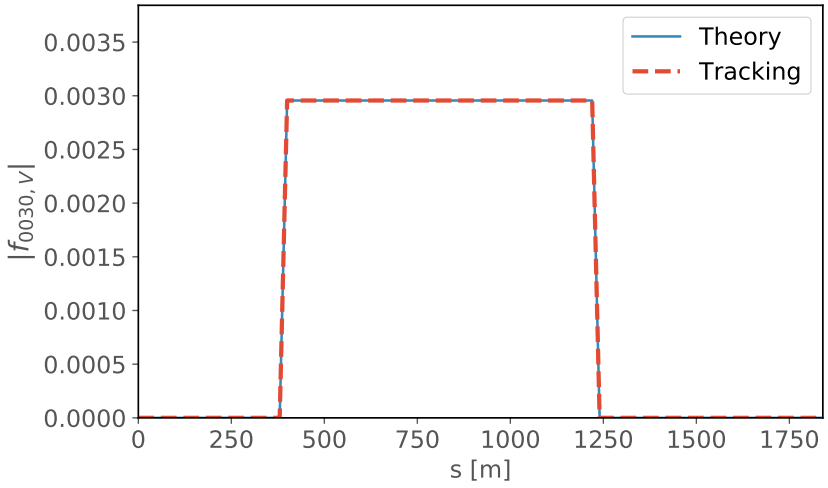

Figure 4.5: *Amplitude of $f_{0030,V}$ driving term from analytical calculations and tracking for a closed driving term bump with skew sextupoles at π phase advance. The vertical natural and forced tunes are $Q_y = 0.25$, and $Q_{\mathrm{d},y} = 0.255$.*

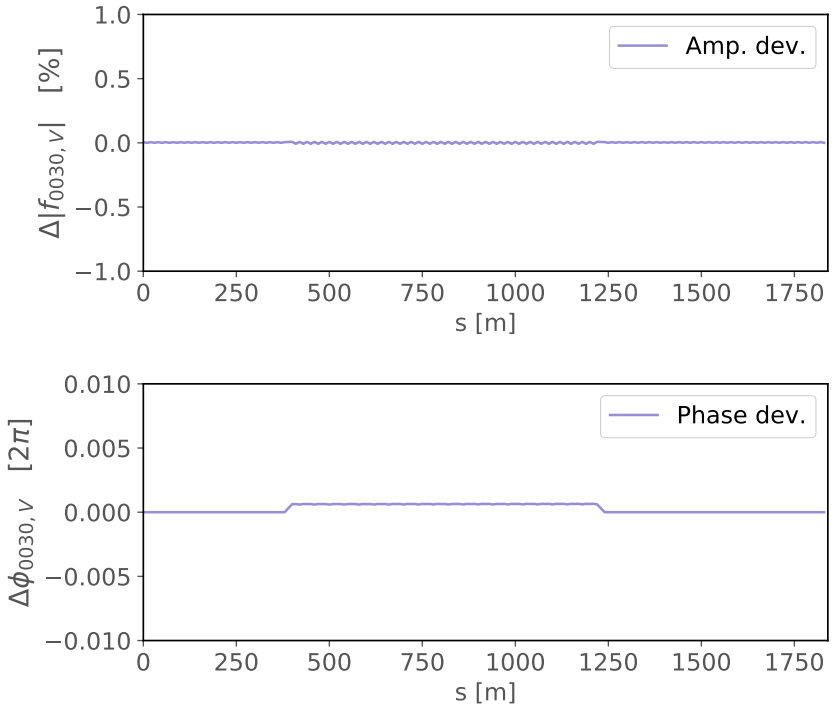

Figure 4.6: *Amplitude and phase deviation of $f_{0030,V}$ driving term between analytical calculations and tracking for a closed driving term bump with skew sextupoles at π phase advance. The vertical natural and forced tunes are $Q_y = 0.25$, and $Q_{\mathrm{d},y} = 0.255$.*

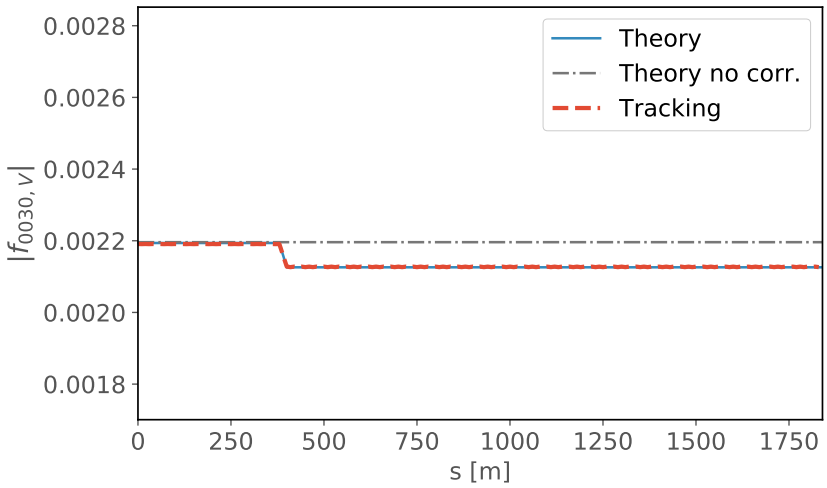

Figure 4.7: *Amplitude of $f_{0030,V}$ driving term from analytical calculations, including and excluding the cross-term contribution from the ac dipole at s=0 m, and tracking for a lattice with a single skew sextupole at s=400 m. The vertical natural and forced tunes are $Q_y = 0.25$, and $Q_{\mathrm{d},y} = 0.255$.*

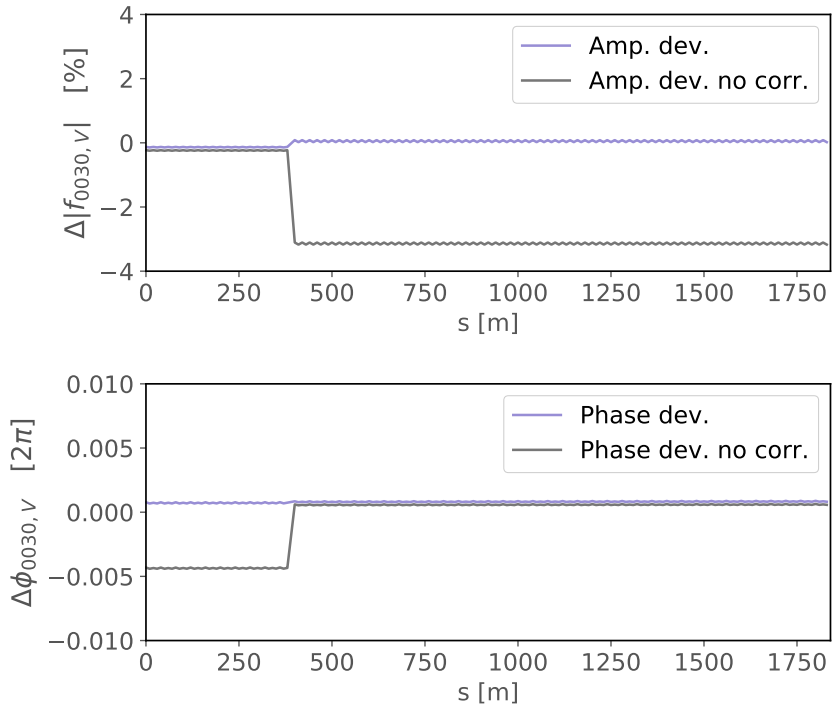

Figure 4.8: *Amplitude and phase deviation of $f_{0030,V}$ driving term from analytical calculations, including and excluding the cross-term contribution, and tracking for a lattice with a single skew sextupole at s=400 m and the ac dipole at s=0 m. The vertical natural and forced tunes are $Q_y = 0.25$, and $Q_{\mathrm{d},y} = 0.255$.*

Firstly a jump in amplitude is observed at the start of the lattice compared to the amplitudes at the end of the lattice. This jump shows the effect of the ac dipole on the amplitude of the resonance driving term. Indeed it is shown that omitting the second order cross-term yields a significant discrepancy between tracking and theory. In contrast, including the cross-term shows an almost perfect agreement with tracking results.

Figure 4.8 shows the relative amplitude and phase deviations between the different theoretical predictions and the results from tracking. Again a much better agreement is observed in the case where the second order cross-term is included.

Lastly, a model is used with six skew sextupoles at arbitrary phase advance between each other and with arbitrary strength. The results for both tracking simulations and analytical calculations are presented in Fig. 4.9. Again a very good agreement is observed between tracking and analytical results. The relative amplitude and phase deviations are still negligibly small as shown in Fig. 4.10.

Behaviour near resonance

General forced motion theory predicts resonances to be dependent on both the free tune as well as the forced tunes. Although this is not obtained by the derivations of Sec. 4.3 this behaviour is recovered from the second order cross-term in Sec. 4.4. The analytical predictions are compared to tracking results near resonances in this section. The same base model with the six skew sextupoles is used as in Sec. 4.5.2. To probe the behaviour near resonances the natural tunes are shifted by introducing a correction quadrupole at the first defocussing quadrupole of the lattice (s = 10 m). The resonance probed is $-Q_y - 2Q_{\mathrm{d},y} = p$, where $\{p \in Z\}$. This quadrupole is modulated to shift the vertical natural tune to $Q_y = 0.327$, while the forced tune is chosen at $Q_{\mathrm{d},y} = Q_y + 0.005$.

Figure 4.11 shows the amplitude of $f_{0030,V}$ obtained from tracking simulations and from theory. The results show that the resonance driving term amplitude increases drastically as expected. Furthermore, as the resonance is approached the phase advance between the skew sextupolar sources aligns such that the local jumps in amplitude become relatively smaller. The result is a constant, high amplitude, resonance driving term over the full machine.

The relative amplitude and phase deviations between theory and results from tracking are shown in Fig. 4.12. The deviations have increased slightly as compared to the results shown in Fig. 4.10, but are still negligibly small. The deviations observed in the amplitude show steps at the locations of the ac dipole and at s=1750,

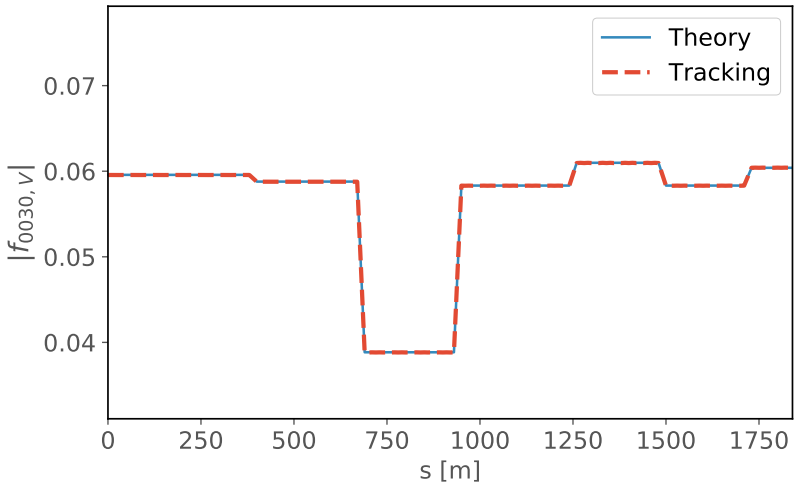

Figure 4.9: *Amplitude of $f_{0030,V}$ driving term from analytical calculations and tracking for a lattice with six skew sextupoles with arbitrary location and strengths and the ac dipole at s=0 m. The vertical natural and forced tunes are $Q_y = 0.25$, and $Q_{d,y} = 0.255$.*

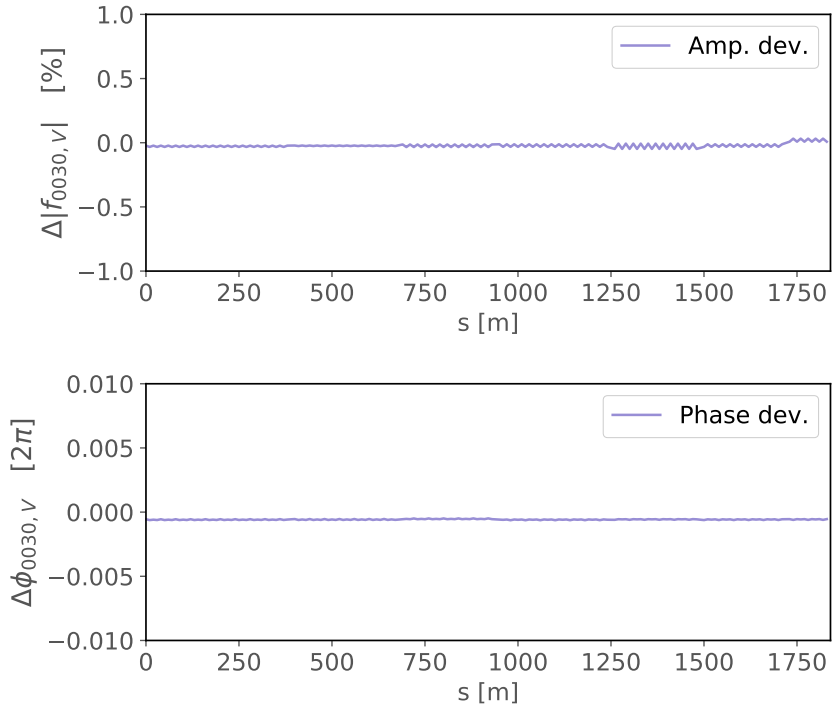

Figure 4.10: *Amplitude and phase deviation of $f_{0030,V}$ driving term from analytical calculations and tracking for a lattice with six skew sextupoles with arbitrary location and strengths and the ac dipole at s=0 m. The vertical natural and forced tunes are $Q_y = 0.25$, and $Q_{d,y} = 0.255$.*

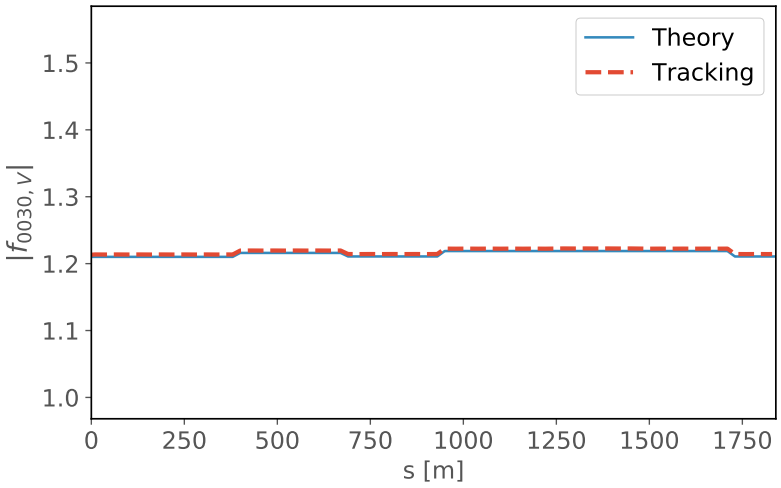

Figure 4.11: *Amplitude of $f_{0030,V}$ driving term from analytical calculations and tracking for a lattice with six skew sextupoles with arbitrary location and strengths and the ac dipole at s=0 m. The vertical natural and forced tunes are $Q_y = 0.327$, and $Q_{\mathrm{d},y} = 0.332$.*

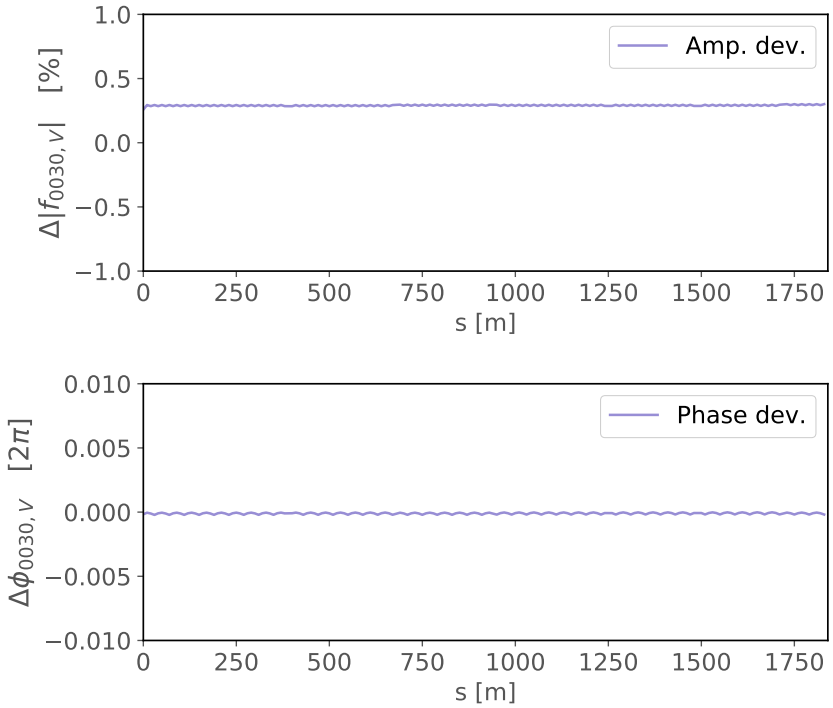

Figure 4.12: *Amplitude and phase deviation of $f_{0030,V}$ driving term from analytical calculations and tracking for a lattice with six skew sextupoles with arbitrary location and strengths and the ac dipole at s=0 m. The vertical natural and forced tunes are $Q_y = 0.327$, and $Q_{\mathrm{d},y} = 0.332$.*

while the phase deviation is constant over the whole lattice.

Larger tune split

The simulations have so far been done with a tune split between the natural tunes and the ac dipole tunes of $Q_{\mathrm{d},y} - Q_y = 0.005$. During optics measurements with ac dipoles in accelerators, the tune splits are generally chosen to be smaller than $|Q_{\mathrm{d},z} - Q_z| < 0.015$. Simulations are done to validate the proposed parametrization of forced resonance driving terms at the edge of these operational bounds of tune splits.

Figure 4.13 shows results from the tracking simulations with the model containing multiple random sources and analytical predictions for the case where $Q_y = 0.31$ and $Q_{\mathrm{d},y} = Q_y + 0.015$. The deviation in amplitude and phase of the driving term between predictions and the results from tracking simulations are shown in Fig. 4.14. A constant phase deviation of (0.97 ± 0.15) mrad is observed, while the amplitude deviation does not exceed 0.2 %. The results still show a very small relative amplitude and phase deviation that is well within tolerated errors on resonance driving terms.

CONCLUSIONS

A theoretical description of forced resonance driving terms with ac dipoles is presented. It is shown that the analysis using the forced Courant-Snyder parameters greatly simplifies the description of resonance driving terms in forced motion. The amplitudes of resonance driving terms in the forced parameter space are constant between sources. This does not agree with the result of the normal form analysis of the forced motion as presented here, where amplitude beating would be expected. The reasons for this discrepancy remain unknown. A new parametrization of forced resonance driving terms is presented in this paper that includes a new cross-term contribution between the ac dipole and the resonance driving terms. In this description the resonance driving terms are constant between nonlinear sources.

Simulations with a closed skew sextupolar driving term bump, and with the ac dipole outside this closed bump, show a good agreement between theory and results from tracking. The ac dipole being in a region where the driving terms are zero does not affect the driving terms.

Results from simulations where the ac dipole is at a location with nonzero driving terms, show a perturbation of second order by the ac dipole. This perturbation

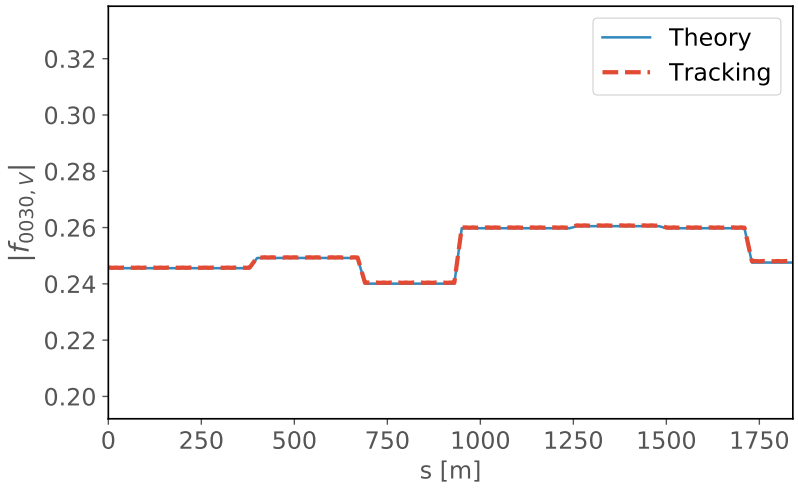

Figure 4.13: *Amplitude of $f_{0030,V}$ driving term from analytical calculations and tracking for a lattice with six skew sextupoles with arbitrary location and strengths and the ac dipole at s=0 m. The vertical natural and forced tunes are $Q_y = 0.31$, and $Q_{\mathrm{d},y} = 0.325$.*

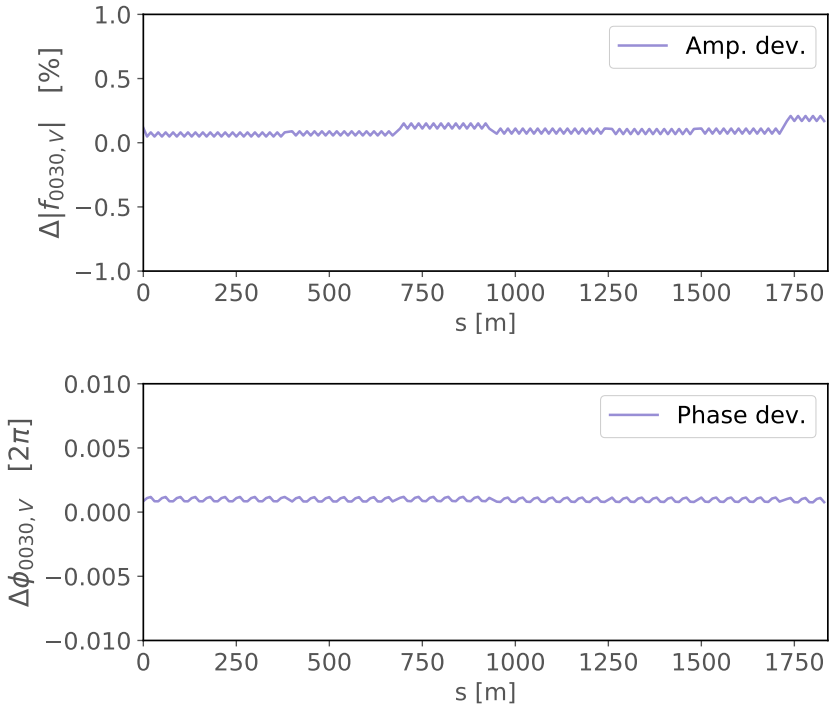

Figure 4.14: *Amplitude and phase deviation of $f_{0030,V}$ driving term from analytical calculations and tracking for a lattice with six skew sextupoles with arbitrary location and strengths and the ac dipole at s=0 m. The vertical natural and forced tunes are $Q_y = 0.31$, and $Q_{\mathrm{d},y} = 0.325$.*

shows up as a jump of both phase and amplitude at the location of the ac dipole. The nonlinearity of the motion at the location of the ac dipole is identified as the source of perturbation. A Hamiltonian term at the location of the ac dipole is derived from the normal form approach. The contribution reproduces the observations of the tracking in theory. The jumps in phase and amplitude of the resonance driving terms at the location of the ac dipole are accurately reproduced, as well as the resonance driving terms around the full lattice.

The results presented in this paper offer a new parametrization of the forced resonance driving terms, while at the same time highlight the complexity of forced motion in synchrotrons. Indeed further studies are needed to fully understand all intricacies of the nonlinear forced motion.

APPENDIX A: NORMAL FORM METHOD

Solving the normal form approach to first order yields complicated analytical expressions. The normal form method consists of finding a transformation that simplifies the motion to an amplitude dependent rotation that satisfies [68, 69],

$$e^{-:F:}e^{:\tilde{H}:}R_{x,y}R_\tau e^{:F:} = e^{:H(I):}R_{x,y}R_\tau \tag{4.51}$$

where F is the generating function, and I is the new invariant of the motion. The generating function is defined in normal form as,

$$F = \frac{1}{1-R_{x,y}R_\tau}\sum_{jklm} h_{jklm}\zeta_{x,+}^j\zeta_{x,-}^k\zeta_{y,+}^l\zeta_{y,-}^m \tag{4.52}$$

Here, the two rotation operators are defined as, $R_x\psi_x = \psi_x + 2\pi Q_x$ and $R_\tau\tau = \tau + 1$. It is the combination of these two rotation operators that will create the complexity in the following derivations. The normal form coordinate can be written in a compact form as,

$$\zeta_{x,\pm} = h_{x,\pm} + g_{x,\pm}e^{\pm i\pi Q_{x,-}} + \lambda_x g_{x,\mp}e^{\pm i\pi Q_{x,+}} \tag{4.53}$$

where

$$\begin{aligned} h_{x,\pm} &= \sqrt{2A_{\mathrm{d},x}}e^{\mp i(\psi_{\mathrm{d},x}(s)+\chi_{\mathrm{d},x})} \\ g_{x,\pm} &= \sqrt{2I'_x}e^{\mp i(\psi_x+\psi_0)} \ . \end{aligned} \tag{4.54}$$

To obtain the nonlinear turn-by-turn motion in linearly normalized space the generating function F can be applied to first order as,

$$\begin{aligned} \xi_{x,-} &= e^{:F:}\zeta_{x,-} \\ &\approx \zeta_{x,-} + [F, \zeta_{x,-}] \end{aligned} \tag{4.55}$$

where the square brackets denote the Poisson brackets and are defined as,

$$[f, g] = \sum_z \frac{\partial f}{\partial \psi_z}\frac{\partial g}{\partial I_z} - \frac{\partial f}{\partial I_z}\frac{\partial g}{\partial \psi_z} \quad .$$

Solving Eq. (4.55) becomes very complicated when the full expansion of Eq. (4.52) is considered. To simplify this it is assumed that the forced amplitude is much greater than the free action, i.e. $A_{\mathrm{d},z} \gg I_z$. The only terms in the expansion of Eq. (4.52) that will remain after the Poisson brackets in Eq. (4.55) are the ones that only depend on $g_{x,\pm}$ to the first order. All other terms dependent on higher orders of $g_{x,\pm}$ will disappear in the limit of $I \to 0$. To solve the Poisson brackets, a few identities are needed.

$$\begin{aligned} [g_{x,+}e^{i\pi Q_{x,-}}, \zeta_{x,-}] &= \frac{-2i}{1-\lambda_x^2} \\ [\lambda_x g_{x,-}e^{i\pi Q_{x,+}}, \zeta_{x,-}] &= \frac{2i\lambda_x^2}{1-\lambda_x^2} \\ [g_{x,-}e^{-i\pi Q_{x,-}}, \zeta_{x,-}] &= \frac{2i\lambda_x e^{-i2\pi Q_{\mathrm{d},x}}}{1-\lambda_x^2} \\ [\lambda_x g_{x,+}e^{-i\pi Q_{x,+}}, \zeta_{x,-}] &= \frac{-2i\lambda_x e^{-i2\pi Q_{\mathrm{d},x}}}{1-\lambda_x^2} \end{aligned} \tag{4.56}$$

The Poisson bracket of Eq. (4.55) can be expanded as,

$$
\begin{aligned}
[F,\zeta_{x,-}] &= \left[\frac{1}{1-R_{x,y}R_\tau}\sum_{jklm} h_{jklm}\zeta_{x,+}^{j}\zeta_{x,-}^{k}\zeta_{y,+}^{l}\zeta_{y,-}^{m} \quad , \quad \zeta_{x,-}\right] \\
&= \sum_{jklm}\frac{j(h^{<}_{jklm}+h^{>}_{jklm}e^{i2\pi Q_{x,-}})h_{x,+}^{j-1}h_{x,-}^{k}h_{y,+}^{l}h_{y,-}^{m}}{1-e^{i2\pi[-Q_x+(k-j+1)Q_{\mathrm{d},x}+(m-l)Q_{\mathrm{d},y}]}}[g_{x,+}e^{i\pi Q_{x,-}},\zeta_{x,-}] \\
&\quad+\sum_{jklm}\frac{j(h^{<}_{jklm}+h^{>}_{jklm}e^{i2\pi Q_{x,+}})h_{x,+}^{j-1}h_{x,-}^{k}h_{y,+}^{l}h_{y,-}^{m}}{1-e^{i2\pi[Q_x+(k-j+1)Q_{\mathrm{d},x}+(m-l)Q_{\mathrm{d},y}]}}[\lambda_x g_{x,-}e^{i\pi Q_{x,+}},\zeta_{x,-}] \\
&\quad+\sum_{jklm}\frac{k(h^{<}_{jklm}+h^{>}_{jklm}e^{-i2\pi Q_{x,-}})h_{x,+}^{j}h_{x,-}^{k-1}h_{y,+}^{l}h_{y,-}^{m}}{1-e^{i2\pi[Q_x+(k-1-j)Q_{\mathrm{d},x}+(m-l)Q_{\mathrm{d},y}]}}[g_{x,-}e^{-i\pi Q_{x,-}},\zeta_{x,-}] \\
&\quad+\sum_{jklm}\frac{k(h^{<}_{jklm}+h^{>}_{jklm}e^{-i2\pi Q_{x,+}})h_{x,+}^{j}h_{x,-}^{k-1}h_{y,+}^{l}h_{y,-}^{m}}{1-e^{i2\pi[-Q_x+(k-1-j)Q_{\mathrm{d},x}+(m-l)Q_{\mathrm{d},y}]}}[\lambda_x g_{x,+}e^{-i\pi Q_{x,+}},\zeta_{x,-}]
\end{aligned}
\tag{4.57}
$$

where $h^{<}$ describes the Hamiltonian terms before the ac dipole, and $h^{>}$ describes the Hamiltonian terms after the ac dipole. Equation (4.57) can be solved using the identities of Eq. (4.56) and is given by,

$$
\begin{aligned}
[F,\zeta_{x,-}] &= \frac{2i}{1-\lambda_x^2}\Bigg(-\sum_{jklm}\frac{j(h^{<}_{jklm}+h^{>}_{jklm}e^{i2\pi Q_{x,-}})h_{x,+}^{j-1}h_{x,-}^{k}h_{y,+}^{l}h_{y,-}^{m}}{1-e^{i2\pi[-Q_x+(k-j+1)Q_{\mathrm{d},x}+(m-l)Q_{\mathrm{d},y}]}} \\
&\quad+\lambda_x^2\sum_{jklm}\frac{j(h^{<}_{jklm}+h^{>}_{jklm}e^{i2\pi Q_{x,+}})h_{x,+}^{j-1}h_{x,-}^{k}h_{y,+}^{l}h_{y,-}^{m}}{1-e^{i2\pi[Q_x+(k-j+1)Q_{\mathrm{d},x}+(m-l)Q_{\mathrm{d},y}]}} \\
&\quad+\lambda_x e^{-i2\pi Q_{\mathrm{d},x}}\sum_{jklm}\frac{k(h^{<}_{jklm}+h^{>}_{jklm}e^{-i2\pi Q_{x,-}})h_{x,+}^{j}h_{x,-}^{k-1}h_{y,+}^{l}h_{y,-}^{m}}{1-e^{i2\pi[Q_x+(k-1-j)Q_{\mathrm{d},x}+(m-l)Q_{\mathrm{d},y}]}} \\
&\quad-\lambda_x e^{-i2\pi Q_{\mathrm{d},x}}\sum_{jklm}\frac{k(h^{<}_{jklm}+h^{>}_{jklm}e^{-i2\pi Q_{x,+}})h_{x,+}^{j}h_{x,-}^{k-1}h_{y,+}^{l}h_{y,-}^{m}}{1-e^{i2\pi[-Q_x+(k-1-j)Q_{\mathrm{d},x}+(m-l)Q_{\mathrm{d},y}]}}\Bigg)
\end{aligned}
\tag{4.58}
$$

The nonlinear coordinate is then obtained using Eq. (4.55) as,

$$\begin{aligned}\xi_{x,-} &= \sqrt{2A_{\mathrm{d},x}}e^{i2\pi(Q_{\mathrm{d},x}\tau+\chi_{\mathrm{d},x})} \\ &\quad -2i\sum_{jklm} f_{jklm}(2A_{\mathrm{d},x})^{\frac{j+k-1}{2}}(2A_{\mathrm{d},y})^{\frac{m+l}{2}}e^{i2\pi[(k-j+1)(Q_{\mathrm{d},x}\tau+\chi_{\mathrm{d},x})+(m-l)(Q_{\mathrm{d},y}\tau+\chi_{\mathrm{d},y})]}\end{aligned} \tag{4.59}$$

where the forced resonance driving terms f_{jklm} are given by,

$$\begin{aligned}f_{jklm} &= \frac{1}{1-\lambda_x^2}\Bigg[j\frac{h^{<}_{jklm}+h^{>}_{jklm}e^{i2\pi Q_{x,-}}}{1-e^{i2\pi[-Q_x+(k-j+1)Q_{\mathrm{d},x}+(m-l)Q_{\mathrm{d},y}]}} \\ &\quad -j\lambda_x^2\frac{h^{<}_{jklm}+h^{>}_{jklm}e^{i2\pi Q_{x,+}}}{1-e^{i2\pi[Q_x+(k-j+1)Q_{\mathrm{d},x}+(m-l)Q_{\mathrm{d},y}]}} \\ &\quad -k\lambda_x e^{-i2\pi Q_{\mathrm{d},x}}\frac{h^{<}_{j-1,k+1,lm}+h^{>}_{j-1,k+1,lm}e^{-i2\pi Q_{x,-}}}{1-e^{i2\pi[Q_x+(k-j+1)Q_{\mathrm{d},x}+(m-l)Q_{\mathrm{d},y}]}} \\ &\quad +k\lambda_x e^{-i2\pi Q_{\mathrm{d},x}}\frac{h^{<}_{j-1,k+1,lm}+h^{>}_{j-1,k+1,lm}e^{-i2\pi Q_{x,+}}}{1-e^{i2\pi[-Q_x+(k-j+1)Q_{\mathrm{d},x}+(m-l)Q_{\mathrm{d},y}]}}\Bigg]\end{aligned} \tag{4.60}$$

4

APPENDIX B: DERIVATION OF NEW FORCED RESONANCE DRIVING TERMS

Using the new expression of the linear map of Eq. (4.30) the normal form transformation can be written as,

$$e^{-:F:}e^{:\tilde{H}:}R_{\mathrm{d}}e^{:F:} = e^{:H(I):}R_{\mathrm{d}} \tag{4.61}$$

This yields the new generating function,

$$F_{\mathrm{d}} = \frac{1}{1-R_{\mathrm{d},z}}\sum_{jklm} h_{jklm}\zeta_{x,+}^{j}\zeta_{x,-}^{k}\zeta_{y,+}^{l}\zeta_{y,-}^{m} \tag{4.62}$$

To obtain the nonlinear turn-by-turn motion in linearly normalized space the generating function F_{d} can be applied to first order as,

$$\begin{aligned}\xi_{x,-} &= e^{:F:}\zeta_{x,-} \\ &\approx \zeta_{x,-}+[F,\zeta_{x,-}]\end{aligned} \tag{4.63}$$

A few properties are needed to solve the Poisson brackets. First it is observed that the property

$$[\zeta_{x,\pm}, \zeta_{x,\pm}] = 0 \tag{4.64}$$

is conserved for the new coordinates. Secondly the Poisson bracket of two conjugate coordinates is given by,

$$[\zeta_{x,\pm}, \zeta_{x,\mp}] \;=\; \mp 2i \tag{4.65}$$

Furthermore, the Poisson brackets of a polynomial is simply given by,

$$[\zeta_{x,+}^{j}, \zeta_{x,-}] \;=\; j\zeta_{x,+}^{j-1}[\zeta_{x,+}, \zeta_{x,-}] \tag{4.66}$$

Using these properties the first order solution of the Poisson brackets $[F, \zeta_{x,-}]$ of Eq. (4.63) is given by,

$$[F, \zeta_{x,-}] = -2i \sum_{jklm} \frac{j h_{jklm}}{1 - e^{i2\pi[(k-j)Q_{\mathrm{d},x} + (m-l)Q_{\mathrm{d},y}]}} \zeta_{x,+}^{j-1} \zeta_{x,-}^{k} \zeta_{y,+}^{l} \zeta_{y,-}^{m} \tag{4.67}$$

The linearly normalized complex coordinate including all contributions from nonlinear sources is now obtained using Eq. (4.63) and the result in Eq. (4.67), and assuming that $A_{\mathrm{d},x} \gg \sqrt{2I_x}$.

$$\begin{aligned} \xi_{x,-} \;\approx\; & \sqrt{2A_{\mathrm{d},x}} e^{i2\pi(Q_{\mathrm{d},x}\tau + \chi_{\mathrm{d},x})} \\ & -2i \sum_{jklm} j f_{jklm,H} (2A_{\mathrm{d},x})^{\frac{j-1+k}{2}} (2A_{\mathrm{d},y})^{\frac{l+m}{2}} \\ & \times e^{i2\pi[(k-j+1)(Q_{\mathrm{d},x}\tau + \chi_{\mathrm{d},x}) + (m-l)(Q_{\mathrm{d},y}\tau + \chi_{\mathrm{d},y})]} \end{aligned} \tag{4.68}$$

where $f_{jklm,H}$ are the resonance driving terms and are defined as,

$$f_{jklm} = \frac{h_{jklm}}{1 - e^{i2\pi[(k-j)Q_{\mathrm{d},x}+(m-l)Q_{\mathrm{d},y}]}} \,. \tag{4.69}$$

The same derivation can be done for the vertical motion, which gives the following result for the evolution of the vertical coordinate,

$$\begin{aligned} \xi_{y,-} \;\approx\; & \sqrt{2A_{\mathrm{d},y}}e^{i2\pi(Q_{\mathrm{d},y}\tau+\chi_{\mathrm{d},y})} \\ & -2i\sum_{jklm} l f_{jklm}(2A_{\mathrm{d},x})^{\frac{j+k}{2}}(2A_{\mathrm{d},y})^{\frac{l-1+m}{2}} \\ & \times e^{i2\pi[(k-j)(Q_{\mathrm{d},x}\tau+\chi_{\mathrm{d},x})+(m-l+1)(Q_{\mathrm{d},y}\tau+\chi_{\mathrm{d},y})]} \end{aligned} \tag{4.70}$$

5

MEASUREMENT AND CORRECTION OF RESONANCE DRIVING TERMS IN THE LARGE HADRON COLLIDER

Resonance driving terms measurements were foreseen as one of the main correction strategies for the LHC during the design phase of the LHC. However, nonlinear corrections from this method were not performed until now. The studies presented in this chapter summarize the extensive measurement campaign undertaken during Run II of the LHC. The highlight of which was the first measurement of decapolar resonance driving terms, and the very first correction of skew octupolar sources in the LHC using measurements of resonance driving terms.

The perturbative impact of nonlinear errors is dependent on the strength of the nonlinear component, as well as the size of the β-function at the location of the error, as presented in Eq. (2.72). In the LHC, the regions where nonlinear errors have the largest impact are found in the final focussing quadrupoles near the experimental insertion regions. Figure 5.1 shows the horizontal and vertical β-functions around IP1 (ATLAS) that reach values of up to 9000 m in the final focus sections. This means that the effect of nonlinear errors is significantly amplified in these regions. During Run II of the LHC the main focus of nonlinear correction strategies was on the correction of errors located in these experimental insertion regions. The large β-functions in these regions do come with a benefit. As the β-functions are so large, the phase advance is close to zero, as described by Eq. (2.17). Any corrector magnet in this region is automatically in phase with the nonlinear errors located in the same region. Dedicated corrector magnets are thus located in these experimental insertion regions.

Two methods were used at the start of Run II for the calculation of beam-based corrections. One is based on measuring tune shifts with beam oscillation amplitude, referred to as amplitude detuning, which is sensitive to octupolar and dodecapolar errors. Another method is based on measurements of tune and linear coupling as a function of crossing angles in the experimental insertions. The crossing angles create an offset with respect to the closed orbit around the collision point. This

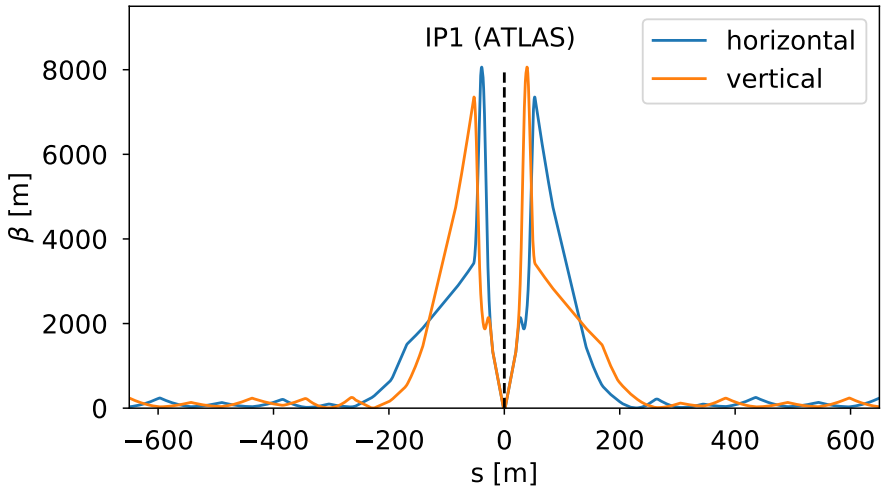

Figure 5.1: *Horizontal and vertical β-functions around IP1 (ATLAS) showing the large increase of β_x and β_y before and after the collision point. The areas with large β-functions are more sensitive to nonlinear errors.*

offset will cause nonlinear magnetic fields to feed down to lower order fields. A particle travelling with a horizontal offset through a sextupole will incur an additional quadrupolar field leading to a tune shift, while vertical offset will result in a skew quadrupolar field leading to linear coupling. Nonlinear errors can thus be measured by characterizing the tune and linear coupling as a function of crossing angles. These two methods, however, rely on measurements of global observables to infer local sources.

Measurements of resonance driving terms promise to provide local information at each BPM on the nonlinear content of the machine. Furthermore, such measurements can distinguish different driving terms, something which other methods struggle to do. The validation of resonance driving terms measurements for the correction of nonlinear errors as presented in this chapter, now offers an additional correction strategy to measure and correct nonlinear errors in the LHC.

MEASUREMENT AND CORRECTION OF RESONANCE DRIVING TERMS IN THE LARGE HADRON COLLIDER

F.S. Carlier, R. Tomás, and E.H. Maclean

Physical Review Accelerators and Beams
Submitted 22 January 2020

5

ABSTRACT

The second run of the LHC has been marked by the developments in methods for nonlinear corrections without which the current unprecedented luminosity would have been challenging to achieve. Nonlinear corrections are now considered a priority in the LHC commissioning strategies due to their effect on Landau damping of instabilities and operational benefits. The measurements of resonance driving terms has now taken a prominent role in the nonlinear correction strategies for the LHC as well as for the the future High Luminosity LHC. This paper presents key developments and advances made during Run II in measurements of resonance driving terms with ac dipoles. This has lead to the first observation of normal and skew decapolar resonance driving terms. Furthermore, the first ever direct correction of skew octupolar driving terms is presented, paving the way for future nonlinear corrections with resonance driving terms.

INTRODUCTION

Measurements of resonance driving terms are in the scope of accelerator physics only a recent development. It was helped by the development of the normal form approach to describe the nonlinear motion in circular accelerators [68, 69]. The relation between the normal form maps and resonances to the spectral content of the complex motion variable $z \pm ip_z$ was established in [73]. This provided a clear path for direct measurements of resonance driving terms by exciting the beam in the transverse planes and recording the turn-by-turn transverse position data using beam position monitors (BPMs).

The first resonance driving terms measurements were done at LEAR [74] and later in the SPS and LEP [75, 76]. Since then measurements of resonance driving terms have been done at RHIC [58, 64, 77, 78], Tevatron [79], PS [80], ALS [81], ESRF [70], Bessy-II [82], Soleil [83], and the ATF Damping Ring [84]. However they have by no means become easy, which is demonstrated by the mixed results obtained at the different laboratories.

The first corrections of resonance driving terms was achieved in the PS at CERN and managed to reduce the $3Q_y$ resonance successfully [76]. Later experiments at the Diamond light source achieved corrections for sextupolar sources by matching spectral line amplitudes [85]. More recently, successful corrections of sextupolar and normal octupolar sources were achieved in the ESRF light source by measuring the combined resonance driving terms from single BPM data [70]. The scarcity of successful corrections reflects the difficulty of the method.

Resonance driving terms in the LHC

In the LHC lattice design, the optimisation of resonance driving terms plays a central role. Though being at the core of the nonlinear design phase, measurements of these resonance driving terms, let alone corrections, are difficult to achieve. First of all, the aperture kicker [52] installed in the LHC, and foreseen for such measurements during the design phase [23], is only considered safe at injection energy and thus prohibits its use at top energy. At top energy the LHC is fully reliant on the ac dipoles to measure resonance driving terms. The forced motion with ac dipoles results in changes in the description of the nonlinear motion. A theoretical description of the nonlinear forced motion in free parameter space is presented in [49], while a description in forced parameter space is presented in [1].

However, using ac dipoles comes with its benefits too. ac dipoles generate a

coherent betatronic oscillation that can last far longer than with a conventional kicker. Figure 5.2 shows the recorded turn-by-turn data at a BPM for two different excitations, one with the aperture kicker in blue and the other with the ac dipole in red. The free kicked beam suffers from decoherence and only 1000 turns can be used. In the ac dipole case, the full duration of the signal can be used, resulting in 6600 turns of high amplitude coherent oscillation data. The larger number of turns and usable data greatly improves the spectral resolution needed for resonance driving terms measurements.

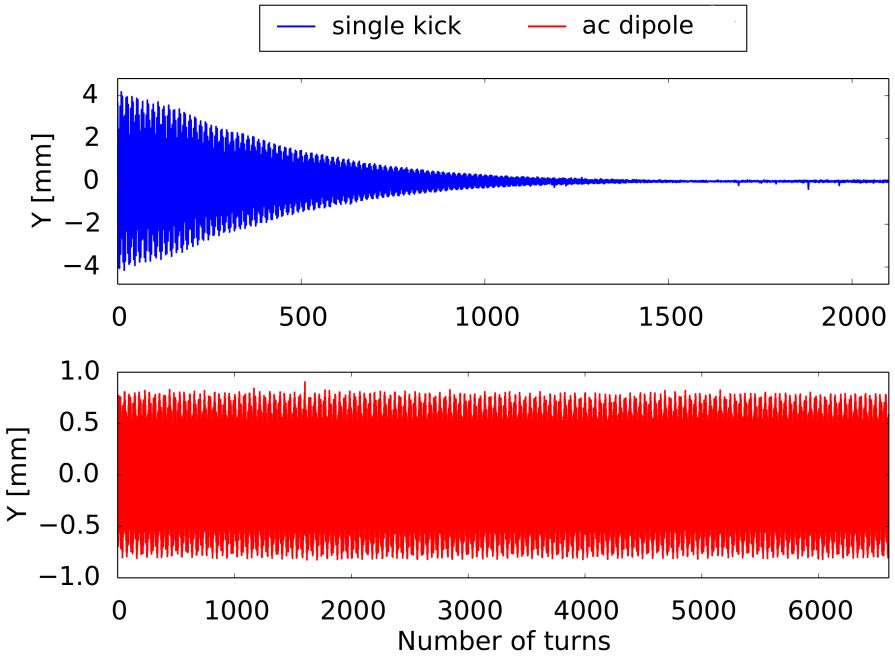

Figure 5.2: *Comparison between turn-by-turn data obtained from a single free kick (blue) and an ac dipole excitation (red) at injection energy.*

As the LHC is being pushed beyond its design parameters, shifts in commissioning strategies are required. Initial correction strategies in the design phase of the LHC assumed corrections based on measured magnetic errors from offline measurements. Unfortunately, beam based measurements of nonlinear sources in Run I showed a large discrepancy with magnetic errors measurements [39, 86]. Beam based measurements have since been the de facto approach for nonlinear corrections in the LHC. A second major shift to nonlinear corrections has been seen in Run II, where these corrections are now an integral part of commissioning [39, 86]. Methods for nonlinear corrections in the LHC were mostly based on measurements of feed-down to tune and coupling with crossing angles, measurements of tune shifts with excitation amplitude, and dynamic aperture measurements with beam

blow-up. Resonance driving terms measurements were so far only used for the validation of corrections. With these methods, successful corrections were achieved for normal and skew sextupolar and normal octupolar sources [39, 86].

The development of the tools for measurements of resonance driving terms in the LHC now facilitates regular measurements of sextupolar and octupolar resonance driving terms and more recently have allowed the first measurements of normal and skew decapolar resonance driving terms. Furthermore, the first correction of skew octupolar sources are achieved in the LHC by directly measuring and correcting skew octupolar resonance driving terms.

The recent results offer a positive outlook for correcting high order nonlinear sources for the LHC in Run III and especially for the High Luminosity LHC. Furthermore measurements of resonance driving terms are fast and allow instantaneous measurement of different orders. They require less machine changes than feed-down measurements, where orbit changes are made at each step, and can for some resonance driving terms even be obtained parasitically from linear optics measurements or amplitude detuning measurements.

This paper reviews the theoretical framework needed for the measurement and correction of forced resonance driving terms in Sec. 5.2. It then proceeds by discussing the measurement and data analysis methods used for resonance driving terms measurements in the LHC in Sec. 5.3. Section 5.4 shows the results of resonance driving terms measurements in the LHC during Run II, including the first measurements of decapolar driving terms. The use of resonance driving terms for the validation of corrections obtained from complementary methods is presented in Sec. 5.5. Finally the first ever correction of skew octupolar sources using ac dipole resonance driving terms is presented in Sec. 5.6.

5

THEORETICAL FRAMEWORK FOR AC DIPOLE RESONANCE DRIVING TERMS

The theoretical description of the ac dipole motion in synchrotrons was established in [1, 43, 49, 53, 54, 65]. The general solution for the particle motion at any longitudinal location s in the ring is given in Courant-Snyder variables as a function of turn τ,

$$\begin{aligned} \hat{z}(\tau) - i\hat{p}_z(\tau) &= \sqrt{2J_z}e^{i(2\pi Q_z\tau+\phi_{z0})} \\ &\quad + e^{-i\phi_{\mathrm{d},z}}(\delta_{z,-}e^{i2\pi Q_{\mathrm{d},z}\tau} - \delta_{z,+}e^{-i2\pi Q_{\mathrm{d},z}\tau}), \end{aligned} \tag{5.1}$$

where $z \in \{x, y\}$ denotes the plane of motion, $Q_{\mathrm{d},z}$ is the ac dipole tune, Q_z is the natural tune, ϕ_{z0} is the initial phase, $\phi_{\mathrm{d},z}$ is the phase advance between location s and the ac dipole, J_z is the linear invariant of the free motion and $\delta_{z,-}$ and $\delta_{z,+}$ are the complex ac dipole strengths defined as,

$$\delta_{z,\pm} = \sqrt{\beta_{\mathrm{acd},z}} \frac{BL}{B_0\rho} \frac{e^{\pm i(\pi Q_{z,\pm} - \psi_0)}}{4\sin(\pi Q_{z,\pm})} \quad , \tag{5.2}$$

where $Q_{z,\pm} = Q_{\mathrm{d},z} \pm Q_z$, ψ_0 is the initial phase of the ac dipole, $\beta_{\mathrm{acd},z}$ is the free β-function at the location of the ac dipole, BL is the integrated field amplitude of the ac dipole, and $B_0\rho$ is the magnetic rigidity. ac dipole tunes are typically set close to the natural tune to enhance the $Q_{\mathrm{d},z} \approx Q_z$ resonance and thus enlarge the $\delta_{z,-}$ mode, referred to here as the main mode. The parameter λ_x can be defined as the ratio of amplitudes between the second mode and the main mode of the ac dipole as,

$$\lambda_x = \frac{\sin[\pi(Q_{x,-})]}{\sin[\pi(Q_{x,+})]} \, . \tag{5.3}$$

The ac dipole working point is typically chosen between 0.015 and 0.008 away from the natural tune. In such conditions we see that the second mode of the ac dipole can have an effect of up to 5% on the motion, as shown in Fig. 5.3.

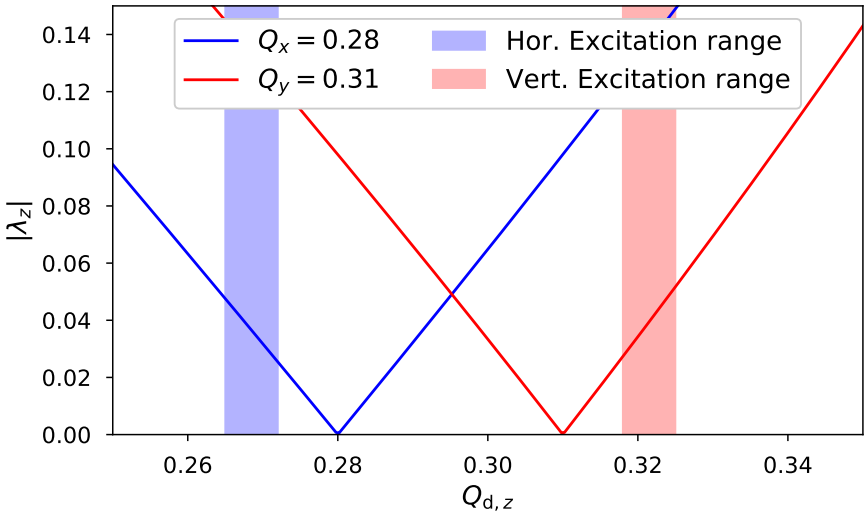

Figure 5.3: *Ratio between $|\delta_{z,-}|$ and $|\delta_{z,+}|$ in percentage showing the almost linear correlation between the relative strength of $|\delta_{z,+}|$ and the tune separation between the ac dipole and natural tune.*

This second mode of the ac dipole causes a distortion in the linear lattice functions α_z, β_z and γ_z. A new parametrization of the ac dipole linear motion is ob-

tained in [54], where both forced modes are combined to a single contribution. The particle position can be expressed as,

$$\begin{aligned} x(s) &= \sqrt{2J_x\beta_x(s)}\cos(\phi_x(s)+\phi_0) \\ &\quad +\sqrt{2A_{\mathrm{d},x}\beta_{\mathrm{d},x}(s)}\cos(\phi_{\mathrm{d},x}(s)+\chi_{\mathrm{d}})\ , \end{aligned} \tag{5.4}$$

where $A_{\mathrm{d},x}$ is a new invariant, and $\phi_{\mathrm{d},x}$ is the new phase advance of forced motion. New optics functions arise as well, such as the forced β-function $\beta_{\mathrm{d},x}$, and the forced $\alpha_{\mathrm{d},x}$ and $\gamma_{\mathrm{d},x}$ functions. The new forced phase $\phi_{\mathrm{d},x}$ is defined by [54],

$$\tan[\phi_{\mathrm{d},x}(s)-\pi Q_{\mathrm{d},x}] = \frac{1+\lambda_x}{1-\lambda_x}\tan[\phi_x(s)-\pi Q_x] \quad , \tag{5.5}$$

while $\beta_{\mathrm{d},x}$ is defined as [54],

$$\beta_{\mathrm{d},x}(s) = \frac{1+\lambda_x^2-2\lambda_x\cos(2\phi_x(s)-2\pi Q_x)}{1-\lambda_x^2}\beta_x(s)\ . \tag{5.6}$$

This description shows a beating of the optics functions that is equivalent to the effect of a gradient error as shown in [54].

5

Resonance driving terms

Resonance driving terms are most commonly derived using the normal form formalism. A derivation of resonance driving terms for forced motion in the free parameter space was first done in [49]. A first derivation of specific resonance driving terms was done for single plane motion and under the assumption that $|\delta_{z,-}| \gg |\delta_{z,+}|$ and $|\delta_{z,-}| \gg 2I_{z,+}$. However, the analysis in the free parameter space requires the observables from BPM turn-by-turn data to be converted to the free parameter space, which introduces errors.

The analysis of forced resonance driving terms in the forced parameter space shows that the description of resonance driving terms is greatly simplified [1]. The amplitude of driving terms now becomes constant between sources. Furthermore, the analysis in forced parameter space allows to use the direct observables, and does not require a conversion of the observables to the free parameter space, thus avoiding the possible introduction of errors during the analysis. Furthermore, it is shown in [1] that a second order perturbative cross-term between the ac dipole and the resonance driving terms acts as a nonlinear source and perturbs the driving

terms around the ring.

The normalized complex Courant-Snyder coordinate under the influence of non-linear perturbations is given in the forced parameter space by [1],

$$\begin{aligned}\xi_{x,-} &\approx \sqrt{2A_{\mathrm{d},x}}e^{i2\pi(Q_{\mathrm{d},x}\tau+\chi_{\mathrm{d},x})} \\ &\quad -2i\sum_{jklm} j f_{jklm,H}(2A_{\mathrm{d},x})^{\frac{j-1+k}{2}}(2A_{\mathrm{d},y})^{\frac{l+m}{2}} \\ &\quad \times e^{i2\pi[(k-j+1)(Q_{\mathrm{d},x}\tau+\chi_{\mathrm{d},x})+(m-l)(Q_{\mathrm{d},y}\tau+\chi_{\mathrm{d},y})]} \quad ,\end{aligned} \tag{5.7}$$

for the horizontal motion, and for the vertical motion by,

$$\begin{aligned}\xi_{y,-} &\approx \sqrt{2A_{\mathrm{d},y}}e^{i2\pi(Q_{\mathrm{d},y}\tau+\chi_{\mathrm{d},y})} \\ &\quad -2i\sum_{jklm} l f_{jklm,V}(2A_{\mathrm{d},x})^{\frac{j+k}{2}}(2A_{\mathrm{d},y})^{\frac{l-1+m}{2}} \\ &\quad \times e^{i2\pi[(k-j)(Q_{\mathrm{d},x}\tau+\chi_{\mathrm{d},x})+(m-l+1)(Q_{\mathrm{d},y}\tau+\chi_{\mathrm{d},y})]} \quad .\end{aligned} \tag{5.8}$$

The resonance driving terms are defined as,

$$f_{jklm,H/V} = \frac{h_{jklm,H/V}}{1-e^{i2\pi[(k-j)Q_{\mathrm{d},x}+(m-l)Q_{\mathrm{d},y}]}} \, , \tag{5.9}$$

where the index H/V specifies the plane in which the resonance driving terms is observed, and $h_{jklm,H/V}$ is defined by,

$$\begin{aligned}h_{jklm,H/V} &= \sum_n h_{n,jklm}e^{i[(j-k)\Delta\phi_{\mathrm{d},n,x}+(l-m)\Delta\phi_{\mathrm{d},n,y}]} \\ &\quad +h^{\mathrm{ac}}_{jklm,H/V}e^{i[(j-k)\Delta\phi_{\mathrm{d,ac},x}+(l-m)\Delta\phi_{\mathrm{d,ac},y}]}\end{aligned} \tag{5.10}$$

Here $h_{n,jklm}$ describes the forced Hamiltonian terms, while $h^{\mathrm{ac}}_{jklm,H/V}$ describes the second order cross-term between the resonance driving terms and the ac dipole expressed in terms of an effective Hamiltonian term, as shown in [1]. The Hamiltonian terms $h_{n,jklm}$ are defined as,

$$h_{n,jklm} = -\frac{[K_{n,q-1}\Omega(l+m) + iJ_{n,q-1}\Omega(l+m+1)]}{j!\ k!\ l!\ m!\ 2^{j+k+l+m}} \times i^{l+m}\beta_{\mathrm{d},x,w}^{\frac{(j+k)}{2}}\beta_{\mathrm{d},y,w}^{\frac{(l+m)}{2}} \quad . \tag{5.11}$$

The multipolar order is given by $q = j + k + l + m$, and $\Omega(i) = 1$ does the job of selecting either the normal (K) or the skew multipoles (J) with,

$$\Omega(i) = 1 \quad \text{if } i \text{ is even} \tag{5.12}$$

$$\Omega(i) = 0 \quad \text{if } i \text{ is odd} \quad . \tag{5.13}$$

The second order cross-term at the location of the ac dipole arises from the ac dipole kick on a distorted phase-space. Derivations of forced motion generally assume a circular normalized phase-space, but this is not the case when nonlinearities are included. A residual r from the ac dipole cross-term can be calculated by summing the contributions at each turn from the kick on the deformed phase-space [1],

$$r = -\frac{1}{2}\sum_{\tau=0}^{N-1} R^{N-\tau}\left([F,h]\Big|_{h=\xi^{\dagger}} - [F,h]\Big|_{h=\xi} \right) \quad , \tag{5.14}$$

where ξ is the normalized complex coordinate, while $\xi^{\dagger}$ is the normalized complex coordinate including the ac dipole kick, and is defined as,

$$\xi^{\dagger}_{z,\pm} = \xi_{z,\pm} \pm i\sqrt{\beta_{\mathrm{acd},z}}\frac{BL}{B_0\rho}\cos(2\pi Q_{\mathrm{d},z}\tau) \quad . \tag{5.15}$$

Detailed derivations of the effective Hamiltonian term describing the second order cross-term are found in [1]. An effective Hamiltonian term for the skew sextupolar resonance driving term $f_{0030,V}$ is derived in [1] and is shown to be,

$$h^{\mathrm{ac}}_{0030,V} = \frac{1}{2}\Bigg[-f_{0030}\left(\frac{\Lambda_y^2}{4} - i\Lambda_y\right) - \frac{1}{3}f_{0012}\frac{\Lambda_y^2}{4} + \frac{2}{3}f_{0021}\left(\frac{\Lambda_y^2}{4} - \frac{i}{2}\Lambda_y\right)\Bigg] \times \left[\frac{1 - e^{i2\pi[-3Q_{\mathrm{d},y}]}}{1 - e^{i2\pi[-Q_y - 2Q_{\mathrm{d},y}]}}\right] \tag{5.16}$$

where,

$$\Lambda_y = \frac{4\sin(\pi(Q_{\mathrm{d},y} - Q_y))}{\sqrt{1-\lambda_y^2}} \quad . \tag{5.17}$$

and where the driving terms in Eq. (5.16) are defined using the first summation of Eq. (5.10) as,

$$f_{jklm} = \frac{\sum_n h_{n,jklm} e^{i[(j-k)\Delta\phi_{\mathrm{d},n,x} + (l-m)\Delta\phi_{\mathrm{d},n,y}]}}{1 - e^{i2\pi[(k-j)Q_{\mathrm{d},x} + (m-l)Q_{\mathrm{d},y}]}} \ , \tag{5.18}$$

Equation (5.16) shows that multiple resonance driving terms will contribute to the second order cross-term. Secondly it is important to notice that in this parametrization the forced resonances of the form $-Q_x + (k-j+1)Q_{\mathrm{d},x} + (m-l)Q_{\mathrm{d},y}$ for the horizontal motion and $-Q_y + (k-j)Q_{\mathrm{d},x} + (m-l+1)Q_{\mathrm{d},y}$ for the vertical motion, are recovered from this second order cross-term.

MEASURING RESONANCE DRIVING TERMS FROM BPM TURN-BY-TURN DATA

The relation between resonance driving terms and secondary spectral lines in the spectra of BPM position turn-by-turn data was first established in [73]. It provides a clear road-map for measuring forced resonance driving terms. A beam is excited in the transverse plane, in one or two planes, to large amplitudes. Simultaneous excitations in both planes are referred to as diagonal excitations. The transverse positions of the bunch are recorded turn-by-turn using BPMs. The spectral content of this turn-by-turn data holds all the necessary information to measure resonance driving terms. However, as only the real position data is known the contributions from different resonance driving terms cannot be untangled. In order to retrieve this information the full complex signal needs to be recovered. The complex signal at a BPM can be recomposed using the turn-by-turn data of two BPMs at close to $\pi/2$ phase advance. For an element at location s_i the forced Courant-Snyder coordinates are given by

$$\begin{aligned} \hat{z}_i &= \sqrt{2A_{\mathrm{d},z}}\cos(\phi_{\mathrm{d},z}(s_i) + \chi_{\mathrm{d}}) \\ \hat{p}_{z,i} &= -\sqrt{2A_{\mathrm{d},z}}\sin(\phi_{\mathrm{d},z}(s_i) + \chi_{\mathrm{d}}) \ . \end{aligned} \tag{5.19}$$

Assuming that there is no significant error between the two BPMs, the phase advance between the two BPMs is given by $\Delta\phi_{\mathrm{d},z} = \phi_{\mathrm{d},z}(s_2) - \phi_{\mathrm{d},z}(s_1)$. The momentum at a BPM can be expressed as a function of the position data (z_1) of that BPM and of the second BPM at $\pi/2$ phase advance (z_2) as,

$$p_{z,1} = \frac{z_2 - z_1 \cos(\Delta\phi_{\mathrm{d},z})}{\sin(\Delta\phi_{\mathrm{d},z})} \quad . \tag{5.20}$$

The complex signal at location s_1 can then be recombined from the real position data at both locations s_1 and s_2 as,

$$z_1 - ip_{z,1} \;=\; z_1\left(1 + i\frac{\cos(\Delta\phi_{\mathrm{d},z})}{\sin(\Delta\phi_{\mathrm{d},z})}\right) - z_2\left(i\frac{1}{\sin(\Delta\phi_{\mathrm{d},z})}\right) \quad . \tag{5.21}$$

The resonance driving terms are related to the secondary spectral line amplitudes from spectra as,

$$\begin{aligned} H(k-j+1, m-l) &= 2j|f_{jklm,\mathrm{H}}|(2A_{\mathrm{d},x})^{\frac{j+k-1}{2}}(2A_{\mathrm{d},y})^{\frac{m+l}{2}} \\ V(k-j, m-l+1) &= 2l|f_{jklm,\mathrm{V}}|(2A_{\mathrm{d},x})^{\frac{j+k}{2}}(2A_{\mathrm{d},y})^{\frac{m+l-1}{2}} \end{aligned} \tag{5.22}$$

where $H(k-j+1, m-l)$ are the secondary spectral line amplitudes in the horizontal plane with frequencies $(k-j+1)Q_{\mathrm{d},x} + (m-l)Q_{\mathrm{d},y}$, and $V(k-j, m-l+1)$ are the secondary spectral line amplitudes in the vertical plane with frequencies $(k-j)Q_{\mathrm{d},x} + (m-l+1)Q_{\mathrm{d},y}$. The phases of the resonance driving terms are given by,

$$\begin{aligned} \phi_{k-j+1,m-l} &= \phi_{jklm,\mathrm{H}} + (k-j+1)\phi_{1,0} + (m-l)\phi_{0,1} - \frac{\pi}{2} \\ \phi_{k-j,m-l+1} &= \phi_{jklm,\mathrm{V}} + (k-j)\phi_{1,0} + (m-l+1)\phi_{0,1} - \frac{\pi}{2} \end{aligned} \tag{5.23}$$

where $\phi_{k-j+1,m-l}$ is the phase of the secondary spectral line in the horizontal plane and $\phi_{k-j,m-l+1}$ is the spectral line phase in the vertical plane, $\phi_{jklm,\mathrm{H/V}}$ is the phase of the resonance driving term, and $\phi_{1,0}$ and $\phi_{0,1}$ are the phases of the main spectral lines of the horizontal and vertical planes respectively.

Procedure for measurements of resonance driving terms

Resonance driving terms measurements are done in the LHC by filling the beams with a single pilot bunch of 10^{10} protons per beam. This low intensity is considered safe for excitation with ac dipoles at top energy. The beams are non-colliding to avoid perturbations from beam-beam effects [5], and the Landau octupoles are turned off to not perturb the amplitude detuning. The linear coupling is corrected to $|C^-| < 10^{-3}$, where the coupling parameter $|C^-|$ is defined as in [87]. All measurements presented in the following sections are done with these base machine settings. Settings of possible crossing angles, orbit bumps in the experimental insertion regions, and β^* at the location of the interaction points are specified per measurement on the corresponding sections.

The beams are excited using the ac dipoles. They can be excited in the vertical and horizontal planes independently, or simultaneously which is referred to as diagonal excitations. The turn-by-turn data is recorded using the BPMs for the duration of the flattop excitation of the ac dipole. The raw BPM data is cleaned of noise by applying the singular value decomposition (SVD) method developed in [88]. The number of retained singular values is increased with respect to linear optics studies, this is done to prevent weaker nonlinear signals to be filtered out. The spectral analysis of the turn-by-turn data at each BPM is done using the spectral analysis code SUSSIX [89]. The frequencies of the secondary spectral lines are expressed as linear combinations of the main tune lines in SUSSIX. The secondary spectral line amplitudes are normalized by the main tune line amplitudes in each BPM, which has the benefit of removing the $\beta_{\mathrm{d},z}$ dependence of the amplitude signal along the ring and taking care of possible calibration errors.

The invariants $A_{\mathrm{d},z}$ are calculated from the amplitudes of the main tune lines in the spectra. Under the assumption that the nonlinear perturbations are weak compared to the linear motion, the invariants may be approximated as the average of the main line amplitudes over all the arc BPMs as,

$$\begin{aligned} 2A_{\mathrm{d},x} &= \frac{1}{N_{\mathrm{BPM}}} \sum_{0}^{N_{\mathrm{BPM}}} \frac{|H(1,0)|^2}{\beta_{\mathrm{d},x}} \quad , \\ 2A_{\mathrm{d},y} &= \frac{1}{N_{\mathrm{BPM}}} \sum_{0}^{N_{\mathrm{BPM}}} \frac{|V(0,1)|^2}{\beta_{\mathrm{d},y}} \quad , \end{aligned} \tag{5.24}$$

where $|H(1,0)|$ is the amplitude of the horizontal ac dipole tune line in the real horizontal spectrum and $|V(0,1)|$ is the amplitude of the vertical ac dipole tune

line in the real vertical spectrum. For measurements, the average over all arc BPMs is taken to avoid possible calibration errors of BPMs in the insertion regions [90]. The error on the actions is defined as the standard deviation over those BPMs. Furthermore, high-order resonance driving terms that contribute to the $H(1,0)$ and $V(0,1)$ lines will generally not propagate with the same phase as the main mode and their perturbation thus averages out when taking the average over the BPMs.

Resonance driving terms are finally calculated by fitting Eq. (5.22) to the measured spectral line amplitude and actions of the series of excitations. The obtained error on the fit provides the error on the amplitude of the driving term. The phase of the resonance driving terms is obtained from Eq. (5.23) for each measurement. The average over all the measurements provides the average phase and corresponding error for the resonance driving term at each BPM.

MEASUREMENTS OF RESONANCE DRIVING TERMS IN LHC

One main objective of Run II in the LHC was to develop and test methods for nonlinear corrections in view of the High Luminosity LHC upgrade. Resonance driving terms measurements were thus taken throughout Run II in commissioning or dedicated Machine Development (MD) periods. Resonance driving terms of normal and skew sextupolar sources and normal and skew octupolar sources are now measured on a regular basis when the machine is in an uncorrected state. This section starts by exploring the effect of the ac dipole and natural working point on the ability to measure the driving terms, and then proceed by presenting the first measurements of higher order driving terms from decapolar orders are presented.

Enhancement of resonance driving terms with working point

The amplitude of resonance driving terms is greatly dependent on the chosen working point. The resonance driving terms amplitude can be enhanced by approaching the forced resonances. By carefully choosing the working point, the amplitude of specific spectral lines can be increased, thus improving the measurement of the corresponding resonance driving terms. Measurements done in 2016 explore the effect of the working points on resonance driving terms measurements. The measurements are done in Beam 2 at top energy with $\beta^* = 40$ cm at IP1 and IP5 and flat orbit. Three working points are chosen to study the enhancement of $f_{0030,V}$, $f_{4000,H}$ and $f_{1210,H}$. The first working point uses the nominal injection tunes at $Q_x = 0.28$ and $Q_y = 0.31$. The second working point is moved closer to the octupolar reso-

Table 5.1: *Natural and forced tunes used for the study of resonance driving terms enhancements. Measurements are done either with horizontal excitations (H) or diagonal excitations (H+V).*

	Q_x	Q_y	$Q_{\mathrm{d},x}$	$Q_{\mathrm{d},y}$	excited plane
wp 1	0.28	0.31	0.27	0.324	H, H+V
wp 2	0.27	0.31	0.26	0.324	H
wp 3	0.29	0.30	0.28	0.314	H+V

nance $-Q_x - 3Q_{\mathrm{d},x} = p$, related to the driving term $f_{4000,H}$. The third working point is closer to the skew octupolar resonance $-Q_x + 2Q_{\mathrm{d},x} - Q_{\mathrm{d},y} = p$ that is driven by $f_{1210,H}$, and further away from the skew sextupolar resonance $-Q_y - 2Q_{\mathrm{d},y}$ that is driven by $f_{0030,V}$. The chosen natural and ac dipole tunes are summarised in Tab. 5.1. The ac dipole tunes are always at the same tune split to the natural working point; $Q_{\mathrm{d},x} = Q_x - 0.01$ and $Q_{\mathrm{d},y} = Q_y + 0.014$, to minimise effects from tune proximity between natural and ac dipole tunes, and to facilitate kicks at identical amplitudes. Measurements with large diagonal ac dipole excitations were taken at the two working points 1 and 3 of Tab. 5.1, while large horizontal excitations were made at working points 1 and 2.

Figure 5.4 shows the measured amplitude of $f_{4000,H}$ for measurements at working points 1 and 2. The amplitude of $f_{4000,H}$ is successfully increased by a factor 1.63 ± 0.06 when moving the working point closer to the octupolar resonance. The BPMs around the IPs are left out of the measurements due to unfavourable phase advances, which result in large outliers. Single particle tracking simulations are done with the nominal 2016 model with flat orbit and the 60 seeds of the WISE [91] error tables available for the LHC, including the normal and skew sextupolar, octupolar and decapolar errors. An average and standard deviation of the resulting driving terms for all the seeds is obtained at each BPM and shown alongside the measurements. Clearly, there is a significant discrepancy between the measured resonance driving terms amplitudes and the simulations results from expected nonlinear errors. This discrepancy is not unexpected as beam-based measurements of nonlinear errors have demonstrated that the errors from offline magnetic measurements do not accurately reproduce the observed machine nonlinearities [39, 86,

92]. Furthermore, jumps in the amplitude of the driving terms are observed in the results from simulations at IP1 and IP5 where the errors have the largest effect due to the large β-functions at the triplets. This behaviour is not as pronounced in measurements and can possibly be due to loss of information in the cleaning of the data [93]. Unfortunately, the cleaning of the data is necessary to observe the secondary spectral lines in the first place. Future improvements and studies on the cleaning may improve the sensitivity to the observation of local jumps in amplitude.

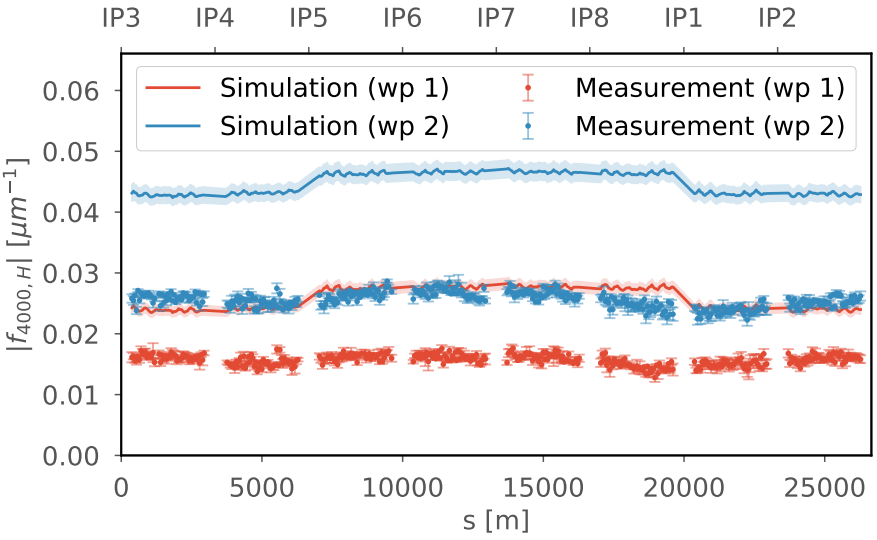

Figure 5.4: *Enhancement of the normal octupolar $f_{4000,H}$ from a change of working point between working points 1 and 2, for Beam 2 at $\beta^* = 40$ cm.*

Still, the relative enhancement of the $f_{4000,H}$ driving term between the two working points can also be probed in simulation regardless of its absolute amplitude. Tracking simulations show an enhancement of $f_{4000,H}$ by a factor of 1.73 ± 0.05, which is compatible with the measured values.

Similar measurements are presented for the skew octupolar and skew sextupolar resonance driving terms $f_{1210,H}$ and $f_{0030,V}$ by moving to the third working point of Tab. 5.1. Again the simulation results are presented alongside the measurements. Figure 5.5 shows the measured and simulated amplitudes of $f_{0030,V}$. The measured driving term amplitudes are larger than predictions from simulations, although the relative deviation is smaller than for the previous case of $f_{4000,H}$. Figure 5.5 shows that the driving term amplitude decreases when the working point is moved away from the third-order resonance. The decrease in amplitude is measured at 0.556 ± 0.011 and simulated to be 0.600 ± 0.018.

As a reference, the amplitude of another skew sextupolar resonance driving term

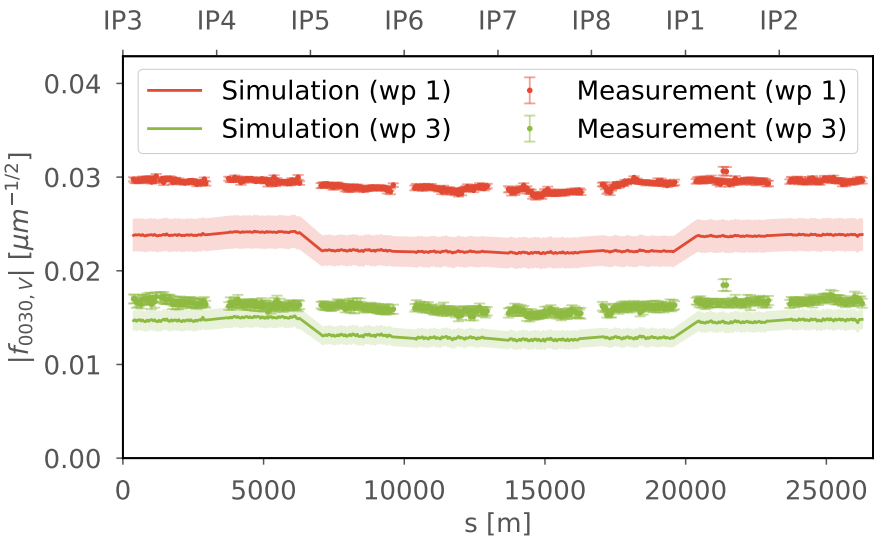

Figure 5.5: *Enhancement of the skew sextupolar $f_{0030,V}$ from a change of working point between the working points 1 and 3, for Beam 2 at $\beta^* = 40$ cm.*

$f_{0012,V}$ is shown in Fig. 5.6. Both working points 1 and 3 are far away from the corresponding resonance, and thus the change in driving term amplitude is minimal. Furthermore, a better agreement is observed between measurements and simulations than for $f_{0030,V}$. Interestingly, a large jump in amplitude is observed in the simulations at IP4, the location of the ac dipole. This jump is generated by the second order cross-term of the ac dipole from Eq. (5.10). A similar jump is not observed in the measurement data.

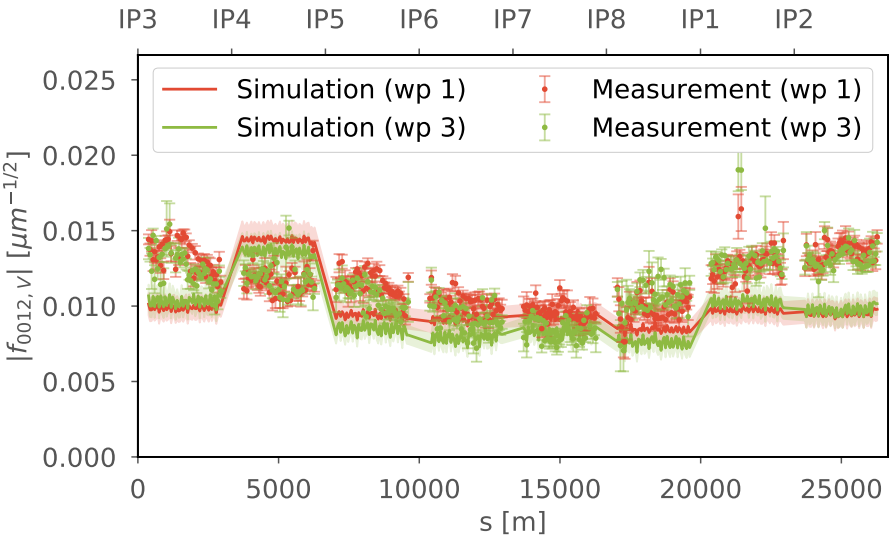

Figure 5.6: *Enhancement of the skew sextupolar $f_{0012,V}$ from a change of working point between the working points 1 and 3, for Beam 2 at $\beta^* = 40$ cm. No enhancement is observed as expected due to the far distance to the resonance condition.*

Lastly, the enhancement of $f_{1210,H}$ is studied for the same change of working point 1 to 3. The results from measurements and tracking simulations for both working points are shown in Fig. 5.7. The measured amplitudes of $f_{1210,H}$ are significantly lower than those observed from tracking simulations. However, the factor of enhancement is measured to be 1.34 ± 0.03 for the beam measurements and 1.45 ± 0.03 for the tracking simulations.

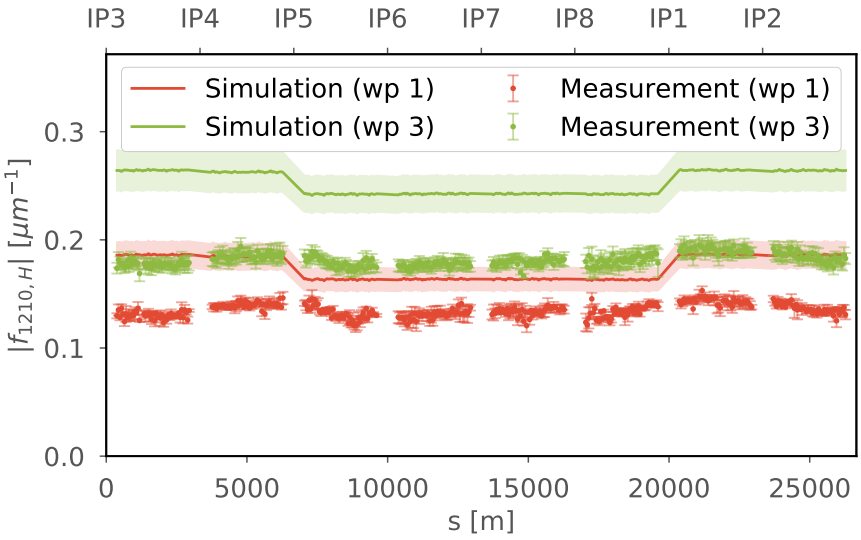

Figure 5.7: *Enhancement of the skew octupolar $f_{1210,H}$ from a change of working point between the working points 1 and 3, for Beam 2 at $\beta^* = 40$ cm.*

The measured amplification factors of resonance driving terms agree relatively well with simulation. These studies show that the resonance driving terms can be enhanced by carefully choosing the natural and forced tunes. This is of significant importance for the study of higher order nonlinear sources that may be difficult to measure, especially so for the High Luminosity LHC where high order nonlinear error are expected to impact performance.

First measurements of decapolar resonance driving terms

No definite beam-based correction strategy has yet been defined for the correction of higher order nonlinear sources such as normal and skew decapolar errors for the High Luminosity LHC [94]. Various methods have shown to be sensitive to such high order errors when probed at their expected strength of the High Luminosity LHC [32] in the LHC. Measurements of resonance driving terms are considered a promising option for the correction of such high order perturbations. Measurements of higher order resonance driving terms require very large amplitude excita-

Table 5.2: *Natural and forced tunes used for the study of decapolar resonance driving terms.*

	Q_x	Q_y	$Q_{\mathrm{d},x}$	$Q_{\mathrm{d},y}$
collision tunes	0.31	0.32	0.302	0.33
shifted tunes	0.305	0.315	0.297	0.325

tions. Such measurements are thus in part limited by physical aperture as well as the available forced dynamic aperture [3]. It is thus crucial to have good corrections of the lower order nonlinear sources to limit amplitude detuning and maximise the forced dynamic aperture to be able to measure decapolar and dodecapolar sources.

This section presents the first measurements of resonance driving terms of decapolar order. Measurements with large vertical excitations were done in 2018 with crossing angles of 145 μrad in the insertion regions of IP1 (ATLAS) and IP5 (CMS), as well as the skew and normal sextupolar and octupolar corrections of 2018. The measurements are done at two different working points to rule out possible fixed noise lines, and the chosen working points are summarized in Tab. 5.2. Note that at collision tunes the working point is exactly on the skew decapolar resonance $-Q_y + 4Q_{\mathrm{d},y} = p$ in the vertical motion, and very close to the $-Q_x + Q_{\mathrm{d},x} - 3Q_{\mathrm{d},y} = p$ resonance in the horizontal motion. The resonance driving terms driving these resonances are thus expected to be large as well. The shifted tunes depart slightly from the two specified resonances, a decrease of the related resonance driving terms is thus expected.

Spectral analysis of the turn-by-turn data reveal two secondary spectral lines of decapolar order in both the horizontal and vertical plane, namely $H(1,-3)$ and $H(0,4)$ that are generated by $f_{1130,H}$ and $f_{1004,H}$ respectively, and in the vertical plane $V(1,-3)$ and $V(0,4)$ that are generated by $f_{0140,V}$ and $f_{0014,V}$ respectively. Figures 5.8 and 5.9 show zoomed spectra of the horizontal and vertical turn-by-turn data for measurements taken at collision tunes and at the shifted working point respectively. The observed secondary spectral lines all shift in frequency with the change of tunes, thus excluding possible observations of fixed noise lines. A very small deviation of the natural tune and ac dipole tune during experiments allows the distinction between the $V(0,4)$ spectral line and the vertical natural tune (Q_y) as can be seen in Fig. 5.8.

The amplitudes of the resonance driving terms measured at collision tunes are

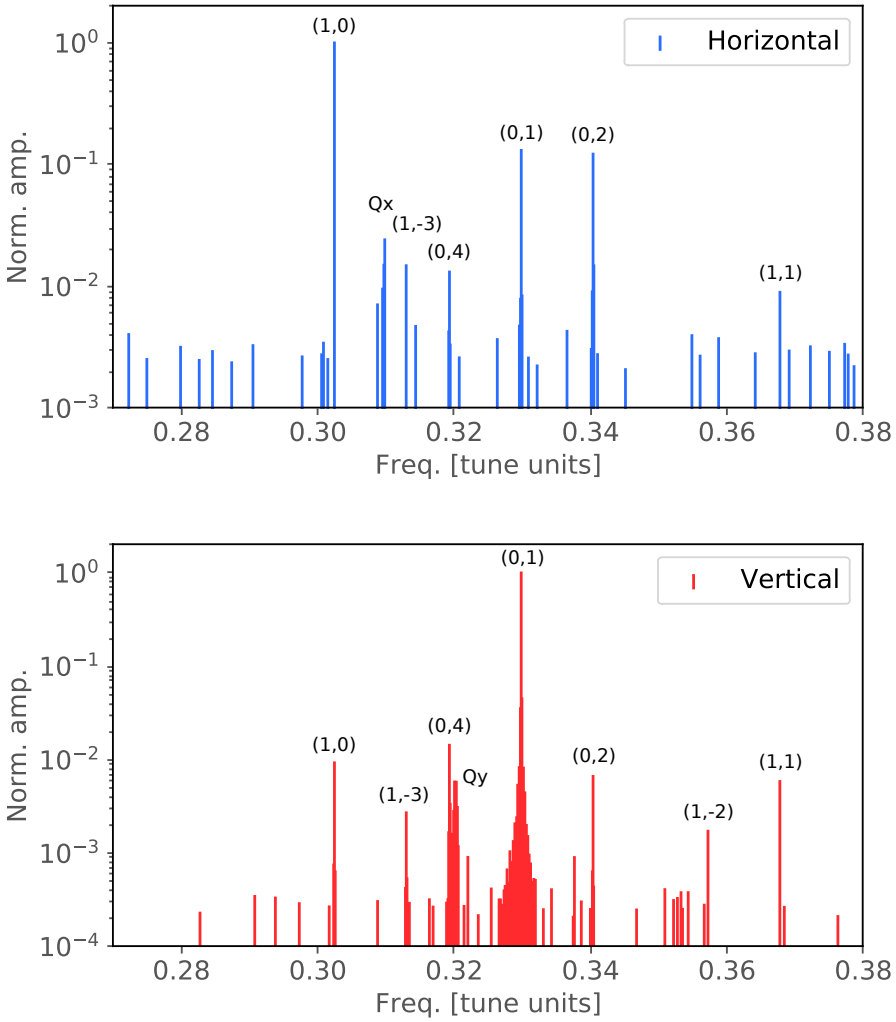

Figure 5.8: *Zoom of horizontal and vertical spectra at BPM.15L5.B1 for measurement at collision tunes. The line* $(0,4)$ *with frequency* $4Q_{\mathrm{d},y}$ *indicates the normal decapolar line in the horizontal spectrum, and the skew decapolar line in the vertical spectrum.*

shown in Fig. 5.10. The amplitudes of both $f_{1130,H}$ and $f_{0014,V}$ are very large compared to the other two driving terms. Single particle tracking simulations are done and the calculated resonance driving terms are compared in Fig. 5.10. First, the amplitude of the two largest driving terms, $f_{1130,H}$ and $f_{0014,V}$, are not well reproduced. The simulated driving terms amplitudes are all smaller than those measured. However the calculated error on the resonance driving term amplitudes from tracking simulations with 60 error seeds increases dramatically for the resonance driving terms that are close or on their respective resonances.

The measurements with the shifted tunes show a general reduction of the resonance driving terms amplitudes, as presented in Fig. 5.11. The $f_{1130,H}$ resonance

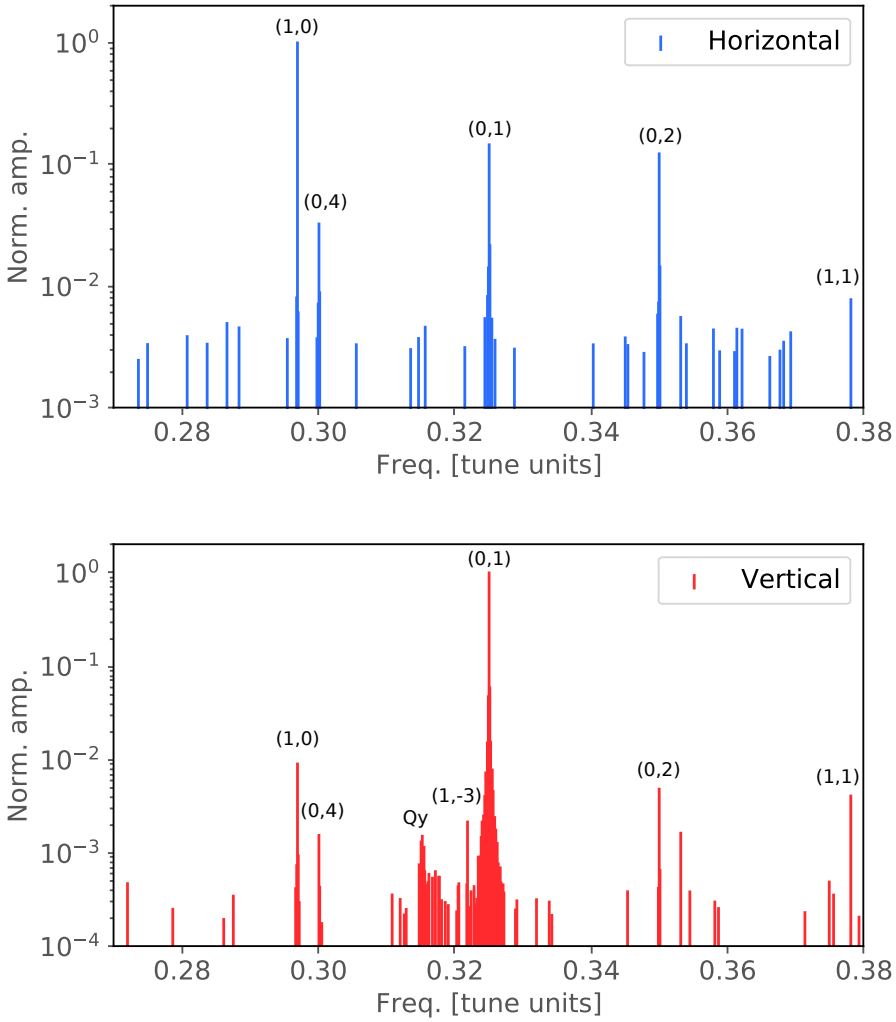

Figure 5.9: *Zoom of horizontal and vertical spectra at BPM.15L5.B1 for shifted tunes. The line* $(0,4)$ *with frequency* $4Q_{d,y}$ *indicates the normal decapolar line in the horizontal spectrum, and the skew decapolar line in the vertical spectrum.*

driving term related to the $H(1,-3)$ spectral line is not properly observed at these tunes, and thus omitted from the results. Tracking simulations confirm a reduction of resonance driving terms amplitudes for those measured. The deviation calculated from the simulations with 60 error seeds is reduced as well as the working points are moved away from the resonances. A discrepancy is observed between measurements and simulations for the $f_{1004,H}$ and $f_{0140,V}$ driving terms. The simulations, however accurately reproduce their relative amplitude difference. Furthermore, the simulations manage to reproduce the measurements of $f_{0014,V}$ more accurately for the case with shifted tunes.

The measured skew and normal decapolar resonance driving terms amplitudes

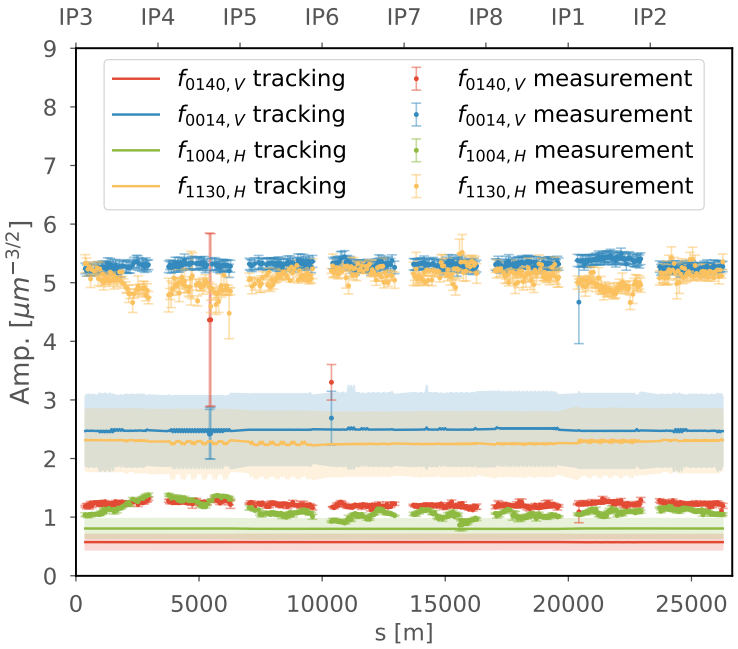

Figure 5.10: *Amplitudes of $f_{1130,H}$, $f_{1004,H}$, $f_{0140,V}$ and $f_{0014,V}$ resonance driving terms measured in Beam 1 for measurements with large vertical excitations at collision tunes, see Tab. 5.2.*

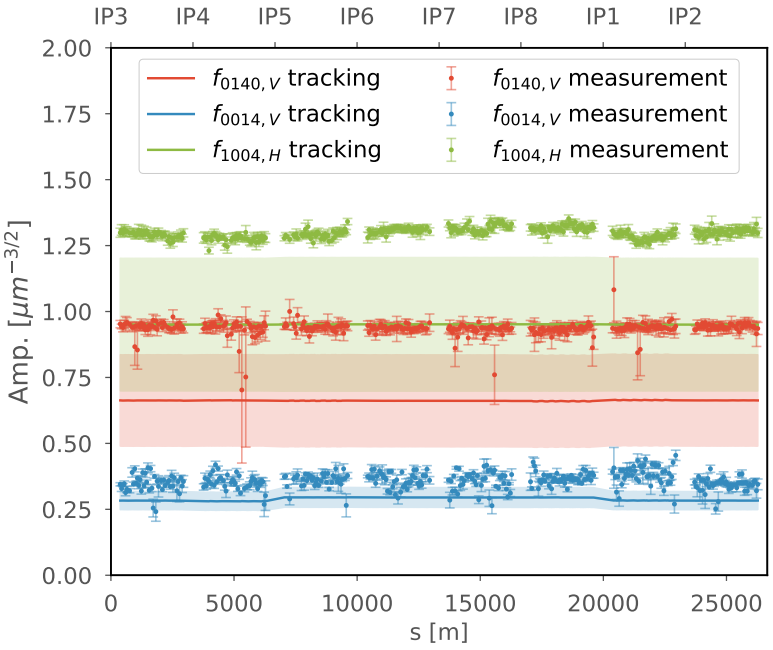

Figure 5.11: *Amplitudes of $f_{1004,H}$, $f_{0140,V}$ and $f_{0014,V}$ resonance driving terms measured in Beam 1 for measurements with large vertical excitations and shifted tunes, see Tab. 5.2.*

are larger than simulated in the current models, which suggests that the decapolar errors are currently underestimated in the LHC. Further measurements of decapolar resonance driving terms should be done to better identify and localize the errors. Unfortunately, there are currently no decapolar correctors in the LHC which significantly complicates any attempt to correct these errors. This first measurement of decapolar resonance driving terms offers a positive outlook on the measurement of high order resonance driving terms for nonlinear correction strategies in the High Luminosity LHC.

Validating nonlinear corrections with measurements of resonance driving terms

Corrections of nonlinear optics at top energy in the LHC are mainly focused on the insertion regions with large β-functions, i.e. ATLAS (IR1) and CMS (IR5). Local nonlinear errors in the final focussing triplets are generally the most perturbative, and the correction of these errors are thus prioritized. Dedicated corrector magnets are located next to the triplets that can be used independently to correct nonlinear errors locally. These corrector magnets include normal and skew sextupoles, normal and skew octupoles, and normal dodecapoles. It must be noted that the triplets as well as the correctors are in regions of shared aperture between Beam 1 and Beam 2, thus affecting both beams. Resonance driving terms measurements of both beams are not always possible due to other parallel studies and limited beam availability. The results presented in this section thus mainly focus on measurements in Beam 2.

Measurements of resonance driving terms were, in the first stages of Run II, initially used to validate the corrections calculated from other complimentary beam-based methods [39, 86, 92]. Run II of the LHC saw an iterative approach to the correction of nonlinear observables at top energy. Firstly, amplitude detuning measurements revealed a significant source of local normal octupolar errors in the triplets of the experimental insertion regions [39, 65, 92], which is to be expected considering the systematic normal octupolar components measured in the triplets during magnetic measurements [91]. Corrections were implemented in 2017 that are based on measurements of tune shifts with amplitude, and measurements of tune shifts with crossing angle. Measurements of the normal octupolar driving term $f_{4000,H}$ before and after correction are presented in Fig. 5.12.

A reduction of the driving term amplitude is observed along the full circumference of the LHC as the local normal octupolar correction in IP1 is implemented, and subsequently a further reduction is observed when the correction in IP5 is added.

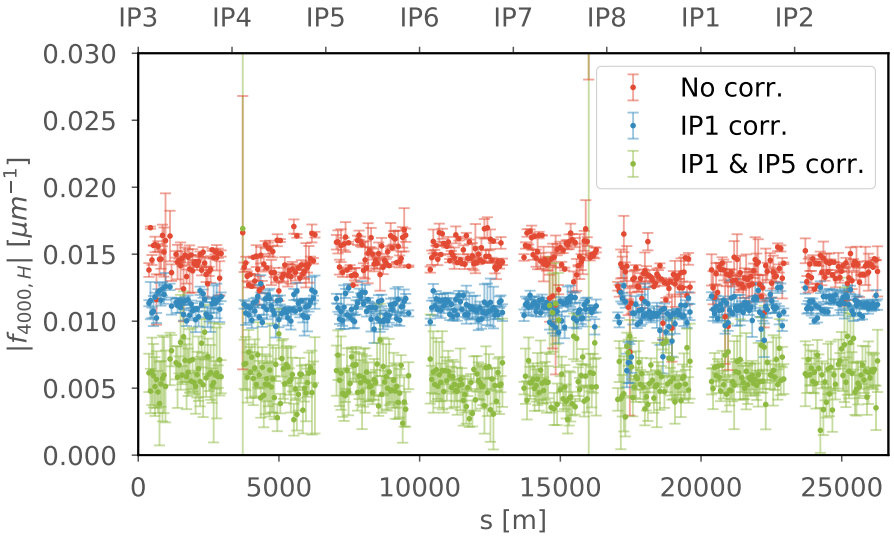

Figure 5.12: *Measurements of $f_{4000,H}$ before and after the implementation of local normal octupolar corrections in IR1 and IR5 in Beam 2. The reduction of driving term amplitude after the implementation of the correction offers a validation of the calculated corrections from amplitude detuning and feed-down measurements.*

The measured driving term in the case where both insertion regions are corrected show a great reduction in the amplitude of $f_{4000,H}$ to levels where the spectral noise level starts to perturb the measurement. As the amplitude of the driving terms is reduced through corrections, the measurement error at each BPM increases. Indeed, for low amplitude driving terms, the corresponding spectral line amplitude is much more sensitive to noise. The measurements offer a validation of the local normal octupolar errors calculated from amplitude detuning measurements and feed-down measurements with crossing angles [39, 92].

Local skew sextupolar errors in IR1 were measured 2017. The corrections were based on feed-down measurements to tune with vertical crossing angles in IR1. The corrections are in part validated with measurements of the skew sextupolar resonance driving term $f_{0030,V}$ related to the $-Q_y - 2Q_{\mathrm{d},y} = p$ resonance. Figure 5.13 shows the amplitude of $f_{0030,V}$ as measured before and after the implementation of the local IR1 corrections. A significant reduction of driving term amplitude is observed, thus validating the correction. Just as for the validation of the $f_{4000,H}$ correction, the results with corrected skew sextupolar errors show a very small amplitude where the signal-to-noise level starts to deteriorate and measurement errors increase.

Local skew octupolar corrections were derived in IR1 and IR5 from measurements of feed-down to coupling with crossing angle in 2017 [95]. While the cor-

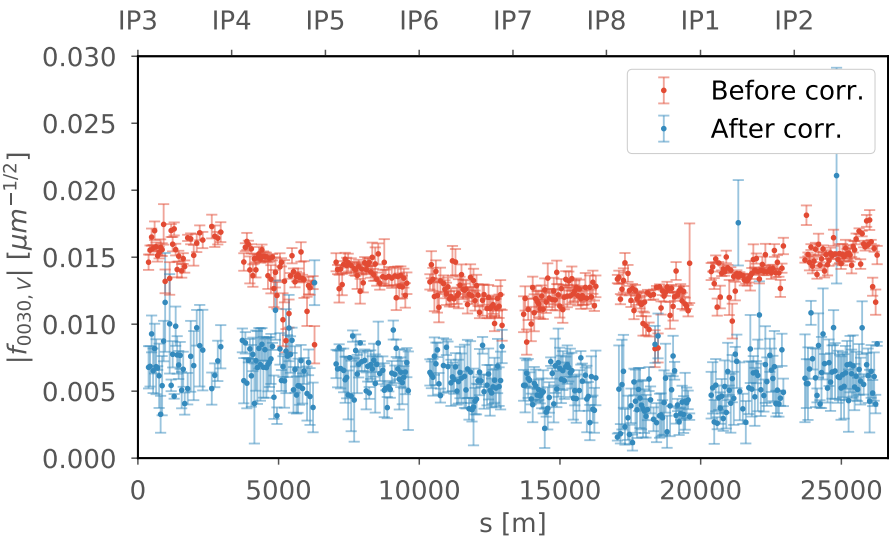

Figure 5.13: *Measurements of $f_{0030,V}$ before and after the implementation of local IR1 skew sextupolar corrections in Beam 2. The reduction of driving term amplitude after the implementation of the correction offers a validation of the calculated corrections from feed-down measurements.*

rections for IR1 were validated with crossing-angle scans and implemented operationally, calculating corrections for IR5 proved more challenging.

Measurements of the skew octupolar resonance driving term $f_{1210,H}$ are used to verify two corrections derived for IR5. All measurements presented are done for the ATS optics [96] at $\beta^* = 30$ cm with a flat orbit. Due to uncertainties about the polarity of the skew octupolar correctors on the left side and right side of IP5 the calculated correction is implemented with both polarities to compare the results. The following results compare three settings of the correctors. The setting without any correction in IR5, the corrector setting assuming a positive polarity of the correctors (Correction 1), and the setting assuming a negative polarity of the correctors (Correction 2). Figure 5.14 shows the measured amplitudes of $f_{1210,H}$ for the corrector settings. Measurements using the negative polarity of the correctors (Corr. 2) show a doubling of the resonance driving term amplitude along the ring. For the case with positive polarity (Corr. 1) the resonance driving term amplitude increases only slightly.

The difference in the resonance driving term phase $\phi_{1210,H}$ between the measurements with corrections and the reference measurement without corrections can be compared and is presented in Fig. 5.15. A constant phase offset is observed in for both corrector settings. Such a phase offset indicates that the phases of the skew octupolar correctors in IR5 may not be aligned with the local skew octupolar error

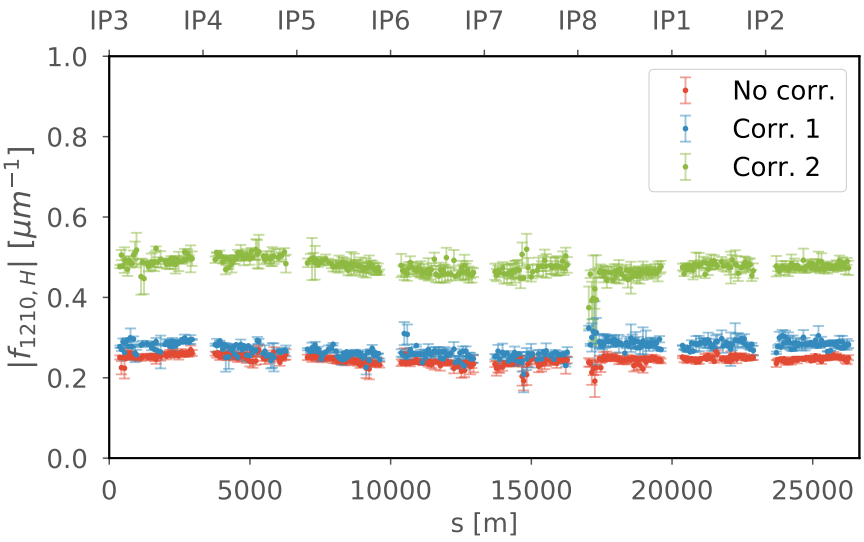

Figure 5.14: *Amplitude of $f_{1210,V}$ for the LHC without skew octupolar corrections and with two different skew octupolar corrections with different polarities, for Beam 2 at 6.5 TeV, $\beta^* = 30$ cm, and flat orbit.*

that the correctors try to correct. The phase offset of the corrections are given in Tab. 5.3. The results suggest that the local correction of IR1 is not perfect, which can cause the phase of the resonance driving term in IR5 to be misaligned with the phase of the correctors and thus deteriorate the correction.

5

FIRST CORRECTION OF SKEW OCTUPOLAR RESONANCE DRIVING TERMS

The aim of resonance driving terms measurements is to directly measure and correct nonlinear errors in the LHC. Corrections of skew octupolar resonance driving terms are for the first time achieved using the ac dipoles in the LHC. This section presents the correction of the skew octupolar driving terms $f_{1210,H}$ and $f_{1012,V}$.

Table 5.3: *Calculated driving term phase ($\phi_{1210,H}$) offset between the local correction and the skew octupolar error from measurements.*

	Polarity	Phase Offset
Correction 1	+1	56 ± 5
Correction 2	-1	109 ± 6

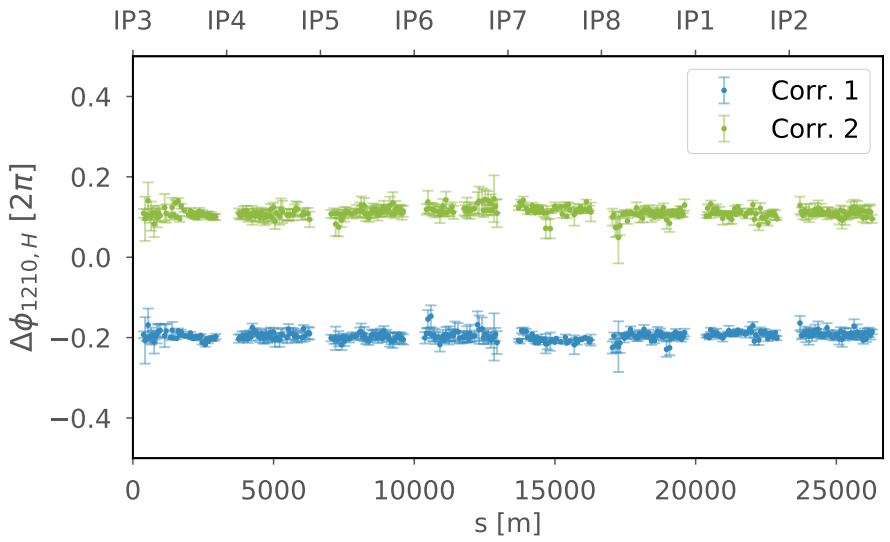

Figure 5.15: *Difference in driving term phases with* $\Delta\phi_{1210} = \phi_{1210,\,\text{no corr}} - \phi_{1210,\,\text{with corr}}$, *for two skew octupolar corrections with different polarities. For Beam 2 at 6.5 TeV,* $\beta^* = 30$ *cm, and flat orbit.*

The measurement approach is identical to what is presented in the previous sections. The natural tunes are chosen are at $Q_x = 0.31$ and $Q_y = 0.32$, while the ac dipole tunes are set to to $Q_{\mathrm{d},x} = 0.302$ and $Q_{\mathrm{d},x} = 0.33$. The crossing angles in IR1 and IR5 are set to 145 μrad. This is a compromise crossing angle that sits in the middle of the range of operational crossing angles used during β^*-levelling in 2018. It is the crossing angle at which most of the linear and nonlinear commissioning was done in 2018. The measurements were done by exciting the beam simultaneously in both horizontal and vertical planes.

The approach for the calculation of the corrections is as follows. First a measurement of the bare machine without any skew octupolar correction is done. Figure 5.16 shows the real and imaginary parts of $f_{1210,H}$ for the bare machine with all the skew octupolar correctors turned off for Beam 1. The real and imaginary parts of the driving term responses of the skew octupolar correctors are calculated from tracking simulations where each corrector is powered individually. Figure 5.17 shows the real and imaginary part of $f_{1210,H}$ which forms the response from the skew octupolar corrector left of IP5. The responses are matched to the measured driving term of the bare machine, and the opposite of the obtained corrector strengths is implemented in the machine.

The corrector responses are calculated with single particle tracking simulations for each available skew octupolar corrector in main experimental insertion regions. Each corrector is simulated individually to obtain a response in both beams per

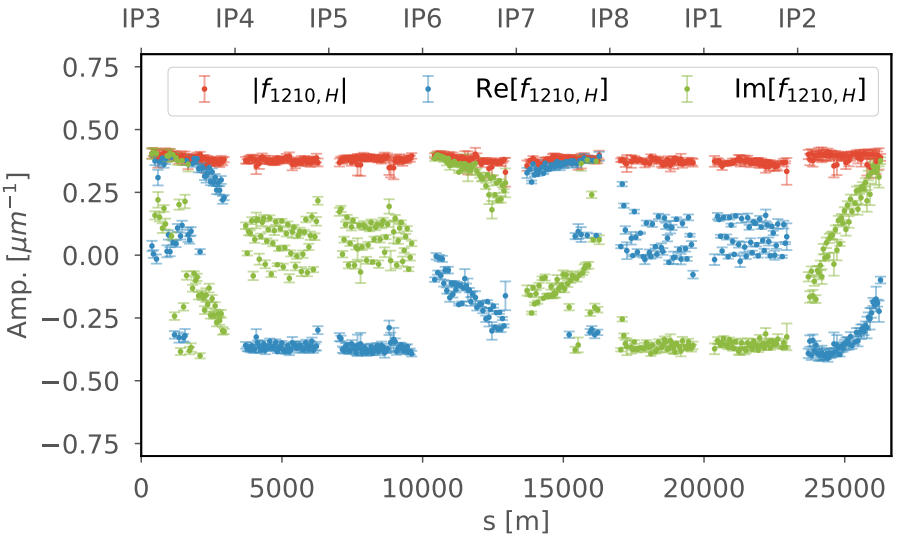

Figure 5.16: *Real and imaginary parts of $f_{1210,H}$ as measured in LHC without any skew octupolar correction in Beam 1, with $\beta^* = 30$ cm and crossing angles of 145 µrad in IR1 and IR5.*

5

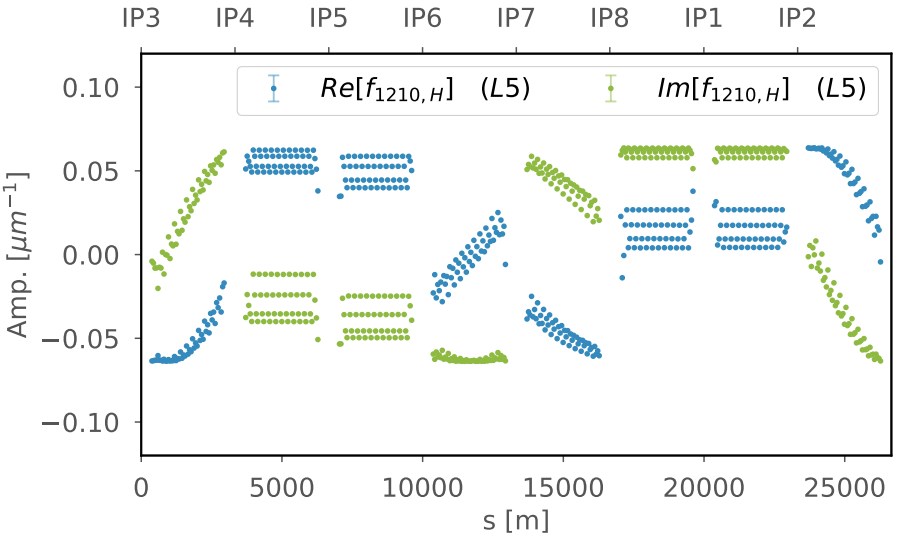

Figure 5.17: *Real and imaginary parts of $f_{1210,H}$ from single particle tracking simulations with only the corrector left of IP5 set to a strength of 0.2 m^{-4} in Beam 1, with $\beta^* = 30$ cm and crossing angles of 145 µrad in IR1 and IR5.*

corrector. There is an additional complexity to the correction of skew octupolar sources in the LHC due to a broken corrector left of IP1 that is thus unavailable for corrections. This missing corrector effectively reduces the degrees of freedom, and a full correction of the measured resonance driving terms may not be expected. The limitations of the correction due to the missing magnet are discussed more detail in Sec. 5.6.1. As the correction cannot be expected to correct both beams fully, the correction is aimed at correcting Beam 1 while not spoiling Beam 2. The calculated corrector strengths are summarized in Tab. 5.4.

Figure 5.18 shows the measured amplitude of the forced resonance driving terms $f_{1210,H}$ and $f_{1012,V}$ in Beam 1 before and after correction. The results show a significant correction of both skew octupolar resonance driving terms in Beam 1. The driving term $f_{1210,H}$ is changed by a factor of 0.27 ± 0.05, while $f_{1012,V}$ is changed by a factor 0.48 ± 0.04. The results further indicate that both $f_{1210,H}$ (related to x^3y in the Hamiltonian) and $f_{1012,V}$ (related to xy^3 in the Hamiltonian) are corrected in Beam 1.

Figure 5.19 compares the same driving terms measured in Beam 2. An improvement of $f_{1012,V}$ by a factor 0.46 ± 0.11 is observed after the implementation of the calculated corrections. The uncorrected state of $f_{1012,V}$ already has smaller amplitude as compared to the other driving term $f_{1210,H}$. As to the skew octupolar driving term with the largest amplitude in Beam 2, $f_{1210,H}$ is still measured at similar amplitudes as those before correction. So although an overall small improvement is observed in Beam 2, the largest driving term in Beam 2 remains uncorrected. The ratio between amplitudes of the driving terms between the corrected state and the

Table 5.4: *Calculated corrections for skew octupolar resonance driving terms. The corrector left of IP1 (MCOSX.L1) is broken and unavailable for corrections.*

Corrector	Strength $[m^{-4}]$
Left of IR1 (ATLAS)	(broken)
Right of IR1 (ATLAS)	0.5
Left of IR5 (CMS)	0.254
Right of IR5 (CMS)	0.263

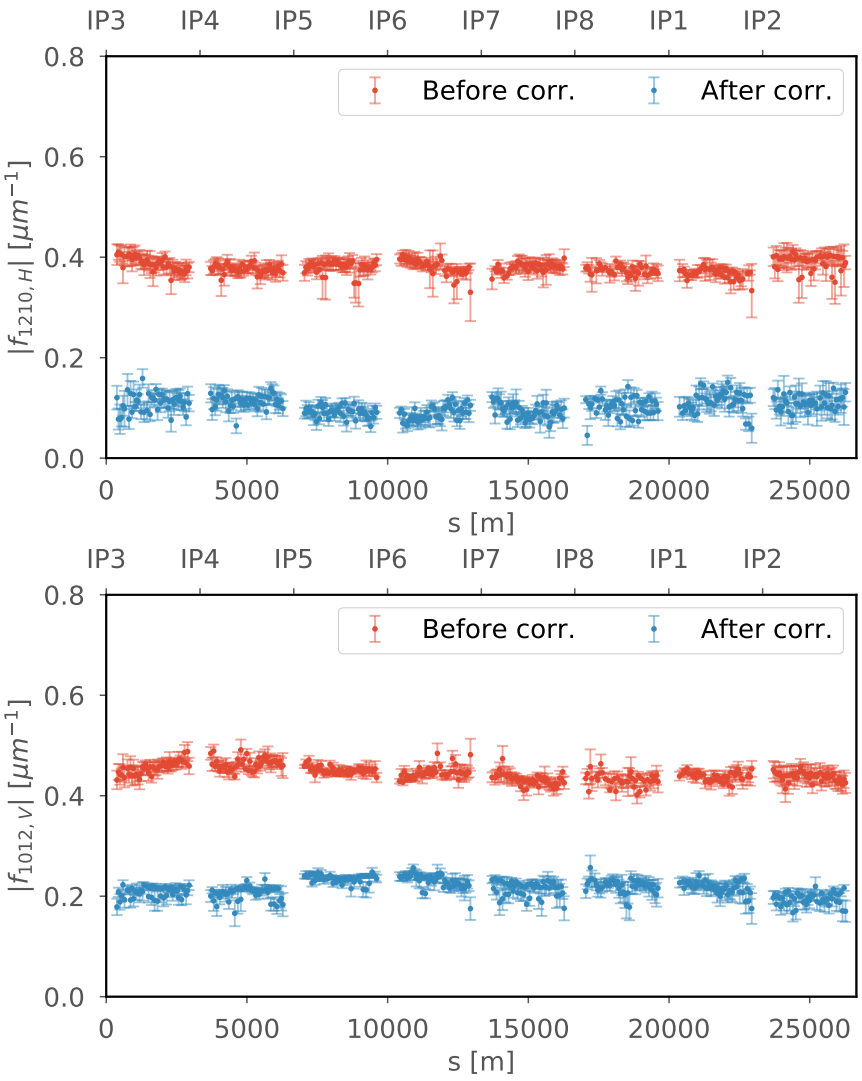

Figure 5.18: *First correction of the skew octupolar resonance driving terms $f_{1210,H}$ and $f_{1012,V}$ in Beam 1, with $\beta^* = 30$ cm and crossing angles of 145 µrad in IR1 and IR5. A significant reduction of the amplitudes is observed for both resonance driving terms.*

uncorrected state of the machine are summarised in Tab. 5.5.

The results show a successful first correction of skew octupolar resonance driving terms using ac dipoles in the LHC. Possible improvements on the correction are discussed in the following section.

Limitations due to broken a4 corrector

The effectiveness of the skew octupolar correction is limited by the unavailability of the broken corrector left of IP1. Figure 5.20 shows the expected average driving term amplitude of $f_{1210,H}$ for Beam 1 and Beam 2 for a scan of different possible

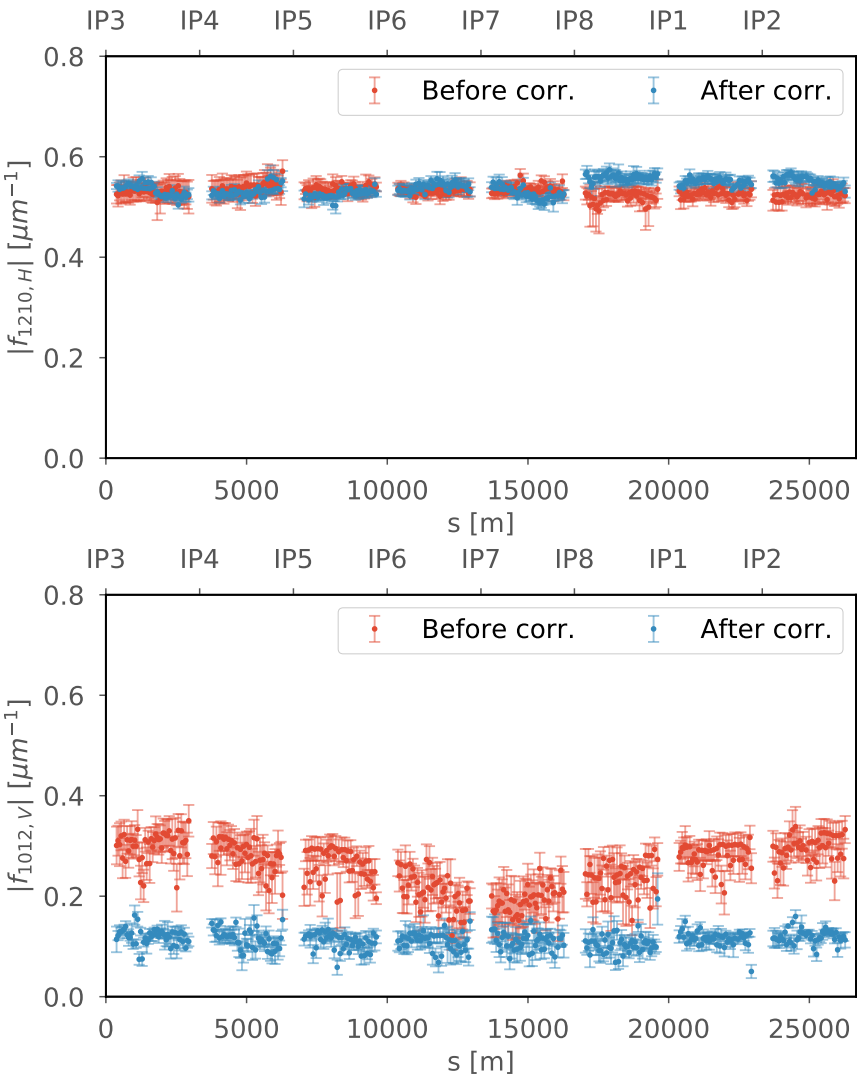

Figure 5.19: *Skew octupolar resonance driving terms $f_{1210,H}$ and $f_{1012,V}$ in Beam 2 after the correction of Beam 1, with $\beta^* = 30$ cm and crossing angles of 145 µrad in IR1 and IR5. The correction does not have a deteriorating effect on the largest driving term in Beam 2 ($f_{1210,H}$), while a reduction of the amplitude is observed for the $f_{1012,V}$ driving term.*

corrections for the machine with crossing angles of 145 μrad in IR1 and IR5. The average resonance driving term amplitudes over the ring is shown for the range of possible corrector settings using only the three available correctors is shown in pink, and in light blue for the case where all four correctors are available. The stepping behaviour observed in the results using three correctors is related to the sampling distance of possible corrector strengths. Increasing the sampling only smoothens the boundary. A clear limitation in the achievable correction level is observed between the two cases. When using only the three available correctors, there are clear trade-offs to be made. Beam 1 can be corrected to levels similar

to those achieved with four correctors at the cost of degrading Beam 2, while the average amplitude of $f_{1210,H}$ after correction in Beam 2 is limited to around 0.21 μm and greatly spoiling Beam 1. Furthermore, there is no setting of the correctors, using all four correctors, that fully correct the measured resonance driving terms for both beams. This could be attributed to the measurement precision as well as the second order cross-term from the ac dipole as a change in the driving term at the location of the ac dipole will change this second order contribution.

The average resonance driving term amplitude for the uncorrected state of the machine is also shown in Fig. 5.20. The average amplitude after implementing the 2017 corrections obtained from feed-down measurements [39], and the correction of 2018 from resonance driving term measurements are also shown in Fig. 5.20. The correction of 2017 offers an improvement in Beam 2 while deteriorating Beam 1. On the other hand the correction calculated from resonance driving terms almost fully corrects Beam 1, while keeping Beam 2 at levels comparable to the bare machine state. This highlights that the absence of a single corrector can have a significant impact on the correction of nonlinear errors, which in turn can have operational consequences [97].

Feed down with crossing angles

During the measurements and correction of skew octupolar errors, initial tests were made with a flat orbit configuration where all crossing angles and orbit bumps are turned off. Measurements of $f_{1210,H}$ at flat orbit and with crossing angles are shown in Fig. 5.21. Clearly a deterioration of the resonance driving term amplitude is ob-

Table 5.5: *Ratio of amplitudes of resonance driving terms between after and before correction. The driving term $f_{1210,H}$ is best corrected in Beam 1 remains at the same level as the uncorrected state in Beam 2, while $f_{1012,V}$ is corrected in both beams to less than half its uncorrected state.*

	$f_{1210,H}$	$f_{1012,V}$
Beam 1	0.27 ± 0.05	0.48 ± 0.04
Beam 2	1.02 ± 0.04	0.46 ± 0.11

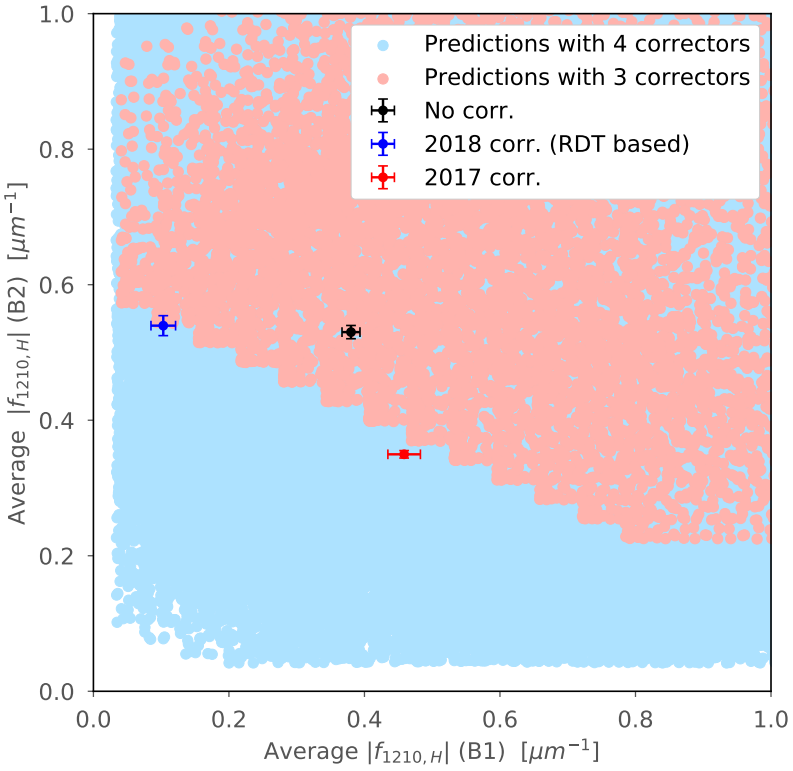

Figure 5.20: *Limitations of corrections due to broken corrector. Starting from the measurement without corrections (black), the points in pink show different predicted average resonance driving term amplitudes for different settings of correctors when using only three correctors. The points in light blue show the predictions when using all four correctors. The correction from 2017 using measurements of feed-down is shown in red, while the correction of 2018 from resonance driving terms measurements is shown in blue.*

served after the introduction of the crossing angles. This points to a contribution from feed-down coming from higher order errors such as normal and skew decapolar sources in the separation dipoles and triplets or second order feed-down from dodecapolar sources in the triplets. Apart from normal dodecapolar sources, such high order perturbations were until now assumed to be negligible.

The change of $f_{1210,H}$ with crossing angles shows that the success of the implemented correction may vary during the crossing angle changes associated with β^*-levelling. However, it is possible to refine the skew octupolar corrections in the future by measuring and correcting the skew octupolar driving terms at different crossing angles.

Simulations are done at $\beta^* = 30$ cm, with and without the crossing angles in IR1 and IR5 to study the possible effect of higher order multipolar errors on skew

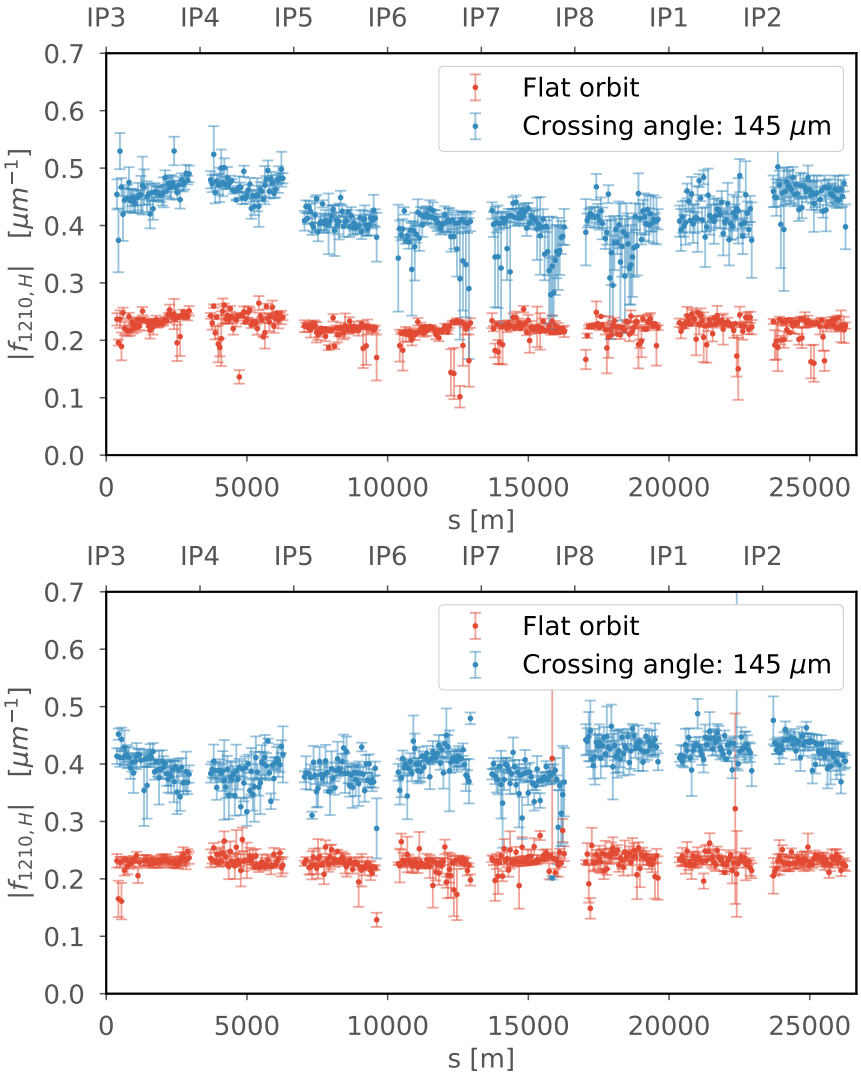

Figure 5.21: *Amplitude of $f_{1210,H}$ for measurements at flat orbit and with crossing angles of 145 μrad, and $\beta^* = 30$ cm. The amplitude of $f_{1210,H}$ changes with crossing angle suggesting feed-down from higher order sources.*

octupolar driving terms. The simulations are done in Beam 1 with the normal and skew decapolar and dodecapolar errors as obtained from WISE [91], and are presented in Fig. 5.22. The amplitude of $f_{1210,H}$ for simulations at flat orbit is shown in red, while the amplitude of $f_{1210,H}$ for simulations with crossing angles of 145 μrad in IR1 and IR5 are shown in blue. A significant increase is observed in the amplitude of $f_{1210,H}$ after implementing the crossing angles. The leading source of feed-down to this skew octupolar driving term is found to be skew dodecapolar errors. Simulations with only skew dodecapolar errors and crossing angles are shown in green, and show a comparable effect of feed-down to $f_{1210,H}$ as the simulations with all decapolar and dodecapolar sources. These results show that skew dode-

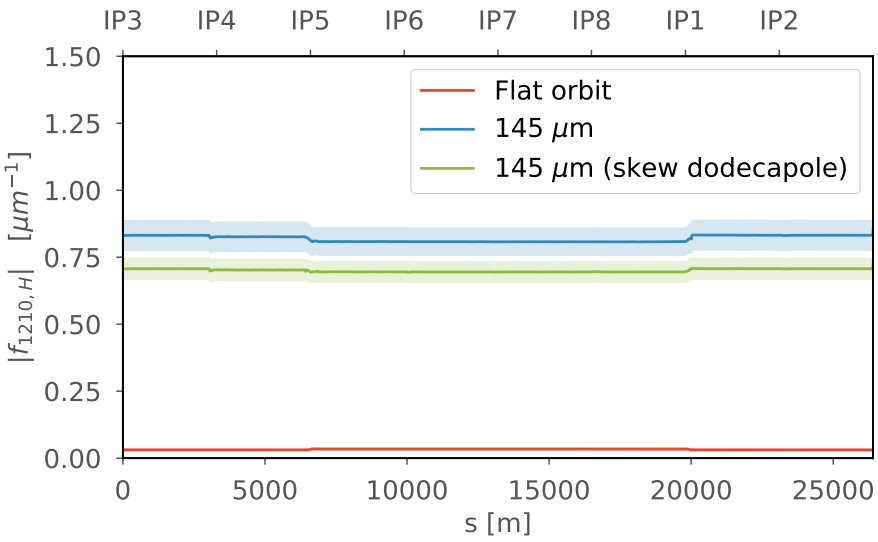

Figure 5.22: *Amplitude of $f_{1210,H}$ for simulations at $\beta^* = 30$ cm in Beam 1 showing the effect of feed-down from higher order multipolar errors. In red is the simulation with normal and skew decapolar and dodecapolar errors at flat orbit, while the same simulation with crossing angles of 145 μrad in IR1 and IR5 is shown in blue. Simulations with the same crossing angles but only skew dodecapolar sources are shown in green, showing that skew dodecapolar errors are the leading sources perturbing the $f_{1210,H}$ driving term.*

capolar errors have a more significant impact on lower order observables, and may impact future correction strategies of nonlinear observables. Just as for the calculation of nonlinear errors from complementary methods [39, 92], the correction of higher order nonlinear errors will be interdependent and will most likely require an iterative order-by-order approach.

CONCLUSIONS

Proper correction of nonlinear magnetic errors becomes increasingly important to achieve the required luminosities. As the operational requirements and optics designs are pushed further, the correction of increasingly higher order nonlinear errors become relevant. Forced resonance driving terms under forced motion with ac dipoles are seen as promising observables to measure, identify, and correct such machine nonlinearities.

Measurements of resonance driving terms in the LHC at top energy are only possible with the use of ac dipoles. The ac dipoles are used to excite large transverse coherent oscillations that provide high quality data for spectral analysis. Using such excitations, it is now possible to measure normal and skew sextupolar and

octupolar resonance driving terms on a regular basis.

It is shown in this paper that the free and forced tunes can be used to change the amplitude of the measured resonance driving terms by approaching forced resonances. Such changes in tunes can now be used to improve the signal-to-noise level of secondary spectral lines and thus in turn improve the measurement resolution of resonance driving terms. Experiments in the LHC show that the skew sextupolar driving term $f_{0030,V}$, normal octupolar driving term $f_{4000,H}$, and skew octupolar term $f_{1210,H}$ are enhanced by moving to their respective resonances. The factor of enhancement is in good agreement with simulations.

The first measurements of decapolar resonance driving terms in a synchrotron are also presented. Normal and skew decapolar resonance driving terms are measured at two different working points with large vertical excitations. This first measurement offers a positive outlook to directly measure and correct decapolar sources.

Measurements of resonance driving terms have been used in Run II to validate corrections that are calculated from complementary methods of nonlinear corrections, such as amplitude detuning and feed-down measurements. A reduction of amplitude of $f_{4000,H}$ is observed when local normal octupolar corrections are implemented in the main experimental insertion regions in IR1 (ATLAS) and IR5 (CMS). The reduction confirms the validity of the calculated corrections. The same approach is used to validate skew sextupolar corrections obtained from feed-down measurements. A reduction in the amplitude of $f_{0030,V}$ is observed after the implementation of the local skew sextupolar corrections in IR1. Furthermore, measurements of $f_{1210,H}$ are used to show a possible phase offset between local skew octupolar errors and calculated skew octupolar corrections from feed-down measurements in 2017.

The correction of skew octupolar resonance driving terms is achieved for the first time in the LHC in 2018. Corrections are for the first time calculated from forced resonance driving terms measurements by matching the skew octupolar responses from tracking simulations to the uncorrected machine state. A successful correction of both $f_{1210,H}$ and $f_{1012,V}$ is achieved in Beam 1 while the correction is only able to improve $f_{1012,V}$ in Beam 2. The driving term $f_{1210,H}$ in Beam 2 is retained at the same level as the uncorrected state of the machine.

A full correction of the skew octupolar resonance driving terms is impossible due to a broken skew octupolar corrector left of IP1. Only three correctors are available thus limiting the degrees of freedom and limiting the effectiveness of the correction. Simulation results show that a close to full correction is possible if the broken

corrector can be used in the future. Furthermore, the role of the second order cross-term from the ac dipole should be studied in the future to better understand the impact on the corrections.

Measurements of $f_{1210,H}$ at flat-orbit and at crossing angles of 145 μrad in the IR1 and IR5 show a significant source of feed-down to the skew octupolar resonance driving term. Although this can reduce the effectiveness of the correction with crossing angle changes, it is possible to refine the corrections by measuring and correcting the skew octupolar driving terms at different settings of crossing angles to span the operational range.

ACKNOWLEDGEMENTS

The authors would like to thank the Optics Measurements and Corrections team, as well as the LHC Operations team for the continuous support in the measurements performed in the LHC.

6

FIRST EXPERIMENTAL DEMONSTRATION OF FORCED DYNAMIC APERTURE MEASUREMENTS WITH LHC AC DIPOLES

Imperfections in the high-field superconducting magnets of the LHC disturb the motion of particles. These sources can arise from imperfections in the construction of the magnets, small misalignments of magnets within the accelerator tunnel, persistent currents in magnets, and hysteresis. All these imperfections are in principle within the design tolerances, but combined, these can have a large impact on the stability of the beams. The stability of particles can be greatly reduced to a point where the dynamic aperture, the area of stable motion in phase-space, becomes smaller than the physical aperture determined by the beam pipe. Beyond the dynamic aperture the motion becomes chaotic and particles are lost. The reduction of the dynamic aperture can thus significantly reduce the beam life-time.

The dynamic aperture is one of the most important design parameters of the LHC. A small dynamic aperture can cause parts of the beams to be lost, and can trigger unscheduled beam dumps. Vast simulation campaigns are performed to accurately predict the available dynamic aperture under the influence of various nonlinear errors, multipolar magnets, beam-beam interactions, and other perturbative sources.

During optics measurements with ac dipoles the motion of particles change, and the dynamic aperture inherently changes too. The forced dynamic aperture, that is the dynamic aperture under the influence of forced oscillations with ac dipoles, is considered for the first time. The forced dynamic aperture may pose limitations on optics measurements with ac dipoles, but can also be used as an alternative observable that allows for the fast characterisation of nonlinearities and validation of nonlinear corrections in the LHC.

The following paper describes the proposed forced dynamic aperture measurements. It offers the first measurements of forced dynamic aperture in synchrotrons and sets out the benefits and challenges of using ac dipoles for the characterisation of nonlinearities using the forced dynamic aperture. This paper is followed by a

second paper describing the first measurements of forced dynamic aperture at top energy that were used for the validation of specific skew octupolar corrections in the LHC.

FIRST EXPERIMENTAL DEMONSTRATION OF FORCED DYNAMIC APERTURE MEASUREMENTS WITH LHC AC DIPOLES

F.S. Carlier, R. Tomás, E.H. Maclean, and T.H.B. Persson

Physical Review Accelerators and Beams 22, 031002
Published 13 March 2019
Available online at
https://doi.org/10.1103/PhysRevAccelBeams.22.031002

6

ABSTRACT

Diagnostics of nonlinear beam dynamics has become more important for the LHC as it advances into increasingly challenging regimes of operation, as well as for the High Luminosity LHC where machine nonlinearities will have a significantly larger impact. Limitations of traditional excitation methods at top energy, in particular due to machine protection, have pushed the development of safe alternative methods using ac dipoles to characterise the nonlinear content of the LHC. One of the methods that has been proposed is the dynamic aperture under forced oscillation of ac dipoles. This new observable has the potential to help characterise relative changes in the nonlinear content of the machine, improve the understanding of the nonlinear models by comparing to simulations, validate nonlinear optics corrections, and give a qualitative lower bound estimate on the free dynamic aperture. This paper presents the first experimental demonstration of forced dynamic aperture measurements under forced oscillations performed using the LHC ac dipoles, and discusses the benefits of forced dynamic aperture measurements in circular colliders.

INTRODUCTION

The ac dipole system is able to generate coherent transverse beam oscillations. It was first developed for synchrotrons to avoid spin resonances in the AGS [42] and later used for the first time to measure linear optics functions in RHIC [53, 55, 59] and the Tevatron [54, 56, 57]. ac dipoles were proposed in the LHC as a complementary tool to measure optics functions alongside the more conventional kickers (MKQ and MKA [52, 98]). However over the years, the importance of the LHC ac dipoles [99, 100] has grown and they have now become critical in correcting linear [37, 38, 101] and nonlinear [49, 65, 86] optics parameters. To such an extent that they are the single most important measurement method for the linear and nonlinear correction strategies in the LHC and for the High Luminosity LHC [94]. This is in part due to the fact that single kicks are not allowed at top energy for machine protection considerations.

The success and reliability of ac dipoles have allowed them to be used for new applications. The LHC ac dipoles have been used to measure the physical aperture of the collider to assist in collimator alignment [63], to measure amplitude detuning in the presence of head-on beam-beam interactions [66] as well as to measure the machine impedance [60]. More recently ac dipoles have been used in lightsources, such as at ESRF [62], PETRA III [61] and ALBA [102]. Furthermore, ac dipoles are currently foreseen for the AGS to compensate spin resonances for the eRHIC project [103] for the transport of polarized helium ions.

It is clear that functionality and importance of ac dipoles have grown significantly. At the core of this success lies the fact that the ac dipole can generate safe coherent transverse beam oscillation while recovering the original beam after the excitation. The slow adiabatic ramp up of the ac dipole current allows for a continuous monitoring of losses and enough time to allow safe dump triggers at top energy in the LHC. Secondly, the slow adiabatic ramp down of the ac dipole current makes sure the beam emittance is recovered after excitations, which means that multiple excitations can be performed in series thus drastically cutting down measurement time.

Similarly to particles in free motion, stable particles under forced oscillations are confined to a region in phase space. Beyond the boundary of stable motion in phase space particles are lost. This stability region under forced oscillations is called the forced dynamic aperture [104] and it is analogous to the dynamic aperture for free motion [105–108] which is defined here as free dynamic aperture. It is important to note that the forced dynamic aperture is a different physical quantity than the free

dynamic aperture. Indeed a direct scaling law between free and forced dynamic apertures may not be trivially found for synchrotrons.

A poor forced dynamic aperture can significantly affect commissioning strategies with ac dipoles for highly nonlinear machines, for example for the High Luminosity LHC [94]. It is thus desirable to maximise the forced dynamic aperture to facilitate linear and nonlinear optics commissioning with ac dipoles. Furthermore, the forced dynamic aperture can be generated by any coherent harmonic excitations and is thus of particular interest to understand the effect of induced forced oscillations coming from imperfect power supplies or possible harmonic excitations from crab cavities [109]. Such sources of forced motion may significantly affect machine performance, and motivate a good understanding of forced oscillations in hadron colliders.

Fortunately, forced dynamic aperture does not only bring limitations. It is also a new alternative observable which has the potential to provide fast characterisation of the nonlinear content of the machine, improve the understanding of the nonlinear models by comparing to simulations, and validate nonlinear optics corrections. It is viewed as an important complementary figure of merit for nonlinear optics commissioning strategies in the LHC and High Luminosity LHC [94].

In this paper we describe the first experimental demonstration of forced dynamic aperture measurements. The LHC ac dipoles are limited to an excitation of 10000 turns while typical free dynamic aperture studies consider measurements lasting above an order of magnitude longer. The studies in this paper are therefore restricted to short term forced dynamic aperture though the concepts are applicable to longer timescales as well. This paper proceeds by describing the influence of an ac dipole on the forced dynamic aperture in section 6.2. This is followed by results obtained through MAD-X [72] single particle tracking simulations in section 6.3 where the effect of the ac dipole driving tunes on the forced dynamic aperture is explored. In section 6.4 the forced dynamic aperture is defined from beam intensity losses. Finally, a first demonstration of forced dynamic aperture measurements at injection energy in the LHC is presented in section 6.5.

INFLUENCE OF AC DIPOLE ON FORCED DYNAMIC APERTURE

Particle dynamics under the driven motion of an ac dipole are considerably altered [49, 54, 65]. The general solution for the driven particle motion with an ac dipole can be expressed at any longitudinal location s of the ring as a function of turn number T as

$$\begin{aligned}\hat{z}(T) - i\hat{p}_z(T) &= \sqrt{2J_z}e^{i(2\pi Q_z T+\phi_{z0})} \\ &\quad +e^{-i\phi_{\mathrm{d},z}}(\delta_{z,-}e^{i2\pi Q_{\mathrm{d},z}T} - \delta_{z,+}e^{-i2\pi Q_{\mathrm{d},z}T}),\end{aligned} \tag{6.1}$$

where $z \in \{x, y\}$ denotes the plane of motion, Q_z is the betatron tune, $Q_{\mathrm{d},z}$ is the ac dipole driving tune, $\phi_{\mathrm{d},z}$ is the phase advance between the location s and the ac dipole, J and ϕ_{z0} are the initial action and phase of the particle, and finally $\delta_{z,-}$ and $\delta_{z,+}$ are the complex ac dipole strengths defined as

$$\delta_{z,\pm} = \sqrt{\beta_{\mathrm{d},z}}\frac{BL}{B_0\rho}\frac{e^{\pm i(\pi(Q_{\mathrm{d},z}\pm Q_z)-\psi_0)}}{4\sin(\pi(Q_{\mathrm{d},z}\pm Q_z))} \tag{6.2}$$

where $\beta_{\mathrm{d},z}$ is the β-function at the location of the ac dipole. Generally the ac dipole tunes are chosen close to the natural tunes which leads to $|\delta_{z,-}| \gg |\delta_{z,+}|$.

In the case of free oscillations, where $\delta_{z,\pm} = 0$, the resonance condition obtained from the normal form formalism [70], is conventionally given by

$$(j-k)Q_x + (l-m)Q_y = p$$

$$\text{with,} \quad p \in \mathbb{Z} \quad \text{and} \quad j,k,m,l \in \mathbb{N}_0, \tag{6.3}$$

where j, k, l and m are the indices of the Hamiltonian term h_{jklm}. The Hamiltonian terms are defined as in [70] as the sum over the individual sources along the accelerator,

$$h_{jklm} = \sum_w h_{w,jklm}e^{i[(j-k)\Delta\phi_x+(l-m)\Delta\phi_y]} \tag{6.4}$$

where w is the location of a multipolar source, and $\Delta\phi_{x,y}$ are the phase advances between the observation point and the sources at locations w. The coefficients $h_{w,jklm}$ are defined using the normal and skew multipolar strengths K_w and J_w respectively,

$$
\begin{aligned}
h_{w,jklm} &= -\frac{[K_{w,n-1}\Omega(l+m) + iJ_{w,n-1}\Omega(l+m+1)]}{j!\ k!\ l!\ m!\ 2^{j+k+l+m}} \\
&\quad i^{l+m}\beta_{x,w}^{\frac{(j+k)}{2}}\beta_{y,w}^{\frac{(l+m)}{2}} \qquad (6.5)\\
\text{with} &\quad \begin{cases} \Omega(i) = 1 & \text{if } i \text{ is even} \\ \Omega(i) = 0 & \text{if } i \text{ is odd} \end{cases} .
\end{aligned}
$$

The addition of ac dipoles introduces new frequencies that lead to new resonances. The derivations presented in [49] may be extended to two dimensions to obtain the resonance condition for ac dipole driven motion, as

$$
\begin{aligned}
&(k_1 - j_1)Q_x + (k_2 - k_3 + j_2 - j_3)Q_{\mathrm{d},x} + \\
&(m_1 - l_1)Q_y + (m_2 - m_3 + l_2 - l_3)Q_{\mathrm{d},y} = p \\
&\text{with,} \quad p \in \mathbb{Z} \quad \text{and} \quad j_i, k_i, m_i, l_i \in \mathbb{N}_0 \,, \qquad (6.6)
\end{aligned}
$$

where the indices fulfill the following conditions,

$$
\begin{aligned}
j_1 + j_2 + j_3 &= j \\
k_1 + k_2 + k_3 &= k \\
l_1 + l_2 + l_3 &= l \\
m_1 + m_2 + m_3 &= m \\
j_1 + l_1 &> 0 \,. \qquad (6.7)
\end{aligned}
$$

In general the number of resonances is larger when exciting the beam with an ac dipole and also include the resonances present in the free motion. The choice of working point for the bare machine tunes as well as for the ac dipole tunes will therefore have a significant influence on the forced dynamic aperture, as explored in section 6.3.

Resonances are approached by the detuning of the natural tunes with amplitude. As the oscillation amplitude increases, the natural tunes will detune on to resonances causing particle losses. Amplitude detuning is in general larger with forced oscillations. It has been shown that the direct linear amplitude detuning terms gen-

erated by normal octupolar fields double under the influence of an ac dipole driven motion [65]. The tune shifts for free and driven motion horizontal excitations are given by

$$\begin{aligned} \Delta Q_x &= \frac{q}{p}\frac{3B_4}{8\pi}(\beta_x^2 J_x^{\text{free}} + 2\beta_x\beta'_x J_x^{\text{forced}}) \\ \Delta Q_y &= -\frac{q}{p}\frac{3B_4}{8\pi}(2\beta_x\beta_y J_x^{\text{free}} + 2\beta'_x\beta_y J_x^{\text{forced}}) \,, \end{aligned} \tag{6.8}$$

where q and p are the particle charge and momentum, B_4 is the integrated field of a normal octupole normalised with the magnetic rigidity, $\beta_{x,y}$ are the β-function at the octupole sources, $\beta'_{x,y}$ are the β-function at the octupoles under the influence of the ac dipole motion [54], $J_{x,y}^{\text{free}}$ and $J_{x,y}^{\text{forced}}$ are the actions of the free oscillation and forced oscillation, respectively. When neglecting $\delta_{z,+}$, the forced action can be defined as $J_x^{\text{forced}} = \frac{1}{2}|\delta_{z,-}|^2$. The expressions for vertical excitations are obtained by swapping the plane indices. Assuming the optics perturbations coming from the ac dipole are small ($\beta_{x,y} \approx \beta'_{x,y}$), and that the forced oscillation is much larger than the free oscillation component ($J_{x,y}^{\text{forced}} >> J_{x,y}^{\text{free}}$), Eq. (6.8) shows that the detuning for forced oscillations is twice as large as for free motion (when $J_{x,y}^{\text{forced}} = 0$) in the plane of oscillation. Further detuning from higher order nonlinear fields, such as second order detuning from dodecapoles, are even more enhanced [65].

The increased amplitude detuning under forced oscillations combined with the larger number of resonances should result in a forced dynamic aperture typically smaller than the free dynamic aperture ($DA_{forced} \lesssim DA_{free}$), and can thus give a qualitative lower bound estimate on the free dynamic aperture.

SIMULATIONS OF FORCED DYNAMIC APERTURE WITH AC DIPOLE

Tracking simulations are done in MAD-X [72] to explore the effect of the ac dipole driving tunes on forced dynamic aperture. For the purpose of this study, the nominal 2016 model of the LHC at top energy (6500 GeV) and end of squeeze ($\beta^* = 0.40$ m) is used. Sources of nonlinearities are introduced to the model in the following ways; The nonlinear magnetic errors as generated by Windows Interface to Simulations Errors (WISE) [91] are applied to all dipoles and quadrupoles. The corrector spool pieces settings for the sextupoles (MCS), octupoles (MCO) and decapoles (MCD) are used as implemented during regular 2016 LHC operation. Misalignments of the separation dipoles are introduced, and the orbit is corrected to zero

with a residual rms orbit of 2×10^{-6} m. The crossing angles in the interaction regions are turned off and all other parameters such as tunes, chromaticity and coupling are corrected to $Q_x = 0.31$, $Q_y = 0.32$, $Q'_{x,y} = 5$, $|C^-| = 5 \times 10^{-4}$, and $\beta^* = 0.40$ m to represent normal conditions during optics measurements in the LHC. The coupling parameter is defined according to [87] by

$$C^- = \frac{1}{2\pi R} \int_0^{2\pi} \sqrt{\beta_x \beta_y} K e^{i[(\phi_x - \phi_y) - (Q_x - Q_y - p)\theta]} d\theta \tag{6.9}$$

where R is the circumference of the accelerator, K is the skew quadrupolar strength as defined in [87], $(Q_x - Q_y - p)$ is the fractional tune difference, $\phi_{x/y}$ are the horizontal and vertical phase advances, $\beta_{x/y}$ are the horizontal and vertical β-functions, and $|C^-|$ is the coupling stopband.

Free kick single particle tracking simulations are done by introducing a Δx and/or Δy offset as initial conditions and then tracked using the MAD-X thin lens tracking module. For the ac dipole single particle tracking simulations the particle is initially at rest ($x = p_x = y = p_y = 0$). The ac dipole excitation starts after 500 turns and the excitation amplitude is ramped up for 2000 turns after which it is kept constant for 6000 turns (flattop) and finally ramped down for 2000 turns till zero amplitude. Figure 6.1 shows the turn-by-turn signal for the particle at BPM.22L1.B1 for the vertical plane as used in simulations. Those parameters are comparable to what is currently used for the ac dipole in the LHC.

Dynamic aperture from simulations is commonly represented as the stable domain as a function of actions, where the actions are obtained from the initial conditions. Such a representation may not be trivially obtained for ac dipole excitations where the particle is initially at rest.

Two methods are used in the paper to measure the actions from turn-by-turn data in both simulations and measurements. In the case of single particle tracking simulations, multiparticle simulations with ac dipole, and measurements with ac dipole, where a sustained coherent oscillation is observed in the turn-by-turn data, the actions are measured from the amplitude of the tune line in the spectrum of the BPM turn-by-turn tracking data. The spectral analysis code SUSSIX [89] is used for all spectral analysis in this paper. However for free kick measurements where large sources of nonlinearity cause the beam to decohere quickly, the usable number of turns for the spectral analysis becomes too small. The quality of spectral analysis quickly deteriorates, and the actions are thus determined from the peak-to-peak amplitude of the turn-by-turn signal.

In single particle simulations, where both free and forced oscillations yield coherent turn-by-turn position data, the actions are calculated by spectral analysis of

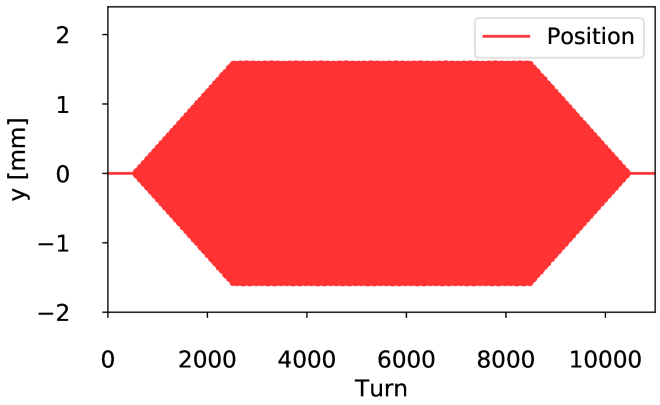

Figure 6.1: *Typical ac dipole excitation showing the turn-by-turn amplitude of a particle in the vertical plane. The excitation is similar in the horizontal plane.*

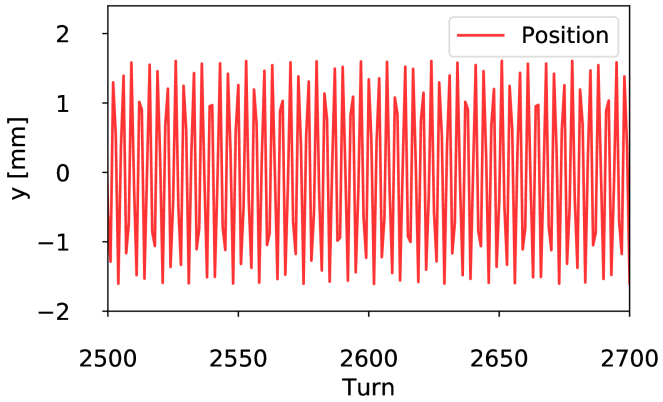

Figure 6.2: *A close-up plot of the first 200 turns of the flattop excitation showing the coherent turn-by-turn oscillation with an amplitude of $A = 1.6$ mm.*

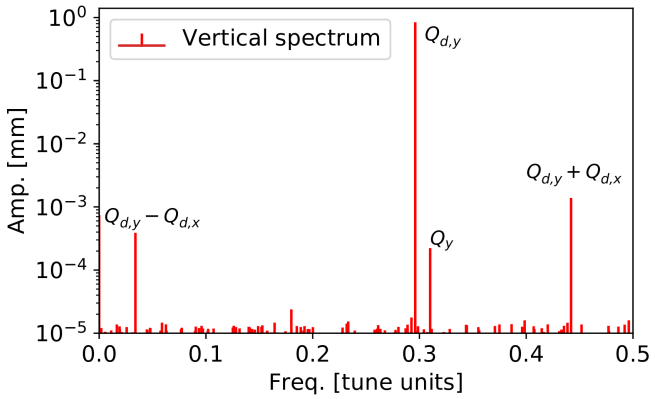

Figure 6.3: *Spectrum of the flattop turn-by-turn data. The main spectral line is measured at the ac dipole vertical tune $Q_{d,y} = 0.296$ and with an amplitude of $A' = 0.80$ mm, i.e. $A = 2A'$.*

the turn-by-turn data of the first 200 turns for the free kick motion, and the first 200 turns of the flattop data of the ac dipole excitations. Only the first 200 turns are used to mitigate the effects of possible emittance growth when exciting close to resonances. Figure 6.2 shows the first 200 turns of flattop turn-by-turn data for a vertical excitation with an oscillation amplitude of $A = 1.6$ mm. The spectrum of the this turn-by-turn data is shown in Fig. 6.3. The amplitude signal A' of the main tune line at frequency $Q_{\mathrm{d},y}$ is observed with an amplitude of $A' = 0.80$ mm in the spectrum and is proportional to the signal amplitude with $A = 2A'$. The actions are calculated with

$$2J_{x,y} = \frac{A^2}{\beta_{x,y}}\,. \tag{6.10}$$

The actions are then normalized to the emittance using

$$N = \sqrt{\frac{2J_{x,y}}{\epsilon_{x,y}}}\,, \tag{6.11}$$

where $\epsilon_{x,y}$ are the physical emittances and are defined as $\epsilon_{x,y} = 7.8 \cdot 10^{-9}$ m at injection energy (0.45 TeV), and $\epsilon_{x,y} = 5.4 \cdot 10^{-10}$ m at top energy (6.5 TeV).

Figure 6.4 shows the free dynamic aperture as a function of initial conditions, while the free dynamic aperture as a function of the calculated actions from the main spectral line is shown in Fig. 6.5. Both results are from the same free kick simulations with 6000 turns. The blue points represent surviving particles and the red points are particles lost during tracking. Certain regions in action space are not fully probed using the usual regular phase space sampling. At large excitation amplitudes, nonlinearities start to distort the sampling from initial conditions and does not guarantee a smooth coverage in action space.

Simulations allow to probe a large area of phase space and define the forced and free dynamic apertures as the minimum radial distance to the first observed losses. The free dynamic aperture is simulated at $12.2\,\sigma_{\mathrm{nom}}$ as shown by the black and white arc in Fig. 6.5. This is slightly lower than the $13.8\,\sigma_{\mathrm{nom}}$ free dynamic aperture found in Fig. 6.4 from the initial conditions.

Effect of driving tunes on forced dynamic aperture

Figure 6.6 shows the simulated forced dynamic aperture for different ac dipole driving tunes. The top figure shows the simulated forced dynamic aperture for symmetric excitation of the ac dipole where $Q_{\mathrm{d},x} = Q_x - 0.012$ and $Q_{\mathrm{d},y} = Q_y + 0.012$.

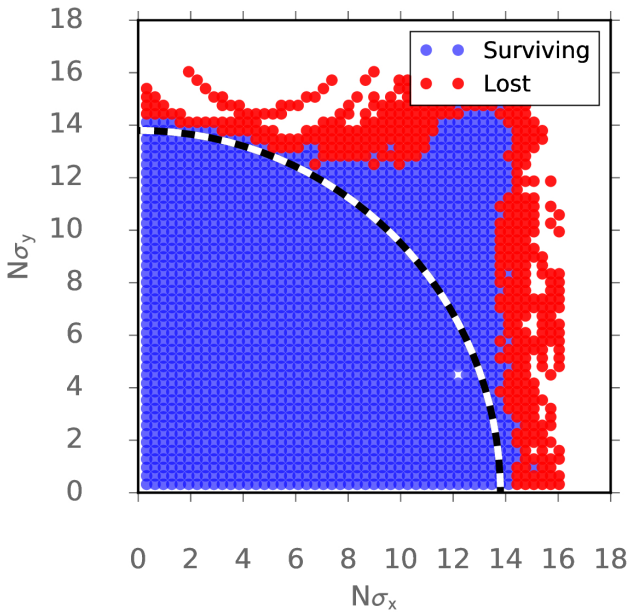

Figure 6.4: *Simulated free dynamic aperture with excitations calculated from initialised amplitude. The machine tunes are* $Q_x = 0.31$ *and* $Q_x = 0.32$.

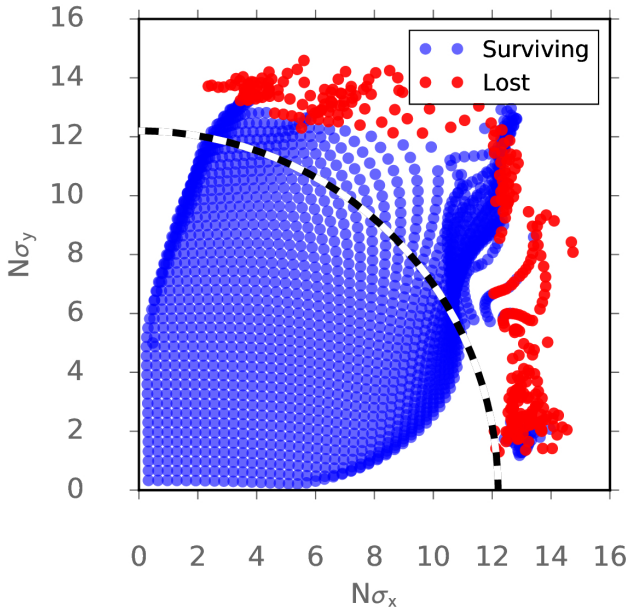

Figure 6.5: *Simulated free dynamic aperture with excitations calculated from the amplitude of the main spectral line. The machine tunes are* $Q_x = 0.31$ *and* $Q_x = 0.32$.

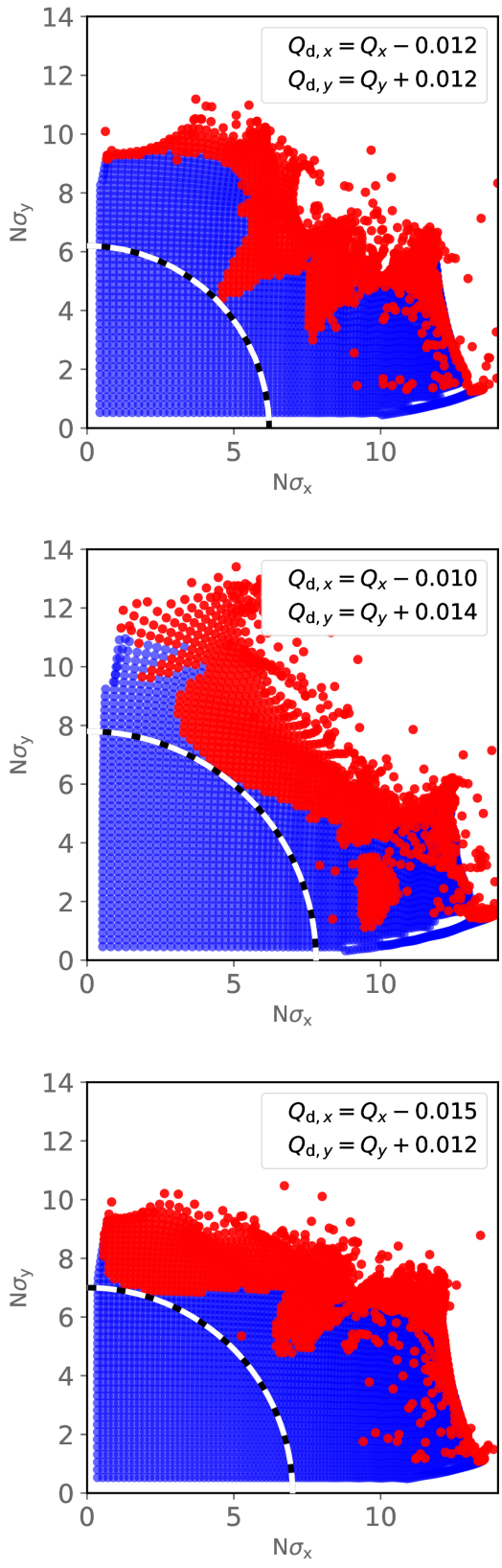

Figure 6.6: *Forced dynamic aperture results for three different ac dipole driving tunes at top energy the natural tunes are $Q_x = 0.31$ and $Q_y = 0.32$.*

The forced dynamic aperture is limited to $6.2\,\sigma_{\mathrm{nom}}$ due to early losses for diagonal excitations as the octupolar resonance $Q_{\mathrm{d},x} + Q_{\mathrm{d},y} - Q_x - Q_y = p$, with p as integer, is excited. This resonance is automatically excited at low amplitudes, though at larger amplitudes its excitation depends on symmetric amplitude detuning in both planes. Results of tracking simulations with two different working points are also presented in Fig. 6.6 with $Q_{\mathrm{d},x} = Q_x - 0.010$ and $Q_{\mathrm{d},y} = Q_y + 0.014$ (middle), and $Q_{\mathrm{d},x} = Q_x - 0.015$ and $Q_{\mathrm{d},y} = Q_y + 0.012$ (bottom), where their respective forced dynamic aperture are found at $7.8\,\sigma_{\mathrm{nom}}$ and $7.0\,\sigma_{\mathrm{nom}}$. In all three cases the forced dynamic aperture is lower than the free dynamic aperture, confirming qualitative predictions from section 6.2. All three simulations with different ac dipole driving tunes show a considerably different forced dynamic aperture. It is clear from these results that the choice of ac dipole driving tunes has a large effect on the forced dynamic aperture and that the angle at which first losses occur is varying. These differences show that to accurately use the forced dynamic aperture as an observable for nonlinearities the same working point should be used throughout all measurements to compare forced dynamic aperture at different nonlinear configurations. Furthermore, it should be emphasized that the choice of working point can greatly increase the available aperture for optics measurements with ac dipole, a fact that will be relevant for the High Luminosity LHC where nonlinear errors are expected to be large.

6

Simulations at injection energy

Single particle tracking simulations of forced dynamic aperture at injection energy (450 GeV) with operational Landau octupole strengths of 2016 [110] are shown in Fig. 6.7 for two different models. The top figure shows the forced dynamic aperture for the nominal injection model with magnetic errors applied in the same way as detailed previously, and the Landau octupoles powered to 40 A. The minimum forced dynamic aperture is simulated at $3.3\,\sigma_{\mathrm{nom}}$. A large distortion of the probed action space is observed at large amplitudes due to the very strong Landau octupoles at injection energy. The bottom figure shows the forced dynamic aperture for simulations with the same model and with the addition of rotational geometric errors in all multipoles. After the introduction of the geometrical rotational errors the coupling is corrected to $|C^-| = 5 \cdot 10^{-4}$, a typical value during optics measurements in the LHC. A reduction of forced dynamic aperture to $2.6\,\sigma_{\mathrm{nom}}$ is observed. Geometrical rotations of multipoles change the nonlinear content of the model, which translates to a change in simulated forced dynamic aperture.

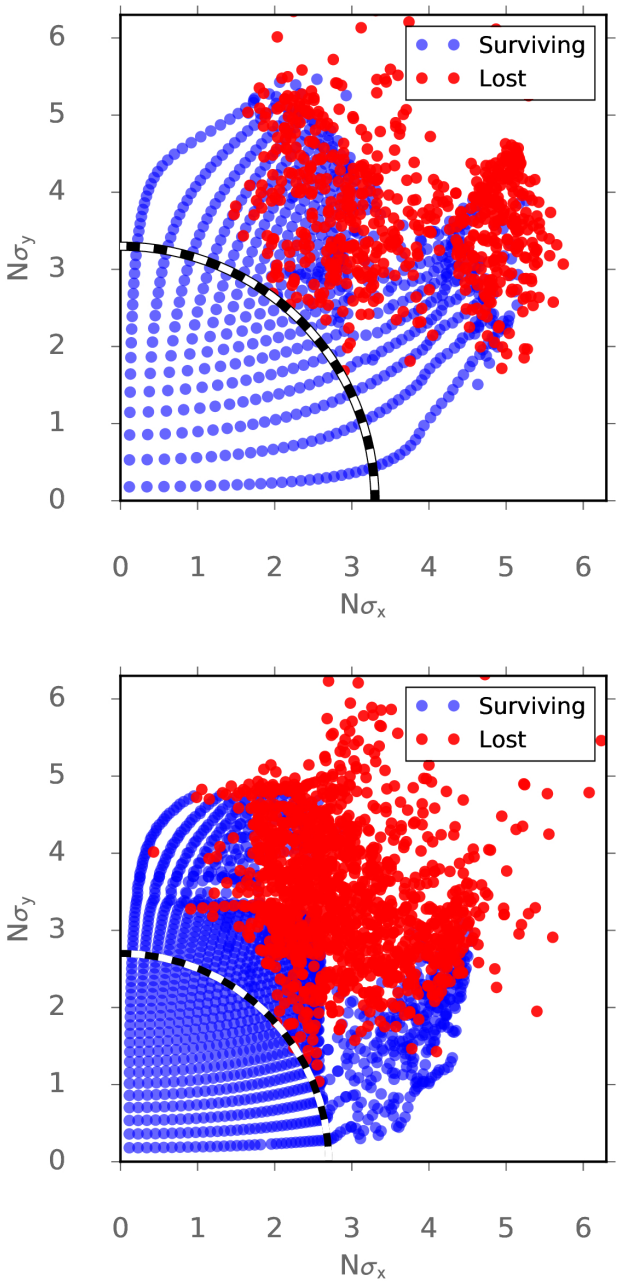

Figure 6.7: *Forced dynamic aperture at injection with Landau octupoles at 40 A. The top figure shows the forced dynamic aperture for a model including magnetic errors, while the bottom figure shows the forced dynamic aperture for a model including geometrical rotational errors as well as magnetic errors. A reduction of forced dynamic aperture is observed when including the geometrical rotational errors in the multipoles.*

EVALUATION OF FORCED DYNAMIC APERTURE FROM BEAM INTENSITY LOSSES

Both free and forced short term dynamic aperture can be measured by probing the beam intensity loss after large transverse excitations. In general, as the excitation amplitude is increased, more particles will cross the free or forced dynamic aperture and become lost. By assuming that the losses are dominant in a single plane and that the free or forced dynamic aperture is smooth, the problem can be simplified to a single dimension. In such a case the condition for loosing a particle from free DA becomes,

$$J^{\text{free}} > DA_{\text{free}} \tag{6.12}$$

and for loosing a particle from forced DA

$$J^{\text{free}} + J^{\text{forced}} > DA_{\text{forced}} \tag{6.13}$$

This is reflected in Fig. 6.8 and Fig. 6.9. Figure 6.8 shows a beam excited with a single free kick. All particles beyond the free dynamic aperture are lost. The free dynamic aperture is determined by fitting an error function to the measured losses over kick amplitudes as described in [92, 111, 112].

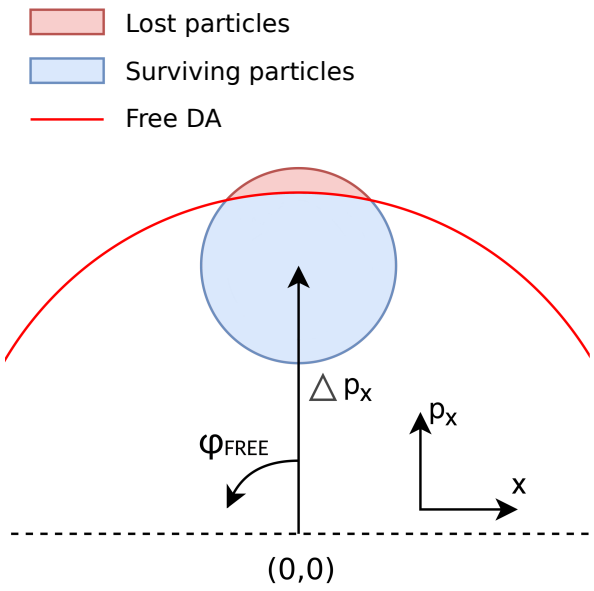

Figure 6.8: *Diagram showing where the losses in the particle bunch occur as a result of reaching the free dynamic aperture. As the kick amplitude (Δp_x) increases more particles will cross the free dynamic aperture and will be lost.*

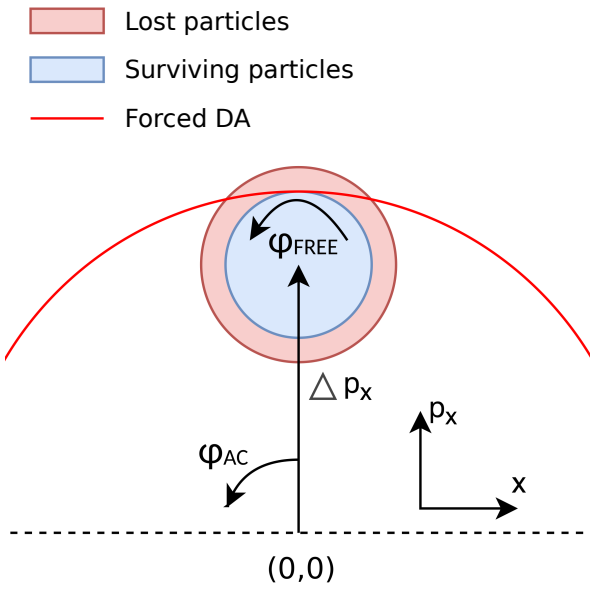

Figure 6.9: *Diagram showing where the losses in the particle bunch occur as a result of reaching the forced dynamic aperture. The remaining free motion inside the bunch will cause the tails of the bunch to be lost.*

The coherent excitation of the ac dipole will not change the initial bunch profile. Multiparticle tracking simulations are done to verify that the Gaussian bunch profile is maintained during the ac dipole excitation. Figure 6.10 shows the Gaussian bunch profile with 4000 particles for a bunch at rest before the ac dipole excitation and the same particles during the flattop excitation of the ac dipole. The bunch size is calculated before the ac dipole excitation at $\sigma = 1.305$ mm, and during the flattop ac dipole excitation at $\sigma = 1.309$ mm. The small deviations between the two are attributed to limited number of particles used in the simulation. This is also representative for the other coordinates x, p_x, and p_y.

Figure 6.9 shows an ac dipole excited beam traversing the forced dynamic aperture. In contrast to the free kick case where only particles beyond the free dynamic aperture are lost, the particle motion with ac dipole excitation will cause all the tails to be lost. By further assuming that the coupling is negligible this simplifies the problem to an integral over the distribution in action space only,

$$\frac{\Delta I}{I}(DA_{\text{forced}}) = \int_{DA_{\text{forced}}}^{+\infty} \frac{1}{\epsilon_z} e^{-\frac{w - J_z^{\text{forced}}}{\epsilon_z}} d\,w \tag{6.14}$$

where $\Delta I/I$ is the normalized measured losses, J_z^{forced} is the measured action of the bunch from forced oscillations, ϵ_z is the beam emittance, w is the integration

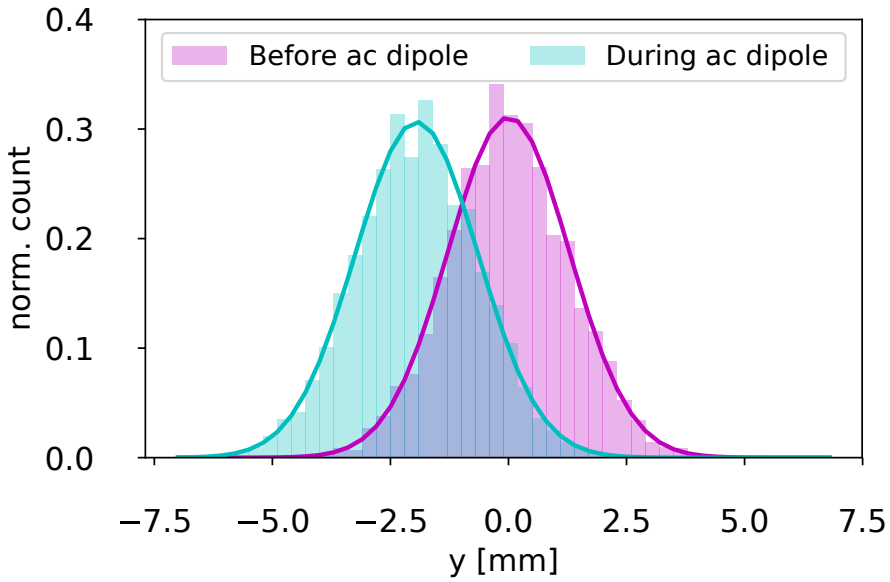

Figure 6.10: *Bunch distributions for vertical excitations of ac dipole for the case before the ac dipole (at rest) and during the flattop ac dipole excitation for multiparticle tracking simulations with 4000 particles. Before the ac dipole the bunch size is $\sigma = 1.305$ mm, and during the flattop ac dipole excitation it is measured at $\sigma = 1.309$ mm.*

variable in units of J_z^{forced}, and $z \in \{x, y\}$ determines the plane of losses. This leads to the following expression of the forced dynamic aperture for given beam losses and forced excitation

$$DA_{\text{forced}} = J_z^{\text{forced}} - \epsilon_z ln\left(\frac{\Delta I}{I}\right). \tag{6.15}$$

which is dependent on J_z^{forced} and $\Delta I / I$. The resulting expression for the forced dynamic aperture is very close to the exponential formula for free dynamic aperture as defined in [108], but now contains a kick term (J_z^{forced}). The forced dynamic aperture can then be calculated from measurements by fitting Eq. (6.15) to the measured beam intensity losses over ac dipole excitation amplitudes.

Further simulations are done with an evenly sampled vertical phase space and the same conditions as presented in Sec. 6.3.2. The horizontal initial conditions are set to $x = p_x = 0$. All particles are excited with the same diagonal excitation close to the forced dynamic aperture. Figure 6.11 shows the lost and surviving particles as a function of their initial conditions in the vertical plane. All tails of the initial distribution are lost due to the forced dynamic aperture which is in line with the representation of Fig. 6.9.

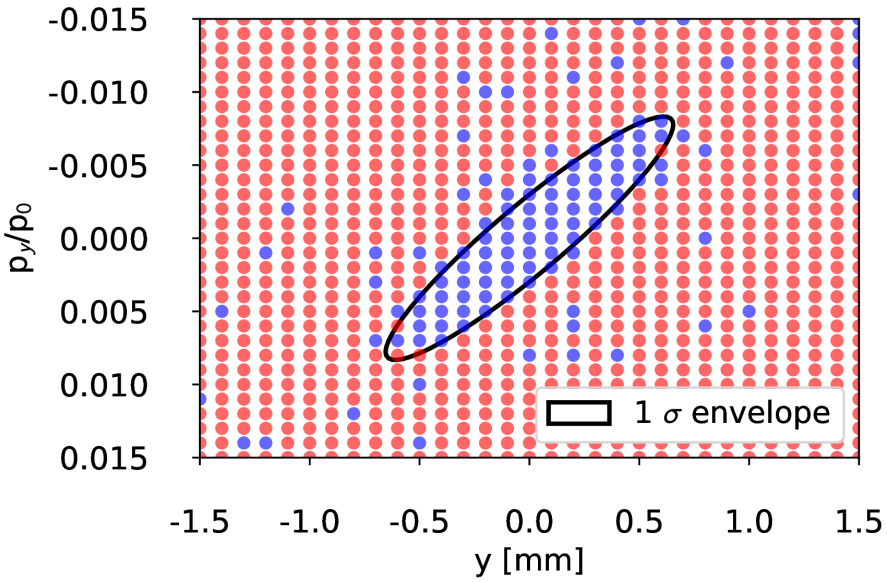

Figure 6.11: *Location of losses from forced DA with evenly sampled vertical phase space. In black the phase space ellipse at* 1σ *is drawn for reference.*

FORCED DYNAMIC APERTURE MEASUREMENTS AT INJECTION ENERGY

A first demonstration of forced dynamic aperture measurements using the LHC ac dipoles at injection energy is presented. The experiments carried out consist of exciting the beam with the LHC aperture kicker (MKA) or the LHC ac dipoles and measuring the beam intensity losses using the LHC beam current transformer system (BCT) [113]. A single pilot bunch is used during the measurements and the collimators are retracted to 12 σ_{nom} to allow for large excitations without scraping the stable beam and providing the necessary aperture to probe the free and forced dynamic aperture. Measurements were performed with the Landau octupoles powered at 40 A, equal to the operational settings in 2016 [110] as well as at 6.5 A. Several series of measurements were done in Beam 2 by exciting the beam in the horizontal plane and vertical planes separately. For the series of free kick measurements a dump and re-inject scheme is used, while during the ac dipole excitations the bunch is dumped and re-injected whenever significant losses occur. The emittance of the injected beams shows no significant variations between different injections and was measured consistently around 1.2 μm with the wirescanners in both planes. Free dynamic aperture measurements were first performed with the aperture kicker (MKA) [52] to obtain a free dynamic aperture reference with a conventional free kick method. The experiment was repeated in both planes using the

ac dipole.

ac dipole excitation amplitudes and frequencies are controlled through an online measurement tool. The ac dipole currents have been demonstrated to be very well regulated with a noise floor at $5 \cdot 10^{-4}$ of the main frequency amplitude and an emittance growth below the 0.1 % level for the excitation ranges used in the LHC [99]. The ac dipole driving tunes was set to $Q_{\mathrm{d},y} = Q_y - 0.014 = 0.296$ and $Q_{\mathrm{d},x} = Q_x - 0.018 = 0.262$ to ensure the $Q_{\mathrm{d},y} = Q_y$ resonance is not approached through detuning with amplitude for vertical excitations. The measurement was repeated with lower octupole strength (+6.5 A) to probe the change of forced dynamic aperture.

Figure 6.12 shows the measured beam losses as percentages of initial beam intensity for measurements with Landau octupoles at 40 A with free kick and ac dipole excitations in the vertical plane in the top plot and the corresponding measured natural tunes in the bottom plot. The actions are calculated at each BPM along the ring by using the main spectral line amplitude for ac dipole excitations and the peak-to-peak of the turn-by-turn signal for the free kicks as discussed in Sec. 6.3. In practice, an average over all arc BPMs is taken, having the benefit of providing an errorbar for the action measurement and excluding the BPMs in the insertion regions. The measurement errors on the actions are defined as the standard deviation of the measured actions in all working arc BPMs. The measured natural tunes are measured from the turn-by-turn data at each BPM using the spectral analysis code SUSSIX. The error is defined as the standard deviation over all BPMs and is in general small.

The beam losses are calculated from the BCT measured intensity before and after excitation. In the case of the ac dipole excitation this gives very clear losses from the BCT data, as there are no beam losses after excitation. For free kicks the difference in beam intensity is measured at the same timescales as the ac dipole excitation. However, continued slow losses are occurring then due to the free dynamic aperture. This results in a larger measured error on the relative beam losses for free kicks.

The forced dynamic aperture is calculated by fitting Eq. (6.15) to the measured losses as a function of ac dipole excitation amplitudes. The fit is also shown in Fig. 6.12 as the blue dotted line. We observe a very good agreement between measurement and the fit. The forced dynamic aperture is measured with the ac dipole at $(2.60 \pm 0.04)\,\sigma_{\mathrm{nom}}$ and is limited by the 3$^{\mathrm{rd}}$ order resonance $3Q_y = p$, as shown in Fig. 6.13. In the case of free kicks, the free dynamic aperture arising from the 3$^{\mathrm{rd}}$ order resonance is $4.3\,\sigma_{\mathrm{nom}}$. The kicks at 3.5 and 4.6 σ_{nom} show very small losses thus

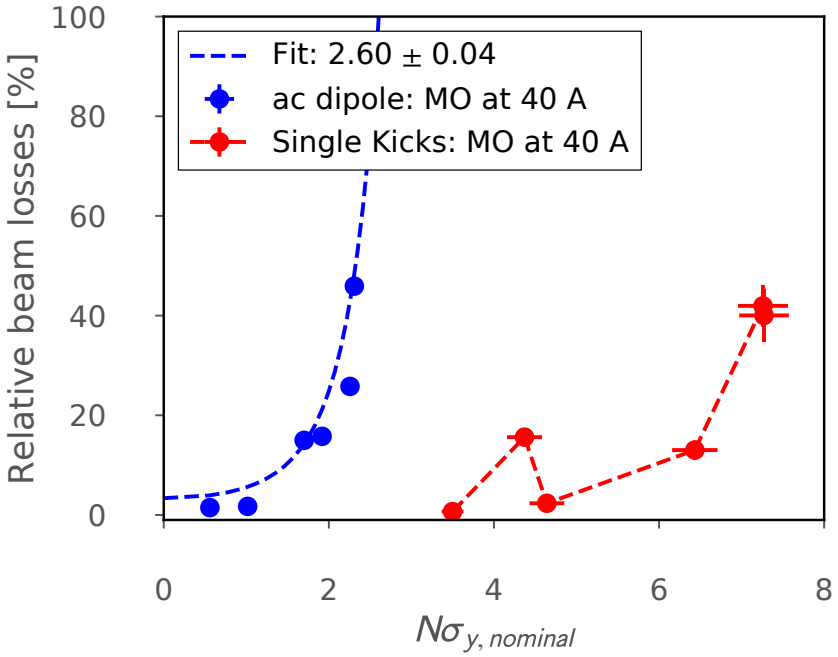

Figure 6.12: *Measured losses for ac dipole excitations (blue) and free kick (red) measurements with Landau octupoles powered at 40 A.*

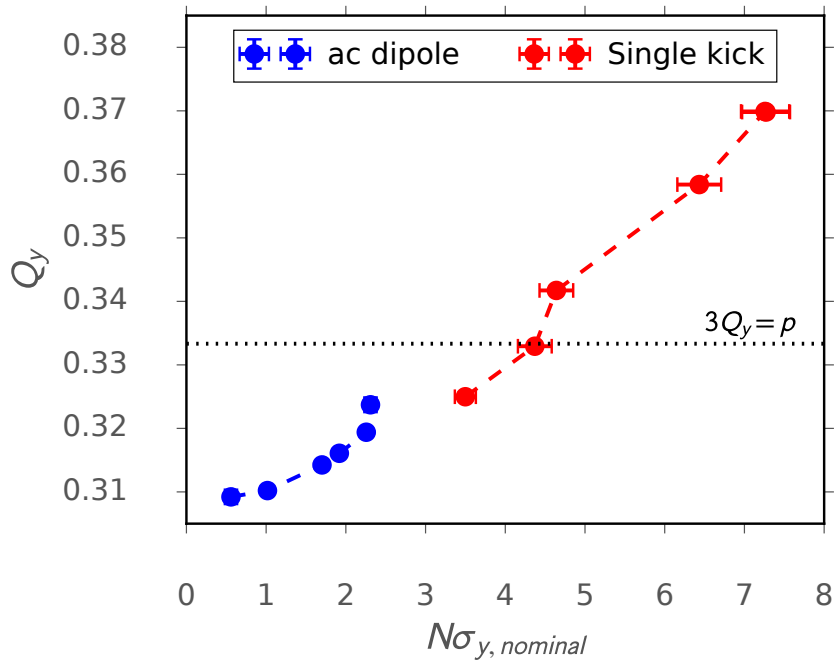

Figure 6.13: *Measured natural vertical tunes vs. vertical excitation amplitudes for measurements with ac dipole (blue) and free kicks (red) and Landau octupoles powered at 40 A.*

enclosing a thin unstable region at the 3rd order resonance. Such a thin unstable region explains the small losses observed for free kicks at the free dynamic aperture. Further free kick measurements at larger amplitude were performed up to $7.3\,\sigma_{\mathrm{nom}}$ where the beam is lost. As free kicks apply an instant change in phase space, it is possible to excite the beam beyond the 3rd order resonance without crossing the resonance for large amplitude kicks. It should be noted that such strong kicks are not present in operational conditions and that any bunch experiencing a gradual increase of amplitude will thus cross the resonance and become resonantly excited. In the case of the ac dipole the 3rd order resonance is dominant in defining the forced dynamic aperture. Due to the ramp up of the ac dipole all particles will slowly cross the resonance and thus be lost.

Figure 6.14 shows the beam losses for vertical kicks with ac dipoles at two different settings of Landau octupoles. The first curve, in blue, shows the same results as in Fig. 6.12 for Landau octupoles powered at 40 A. The forced dynamic aperture for measurements with lower octupole powering (6.5 A) is shown in green, and forced dynamic aperture from the fit is calculated at $(6.86 \pm 0.12)\,\sigma_{\mathrm{nom}}$. An increase of forced dynamic aperture is observed with a reduction of Landau octupole strength. This can be related to much weaker amplitude detuning coming from the Landau octupoles, as shown in Fig. 6.15. Amplitude detuning is linear in octupole current and quadratic in σ_{nom}. The expected increase of forced dynamic aperture from reduced amplitude detuning with weaker octupoles is thus $\sqrt{6.5/40} = 2.48$, while the observed increase of $DA_{\mathrm{forced}}(40)\ /\ DA_{\mathrm{forced}}(6.5) = 2.64$. In both cases the forced dynamic aperture is limited by the 3rd order resonance. The measurements demonstrate that changes in the nonlinear state of the machine can be measured with forced dynamic aperture measurements.

Further measurements with horizontal excitations are presented in Fig. 6.16. The resulting particle losses for measurements at horizontal excitations with both the ac dipole (in blue) and the MKA (in red) are shown. The forced dynamic aperture in the horizontal plane for the ac dipole was measured at $(2.9 \pm 0.3)\,\sigma_{\mathrm{nom}}$, while the free dynamic aperture was measured at $(5.2, \pm 0.2)\,\sigma_{\mathrm{nom}}$. Note that the fit for the free dynamic aperture is done with the error function as described in [92]. In the case of the ac dipole driven motion, the horizontal natural tune is detuning onto the linear resonance $Q_x = Q_{\mathrm{d},y}$ and nonlinear resonance $2Q_x = 2Q_{\mathrm{d},y}$, as shown in Fig. 6.17. Most likely, both linear and nonlinear resonances influence the observed particle losses. The free dynamic aperture is reached when approaching the difference linear coupling resonance $Q_x = Q_y$ and octupolar resonance $2Q_x = 2Q_y$ as both the vertical and horizontal tunes approach each other, as presented

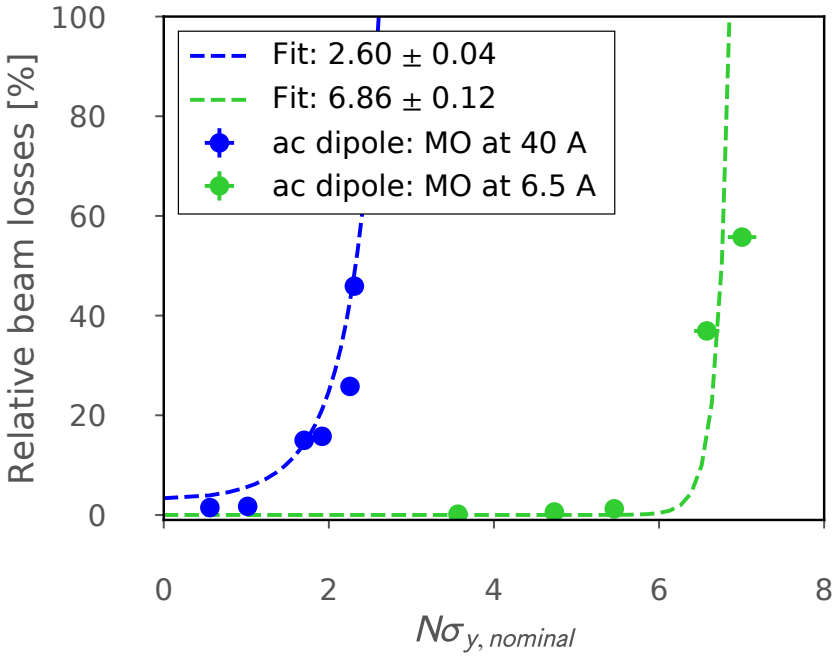

Figure 6.14: *Measured losses for ac dipole excitations with Landau octupoles powered at 40 A (blue) and 6.5 A (green).*

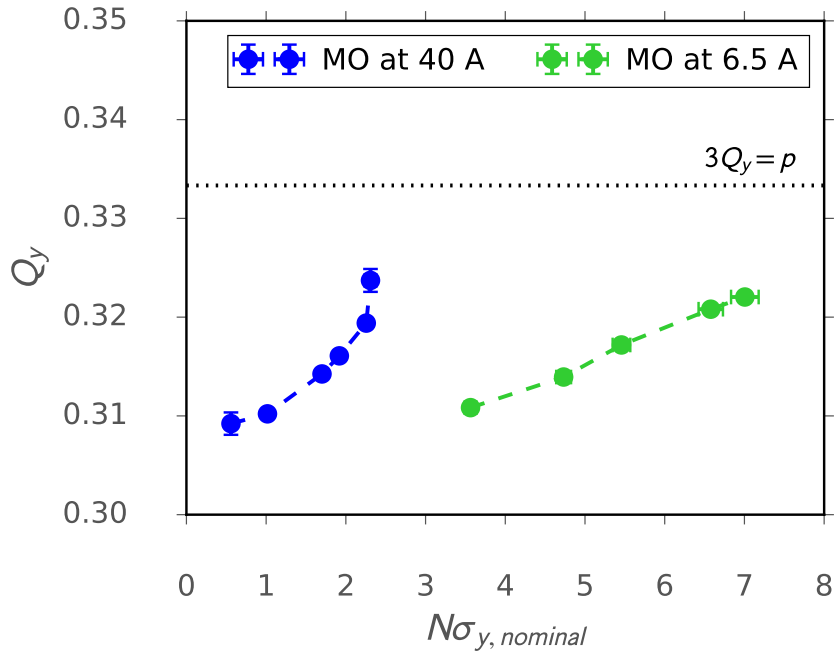

Figure 6.15: *Measured natural vertical tunes vs. vertical excitation amplitudes for measurements with ac dipole and Landau octupoles powered at 40 A (blue) and 6.5 A (green).*

in Fig. 6.17. The losses are most likely caused by the octupolar resonance, as the difference linear coupling resonance is a stable resonance.

Comparison to multi-particle tracking simulations

The nonlinear content of the machine can be probed by comparing measurements to simulation. By simulating the beam intensity losses after ac dipole excitation in multiparticle simulations a direct comparison to measurements can be made. Multiparticle bunches are initialized as a Gaussian distribution with 10000 particles following [34] and tracked in MADX. The intensity losses and turn-by-turn data of the centroid of charge are observed just like in measurements. The actions are calculated in the same way as with the measurements, by using the turn-by-turn data of the centroid of charge. Multiparticle tracking simulations are done at injection energy with Landau octupole at 40 A with the two models described in Sec. 6.3.2. Figure 6.18 shows the comparison between measurement and multiparticle simulations for vertical ac dipole excitations with Landau octupoles at 40 A, while Fig. 6.19 shows the same comparison at 6.5 A. The simulations with the nominal injection model using only magnetic errors are shown in pink. The nonlinear model used in this case fails to reproduce the observed losses in the forced dynamic aperture measurement. The sources of this discrepancy can be related to the fact that the skew sextupolar sources present in the model are much smaller than the beam based observations. The forced dynamic aperture using a model with geometrical rotational errors is shown in light blue. The second model is in good agreement with the measurements. This exercise demonstrates that the nonlinear content of the machine may be probed by directly comparing to simulation, and that improvements in the machine models may be derived from forced dynamic aperture measurements. As this method is allowed at top energy in the LHC this provides a distinct advantage over the conventional single kick methods that are currently forbidden at top energy in the LHC.

Simulations for the case with lower Landau octupole strengths show a similar behaviour as with the large octupole powering. When the model without rotational lattice errors is used forced dynamic aperture is at $10.8\,\sigma_{\mathrm{nom}}$, and does not reproduce the measurements. After including the rotational lattice errors the forced dynamic aperture reduces to $8\,\sigma_{\mathrm{nom}}$ and is limited by the third-order resonance $3Q_y$. Though this is still 1σ away from the measured values it shows a significant improvement in the model. Excitations at larger amplitudes show reduced losses at around 35% until the bunches are fully lost again. The losses observed between

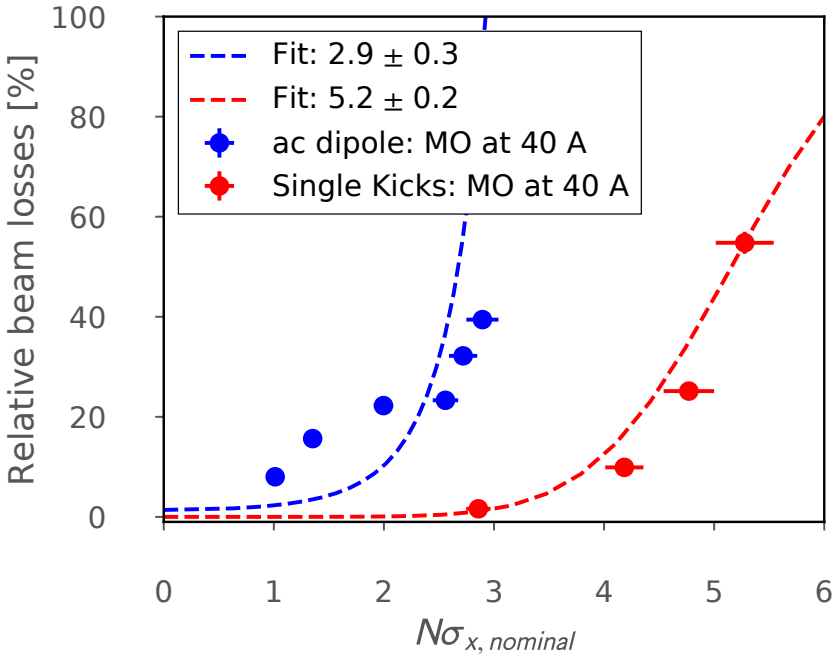

Figure 6.16: *Measured losses for both free kicks (red) and ac dipole excitations (blue) in the horizontal plane with Landau octupoles powered at 40 A. The blue fit is done with Eq. 6.15, while the red fit is done with the error-function of [92]*

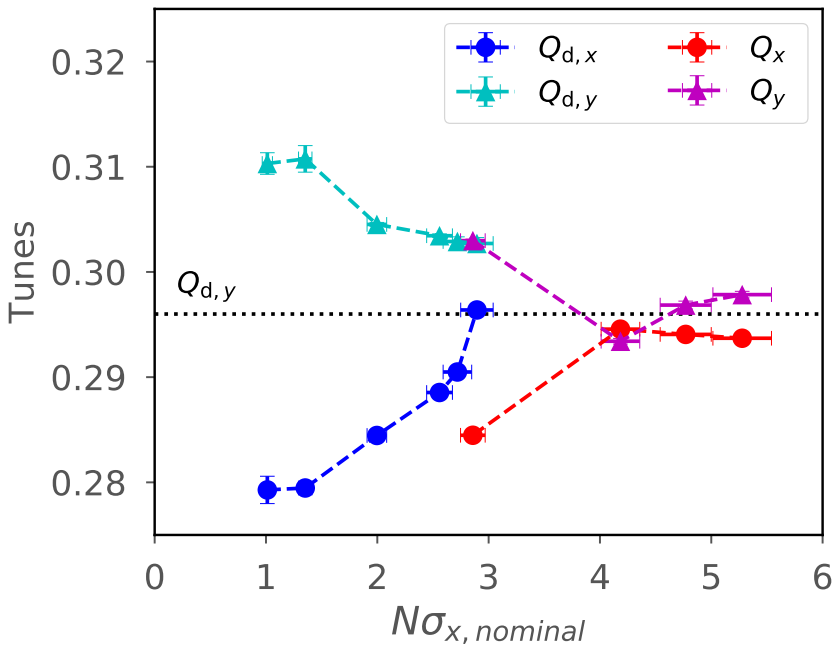

Figure 6.17: *Measured natural horizontal and vertical tunes vs. horizontal excitation amplitudes with Landau octupoles powered at 40 A for ac dipole excitations and free kicks excitations.*

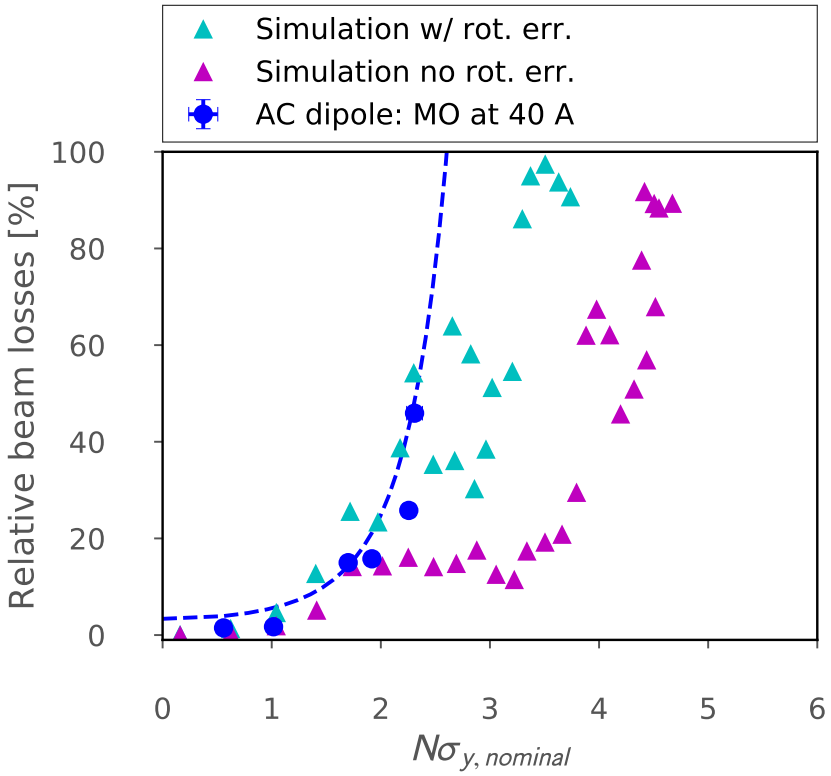

Figure 6.18: *Measured losses for ac dipole excitations with Landau octupoles at 40 A from measurements and multiparticle simulations. The simulations results without geometrical rotational lattice errors are shown in pink, while the simulations including those rotational errors are shown in light blue.*

$8\,\sigma_{\mathrm{nom}}$ and $10.8\,\sigma_{\mathrm{nom}}$ occur during the ramp-up and ramp-down of the ac dipole during which the $3Q_y$ resonance is crossed. Future studies will be needed for a more accurate model and exploration of advanced features of this method.

CONCLUSIONS

In recent years ac dipoles have obtained a prominent role in the commissioning of the LHC, and have been used or envisaged for many other machines. The forced dynamic aperture may become a limiting factor for future applications of ac dipoles. Fortunately the forced dynamic aperture can also be used as a new alternative observable for probing machine nonlinearities.

The nonlinear dynamics under the influence of an ac dipole are altered and the measured forced dynamic aperture is expected to be smaller than the free dynamic aperture. This is related to the appearance of new resonances and to the doubling

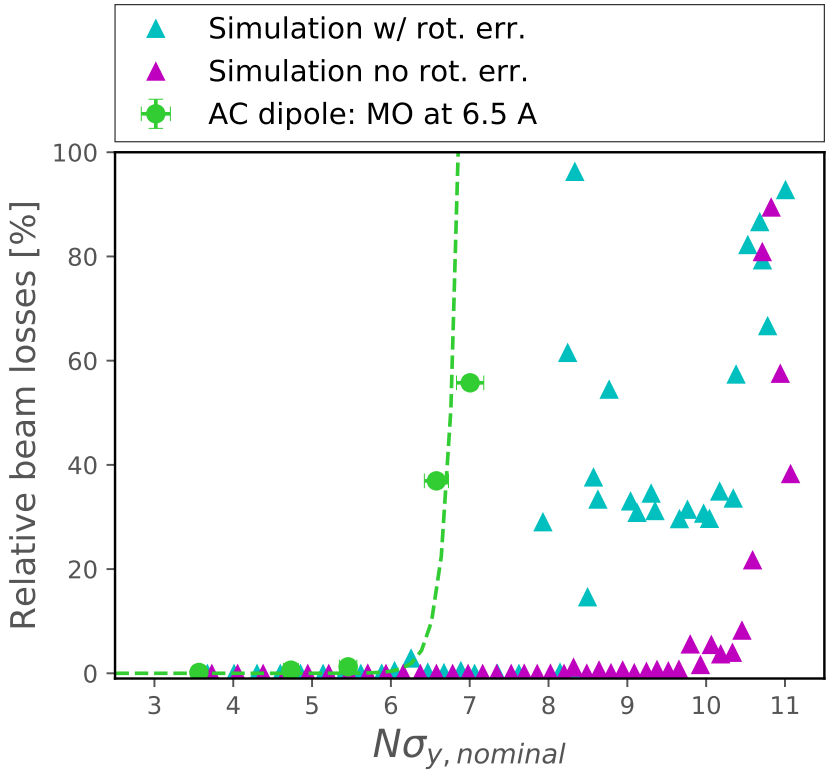

Figure 6.19: *Measured losses for ac dipole excitations with Landau octupoles at 6.5 A from measurements and multiparticle simulations. The simulations results without geometrical rotational lattice errors are shown in pink, while the simulations including those rotational errors are shown in light blue.*

of first order direct detuning terms in the ac dipole driven motion. Assuming direct detuning terms are the dominant detuning terms, this means enclosing resonances are approached with actions twice smaller than under free oscillations, thus narrowing the stability region in phase-space.

Single particle tracking simulations were done for both forced and free dynamic aperture. At top energy and without Landau octupoles the free dynamic aperture is 12.2 σ_{nom}. The forced dynamic aperture in single particle tracking simulations with ac dipole is found to be between 6.2 and 7.8 σ_{nom} depending on the chosen working point. Results show that the measured forced dynamic aperture is significantly reduced compared to the free dynamic aperture, confirming expectations. Furthermore, the role of the choice of ac dipole driving tunes is demonstrated. Depending on the working point, various resonances are observed to reduce the minimum forced dynamic aperture. It is thus crucial to use the same working point to probe and compare the forced dynamic aperture of different machine configurations. Secondly, this motivates a study to find a working point that maximizes

forced dynamic aperture to facilitate optics measurements in the LHC and High Luminosity LHC.

A first demonstration of forced dynamic aperture measurements is presented at injection energy with Landau octupoles powered to 40 A, and later to 6.5 A. At 40 A, measurements with the aperture kicker (MKA) showed a vertical kick free dynamic aperture at the 3$^{\text{rd}}$ order resonance at $4.3\,\sigma_{\text{nom}}$. The ac dipole forced dynamic aperture was measured at $(2.60 \pm 0.04)\,\sigma_{\text{nom}}$, limited also by the 3$^{\text{rd}}$ order resonance. Lowering of the Landau octupole powering to 6.5 A resulted in a significant measurable increase of forced dynamic aperture. A reduction of octupole currents to 6.5 A shows an increase of forced dynamic aperture to $(6.86 \pm 0.12)\sigma_{\text{nom}}$, and illustrates the potential use to characterize relative changes in the nonlinear state of the machine using forced dynamic aperture measurements. Measurements with horizontal excitations show a forced dynamic aperture of $(2.9 \pm 0.3)\,\sigma_{\text{nom}}$, and a free dynamic aperture of $(5.2 \pm 0.2)\,\sigma_{\text{nom}}$ for free oscillations.

Both results in the vertical and horizontal planes show a reduced forced dynamic aperture compared to the free dynamic aperture. This is of particular significance for top-energy applications in the LHC and High Luminosity LHC where ac dipole measurements are central to all beam optics commissioning strategies, and are limited in excitation amplitudes by the forced dynamic aperture. Forced dynamic aperture optimisation is therefore crucial to allow optics measurements in highly nonlinear machines such as the High Luminosity LHC.

Multiparticle simulations show that the nominal model used with nonlinear magnetic errors fails to reproduce the measured forced dynamic aperture. The introduction of measured geometrical rotational errors and matching the coupling to the measured experimental values is needed in the model to reproduce the measured forced dynamic aperture. It demonstrates the usefulness of forced dynamic aperture measurements to characterise the nonlinear model.

The results presented in this paper demonstrate the potential of forced dynamic aperture as a new observable to provide insight on the nonlinear content of the machine, validate nonlinear corrections, improve the nonlinear model, and provide qualitative estimates of a lower bound for the free dynamic aperture.

PROBING THE FORCED DYNAMIC APERTURE IN THE LHC AT TOP ENERGY USING AC DIPOLES

F.S. Carlier, M. Giovannozzi, R. Tomás, E.H. Maclean, T.H.B. Persson, and R. Tomás

Proceedings of 9th International Particle Accelerator Conference (IPAC'18), Vancouver, Canada, MOPMF0033 Published July 2018

Available online at

https://doi.org/10.18429/JACoW-IPAC2018-MOPMF033

6

ABSTRACT

Measurements of the dynamic aperture in colliders are a common method to ensure machine performance and offer an insight in the nonlinear content of the machine. Such direct measurements are very challenging for the LHC and High Luminosity LHC. Forced dynamic aperture has been demonstrated for the first time in the LHC at injection energy as a potential new observable to safely probe the nonlinear content of the machine. This paper presents the first measurements of forced dynamic aperture at top energy and discusses the proposed measurement schemes and challenges.

INTRODUCTION

Measurements of forced dynamic aperture have been proposed as an alternative observable to probe machine nonlinearities in particle colliders [3, 94, 114]. The availability of forced dynamic aperture measurements has opened up the possibility for fast and reliable characterisation of the nonlinear state of the machine where conventional free dynamic aperture measurements with free kicks are too time consuming [92, 94], and is complementary to the alternative method based on beam heating as presented in [108, 115]

The motion under forced coherent oscillation of an ac dipole is altered compared to the free betatron motion [42, 43, 49, 53, 65]. Due to the presence of extra resonances [49], and an increase in amplitude detuning for the direct detuning terms [65] during forced coherent oscillations the forced DA is expected to be smaller than the dynamic aperture under free motion. Nonetheless, measurements of forced DA can provide useful insights in nonlinearities in the LHC and can be used as a valuable figure of merit for nonlinear optics corrections.

The LHC ac dipoles are limited to short excitations of 6600 turns due to hardware heating protections. As such, the presented work in this paper focusses on short term forced DA only. A generalisation to longer time scales is of course possible, but not considered in this paper. Measurements of forced DA are done by probing the beam intensity loss after large coherent oscillations using the LHC ac dipoles. As the excitation amplitude is increased, more particles will cross the forced DA and become lost. By characterising the beam intensity losses with ac dipole excitation amplitude the forced DA can be calculated. Under the assumption that the losses occur dominantly in a single plane the problem can be simplified to a single dimension. Figure 6.20 shows an ac dipole excited beam traversing the forced DA. In contrast to the free kick case where only particles beyond the free DA are lost, the intrabunch evolution of the particles due to the residual free motion will cause all the tails to be lost. This now greatly simplifies the problem to an integral over the distribution in action space.

$$\frac{\Delta I}{I}(A) = \int_{DA_{\text{forced}}}^{+\infty} \frac{1}{\epsilon_z} e^{-\frac{J_z - A}{\epsilon_z}} d J_z \tag{6.16}$$

where $\Delta I / I$ is the normalized measured losses, $2J_z$ are the measured actions, ϵ_z is the measured physical emittance, and $z \in \{x, y\}$ determines the plane of losses.

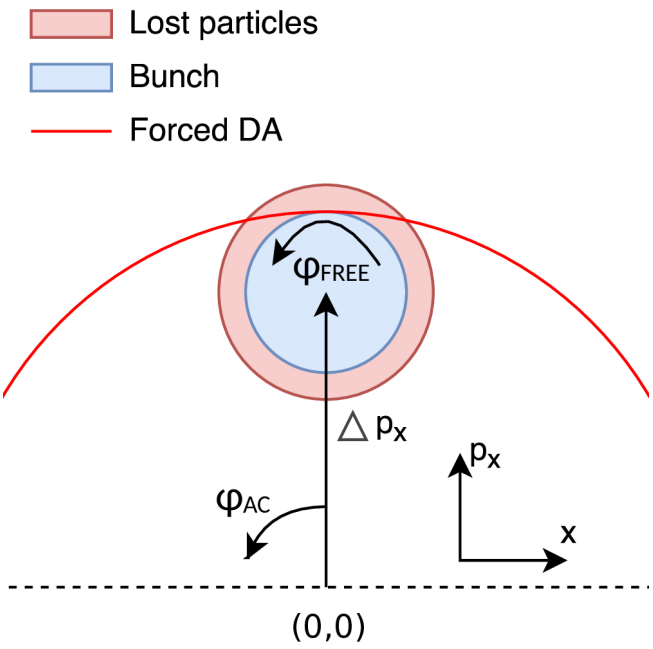

Figure 6.20: *Losses of distribution from ac dipole excitations. The bunch rotates as a whole in phase space with the ac dipole frequency, while the bunch itself revolves with the natural frequency.*

This leads to the following expression for the forced DA

$$DA_{\text{forced}}(J_z, \Delta I/I) = 2J_z - 2\epsilon_z ln\left(\frac{\Delta I}{I}\right) \tag{6.17}$$

6

FORCED DA AT TOP-ENERGY

Measurements of forced DA at top energy (6.5 TeV) and end-of-squeeze ($\beta^* =$ 40 cm) are presented. Several different magnetic configurations of the Landau octupoles and dodecapolar corrector magnets in the insertion regions are probed. The settings are reported in Tab. 6.1

The transverse beam size is recorded using the Beam Synchrotron Radiation Telescope (BSRT) [116]. Calibration of the BSRT data is done with wirescanner measurements [116] at the start of the forced DA measurements. The BSRT data is particularly interesting to measure the evolution of the beam size and detect possible beam blow-up. Figure 6.21 shows the measured beam size for the vertical and horizontal plane of Beam 1 in units of nominal emittance. Where the nominal normalized emittance is defined as $\sigma_{\text{nom}} = 3.75\,\mu$m. The large vertical spikes in the data correspond to the ac dipole excitations.

Table 6.1: *Summary of different magnetic configurations with $\epsilon_{\text{nom}} = 3.75\,\mu m$, and measured forced DA.*

	MO [m^{-4}]	MCTX [m^{-6}]	forced DA [σ_{nom}]
Settings 1	10.8	-	4 ± 2
Settings 2	14.3	-	3.3 ± 1.6
Settings 3	14.3	38000	2.7 ± 1.3

Some beam blow-up is observed in the horizontal plane for the first 4 vertical excitations with low octupole currents (Settings 1). The beam size later stabilizes and no further blow-up is observed. Fortunately the blow-up occurs in the plane opposite to the excitation and the effect on measured losses for the first view excitations is negligible as will be presented later. All further measurements are performed with stable beam size and can thus be directly compared.

Figure 6.21 shows the measured beam intensity from the Beam Current Transformers System (BCT) [113] for Beam 1. At each excitation a reduction of beam intensity is observed. By characterising the losses over the measured actions an estimate on forced DA may be obtained.

The measured losses in percentages of beam intensity before the excitation are presented in Fig. 6.22 as a function of the measured excitation amplitudes for the different magnetic configurations. By fitting Eq. (6.17) to the measured data, using the physical emittances measured from the wirescanners, an estimate of forced DA is acquired for the three settings. The results are presented in Tab. 6.1. The configuration with the lowest octupole strengths shows the largest forced DA at $(4 \pm 2)\,\sigma_{\text{nom}}$. The forced DA decreases to $(3.3 \pm 1.6)\,\sigma_{\text{nom}}$ when increasing the MO strengths and further down to $(2.7 \pm 1.3)\,\sigma_{\text{nom}}$ when also including the dodecapoles. Unfortunately the fit errors are large due to the limited number of measurements and the limited allowed beam intensity losses due to machine protection thresholds on the Beam Loss Monitors. Furthermore, a closer look at the beam profiles from the wirescanners may improve the modelling of the beam distribution and thus improve the fit quality.

A significant decrease in forced DA is observed as the nonlinear magnetic sources are increased. Secondly, a direct effect of the dodecapolar sources on the forced DA is measured. Forced DA may form a valuable figure of merit to correct dodecapolar

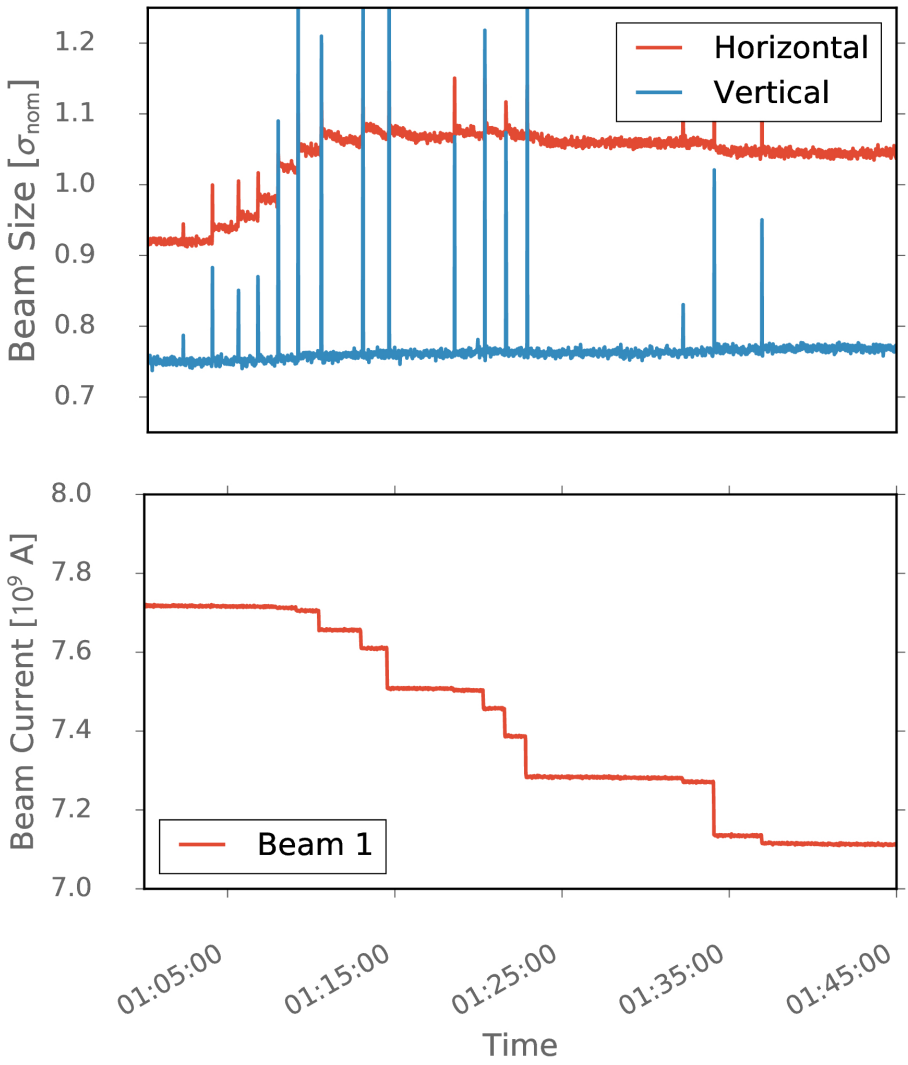

Figure 6.21: *Measured beam size for horizontal and vertical planes of Beam 1 at top energy (6.5 TeV) and $\beta^* = 40$ cm, using the LHC BSRT system (top figure). Measured beam current of Beam 1 at top energy (6.5 TeV) and $\beta^* = 40$ cm, using the LHC BCT system (bottom figure).*

sources in the insertion regions of the High Luminosity LHC, alongside the method of beam heating [94].

FORCED DA WITH SKEW OCTUPOLAR CORRECTIONS

Correction of nonlinear magnetic errors in the insertion regions of the LHC have been a priority in 2017, and successful correction of b_3, a_3 and b_4 sources have been achieved [117]. Local corrections for skew octupolar sources (a_4) have been

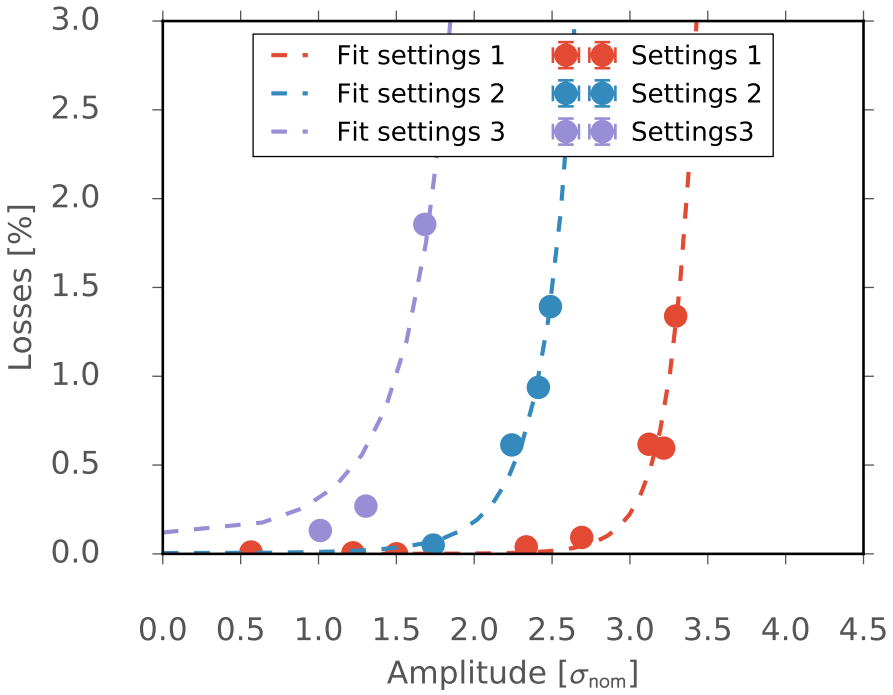

Figure 6.22: *Measured beam intensity losses with vertical ac dipole excitation amplitude for Beam 1 at top energy (6.5 TeV) and $\beta^* = 40$ cm. Measured forced DA from fits is summarised in Tab. 6.1.*

calculated from feed down measurements to tune as a function of crossing angles. While corrections of IR1 have been validated with crossing angle scans and implemented operationally in 2017, IR5 corrections proved more challenging. Part of the challenge comes from confusion about the polarity of the a_4 correctors in IR5 due to differences in conventions between simulation codes and the magnet powering architecture in the LHC. There are two a_4 correctors in IR5, one left of the IP and one right of the IP. The corrector strengths were calculated as potential local corrections from feed down measurements. The two configurations of correctors have the same strengths but opposite polarity, as specified in Tab. 6.2.

Forced DA measurements taken parasitically at top energy (6.5 TeV) and $\beta^* = 30$ cm are shown for three different configurations of the a_4 correctors in IR5 in Fig. 6.23. The forced DA is again calculated by fitting the measurements with Eq. (6.17) and using the physical emittance measured with the wirescanners. The reference measurement with no powering of the correctors shows the largest forced DA of $(4.5 \pm 2)\,\sigma_{nom}$, while the forced DA decreases to $(4 \pm 2)\,\sigma_{nom}$ and $(3.8 \pm 1.9)\,\sigma_{nom}$ for the configurations with respectively the positive and negative polarity. The measurement errors are very large and prevent these studies from being

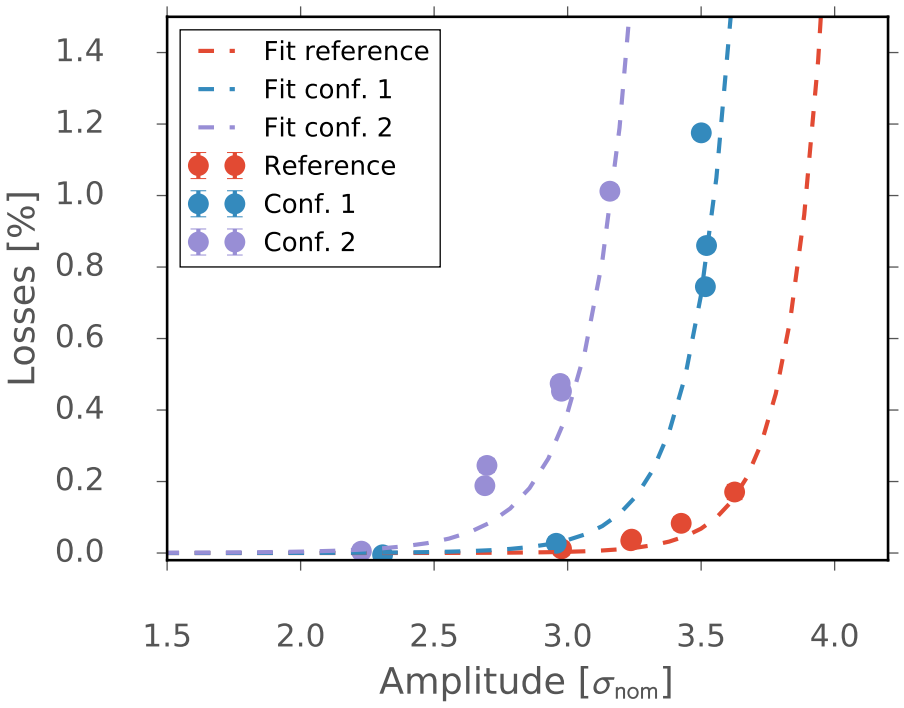

Figure 6.23: *Measured beam intensity losses with vertical ac dipole excitation amplitude for 3 different corrector settings in Beam 2 at top energy (6.5 TeV) and $\beta* = 30$ cm.*

conclusive. It is critical for future studies to increase the number of measurements to reduce the fitting errors. The forced DA is observed to deteriorate for both configurations, which suggests a mismatch between a_4 errors and the attempted local correction. These findings are in line with resonance driving terms measurements presented in [95].

Furthermore, it is interesting to see that a small change in the a_4 correctors in the insertion regions, at $\beta^* = 30$ cm, produces a reduction in forced DA of the

Table 6.2: *Summary of different magnetic configurations.*

	a_4 left [m^{-4}]	a_4 right [m^{-4}]	forced DA [σ_{nom}]
No correction	-	-	4.5 ± 2
Configuration 1	-0.36	-0.53	4 ± 2
Configuration 2	0.36	0.53	3.8 ± 1.9

same order of magnitude as an increase of the MOs to 14.3 m^{-4}. This underlines the importance of a_4 errors in the insertions regions as significant sources of forced DA and motivates further studies for successful corrections in view of the High Luminosity LHC.

CONCLUSIONS

Measurements of forced DA have been successfully performed at top energy in the LHC. Changes in forced DA resulting from increased Landau octupole strengths as well as dodecapolar corrector magnets are shown to be measurable. Forced DA has demonstrated to be a promising observable to measure nonlinear sources, and may at some point be used for validation of dodecapolar corrections in the High Luminosity LHC. Furthermore, attempted local skew octupolar corrections in IR5 are studied. The implementation of both corrections independently result in a decrease in forced DA. The second correction (assuming negative polarity of the corrector magnets) shows the largest degradation. The results presented in this paper reject the proposed local a_4 corrections in IR5. The successful correction of a_4 in the insertion regions of the LHC is considered as one of the main objectives of the 2018 commissioning campaign.

In general the fit quality is poor, but as a first demonstration the results are promising. Great care should be taken to take more measurements and improve statistics. To conclude, the method of forced DA has been demonstrated to be a valuable observable to probe machine nonlinearities as well as the validity of nonlinear optics corrections.

ACKNOWLEDGEMENTS

The authors would like to thank the whole OMC team for their help with the measurements.

7

FIRST MEASUREMENT OF RESONANCE DRIVING TERMS FROM HEAD-ON BEAM-BEAM INTERACTION IN THE LHC

All the studies presented up till now discuss the dynamics of particles for non-colliding beams. However, for colliding beams, the opposing beams at and near the collision points will be a large source of nonlinearity. Figure 7.1 shows a schematic representation of beams in collision. There are two places where the opposing beam will perturb the particle motion. The first is before and after the collision point and is referred to as the long-range beam-beam interaction. The second is at the collision point, where it is referred to as the head-on beam-beam interaction. This chapter focuses solely on the head-on beam-beam interaction, and at times refers to it as the beam-beam interaction, omitting the head-on description.

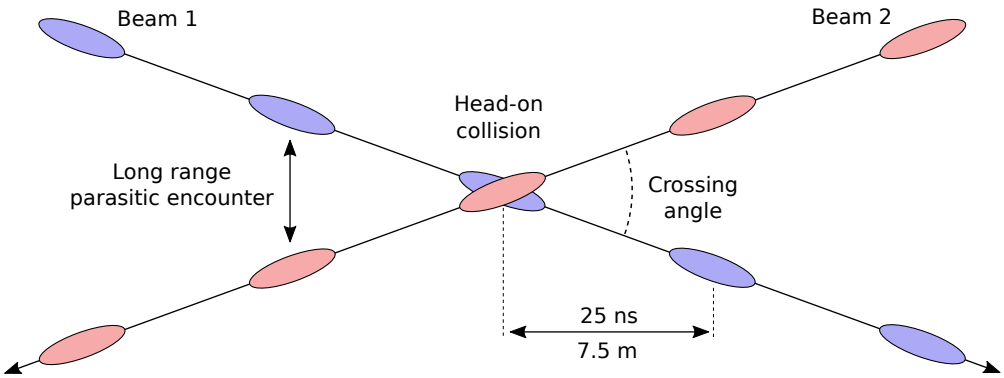

Figure 7.1: *Schematic representation of colliding beams showing the crossing angles. The head-on beam-beam interaction is generated at the collision point [118].*

The beam-beam interaction is a collider specific effect that describes the interaction between the two opposing colliding beams. The electromagnetic potential of the opposing beam creates a large perturbation in the beam motion, and its forces are highly nonlinear as shown in Fig. 7.2. For particles with small transverse amplitudes the beam-beam effect is equivalent to a quadrupolar perturbation and induces a tune shift. However, for particles oscillating with larger amplitudes the nonlinear effects of the beam-beam interaction become increasingly important.

As the perturbative force is highly nonlinear the beam-beam interaction can cause resonances and significantly reduce the dynamic aperture. The beam-beam interaction forms one of the central limits in colliders and requires extensive optimisation during the design phase of colliders. However, while the beam-beam interaction is critical to the design of colliders, it is scarcely studied in experiments due to challenging nature of the measurements.

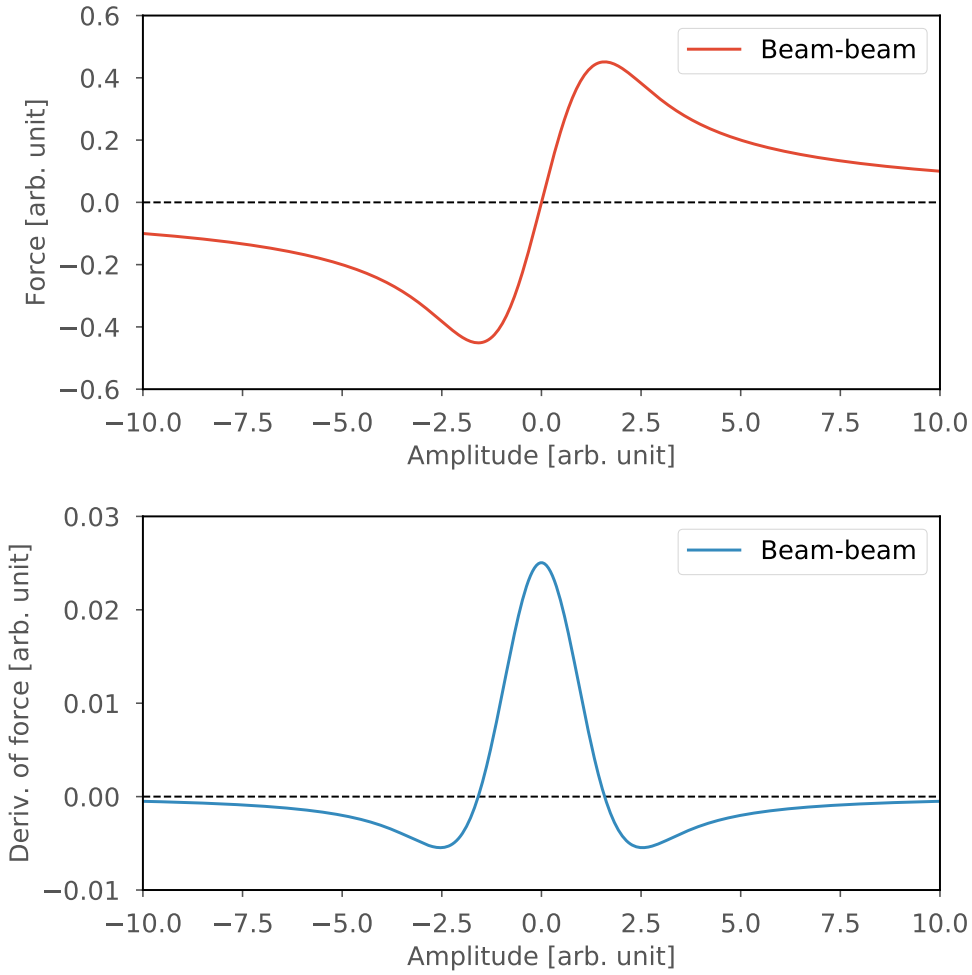

Figure 7.2: *Force generated by the head-on beam-beam interaction and the derivative of the force.*

Direct measurements of the nonlinear effects of the beam-beam interaction are challenging. Measurements of beam lifetime have shown the detrimental effect of the beam-beam interaction due to the increased nonlinearities in the machine. However, these are measurements of averaged effects of all nonlinear orders. Direct measurements of specific nonlinear modes generated by the beam-beam interaction were until now not successful.

The following chapter presents the first ever measurements of beam-beam gen-

erated resonance driving terms in a collider. The key to these measurements lie in the use of ac dipoles for coherent large amplitude excitations of the beam. Note that to fit previous literature on this topic, the derivations are described in terms of the betatron phase advance over one turn μ_z instead of the tune Q_z. Their relation is given by $\mu_z = 2\pi Q_z$, as specified in the chapter.

FIRST MEASUREMENT OF RESONANCE DRIVING TERMS FROM HEAD-ON BEAM-BEAM INTERACTION IN THE LHC

F.S. Carlier, R. Tomás, and X. Buffat

Physical Review Accelerators and Beams
Submitted 15 October 2019

ABSTRACT

Beam-beam interactions typically limit the performance of colliders. Monitoring beam-beam effects, possibly including compensation devices, will be crucial for operation of the next generation of high intensity colliders. Direct measurements of beam-beam driven resonance terms are challenging to perform due to the fast decoherence of kicked beams. This paper describes the theoretical background for measuring beam-beam resonance driving terms from turn-by-turn data of excited beams for both the free excitations as well as forced excitations with an ac dipole. It also presents measurements of octupolar and dodecapolar beam-beam generated resonance driving terms in the LHC, the first of such measurements in any collider.

INTRODUCTION

The head-on beam-beam interaction is a major limitation for particle colliders. It generates amplitude detuning and tune spread, reduces the dynamic aperture, and can lead to excited resonances [119, 120]. Modelling of the head-on beam-beam interaction is a critical tuning parameter during the lattice design phase of colliders. However, direct measurements of resonance driving terms resulting from the beam-beam interactions from collisions remain elusive. Measurements of beam-beam resonance driving terms are very challenging to achieve. The beam-beam interaction introduces a large tune spread and amplitude detuning that cause free oscillations of the beams to decohere very quickly.

Direct measurements of beam-beam effects on the beam dynamics are crucial to improve the understanding of the beam-beam interactions, study beam-beam induced limitations, resonances, and help develop mitigation strategies using for example electron lenses [121–125] or compensating wires [126].

In this paper the theoretical framework to characterize the secondary spectral line amplitudes in terms of beam-beam generated resonance driving terms is presented in Sec. 7.2 for free oscillations and in Sec. 7.3 for forced oscillations with an ac dipole. It is followed by validations of the analytical expressions to single particle tracking simulations in Sec. 7.5. The first measurements of beam-beam resonance driving terms at injection energy in the LHC, as well as the first observation of dodecapolar resonance driving terms are presented in Sec. 7.6.

7 ANALYTICAL DESCRIPTION OF SPECTRAL LINE AMPLITUDES FROM BEAM-BEAM IN FREE MOTION

Resonance driving terms measurements are generally done by kicking the beam in the transverse plane and measuring the transverse position at the beam position monitors (BPMs). Spectral analysis of the obtained turn-by-turn data reveals the spectral composition and gives insights in the nonlinear sources in the accelerator. For regular magnetic multipoles or multipolar sources a straight forward conversion between spectral line amplitudes and resonance driving terms is possible [70, 73, 127]. It will be shown in this section that such a conversion in the case of beam-beam resonance driving terms is complicated, as the spectral line amplitude dependence on the kick amplitude is a composition of Bessel functions. The following derivations will thus aim to describe the expected spectral line amplitude as generated by a single beam-beam interaction.

The derivation follows the approach described in [46] to establish the beam-beam map. To start the derivations are done in a single dimension before generalizing to two dimensions and adding the ac dipole. The Courant-Snyder map is defined in a Lie map representation as

$$e^{:f_2:}, \quad \text{where} \quad f_2 = -\frac{\mu_z}{2}(\hat{z}^2 + \hat{p}_z^2) \tag{7.1}$$

where $z \in \{x, y\}$ specifies the plane of motion, μ_z is the betatron phase advance over one turn and relates to the machine tune Q_z with $\mu_z = 2\pi Q_z$, β_z is the β-function at the location of observation and $\hat{z}$ and $\hat{p}_z$ are the linearly normalized coordinates that are defined using the action angle variables (ϕ_z, J_z),

$$\hat{z} = \sqrt{2J_z}\cos\phi_z \tag{7.2}$$
$$\hat{p}_z = -\sqrt{2J_z}\sin\phi_z \quad . \tag{7.3}$$

from which the linearly normalized complex coordinates can be defined,

$$\zeta_{z,\pm} = \hat{z} \pm i\hat{p}_z \quad . \tag{7.4}$$

The linear map in action angle variables then becomes

$$e^{:f_2:} = e^{:-\mu_z J_z:} \quad . \tag{7.5}$$

The beam-beam force for round Gaussian beams of *rms*-radius σ is given by:

$$f(z) = \frac{Nr_0}{\gamma}\frac{2}{z}(1 - e^{-z^2/2\sigma^2}) \ , \tag{7.6}$$

where N is the number of particles in the opposing bunch, γ is the relativistic Lorentz factor, r_0 is the classical radius of the colliding particle, and σ is the beam size of the opposing beam at the location of the head-on beam-beam interaction. As this is in normalized coordinates, σ is normalized by the β-function of the beam of interest.

The beam-beam map in Lie operator form can be expressed as,

$$e^{:h_{\text{bb}}:} \quad \text{with} \quad h_{\text{bb}} = \int_0^z dz' f(z') \ , \tag{7.7}$$

where $-h_{\text{bb}}$ is the potential from the beam-beam force. The potential h_{bb} can be

decomposed as a Fourier series as

$$h_{\mathrm{bb}} = \sum_{n=-\infty}^{\infty} c_n(J_z) e^{in\phi_z} \ . \tag{7.8}$$

The one-turn map of a system with a single head-on beam-beam source is expressed as

$$M \ = \ e^{:h_{\mathrm{bb}}:} e^{:f_2:} \ . \tag{7.9}$$

The normal from method [68, 69] can be applied to this one-turn map to obtain a rotational one-turn map that only depends on the amplitude. A generating function F exists for which,

$$e^{:-F:} e^{:h_{\mathrm{bb}}:} e^{:f_2:} e^{:F:} = e^{:H(J_z):} R \ , \tag{7.10}$$

where $H(I_z)$ is the amplitude dependent Hamiltonian. The solution to Eq. (7.10) is obtained from the Campbell-Baker-Hausdorf (CBH) theorem and is given to first order by,

$$F = \frac{1}{1 - R_z} h_{\mathrm{bb}} - \bar{h} \tag{7.11}$$

where R_z is the linear rotation operator defined as $R_z = e^{:-\mu_z J_z:}$, $\bar{h}$ is the average of h_{bb} over the phase variables and is in this case given by $\bar{h} = c_0(J_z)$. Note that $\bar{h}$ defines the beam-beam amplitude detuning of the beam-beam potential. Inserting the expansion of h_{bb} into Eq. (7.11) yields the generating function,

$$F \ = \ \sum_{n \neq 0} c_n(J_z) \left(\frac{1}{1 - e^{in\mu_z}} \right) e^{in\phi_z} \tag{7.12}$$

The coefficients $c_n(J_z)$ in single dimension are calculated as done in [46] and are defined as,

$$c_n(J_z) \ = \ \frac{N r_0}{\gamma} \int_0^{J_z/2\sigma_z^2} \frac{d\alpha}{\alpha} \begin{cases} -e^{-\alpha} \mathrm{I}_{n/2}(\mathrm{ff}) & n = \text{even} \neq 0 \\ 0 & \text{otherwise} \end{cases} \tag{7.13}$$

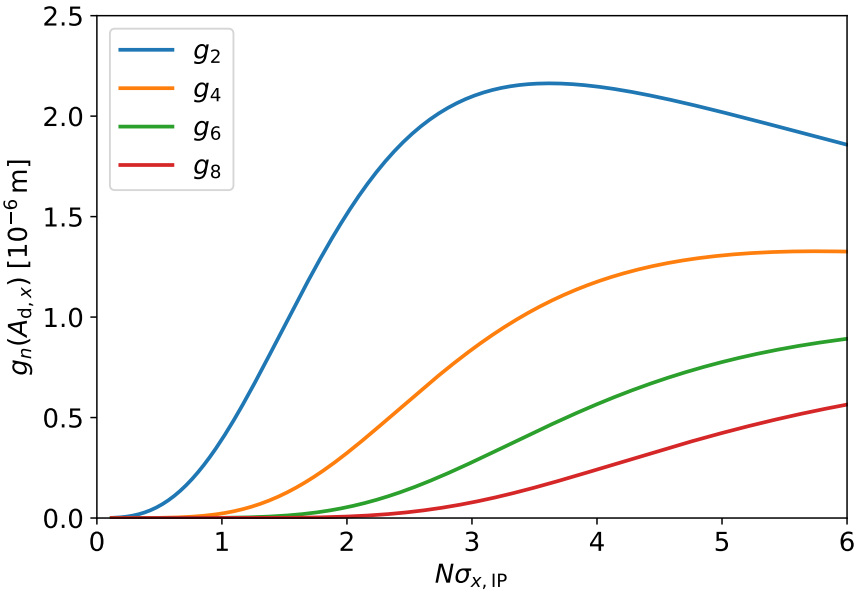

Figure 7.3: *The amplitude of coefficients g_n in one dimension as specified in Eq. (7.20) over horizontal excitation amplitudes.*

where $\mathrm{I_n}$ are the modified Bessel functions of the first kind, and β_z and σ_z are respectively the β-function and beam size at the location of the beam-beam interaction. The coefficients are shown in Fig. 7.3 as a function of normalized excitation amplitudes.

The computation of the nonlinear perturbations are obtained by deriving the change of coordinates from normal form complex coordinates $\zeta_{z,\pm}$ to the linearly normalized complex coordinates $\xi_{z,\pm}$ by applying the generating function as a Lie operator,

$$\xi_{z,\pm} = e^{:F:}\zeta_{z,\pm}\,. \tag{7.14}$$

where the normal form coordinate is a nonlinear generalization of the normalized complex coordinate with a new phase ψ_z and a new invariant of the motion I_z,

$$\zeta_{z,\pm} = \sqrt{2I_z}e^{\mp i(\psi_z+\psi_{z,0})} \quad . \tag{7.15}$$

The generating function F in normal form space is given as a function of the normal form variables,

$$F = \sum_{n\neq 0} c_n(I_z)\left(\frac{1}{1-e^{in\mu_z}}\right)e^{in\psi_z} \tag{7.16}$$

The solution to the transformation of Eq. (7.14) is given to first order by,

$$\xi_{z,\pm} = \zeta_{z,\pm} + [F, \zeta_{z,\pm}] \tag{7.17}$$

where the square bracket are the Poisson brackets and are defined by,

$$[f,g] = \sum_z \frac{\partial f}{\partial \psi_z}\frac{\partial g}{\partial I_z} - \frac{\partial f}{\partial I_z}\frac{\partial g}{\partial \psi_z} \quad . \tag{7.18}$$

By substituting Eqs (7.15) and (7.16) in Eq. (7.17) and solving the Poisson bracket while taking into account that $c_n(I_z) = 0$ for odd n, the result for $\xi_{z,-}$ is given by,

$$\begin{aligned}\xi_{z,-} &= \sqrt{2I_z}e^{i(\mu_z N+\psi_{z,0})} \\ &\quad +i\sum_{\substack{n\in 2\mathbb{Z}\\ n\neq 0}} \frac{g_n(I_z)}{1-e^{in\mu_z}}e^{i(n+1)(\mu_z N+\psi_{z,0})} \ ,\end{aligned} \tag{7.19}$$

where,

$$g_n(I_z) = \left(\frac{n}{\sqrt{2I_z}}c_n(I_z) - \sqrt{2I_z}\frac{\partial c_n(I_z)}{\partial I_z}\right) , \tag{7.20}$$

and with the resonance condition given by $n\mu_z = 2\pi p$ for $p \in \mathbb{Z}$. The derivative of the coefficients are then given by,

$$\frac{\partial c_n(J_z)}{\partial J_z} = \frac{Nr_0}{\gamma J_z}\begin{cases} -e^{-J_z/2\sigma_z^2}\mathrm{I_{n/2}(J_z/2\text{œ}_z^2)} & n = \text{even} \neq 0 \\ 0 & \text{otherwise}\end{cases} \tag{7.21}$$

Equation (7.19) shows all the spectral modes contained in the motion of a particle under the influence of a single head-on beam-beam interaction. In fact the sec-

ondary spectral line amplitudes in spectra of turn-by-turn complex position data are fully determined by the function $g_n(I_z)$ and its corresponding resonance denominator. The beam-beam resonance driving terms can thus be studied by observing the secondary spectral line amplitudes, as will be shown in Sec. 7.5.

HEAD-ON BEAM-BEAM WITH AC DIPOLE

The calculation of resonance driving terms under the influence of an ac dipole need a more involved approach. First the forced motion normal form coordinate is defined as

$$\zeta_z^{\pm} = \sqrt{2I_z}e^{\mp i(\psi_z+\psi_{z,0})} + \sqrt{2A_{\mathrm{d},z}}e^{\mp i(\mu_{\mathrm{d},z}\tau+\chi_{\mathrm{d},z})}\,, \tag{7.22}$$

where $\mu_{\mathrm{d},z}$ is the ac dipole phase advance after one turn, $\chi_{\mathrm{d},z}$ is the ac dipole initial phase, τ is the turn like variable, $A_{\mathrm{d},z}$ is the action of the ac dipole driven motion [54], and the second mode of the ac dipole is neglected. The forced motion can now be derived using the generating function for the forced motion (F_{d}) as defined in [49],

$$F_{\mathrm{d}} \;=\; \frac{1}{1-R_zR_\tau}h^* \tag{7.23}$$

where R_τ is the one-turn rotation operator acting on the variable τ as $R_\tau\tau = \tau + 1$. Starting with the Hamiltonian h^* of the generating function, the coefficients $c_n(J_z)$ of h^* are expanded in terms of the eigen functions of Eq. (7.15) as,

$$h^* \;=\; \sum_{n\neq 0}\sum_k \frac{c_k}{2^k}\zeta_{z,-}^{k+\frac{n}{2}}\zeta_{z,+}^{k-\frac{n}{2}}\,. \tag{7.24}$$

and the corresponding derivative of the expanded coefficients is given by,

$$\frac{\partial c_n(J_z)}{\partial J_z} \;=\; \sum_k k c_k J_z^{k-1} \tag{7.25}$$

Two properties of Poisson brackets are used. First the Poisson bracket of conjugate coordinates is given by,

$$[\zeta_{z,+}^{v}, \zeta_{z,-}] = -2iv\zeta_{z,+}^{v-1} \tag{7.26}$$

and secondly the rotation operator may be extracted from the Poisson bracket as in [49],

$$\left[\frac{1}{1-R_z R_\tau}h^*, \zeta_{z,-}\right] = \frac{1}{1-e^{-i\mu_z}R_z R_\tau}[h^*, \zeta_{z,-}] \,. \tag{7.27}$$

Using these properties and inserting the new Hamiltonian expansion into Eq. (7.17) the linearly normalized coordinate is given by,

$$\begin{aligned} \xi_{z,-} &= \zeta_{z,-} - 2i\frac{1}{1-e^{-i\mu_z}R_z R_\tau} \\ &\quad \times \sum_{n\neq 0}\sum_{k}\left(k-\frac{n}{2}\right)\frac{c_k}{2^k}\zeta_{z,-}^{k+\frac{n}{2}}\zeta_{z,+}^{k-\frac{n}{2}-1} \,. \end{aligned} \tag{7.28}$$

For the free motion where $R_\tau = 1$ and with the normal form coordinate as defined by Eq. (7.15), this reduces to the previous result of Eq. (7.19).

For the forced motion the new forced normal form coordinate of Eq. (7.22) are used. Making use of the assumption that $A_{\mathrm{d},z} \gg I_z$, and using the definition of Eq. (7.25) the forced turn-by-turn motion in normalized coordinate is found to be,

$$\begin{aligned} \xi_{z,-} &= \sqrt{2A_{\mathrm{d},z}}e^{i(\mu_{\mathrm{d},z}\tau+\chi_{\mathrm{d},z})} \\ &\quad + i\sum_{n\in 2\mathbb{Z},\, n\neq 0}\frac{g_n(A_{\mathrm{d},z})}{1-e^{i[-\mu_z+(n+1)\mu_{\mathrm{d},z}]}}e^{i(n+1)(\mu_{\mathrm{d},z}\tau+\chi_{\mathrm{d},z})} \,. \end{aligned} \tag{7.29}$$

where,

$$g_n(A_{\mathrm{d},z}) = \left(\frac{n}{\sqrt{2A_{\mathrm{d},z}}}c_n(A_{\mathrm{d},z}) - \sqrt{2A_{\mathrm{d},z}}\frac{\partial c_n(A_{\mathrm{d},z})}{\partial A_{\mathrm{d},z}}\right) . \tag{7.30}$$

This result is almost identical to the free motion case, expect for the new resonance condition is now defined as $-\mu_z + (n+1)\mu_{\mathrm{d},z} = 2\pi p$ for $p \in \mathbb{Z}$.

DERIVATIONS IN TWO DIMENSIONS

The previous derivations are extended to two dimensions for cases where both the horizontal and vertical planes are excited. The two dimensional beam-beam potential is now decomposed as,

$$h_{\mathrm{bb}}(J_x, J_y, \phi_x, \phi_y) = \sum_{m,n\in\mathbb{Z}} c_{mn}(J_x, J_y) e^{im\phi_x} e^{in\phi_y} \tag{7.31}$$

The steps described in Sec. 7.3 are applicable to the two dimensional case as well, from which the following horizontal coordinate is obtained for the free motion,

$$\begin{aligned} \xi_{x,-} &= \sqrt{2I_x} e^{i(\mu_x N + \psi_{z,0})} \\ &\quad + \sum_{\substack{m,n\in 2\mathbb{Z} \\ m,n\neq 0}} i \frac{g_{mn}(I_x, I_y)}{1 - e^{i[m\mu_x + n\mu_y]}} \\ &\quad \times e^{i[(m+1)(\mu_x N + \psi_{x,0}) + n(\mu_y N + \psi_{y,0})]} \end{aligned} \tag{7.32}$$

with,

$$g_{mn}(I_x, I_y) = \frac{n}{\sqrt{2I_x}} c_{mn}(I_x, I_y) - \sqrt{2I_x} \frac{\partial c_{mn}(I_x, I_y)}{\partial I_x} \tag{7.33}$$

and for the forced motion,

$$\begin{aligned} \xi_{x,-} &= \sqrt{2A_{\mathrm{d},x}} e^{i\mu_{\mathrm{d},x}\tau} \\ &\quad + \sum_{\substack{m,n\in 2\mathbb{Z} \\ m,n\neq 0}} i \frac{g_{mn}(A_{\mathrm{d},x}, A_{\mathrm{d},y})}{1 - e^{i[-\mu_x + (m+1)\mu_{\mathrm{d},x} + n\mu_{\mathrm{d},y}]}} \\ &\quad \times e^{i[(m+1)\mu_{\mathrm{d},x}\tau + n\mu_{\mathrm{d},y}\tau]} \end{aligned} \tag{7.34}$$

with,

$$g_{mn}(A_{\mathrm{d},x}, A_{\mathrm{d},y}) = \frac{n}{\sqrt{2A_{\mathrm{d},x}}} c_{mn}(A_{\mathrm{d},x}, A_{\mathrm{d},y}) - \sqrt{2A_{\mathrm{d},x}} \frac{\partial c_{mn}(A_{\mathrm{d},x}, A_{\mathrm{d},y})}{\partial A_{\mathrm{d},x}} \,. \tag{7.35}$$

The results are very similar to the single dimensional case, although the coefficients c_{mn} now come from the two dimensional decomposition of Eq. (7.31). Unfortunately there is no nice analytical form for the two dimensional coefficients as there is for the one-dimensional coefficients. However, the coefficients $c_{mn}(A_{\mathrm{d},x}, A_{\mathrm{d},y})$ can be evaluated numerically by numerically performing the integrals as,

$$c_{mn}(A_{\mathrm{d},x}, A_{\mathrm{d},y}) = \frac{1}{4\pi^2} \int_0^{2\pi}\int_0^{2\pi} e^{im\phi_x} e^{in\phi_y} \int_0^{r} f(r')dr'd\phi_x d\phi_y \tag{7.36}$$

where

$$r = \sqrt{2A_{\mathrm{d},x}\sin^2\phi_x + 2A_{\mathrm{d},y}\sin^2\phi_y} \tag{7.37}$$

A similar integral can be solved for the derivative of $c_{mn}(A_{\mathrm{d},x}, A_{\mathrm{d},y})$,

$$\frac{\partial c_{mn}(A_{\mathrm{d},x}, A_{\mathrm{d},y})}{\partial A_{\mathrm{d},x}} = \frac{1}{4\pi^2} \int_0^{2\pi}\int_0^{2\pi} e^{im\phi_x} e^{in\phi_y} \frac{\partial r}{\partial A_{\mathrm{d},x}} f(r) d\phi_x d\phi_y \tag{7.38}$$

Figure 7.4 shows the two-dimensional composition of coefficients $g_{mn}(A_{\mathrm{d},x}, A_{\mathrm{d},y})$ from Eq. (7.35), obtained by numerical integration for diagonal excitations with $A_{\mathrm{d},x} = A_{\mathrm{d},y}$. The coefficients are set over the r normalized by the design beam size at the interaction point.

7

COMPARING ANALYTICAL DERIVATIONS WITH SINGLE PARTICLE TRACKING SIMULATIONS

Simulations are done to compare the previously derived analytical expressions of the nonlinear motion for the case of free and forced oscillations. The simulations are done with the nominal LHC model at injection energy for the 2016 optics with nominal natural tunes $Q_x = 0.31$, $Q_y = 0.32$. All sextupoles are turned off to exclude second order contributions to secondary spectral lines for large amplitude excitations. The normalized beam emittances are used in the simulations

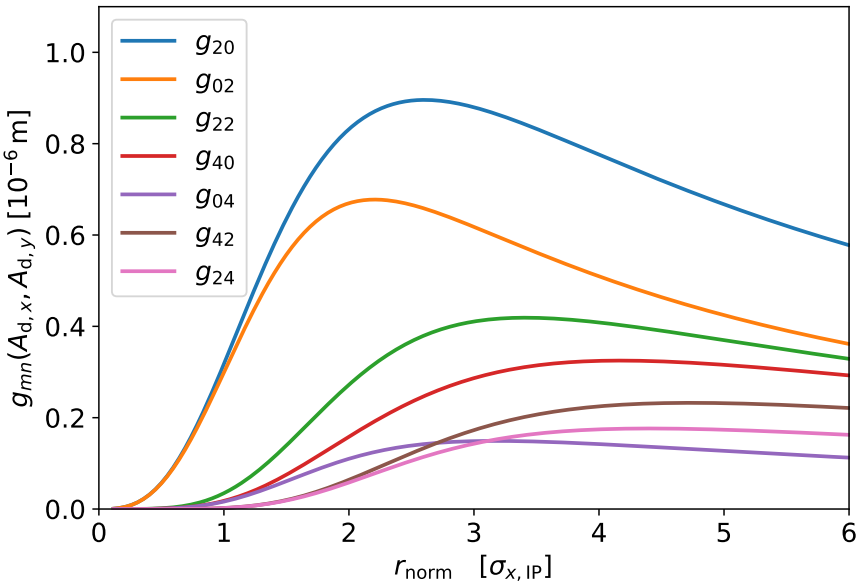

Figure 7.4: *The amplitude of coefficients g_{mn} in two dimensions as specified in Eq. (7.33) over diagonal excitation amplitudes with $A_{d,x} = A_{d,y}$ where $r_{norm} = r/\sqrt{\epsilon}$.*

$\epsilon_{x,nom} = \epsilon_{y,nom} = 1.0$ μm, and the beams are setup with $1.1 \cdot 10^{11}$ protons per bunch. The beam-beam interaction is modelled by installing five equally strong and equally spaced beam-beam elements at IP1 over a longitudinal distance of 0.10 m. Simulations with this approach accurately reproduce the linear beam-beam tune shift as calculated from theory [128, 129]. Tracking is done in MAD-X [72] for both free and forced excitations, and the SUSSIX code [89] is used to do all the spectral analyses. The spectral lines are labelled as $H(u, v)$ for lines in the horizontal spectra with frequency $u\mu_x + v\mu_y$, and $V(u, v)$ for the vertical spectra. For the forced motion, the line labels will refer to the frequency defined by the forced tunes $u\mu_{d,x} + v\mu_{d,y}$.

In the case of single kicks for free motion, a series of simulations is done with increasing initial horizontal displacement. The particle is tracked for 3000 turns, and the obtained turn-by-turn data is used to do the spectral analysis. The spectral content of the real turn-by-turn data will yield symmetric spectra around 0. In such a state there can be no distinction between spectral lines with opposite frequencies, such as for example for $H(3, 0)$ and $H(-3, 0)$. To distinguish between the two lines the complex signal $z - ip_y$ needs to be reconstructed from two BPMs at $\pi/2$ phase advance. This is done in the same way as in [1].

Figure 7.5 shows the secondary spectral line amplitude of H(3,0) along the ring.

The amplitude is observed to be mostly constant. Indeed a single source is expected to yield a resonance driving term with a constant amplitude that propagates with its corresponding phase. As the spectral line amplitude is constant the average of the amplitude over the whole accelerator is taken to characterize the secondary spectral line amplitude as a function of kick amplitudes and provide a measure of the resonance driving term amplitude.

The secondary spectral line amplitudes obtained from particle tracking simulations are compared to the theoretical predictions from Eq. (7.19) in Fig. 7.6. The lines $H(3,0)$ and $H(-3,0)$ correspond to the spectral lines of octupolar order, while the lines $H(5,0)$ and $H(-5,0)$ relate to dodecapolar spectral lines. A very good agreement is observed between the analytical predictions and the results from tracking simulations, with only small deviations observed for the peak line amplitudes of $H(\pm 3,0)$ between 1.5 σ_{nom} and 3.5 σ_{nom}. This is likely due to higher order contributions to the same spectral line from the normal form transformation of Eq. (7.17).

In the case of forced motion with ac dipoles the β-functions around the ring are perturbed [54]. To calculate the spectral line amplitudes from theory, the perturbed β at IP1 is obtained by modelling the ac dipole as a quadrupolar kick in the lattice [54]. This effective quadrupole is only used to obtain the β-functions and is not applied during tracking. Tracking simulations with the ac dipole are done with a particle initially at rest ($x = p_x = y = p_y = 0$). The ac dipole tunes are chosen at $\{Q_{\text{d},x}, Q_{\text{d},y}\} = \{0.268, 0.278\}$ such that both ac dipole tunes are below the full beam-beam footprint, in order to avoid to excite resonantly for the range of amplitudes. A ramp up time of 2000 turns is used, and the spectral analysis is done on 3000 turns of flattop ac dipole excitation data. The detuning of the natural tune with amplitude for forced oscillations is obtained as in [66] and is used in the resonance denominator of Eq.(7.29)

Figure 7.7 shows the spectral line amplitudes from Eq. (7.29) of single plane octupolar and dodecapolar order, and are compared to results from tracking simulations. In general, a good agreement is observed between the two, although a larger deviation is seen at peak values compared to the free motion case.

Simulations are done with simultaneous excitations in the horizontal and vertical planes to validate the derivations in two dimensions of Sec. 7.4. Figure 7.8 compares the octupolar spectral line amplitudes of $H(3,0)$, $H(-3,0)$, $H(-1,2)$ and $V(2,-1)$ obtained from the turn-by-turn data of single particle tracking simulations to the analytical predictions of Eq. (7.32). The coefficients of Eq. (7.32) are derived numerically using the excitation amplitudes from the tracking simulations. This ensures that any deviation from perfectly diagonal excitations in simulations

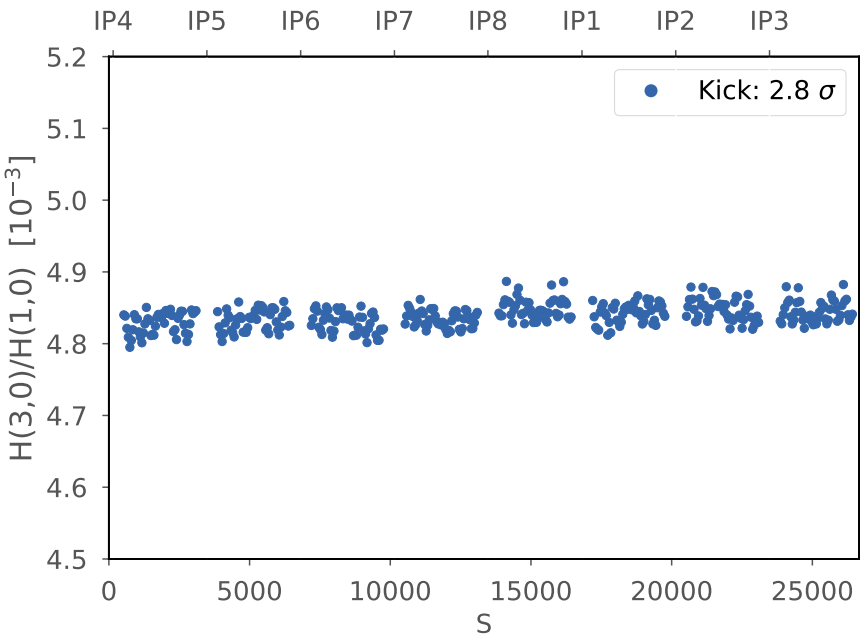

Figure 7.5: *Normalized amplitude of the secondary spectral line $H(3,0)$ along the circumference of the LHC in single particle simulations. For the case with a single head-on beam-beam interaction at IP1, with an opposite beam intensity of $1.1 \cdot 10^{11}$ and a round beams with $\epsilon = 1.0\,\mu\mathrm{m}$*

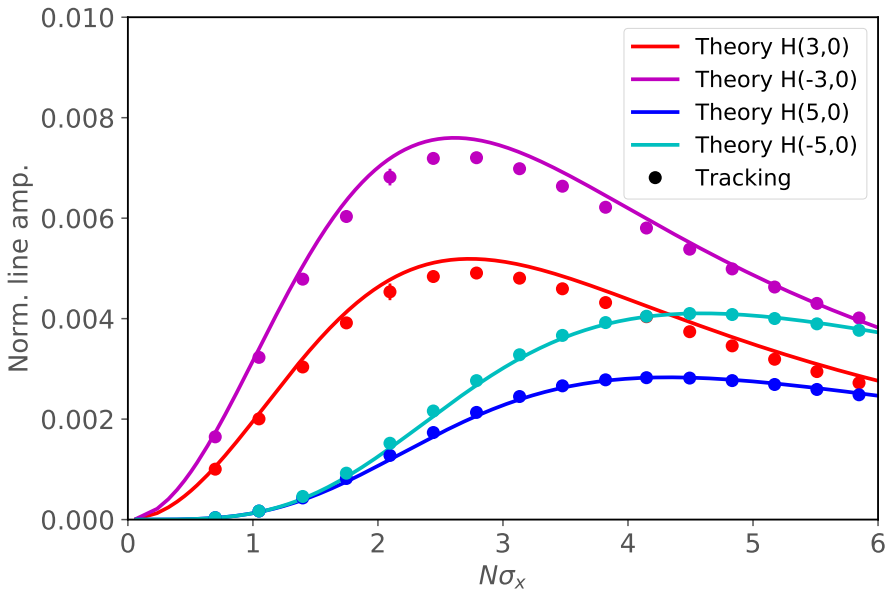

Figure 7.6: *Comparison of spectral line amplitudes between single particle tracking simulations with a single free kick and analytical derivations for the free motion of Eq. (7.19).*

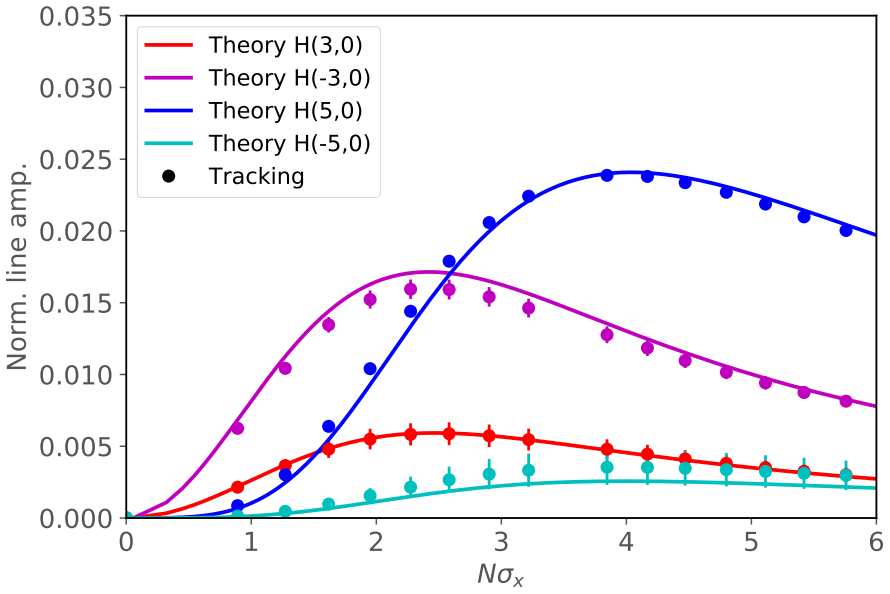

Figure 7.7: *Comparison of spectral line amplitudes between single particle tracking simulations using ac dipoles and analytical derivations for the forced motion of Eq.* (7.29).

is accounted for. The results for the single plane lines $H(3,0)$ and $H(-3,0)$ are well reproduced analytically. However, for the two dual plane spectral lines $H(-1,2)$ and $V(2,-1)$ a discrepancy is observed between analytical calculations and the results from tracking simulations. Firstly, while the two line amplitudes are expected to be the same for perfectly diagonal excitations, they differ significantly in the tracking simulations. This can partly be explained by the slight asymmetry in excitation amplitudes, as is seen in the theoretical predictions of Fig. 7.8. Furthermore, the change of optical functions with amplitude can perturb the two driving terms asymmetrically which can contribute to this discrepancy.

Again the forced motion is also tested in tracking simulations in the case of diagonal excitations. The comparison between Eq. (7.34) and is shown in Fig. 7.9. The maximal deviation between simulation and analytical calculations is of 7% for the $H(-1,2)$ line for large excitation amplitudes. Simulations are larger excitation amplitudes are omitted as the 8^{th} order resonance $\mu_x = -3\mu_{\text{d},x} + 4\mu_{\text{d},y}$ is crossed and spoils the simulations.

Simulations in two dimensions show a complication of the analysis of beam-beam generated driving terms. The amplitude of spectral lines become more sensitive to changes in optics parameters. Although the results for diagonal excitations are less accurately reproduced with theoretical calculations, the presented

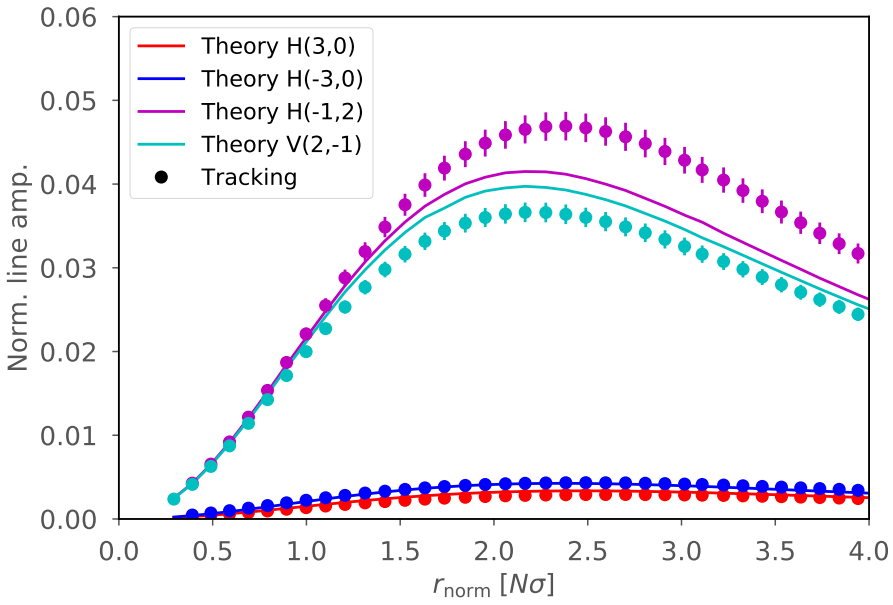

Figure 7.8: *Comparison of spectral line amplitudes between single particle tracking simulations with free single kicks and analytical derivations for the free motion in two dimensions of Eq.* (7.32).

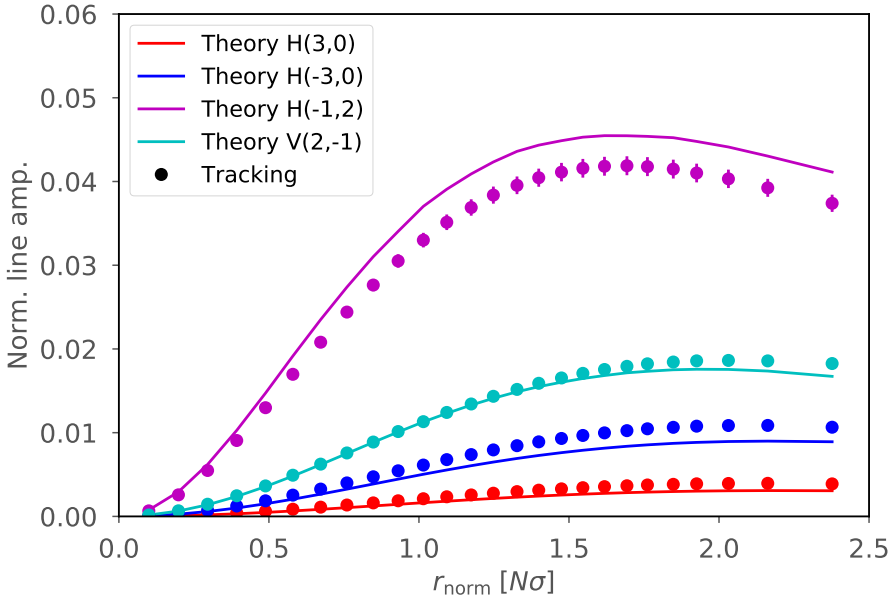

Figure 7.9: *Comparison of spectral line amplitudes between single particle tracking simulations using ac dipoles and analytical derivations for the forced motion in two dimensions of Eq.* (7.34).

analytical derivations still offer a clear cut path to measuring beam-beam generated driving terms by characterizing spectral line amplitude as a function of beam oscillation.

FIRST MEASUREMENTS OF BEAM-BEAM DRIVEN RESONANCE DRIVING TERMS

Measurements of beam-beam generated resonance driving terms are very challenging. One of the main issues faced when attempting to measure with colliding beams is how to obtain high quality turn-by-turn data. The beam-beam interaction generates very large amplitude detuning that results in extremely quickly decohering bunches when kicked with single kicks and thus a very limited usable number of turns for spectral analysis.

Secondly measuring the head-on beam-beam interaction of two colliding beams of comparable intensities is made even more challenging due to oscillation coupling between the two beams. The static beam will be excited by the kicked beam, and will in turn excite the kicked beam. As disentangling this beam coupling from the turn-by-turn data is very complicated, a simpler setup is explored to mitigate this in experiments in the LHC.

Measurements of head-on beam-beam driving terms in the LHC

The ac dipoles in the LHC combined with the flexibility of beam setup at injection offer a unique setup to measure beam-beam generated driving terms. Measurements were taken in 2016 to measure beam-beam generated resonance driving terms at injection energy in the LHC. A review of the setup is presented below, while a complete overview can be found in [130].

To mitigate the coupling between the two beams the weak-strong beam-beam interaction is examined. The weak beam is used for the excitation while the strong beam is kept at rest. Beam 2 is filled with two nominal bunches ($1.097 \pm 0.002 \cdot 10^{11}$ protons) with round beams with small emittances of 1.0 μm to function as the strong beam. The exact beam parameters are reported in [130]. It should be noted that the emittance measurements from the Beam Synchrotron Radiation Telescope (BSRT) [116] for such small beams are of poor quality [131]. Studies reported emittances that may be 20% larger than the BSRT measured emittances [130], and further deviations are not excluded.

Only a single bunch in Beam 2 is colliding, while the second bunch in Beam 2 is used for diagnostic purposes. Beam 2 is operated with Landau octupoles at

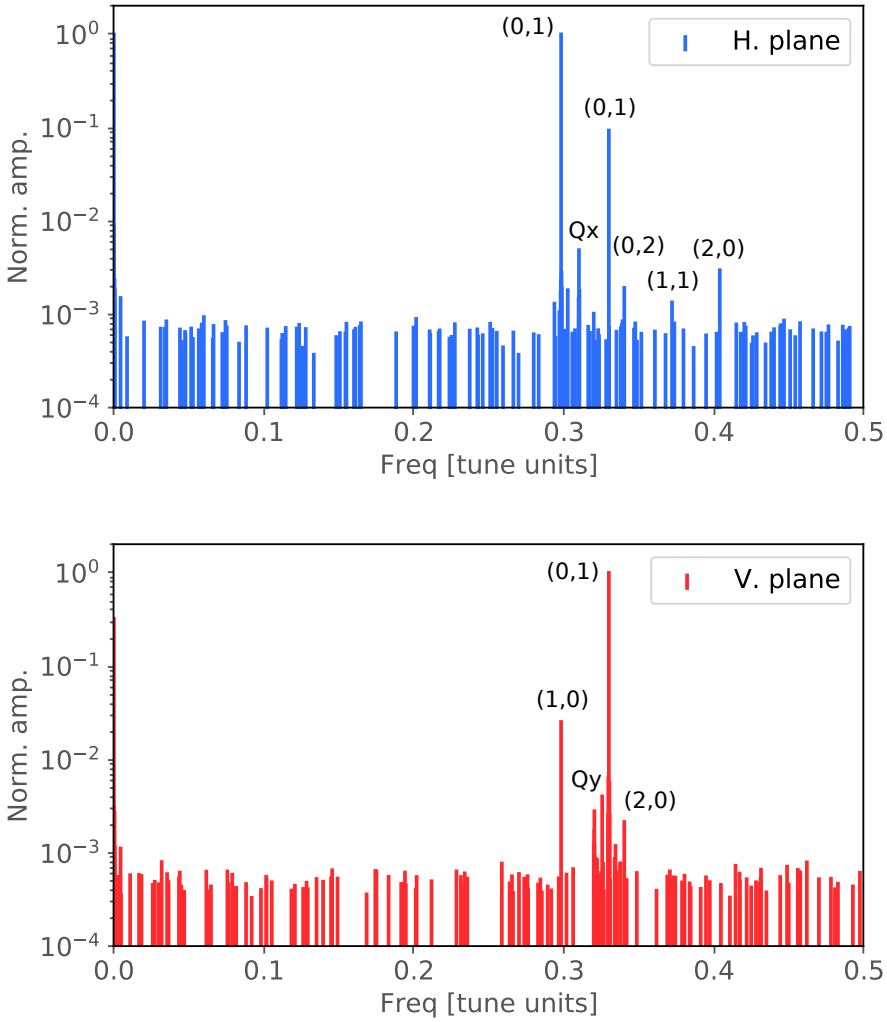

Figure 7.10: *Spectra from horizontal and vertical turn-by-turn position data at BPM.14L5.B1 for the horizontal plane (top) and BPM.15L5.B1 for the vertical plane (bottom) for non-colliding Beam 1. The main ac dipole tunes ($Q_{\mathrm{d},x}$ and $Q_{\mathrm{d},y}$) are the largest two spectral lines observed.*

nominal injection settings and the transverse damper turned on to mitigate any sort of coherent excitation of Beam 2. Beam 1 is filled with a single colliding pilot bunch with low intensity ($7.5 \cdot 10^9$ protons) as the weak beam.

Reference measurements are done with the ac dipole during setup to measure and correct the linear coupling. The working point for these measurements is $Q_x = 0.31$ and $Q_y = 0.32$ and the ac dipole tunes are chosen as $Q_{\mathrm{d},x} = 0.298$ and $Q_{\mathrm{d},y} = 0.33$. The coupling is corrected to values below $|C^-| < 10^{-3}$, where $|C^-|$ is defined by the integral notation of [87].

Figure 7.10 shows the horizontal and vertical spectra for non-colliding beams at

BPM.14L5.B1 and BPM.15L5.B1 respectively, both BPMs located at focussing arc quadrupoles of their respective planes for a kick amplitude of 2.1 σ_{B2}. The spectra reveal the main ac dipole tune lines as the largest lines $\{H(1,0),\ V(0,1)\}$, and several smaller spectral lines $\{H(0,2),\ H(1,1),\ H(2,0),\ V(2,0)\}$ corresponding to sextupolar sources, as well as the natural tunes $\{N_x,\ N_y\}$. These measurement do not indicate any visible source of b_4 or b_6 at this working point and amplitude.

Due to the combination of the low intensity of the pilot bunch in Beam 1, the low energy of both beams and the large β^* at the point of interaction, the generated luminosity is very low and collision optimization is thus practically impossible. The head-on collision of the two beams is assured by aligning collision with nominal bunches in both beams and then emptying Beam 1 before filling it with a single pilot bunch in the previously occupied slot. It is assumed in this approach that there is no significant orbit drift between dumping and re-injecting in Beam 1.

Different ac dipole tunes are used for the measurements with colliding beams, with $Q_{\mathrm{d},x} = 0.268$ and $Q_{\mathrm{d},y} = 0.278$. The ac dipole tunes have to be chosen beyond to beam-beam induced detuning, as to avoid resonantly exciting part of the beam. Figure 7.11 shows the expected footprint coming from the head-on beam-beam interaction as well as the ac dipole working point used during the experiments. One of the disadvantages of this working point is that as the excitation amplitude increases the tune footprint moves away from the ac dipole tunes, thus weakening the ac dipole. At injection energy in the LHC this does not pose severe limitations as the ac dipoles are powerful enough. However, this may become challenging at top-energy where ac dipole strengths are limited.

Measurements of resonance driving terms are done in Beam 1. The beam is excited with both the vertical and horizontal ac dipoles simultaneously. This results in diagonal kicks in action-space. Turn-by-turn position data is recorded at each BPM to be used for spectral analysis. Spectra from turn-by-turn data obtained with colliding beams are shown in Fig. 7.12. The spectra are obtained at the same BPMs as in Fig. 7.10 and the amplitudes have been normalized to the main tune line amplitude.

Secondary spectral lines corresponding to octupolar order sources from the beam-beam collision are now clearly visible in both planes, $\{H(1,2),\ H(3,0),\ H(-1,2)\}$ in the horizontal plane, and $\{V(0,-3),\ V(2,1),\ V(2,-1)\}$ in the vertical plane. Furthermore, the dodecapolar order line $V(-2,3)$ with frequency $-2Q_x + 3Q_y$ is observed. These measurements not only show the first ever measurement of beam-beam driving terms, but also the first ever observation of dodecapolar spectral lines in turn-by-turn data from synchrotrons.

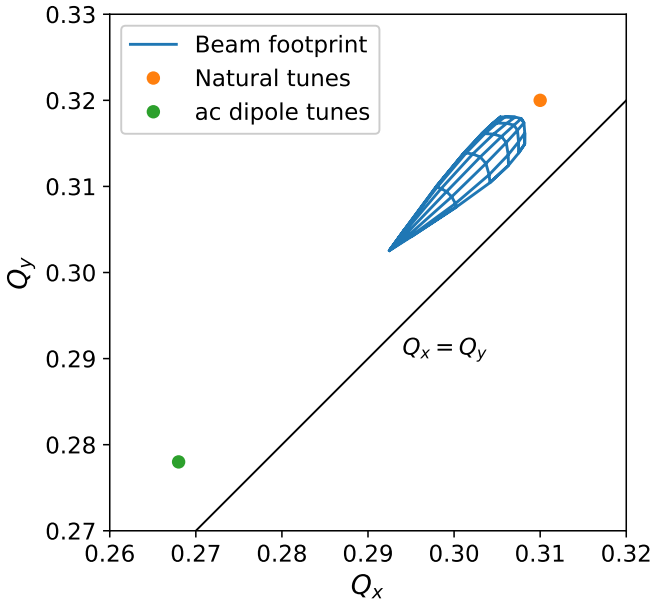

Figure 7.11: *Footprint of beam with measured beam-beam parameters. The ac dipole working point is indicated by the green point at* $Q_{\mathrm{d},x} = 0.268$ *and* $Q_{\mathrm{d},y} = 0.278$*, while the natural tunes are indicated by the orange point at* $Q_x = 0.31$ *and* $Q_y = 0.32$*.*

Figure 7.13 shows the measured normalized spectral line amplitude of $H(-1,2)$ over the circumference of the LHC. As there is only a single beam-beam interaction, at IP1, the line amplitude does not show significant changes as discussed in Sec. 7.5. These measurements can thus be presented in the same way as shown in Sec. 7.5 as the average spectral line amplitude over kick amplitude. Figure 7.14 shows the average octupolar order spectral line amplitude of $H(-1,2)$, $V(2,-1)$ and $V(0,-3)$ over the combined 2-dimensional action $\sqrt{A_x^2 + A_y^2}$ in units of σ_{B2}, where $\sigma_{B2} = 1.0\mu$m. Several measurements are done at the same kick amplitude. The measurement errors in the spectral line amplitude is obtained from the standard deviation of the measurements with the same kick amplitudes. Firstly a lack of quality data is observed for low amplitude kicks, where the errors are large. As the ac dipole excitation amplitude is increased the secondary spectral line amplitudes increase over the noise floor.

Due to the change of tunes between the reference measurement and the measurements with colliding beams, some spectral lines may be enhanced by this new working point and become visible. To assure the observed secondary spectral lines are not a result of this change of tunes, and validate the measurement of beam-beam generated driving terms, the noise floor of the non-colliding beams measurement is used to set a threshold on the maximum possible spectral amplitude from moving the tunes. The noise floor of the spectra for non-colliding beam is used as the

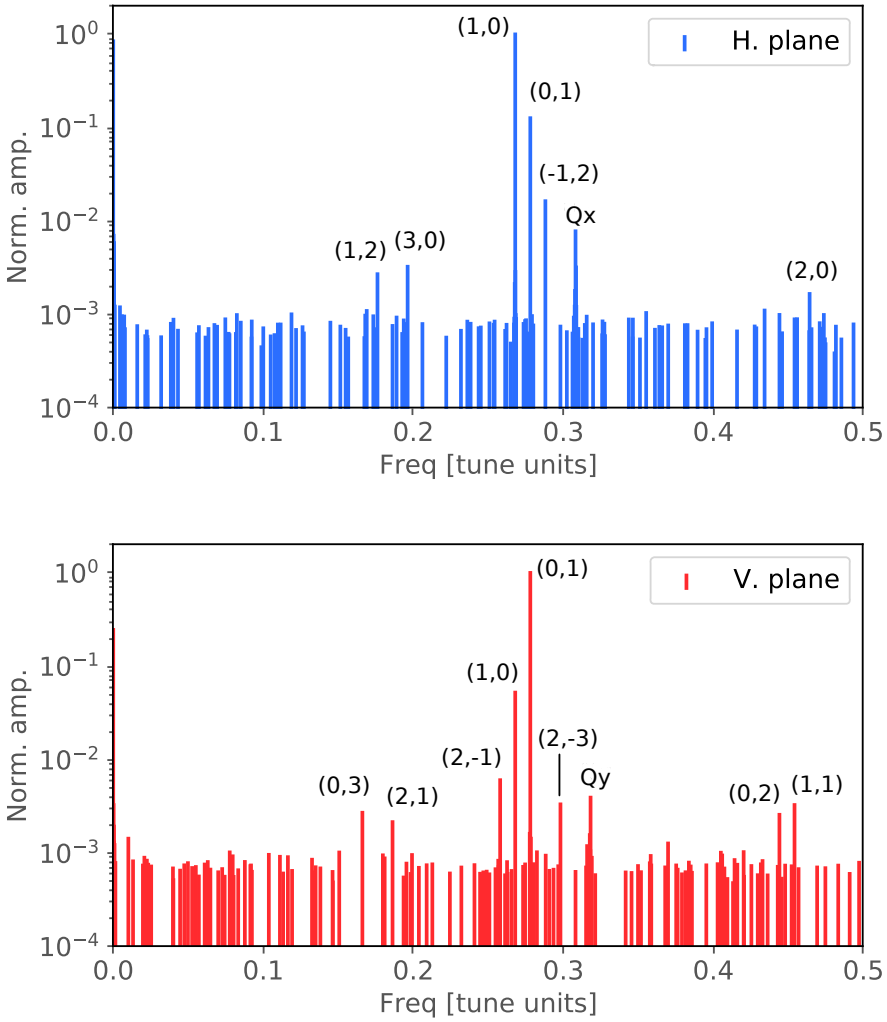

Figure 7.12: *Spectra from horizontal and vertical turn-by-turn position data at BPM.14L5.B1 for the horizontal plane (top) and BPM.15L5.B1 for the vertical plane (bottom) for Beam 1 with head-on collisions. The main ac dipole tunes ($Q_{\mathrm{d},x}$ and $Q_{\mathrm{d},y}$) are the largest two spectral lines observed.*

maximum line amplitude at those settings, and the effect of moving the tunes on this noise floor yields a threshold value for the new working point. This threshold is shown as a dashed line with corresponding color to the line measurements. The measured driving term amplitudes of $H(-1,2)$, $V(2,-1)$, and $V(0,3)$ surpass this threshold, thus indicating a clear first measurement of beam-beam driving terms.

The same is done for the dodecapolar spectral line and presented in Fig. 7.15. For large enough oscillation amplitudes ($> 1.3\sigma_{B2}$) the spectral line $V(-2,3)$ rises above the threshold value from the reference measurement. This serves as the first measurement of dodecapolar resonance driving terms in a synchrotron.

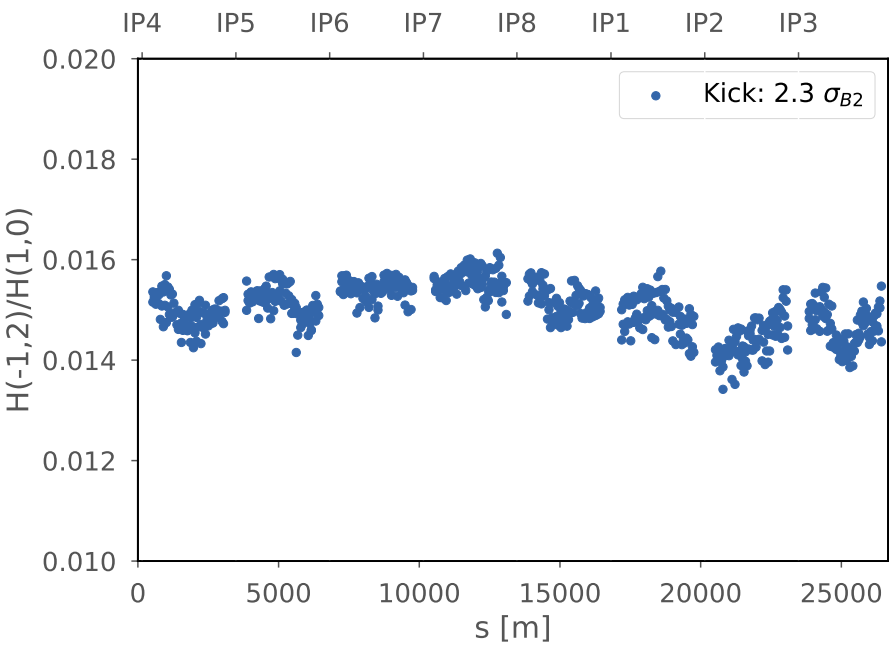

Figure 7.13: *Measured normalized spectral line amplitude of $H(-1,2)$ for the largest kicks with ac dipole, with kick size $r_{\text{norm}} = 2.3\sigma_{\text{B2}}$.*

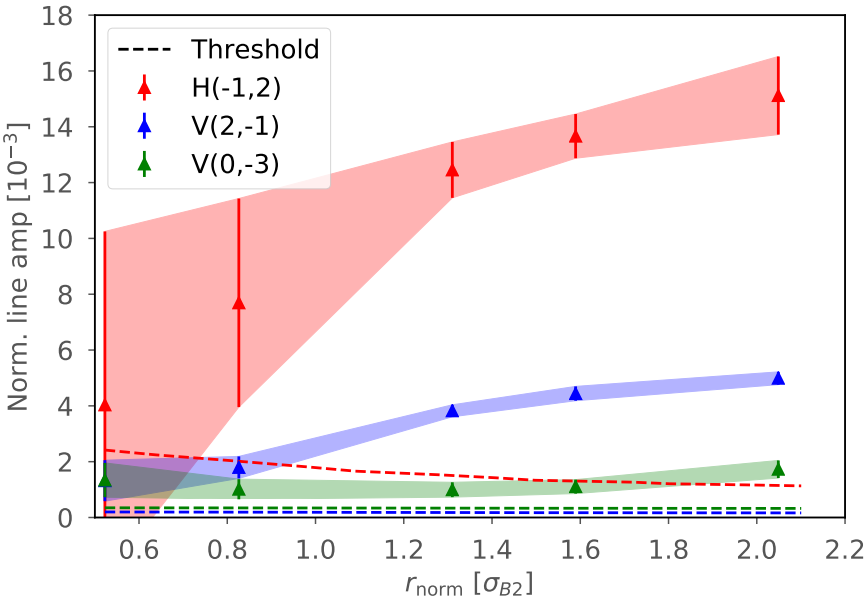

Figure 7.14: *Measurements of octupolar spectral lines generated by head-on beam-beam in the LHC. The noise threshold sets limit obtained from the reference measurement.*

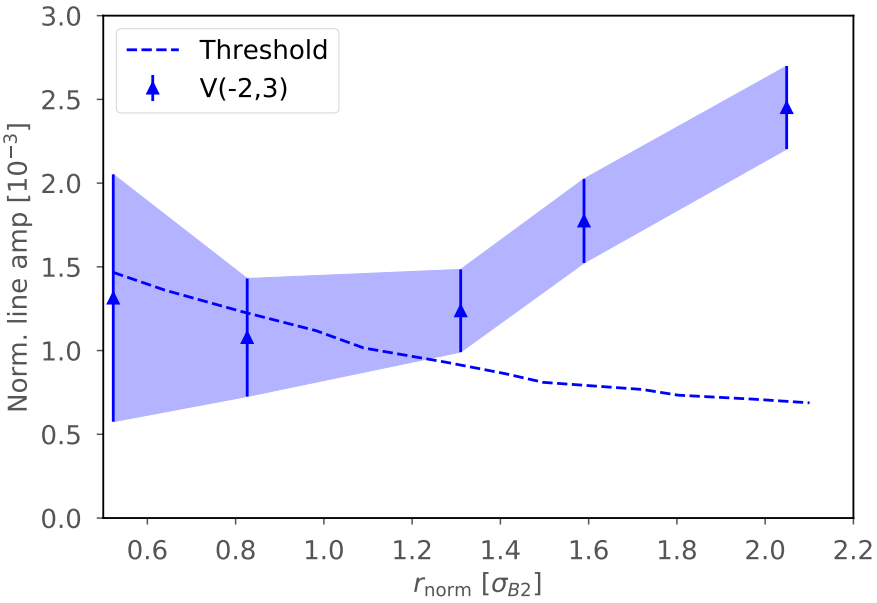

Figure 7.15: *Measurement of the dodecapolar spectral line V(-2,3) generated by head-on beam-beam in the LHC. The noise threshold sets limit obtained from the reference measurement.*

Comparison of measurements to multiparticle simulations

Multiparticle simulations are required to attempt to accurately reproduce the measurements. Due to the beam-beam induced footprint, the distance between the ac dipole tune and particle tune will depend significantly on the amplitude of the particles. The ac dipole will thus have a varying effect on all the particles inside the bunch, resulting in different excitation amplitudes. When considering a full bunch the response of a kick in the turn-by-turn data will reflect the centroid of charge and can thus deviate from the idealized particle at rest. In general, the simulations done in Sec. 7.5 with a single idealized particle at rest will overestimate the secondary spectral line amplitudes compared to the multiparticle systems of bunches.

Multiparticle tracking simulations with 20000 particles are done in MAD-X using the same model as detailed in Sec. 7.5. To start with the simulations are done with two sets of round beams, with emittances set to 1.0 μm and 1.2 μm. This encompasses the measured emittances, and the proposed 20% increase from beam based measurements [130]. The beam intensity of Beam 2 is set at $1.1 \cdot 10^{11}$ protons, as measured with the Beam Current Transformers (BCT) [113]. The simulations are done for a series of increasing flattop ac dipole amplitude. The simulated turn-by-

turn data is analysed in the same way as done for the measurements. Results of the multiparticle simulations are shown in Fig. 7.16. The simulations with round beams of $\epsilon = 1.0$ μm are shown in green, while the simulations with round beams of $\epsilon = 1.2$ μm are shown in blue. The simulated spectral line amplitude of $H(-1,2)$ for the $\epsilon = 1.0$ μm case agrees well with measurements. However, a weaker beam-beam effect is observed for the case with larger emittance of $\epsilon = 1.2$ μm. The opposite is true for the vertical octupolar spectral line amplitude $V(2,-1)$. Indeed, in this case the smaller emittance over estimates the beam-beam force, while the larger round beams reproduce the measurements.

Figure 7.17 shows the results of the same simulations for the dodecapolar spectral line $V(-2,3)$ compared to measurements. In this case the simulations with $\epsilon = 1.0\mu$m over-estimate the strength of the beam-beam interaction. A much better agreement is found with the larger beams with $\epsilon = 1.2\mu$m. Note that, as shown previously in Fig. 7.15, the low amplitude kicks are close to the noise floor and have very large errors, which explains the discrepancy between simulations and measurements. Furthermore, the rise in amplitude of the spectral line occurs for higher amplitudes than in the case of octupolar lines. This result is consistent with the simulations of Sec. 7.5.

The BSRT measured a larger horizontal emittance than the vertical emittance, pointing to possible elliptical beams. Multiparticle simulations are done with elliptical beams with emittances of $\epsilon_x = 1.2$ μm and $\epsilon_y = 1.0$ μm to explore the effect of non-round Gaussian beams on the measured driving terms. Figure 7.18 shows the results of the simulations compared to the measurements for the octupolar driving terms. The agreement between measurements and simulation is better than for the round beam case as both line amplitudes are well reproduced. For large amplitude kicks, however, the measurements and simulations start to deviate. In the case of the driving term generating $V(-2,3)$ a larger discrepancy is observed for elliptical beams, as is shown in Fig. 7.19. While the simulations better reproduce the measurements of octupolar order, they also point to possible other sources of uncertainty in the collision parameters.

Figure 7.17 presents the comparison between the dodecapolar spectral line amplitudes of $V(-2,3)$ obtained from the same multiparticle simulations to the the measurements. At low amplitudes a discrepancy between the simulations and measurements is observed, which is due to the poor measurement quality at low amplitudes. However, for higher excitation amplitudes the results from simulation and measurements converge to form a good agreement.

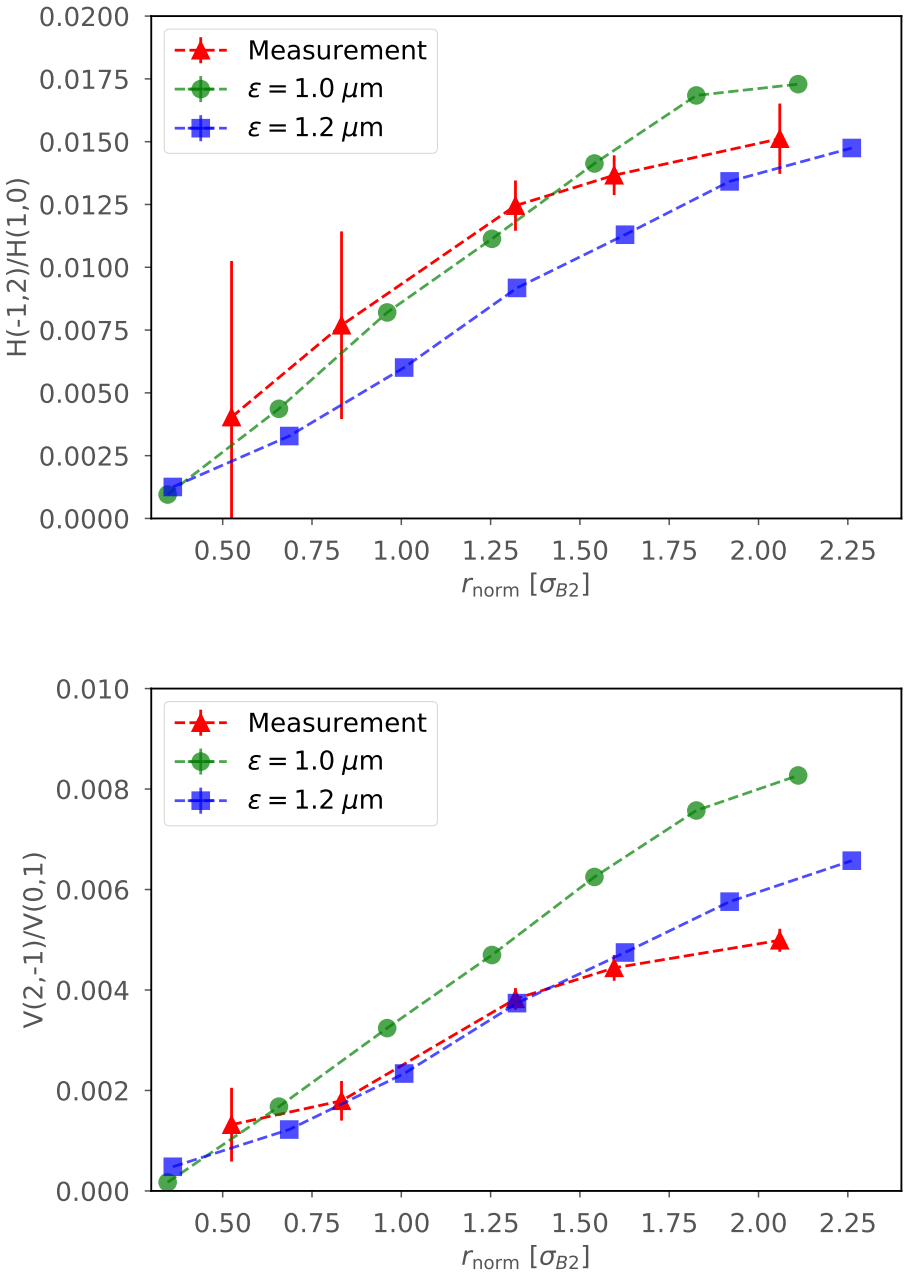

Figure 7.16: *Octupolar spectral line amplitudes of $H(-1,2)$ and $V(2,-1)$ as a function of oscillation amplitude for measurements and multiparticle simulations with emittances of $\epsilon = 1.0\mu$m (green) and $\epsilon = 1.0\mu$m (blue).*

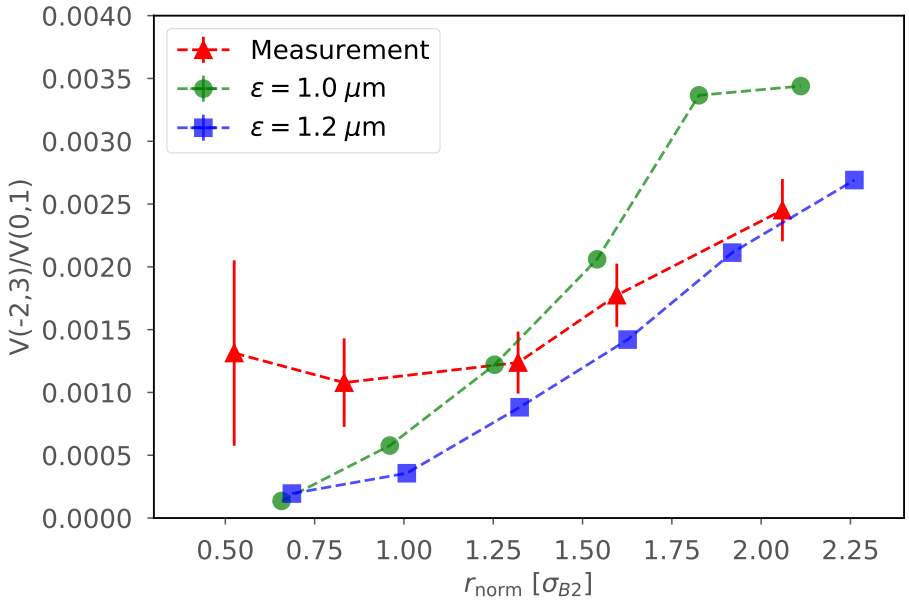

Figure 7.17: *Dodecapolar spectral line amplitudes of $V(-2,3)$ as a function of oscillation amplitude for measurements and multiparticle simulations with emittances of $\epsilon = 1.0\mu$m (green) and $\epsilon = 1.0\mu$m (blue).*

CONCLUSIONS

The effects of beam-beam interactions are starting to be studied in more detail, and various compensation methods have been proposed and tested in several machines. Studies of beam-beam effects often rely on indirect measurements or on measurements of global effects. Measurements of resonance driving terms generated by head-on beam-beam interactions offer a direct measurement of beam-beam nonlinearities in the accelerator, and of the interplay between various sources.

An analytical derivation is presented to characterize the secondary spectral line amplitudes of even orders coming from a single head-on beam-beam collision as a function of oscillation amplitude. The analytical approach is shown to be in good agreement with single particle tracking simulations for both free oscillations as well as forced oscillations with ac dipole excitations. These results offer a new method to study resonance driving terms from head-on beam-beam collisions, and pave the way for compensation studies with for example electron lenses.

The first direct measurements of resonance driving terms resulting from head-on collisions are done in the LHC. A setup with a weak-strong interaction between the two beams allows to excite the weak beam and use it for turn-by-turn diagnos-

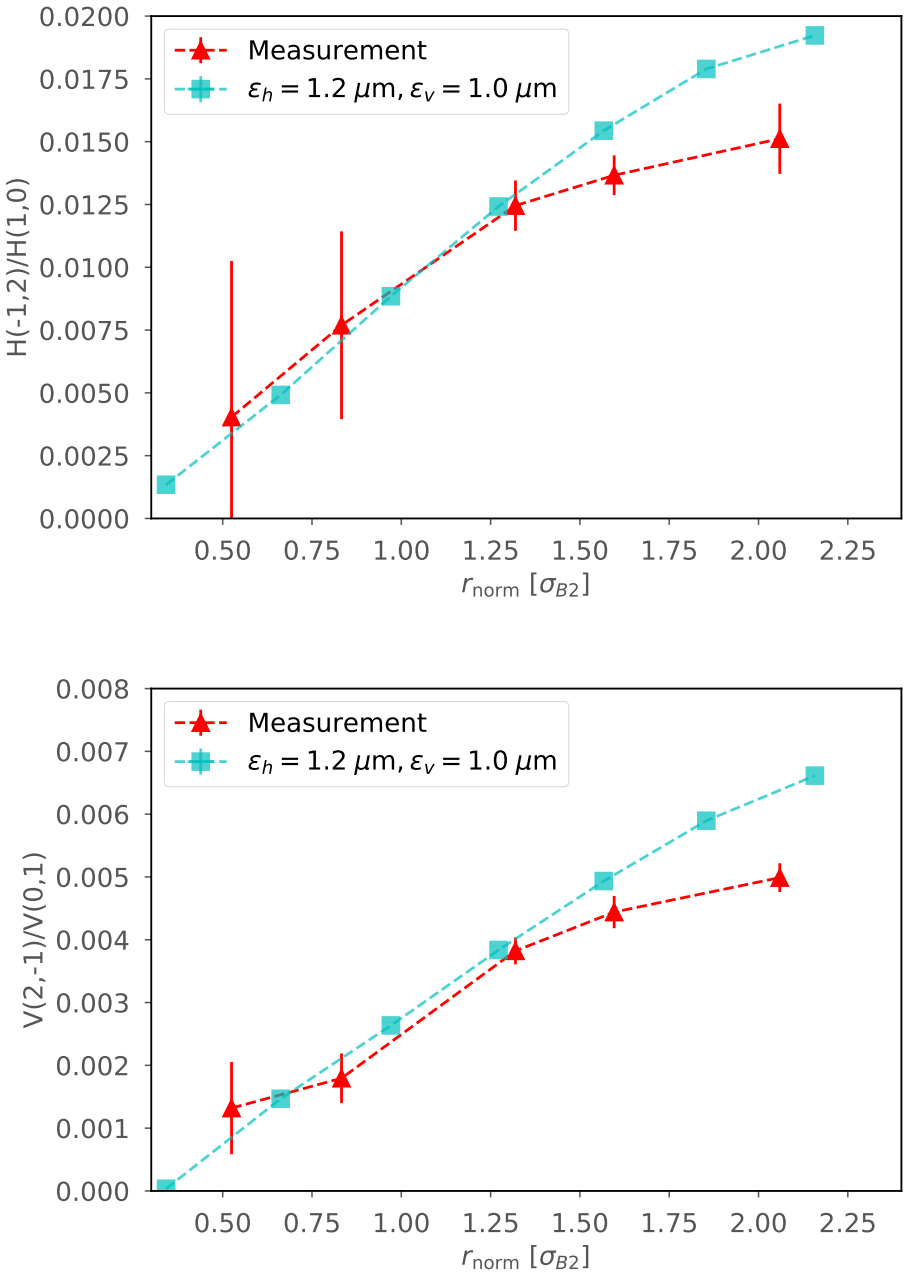

Figure 7.18: *Octupolar spectral line amplitudes of $H(-1,2)$ and $V(2,-1)$ as a function of oscillation amplitude for measurements and multiparticle simulations with elliptical beams with emittances of $\epsilon_h = 1.2\mu$m and $\epsilon_v = 1.0\mu$m.*

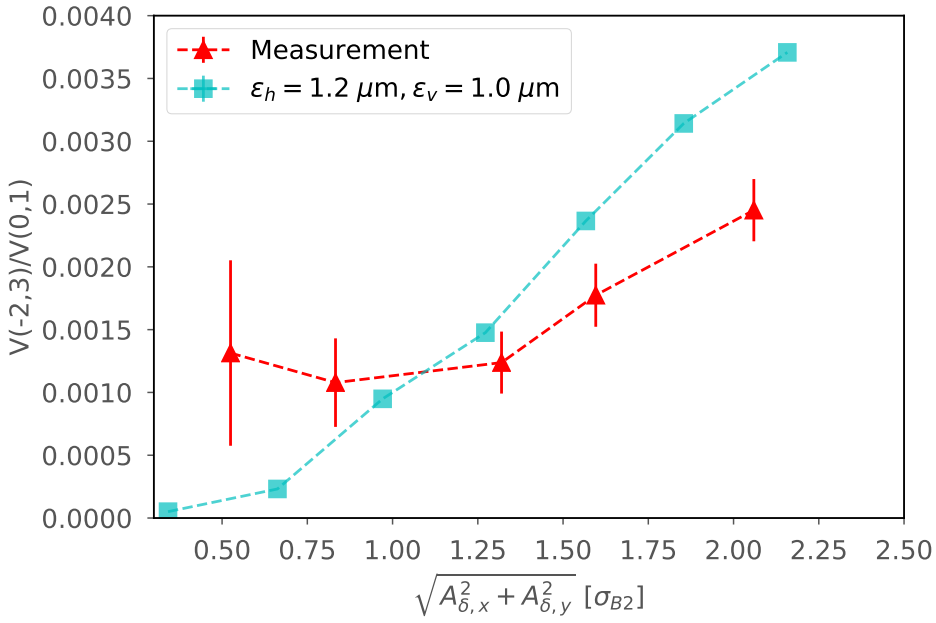

Figure 7.19: *Dodecapolar spectral line amplitudes of $V(-2,3)$ as a function of oscillation amplitude for measurements and multiparticle simulations with elliptical beams with emittances of $\epsilon_h = 1.2\mu$m and $\epsilon_v = 1.0\mu$m.*

tics. Measurements are done at injection energy and with the ac dipoles to obtain large enough coherent oscillation data. Analysis of measurements with diagonal ac dipole kicks show large octupolar and dodecapolar secondary spectral lines generated by the beam-beam collision. These measurements offer the first measurements of beam-beam generated resonance driving terms, as well as the first measurements of dodecapolar resonance driving terms in synchrotrons.

The ac dipoles are critical to measure beam-beam generated resonance driving terms in the LHC. Using the ac dipoles slightly complicates the analysis, but in return provide long coherent excitations allowing for spectral analysis.

Multiparticle simulations are done in MAD-X to validate the current injection models with beam-beam interactions. Simulations with round beams with emittances of 1.0 μm and 1.2 μm show some discrepancies in the octupolar spectral line amplitudes. A correction to the beam profile to $\epsilon_x = 1.2\ \mu$m and $\epsilon_y = 1.0\ \mu$m is necessary to better reproduce the measurements. This correction of emittance is in line previous analysis of the measurements.

To conclude, the presented results offer a new path for beam based measurement and correction of beam-beam nonlinearities.

ACKNOWLEDGEMENTS

The authors would like to thank the LHC Operations team, T. Pieloni, L. Medina, C. Tambasco, and P. Gonçalves Jorge for the support in the measurements performed in the LHC.

8

OUTLOOK

Nonlinear magnetic errors are a major limitation in the operation of the LHC and are predicted to have a critical impact on the High Luminosity LHC. The measurement and correction of these nonlinear sources of perturbation is crucial to envisage pushing the operational parameters of the LHC, and to achieve the design performance of the High Luminosity LHC. During Run II of the LHC, significant studies were performed to develop and test correction strategies for the nonlinear beam dynamics. Measurements of resonance driving terms were foreseen as an important correction strategy in the LHC, but had until now not yet demonstrated their full potential.

The aim of this thesis is to develop, test and validate the use of resonance driving terms measurements for the correction of nonlinear beam dynamics in the LHC using ac dipoles. The forced motion under ac dipole excitations is seen as one of the main diagnostic tool for the measurement and correction of nonlinear errors for Run III of the LHC, as well as for the High Luminosity LHC upgrade. The main promise of forced excitations is the possibility to measure specific resonance driving terms and allow for a direct order by order correction of specific driving terms.

This thesis has explored the theoretical parametrization of the nonlinear forced motion and studied it both in simulations and in experiments in the LHC. It provides an improved understanding of the nonlinear motion with ac dipoles, and presents the first experimental demonstration of specific correction strategies in the LHC.

To shortly summarize, a new parametrization of the nonlinear forced motion is presented in Chapter 4. The first direct correction of skew-octupolar errors using forced resonance driving terms measurements are achieved and presented in Chapter 5. Chapter 6 presents the first experimental demonstration of forced dynamic aperture measurements, while Chapter 6 presents the first measurements of forced dynamic aperture at top energy in the LHC. Finally the first measurement of beam-beam generated resonance driving terms is presented in Chapter 7. A discussion of the remaining challenges and proposed studies is presented for each chapter

below.

CHAPTER 4: FORCED RESONANCE DRIVING TERMS

It is shown in Chapter 4 that the analysis using the forced Courant-Snyder parameters greatly simplifies the description of resonance driving terms in forced motion. The amplitudes of resonance driving terms in the forced parameter space are constant between sources. This does not agree with the results of the normal form analysis of the forced motion, where amplitude beating would be expected. Chapter 4 derives a new parametrization of forced resonance driving terms that accurately reproduces the observations in simulations.

Furthermore, the results presented in Chapter 4 show a second order perturbation from the ac dipole. This perturbation manifests itself as a jump in both phase and amplitude of the resonance driving terms at the location of the ac dipole. It is the first time that such a second order contribution is considered for the nonlinear forced motion. The new proposed parametrization of resonance driving terms accurately reproduces this second order contribution as well. However, open questions still remain that should be addressed in future studies.

Firstly, future studies should try to clarify why the first normal form approach presented in this chapter fails to reproduce the obtained results from simulations. Certain conceptual inaccuracies may have been overlooked and new approaches may yield an even better understanding of the forced motion. One approach that conceptually differs from the presented studies, would be to apply the generating function obtained from the normal form transformation to the normalized coordinate in free parameter space, before transforming the result again to the forced parameter space.

Furthermore, the second order contribution from the ac dipole should be studied in greater detail. The effect of the resonance driving terms amplitude and phase on the driving terms around the ring poses interesting challenges and raises the question of what the impact is on measurements and corrections. This is a new observation of perturbation of the driving terms and its implications may not yet be fully understood.

CHAPTER 5: MEASUREMENT AND CORRECTION OF RESONANCE DRIVING TERMS IN THE LARGE HADRON COLLIDER

Measurements of forced resonance driving terms under forced motion with ac dipoles are seen as a promising correction strategy for machine nonlinearities for the LHC and High Luminosity LHC. Chapter 5 presents the measurements of resonance driving terms and the accompanying experimental developments performed in Run II of the LHC. A first measurement of decapolar resonance driving terms is presented which motivates the use of resonance driving terms measurements for the correction of higher order nonlinear sources. Chapter 5 concludes with the highlight of the first direct skew octupolar correction using resonance driving terms measurements with ac dipoles. This successful correction opens up the field for the wider application of resonance driving terms measurements for the correction of nonlinear errors in Run III of the LHC and most importantly for the High Luminosity LHC where the correction of nonlinear errors is critical for operation. The results provide a milestone validation for using resonance driving terms measurements as a correction strategy in future colliders. Further improvements and studies should be foreseen for the wide application of this method.

The main challenge in measuring resonance driving terms is to increase the secondary spectral line content from the turn-by-turn data, and improve the signal-to-noise ratio. This is one of the main strengths of using ac dipoles as they provide clean coherent oscillations for a large number of turns. However, even with the current diagnostics tools and measurement strategies the observed secondary spectral lines are small compared to the main spectral lines.

The measurements can be improved in two ways. One improvement can come from longer ac dipole excitations. The ac dipole is currently limited to 6,600 turns of flattop excitation due to thermal constraints, while the BPM system can acquire 25,000 turns of data. Significant improvements in noise reduction can be obtained by upgrading the ac dipole electronics and increase the excitation period to 25,000 turns. Secondly, the excitation amplitude is directly proportional to the ac dipole strength. An increase of ac dipole strength over a wide bandwidth should improve measurements and allow measurements of driving terms over a wider range of tunes. These two improvements could be combined in the form of an ac dipole upgrade for the High Luminosity LHC.

The measurements of resonance driving terms in the LHC currently do not reproduce the detailed structure of amplitude jumps observed in simulations. This can possibly arise from the loss of information in the cleaning process when the

secondary spectral lines are small. Future studies should clarify this loss of structure in the driving terms around the ring and, if needed, an improved cleaning approach should be used. A reduction of the noise floor as discussed previously can further improve these observations.

The studies presented in Chapter 5 discuss the measurements of driving terms on an order-by-order basis. However, both lower order and higher order multipoles can affect the measurements of specific driving terms. Measurements of resonance driving terms can be perturbed by higher order resonance driving terms driving the same spectral line, i.e. f_{4000} and f_{5100} both driving the $H(-3,0)$ line, and may be further perturbed by second order contributions from sources of different multipolar order. Further perturbations can arise from feed-down from higher order sources as presented in Chapter 5. Measurements of $f_{1210,H}$ at flat-orbit and at crossing angles of 145 μrad in the IR1 and IR5 show a significant source of feed-down to the skew octupolar resonance driving term. The effect of such perturbations on measurements of resonance driving terms should be understood in more detail to improve the models and corrections.

Lastly, the effect of the second order cross-term from the ac dipole on measurements should be studied. Deviations between machine and model can introduce discrepancies between simulated second order contribution and the actual second order contribution in the machine. This discrepancy can impact the calculation of the resonance driving terms responses and thus have an impact on the quality of corrections of driving terms.

Chapter 6: First experimental demonstration of forced dynamic aperture measurements with LHC ac dipoles

The forced dynamic aperture is proposed as a new observable in Chapter 6 for the study of nonlinear beam dynamics. A first measurement of forced dynamic aperture at injection energy in the LHC shows that the method is sensitive to changes in the nonlinear content of the machine. These results show that the forced dynamic aperture can be used to probe machine nonlinearities and can be used as a complementary observable to validate nonlinear corrections. Measurements of forced dynamic aperture can further be used to provide a qualitative lower bound estimate on the free dynamic aperture.

Measurements performed in the LHC at top energy show a sensitivity to magnetic changes of the Landau octupoles, as presented in Chapter 6. Forced dynamic aperture measurements have also been used to evaluate the effect of skew octupolar

corrections calculated with different methods. Furthermore, a good understanding of the forced dynamic aperture is important as it is the forced dynamic aperture and not the free dynamic aperture that is the limiting factor during optics measurements with ac dipoles.

As part of future studies, forced dynamic aperture simulations should be performed to find working points where the forced dynamic aperture is maximized. At such working points the excitation amplitudes are not limited by the forced dynamic aperture. Larger oscillation amplitudes can thus be reached that in turn improve the measurements of resonance driving terms.

A recurrent question from the journal referees for this publication was about the relationship between the free dynamic aperture and the forced dynamic aperture. Although the studies presented explicitly do not try to prove a relation between the two, it is a question that is of great interest. The free dynamic aperture is one of the most important design parameters for particle colliders, while being difficult to measure. A relation between the free and forced dynamic apertures is not guaranteed, but an exploration of such a relation may yield positive results that may permit fast estimates of free dynamic aperture in the future.

Chapter 7: First measurement of resonance driving terms from head-on beam-beam interaction in the LHC

An analytical derivation is presented to characterize the secondary spectral line amplitudes of even orders coming from a single head-on beam-beam collision as a function of oscillation amplitude. The analytical approach is shown to be in good agreement with single particle tracking simulations for both free oscillations as well as forced oscillations with ac dipole excitations. These results offer a new method to study resonance driving terms from head-on beam-beam collisions, and pave the way for compensation studies with, for example, electron lenses.

Chapter 7 presents a theoretical derivation for beam-beam generated resonance driving terms and offers a new measurement approach. Direct measurements of resonance driving terms resulting from head-on collisions are achieved for the first time in the LHC and presented in Chapter 7. The results offer a first validation of the method and a promising outlook on future studies of beam-beam resonance driving terms. Two studies are suggested to continue the research on beam-beam resonance driving terms measurements.

Measurements of beam-beam generated resonance driving terms should be repeated with less aggressive beam parameters. The colliding beam emittance should

be larger, such that accurate emittance measurements are possible. A larger emittance will furthermore decrease the beam-beam parameter. This has the effect of narrowing the tune distribution of the test beam, which can improve the measurement of the natural tune and thus improve the models to reproduce resonance driving terms measurements.

Future studies of the LHC can explore the compensation of specific resonance driving terms with dedicated octupolar or dodecapolar correctors. Another experiment of great interest is to study the compensation schemes using electron lenses. Such measurements can possibly be achieved in the Relativistic Heavy Ion Collider (RHIC), where both an electron lens and an ac dipole are present.

To conclude, the achievements presented in this thesis significantly improve the understanding of the nonlinear motion under the influence of ac dipoles on a theoretical basis, as well as in simulations and in experiments. This thesis offers the first experimental demonstration of specific nonlinear correction strategies using the ac dipoles at top energy. The validation of these methods now offer new strategies to improve the beam control, push for more challenging optics parameters, and achieve higher luminosities.

A

APPENDIX: FORCED NORMAL FORM IN FREE PARAMETER SPACE

The theoretical description of the ac dipole motion in synchrotrons was established in [53]. The general solution for the particle motion at any longitudinal location s in the ring is given in Courant-Snyder variables as a function of turn T,

$$\begin{aligned} \hat{z}(T) - i\hat{p}_z(T) &= \sqrt{2J_z}e^{i(2\pi Q_z T + \phi_{z0})} \\ &\quad + e^{-i\phi_{\mathrm{acd},z}}\left(\delta_{z,-}e^{i2\pi Q_{\mathrm{d},z}T} - \delta_{z,+}e^{-i2\pi Q_{\mathrm{d},z}T}\right) \quad , \end{aligned} \tag{A.1}$$

where $z \in \{x, y\}$ denotes the plane of motion, $Q_{\mathrm{d},z}$ is the ac dipole tune, Q_z is the natural tune, ϕ_{z0} is the initial phase, $\phi_{\mathrm{acd},z}$ is the phase advance between location s and the ac dipole, J_z is the linear invariant of the free motion and $\delta_{z,-}$ and $\delta_{z,+}$ are the complex ac dipole strengths defined as

$$\delta_{z,\pm} = \sqrt{\beta_{\mathrm{acd}}}\frac{BL}{B_0\rho}\frac{e^{\pm i(\pi Q_{z,\pm} - \psi_0)}}{4\sin(\pi Q_{z,\pm})} \quad , \tag{A.2}$$

where $Q_{z,\pm} = Q_{\mathrm{d},z} \pm Q_z$, β_{acd} is the β-function at the location of the ac dipole, BL is the field strength of the ac dipole, $B_0\rho$ is the rigidity, and ψ_0 is the initial phase of the ac dipole. ac dipoles tunes are typically set close to the natural tune to enhance the $Q_{\mathrm{d},z} \approx Q_z$ resonance and thus enlarge the $\delta_{z,-}$ mode. The ratio of amplitudes between $\delta_{z,+}$ and $\delta_{z,-}$ is given by,

$$\lambda_z = \frac{\delta_{z,+}}{\delta_{z,-}} \quad . \tag{A.3}$$

The normal form formalism for ac dipole motion was first derived in [49]. A first derivation of specific resonance driving terms was done for single plane motion and under the assumption that $|\delta_{z,-}| \gg |\delta_{z,+}|$ and $|\delta_{z,-}| \gg 2I_{z,+}$. This approach is extended to include the dual plane resonance driving terms as well as the contri-

bution from the second ac dipole mode, $\delta_{z,+}$. The treatment is done straight away for any location in the accelerator. The normal form coordinates under forced oscillation of ac dipoles are given at locations before the ac dipole by,

$$\begin{aligned}\zeta_{<z,\pm} &= \sqrt{2I_z}e^{\mp i(\psi_z+\psi_{z,0})} + |\delta_{z,-}|e^{\mp i(2\pi Q_{\mathrm{d},z}\tau-\eta_{z-})} \\ &\quad -|\delta_{z,+}|e^{\pm i(2\pi Q_{\mathrm{d},z}\tau+\eta_{z+})} \quad ,\end{aligned} \tag{A.4}$$

and after the ac dipole by,

$$\begin{aligned}\zeta_{>z,\pm} &= \sqrt{2I_z}e^{\mp i(\psi_z+\psi_{z,0})} + |\delta_{z,-}|e^{\mp i[2\pi(Q_{\mathrm{d},z}\tau+Q_-)-\eta_{z-}]} \\ &\quad -|\delta_{z,+}|e^{\pm i[2\pi(Q_{\mathrm{d},z}\tau+Q_+)+\eta_{z+}]} \quad ,\end{aligned} \tag{A.5}$$

where $\delta_{z,\pm}$ are split into their phase $e^{i\eta_{z\pm}}$ and amplitude $|\delta_{z,\pm}|$ terms, I_z is the new action invariant, ψ_z is the new phase variable and τ is the the time-like variable as defined in [49].

The linear normalised coordinates $\boldsymbol{\xi}$ are retrieved to first order by,

$$\boldsymbol{\xi} \approx \boldsymbol{\zeta} + [F_r, \boldsymbol{\zeta}] \quad , \tag{A.6}$$

where $\boldsymbol{\xi}$ are the linear normalised coordinates $(\xi_{x,+}, \xi_{x,-}, \xi_{y,+}, \xi_{y,-})$, $\boldsymbol{\zeta}$ are the normal form coordinates $(\zeta_{x,+}, \zeta_{x,-}, \zeta_{y,+}, \zeta_{y,-})$, and F_r is the generating function to transform to normal form defined as [49]. The variable $\xi_{x,-}$ is then derived at the location of the ac dipole as,

$$\begin{aligned}\xi_{x,-} &= \zeta_{x,-} - 2i\sum_{jklm} j\frac{1}{1-e^{-i2\pi Q_x}R_{x,y}R_\tau} \\ &\quad \times(h_{<,jklm}\,\zeta_{<x,+}^{j-1}\zeta_{<x,-}^{k}\zeta_{<y,+}^{l}\zeta_{<y,-}^{m} \\ &\quad +h_{>,jklm}\,\zeta_{>x,+}^{j-1}\zeta_{>x,-}^{k}\zeta_{>y,+}^{l}\zeta_{>y,-}^{m}) \quad ,\end{aligned} \tag{A.7}$$

where $h_{<,jklm}$ are the Hamiltonian terms before the ac dipole ($\phi_w - \phi_s < \phi_{\mathrm{acd}} - \phi_s$) and $h_{>,jklm}$ are the Hamiltonian terms after the ac dipole ($\phi_w - \phi_s > \phi_{\mathrm{acd}} - \phi_s$).

To obtain the full description of the nonlinear turn-by-turn motion, the coordi-

nates $\zeta_{>/<,z,\pm}$ have to be replaced by the content of Eqs. (A.4) and (A.5). This then yields the nonlinear turn-by-turn motion as a function of its eigenvectors. Though the normal form approach simplifies the derivation of the nonlinear motion, expanding the product of the normal form coordinates in Eq. (A.7) still gives considerable complexity to the problem. This can be simplified by observing that $|\delta_{z,-}| \gg \sqrt{2I_z}$ and $|\delta_{z,+}| \gg \sqrt{2I_z}$. Using the binomial theorem the expansion of powers of a single normal form coordinate can be derived to any order n,

$$\begin{aligned}\zeta_{z,\pm}^{n} &= \sum_{u=0}^{n} \binom{n}{u} (|\delta_{z,-}| e^{\mp i(2\pi Q_{\mathrm{d},z}\tau - \eta'_{z-})})^{n-u} \\ &\quad \times (-|\delta_{x,+}| e^{\pm i(2\pi Q_{\mathrm{d},z}\tau + \eta'_{z+})})^{u} \quad . \end{aligned} \tag{A.8}$$

Applying this to all coordinates of Eq. (A.7), using (A.3) and with some refactoring the variable $\xi_{x,-}$ can now be expressed as,

$$\begin{aligned}\xi_{x,-} &= |\delta_{x,-}| e^{\mp i(2\pi Q_{\mathrm{d},x}\tau - \eta_{x-})} - |\delta_{x,+}| e^{\pm i(2\pi Q_{\mathrm{d},x}\tau + \eta_{x+})} \\ &\quad - \sum_{jklm} 2ij\, h'_{jklm,\mathrm{H}} \sum_{a=0}^{j-1} \sum_{b=0}^{k} \sum_{c=0}^{l} \sum_{d=0}^{m} \binom{j-1}{a} \binom{k}{b} \binom{l}{c} \binom{m}{d} \\ &\quad \times (-1)^{a+b+c+d} |\delta_{x,-}|^{j-1+k} |\delta_{y,-}|^{l+m} \lambda_x^{a+b} \lambda_y^{c+d} \\ &\quad \times \frac{e^{i2\pi\{[k-j+1+2(a-b)]Q_{\mathrm{d},x}\tau + [m-l+2(c-d)]Q_{\mathrm{d},y}\tau\}}}{1 - e^{i2\pi(-Q_x + [k-j+1+2(a-b)]Q_{\mathrm{d},x} + [m-l+2(c-d)]Q_{\mathrm{d},y})}} \\ &\quad \times e^{i\{[k-j+1+2(a-b)]\eta_{x,-} + [m-l+2(c-d)]\eta_{y,-}\}} \quad . \end{aligned} \tag{A.9}$$

The equivalent in the vertical variable $\xi_{y,-}$ is given by,

$$
\begin{aligned}
\xi_{y,-} \;=\;& |\delta_{y,-}| e^{\mp i(2\pi Q_{\mathrm{d},y}\tau - \eta_{y-})} - |\delta_{y,+}| e^{\pm i(2\pi Q_{\mathrm{d},y}\tau + \eta_{y+})} \\
& - \sum_{jklm} 2il\, h'_{jklm,\mathrm{V}} \sum_{a=0}^{j}\sum_{b=0}^{k}\sum_{c=0}^{l-1}\sum_{d=0}^{m} \binom{j}{a}\binom{k}{b}\binom{l-1}{c}\binom{m}{d} \\
& \times (-1)^{a+b+c+d} |\delta_{x,-}|^{j+k} |\delta_{y,-}|^{l-1+m} \lambda_x^{a+b} \lambda_y^{c+d} \\
& \times \frac{e^{i2\pi\{[k-j+2(a-b)]Q_{\mathrm{d},x}\tau + [m-l+1+2(c-d)]Q_{\mathrm{d},y}\tau\}}}{1 - e^{i2\pi(-Q_y + [k-j+2(a-b)]Q_{\mathrm{d},x} + [m-l+1+2(c-d)]Q_{\mathrm{d},y})}} \\
& \times e^{i\{[k-j+2(a-b)]\eta_{x,-} + [m-l+1+2(c-d)]\eta_{y,-}\}} \quad , \qquad \text{(A.10)}
\end{aligned}
$$

where $h'_{jklm,\mathrm{H}}$ and $h'_{jklm,\mathrm{V}}$ are given by,

$$
\begin{aligned}
h'_{jklm,\mathrm{H}} &= h_{<,jklm} + h_{>,jklm} \quad e^{i2\pi[(k-j+1)Q_{x,-} + 2(b-a)Q_x + (m-l)Q_{y,-} + 2(d-c)Q_y]} \quad , \\
h'_{jklm,\mathrm{V}} &= h_{<,jklm} + h_{>,jklm} \quad e^{i2\pi[(k-j)Q_{x,-} + 2(b-a)Q_x + (m-l+1)Q_{y,-} + 2(d-c)Q_y]} \quad . \qquad \text{(A.11)}
\end{aligned}
$$

The terms on the first line of Eqs. (A.9) and (A.10) describe the linear motion of both modes of the ac dipole. The second part describes the nonlinear motion and gives a slightly complicated view of which frequencies are driven by which Hamiltonian terms. However a few things can be stated. First of all, a Hamiltonian term will drive different resonances in the horizontal and vertical planes with different orders in $\lambda_{\delta,x/y}$. This is displayed in Tab. A.1 for the Hamiltonian term h'_{1020} in the horizontal and vertical motion. Secondly, multiple Hamiltonian terms will contribute to the same spectral line, as illustrated in Tab. A.2.

In general, it becomes quite complicated to derive all the contributions to the various spectral line, especially when dual plane resonance driving terms are considered, as well as all orders of nonlinear sources. An analogue to the resonance driving terms of the free motion can be defined. To do this, only the contributions of the lowest order multipoles to a specific oscillation frequency are considered, i.e. contributions of decapoles to sextupolar frequencies are not taken into account. Secondly the resonance driving term is labelled according to the dominant Hamiltonian term, that is, the Hamiltonian term that contributes to the specified frequency

Table A.1: *Table showing the different spectral lines generated in the horizontal and vertical spectra from the Hamiltonian term h_{1020} , including the different orders in λ_z with which the spectral modes are excited.*

Spectral line	jklm	abcd	$\lambda_{\delta,x/y}$
H(0,-2)	1020	0000	1
H(0,0)	1020	0010	λ_y
H(0,2)	1020	0020	λ_y^2
V(-1,-1)	1020	0000	1
V(1,-1)	1020	1000	λ_x
V(-1,1)	1020	0010	λ_y
V(1,1)	1020	1000	$\lambda_x\lambda_y$

Table A.2: *Table showing the different octupolar resonance driving terms that excite the horizontal octupolar spectral line H(-3,0), including the different orders in λ_z with which the spectral modes are excited.*

	jklm	abcd	$\lambda_{\delta,x/y}$
H(-3,0)	4000	0000	1
H(-3,0)	3100	0100	λ_x
H(-3,0)	2200	0200	λ_x^2
H(-3,0)	1300	0300	λ_x^3
H(-3,0)	0400	0400	λ_x^4

for which $a = b = c = d = 0$. The resonance driving term is then defined as the sum of all contributing Hamiltonian terms. This is illustrated here using $f'_{4000,\mathrm{H}}$. Using Tab. A.2 $f'_{4000,\mathrm{H}}$ can be defined as,

$$\begin{aligned} f'_{4000,\mathrm{H}} &= \frac{1}{1 - e^{2\pi i(-Q_x - 3Q_{\mathrm{d},x})}} \\ &\quad \times \left[4h'_{4000} - 3h'_{3100}\lambda_x + 2h'_{2200}\lambda_x^2 - h'_{1300}\lambda_x^3 \right]. \end{aligned} \tag{A.12}$$

Note that the last term in Tab. A.2 is not driving the line as the index j is zero. The resonance driving term contains the descriptor H/V that specifies the plane of motion. This is important as, unlike the case in free motion, the resonance driving term drives different resonances in the different planes.

SUMMARY

(OF: A NONLINEAR FUTURE)

It is with great pleasure that I take this opportunity to diverge from the beaten path and indulge in a little creative freedom in summarizing this thesis for the general public. A word of warning to the seasoned physicists is appropriate; some oversimplification may have taken place. Yet this will hopefully help to explain some of the key elements of this research, and at the very least, make it an enjoyable read. For fear of losing you, the reader, at the first page, a more thoughtful introduction is presented. I hope to convey a better sense of the context, challenges and methods on which this thesis is built before diving into the results of the presented research.

Before addressing the core of this thesis, it is worth discussing the setting. The research presented in this thesis was performed at the European Organisation for Nuclear Research, more commonly known as CERN. The main mission of CERN is to find experimental evidence for the physical laws that govern the universe at the most fundamental level. To date, the Standard Model of particle physics is the most accurate model describing the interactions of elementary particles and fundamental forces. It has been tested and validated extensively, and has been valuable at predicting a wide range of phenomena. However, there are still many open problems to which physicists have not found an explanation. *Why is matter more abundant than anti-matter? Can the gravitational force be unified with the other fundamental forces? What is that dark matter people talk about?* Or even more exotic, *what is dark energy?* All these topics describe physical phenomena and observations that lie beyond the Standard Model and require a new understanding of physics. It is exactly these sort of questions that CERN tries to address in its research programme.

To study physics at this level, CERN attempts to recreate the conditions of the early universe. The most successful way to approach these conditions is by colliding particles at very high velocities in what are called particle colliders. In particle colliders, particles are accelerated close to the speed of light and brought to collision with each other. By colliding protons together at large velocities, i.e. high energies, new particles are created by converting the energy of the protons into mass, as described by the famous equation, $E = mc^2$. The higher the energies of the protons, the more massive the created particles can be. By studying what par-

ticles are created and how these new particles behave and decay, researchers try to uncover the deeper physical laws. In fact, researchers are still trying to answer the age-old question; How are babies born? Although now at the smallest possible scale.

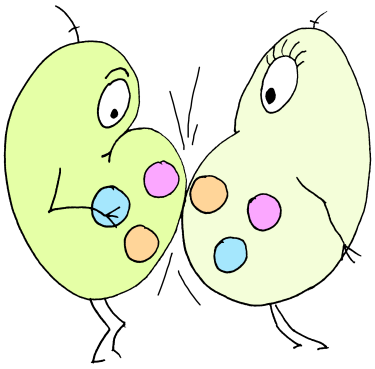

The world's largest and most powerful particle collider is the Large Hadron Collider, or LHC for short. The LHC is a circular collider with a circumference of 27 km and lies 100 m underground at CERN, near Geneva (Switzerland). It is the largest scientific facility to date. The LHC has the task of accelerating the protons and setting up the collisions. There are two accelerators in the collider. One accelerates protons in a clockwise direction, while the other accelerates protons in an anti-clockwise direction. The two beams intersect at four different locations in the collider where dedicated detectors look for the newly created particles. These detectors are ATLAS, CMS, LHCb, and ALICE.

The topic of this thesis however, is not about the result of the collisions or the detectors. It is strictly about the LHC and how the protons travel through this particle collider. The task of accelerating and colliding the protons is a whole challenge on its own.

The trajectory of the particles through the collider is fully determined by magnets. All the magnets will exert a force that is perpendicular to the direction that a particle is traveling in[1]. A multitude of magnets are used in the LHC to bend, twist, mold and kick the protons onto the designed trajectory. In total, the LHC contains about 9,600 magnets. These are generally named by the number of magnetic poles they contain. A dipole has two poles, a quadrupole has four poles, and so forth.

The dipoles are the toughest of all the magnets in the LHC, the bodybuilders under the magnets, and by far the most numerous in the LHC. They are tasked with the job to bend the trajectory of the particles into a ring. Secondly, there

1 For those who attended Dutch high school, the '*BIL*' rule might ring a bell, while others may recognise it as the Lorentz force.

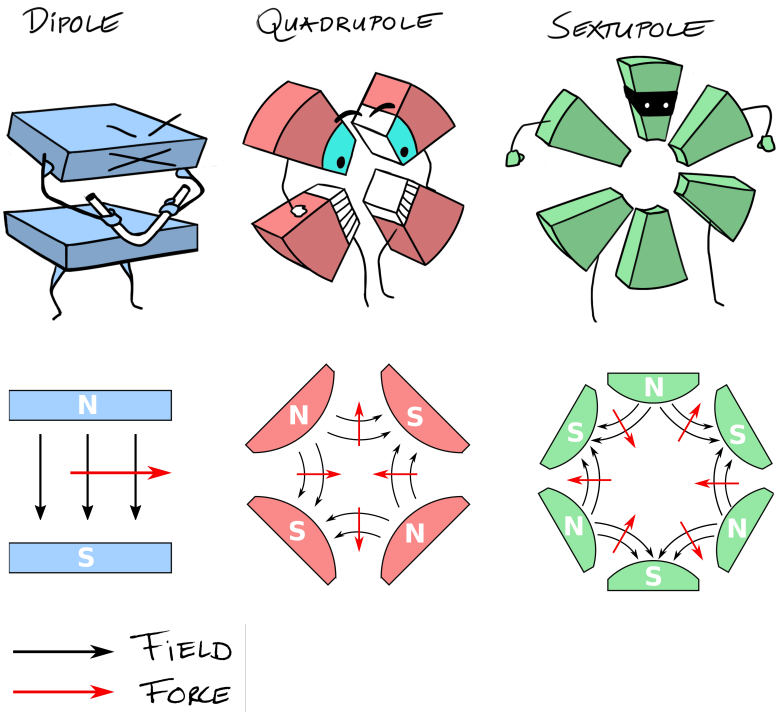

are quadrupoles that maintain the order in the LHC. Quadrupoles guarantee that bunches of particles stay grouped and focused on the job. Then there are also sextupoles. Sextupoles ensure that particles with energy deviations stay on the right track. There are also octupoles that can detune certain particles. If well controlled, they can be useful to tame some unstable particles. Lastly, there are higher order magnets with even more poles. From here on it does get messy. The naming of higher order magnets can become quite a mouthful. There are the decapoles with ten poles, dodecapoles with 12 poles. Rumour has it that someone once tried to use tetradecapole to describe a 14 pole magnetic field. Of all these magnets, the sextupoles, octupoles and higher order multipoles are called nonlinear magnets.

Although much is known about all these magnets, it is unavoidable that these magnet may have some character traits of other magnets. It is thus very possible that what is believed to be a perfect quadrupole, may in fact hold some unknown octupolar traits. These are called magnetic errors. In fact, all the magnets in the LHC can deviate slightly from their designed magnetic field. These errors can be the result of manufacturing processes, as well as misalignments or tilts of the magnets that occur during the installation phase. In some cases this is not so important, but in certain cases this has severe implications. Deviations in magnetic fields can severely distort the trajectories of the particles from the design trajectory. The particles in a beam can get lost, gradually or even all at once. Not only does this deteriorate the performance of the machine when particles are lost gradually, it can

also be damaging to the machine when all particles are lost at once.

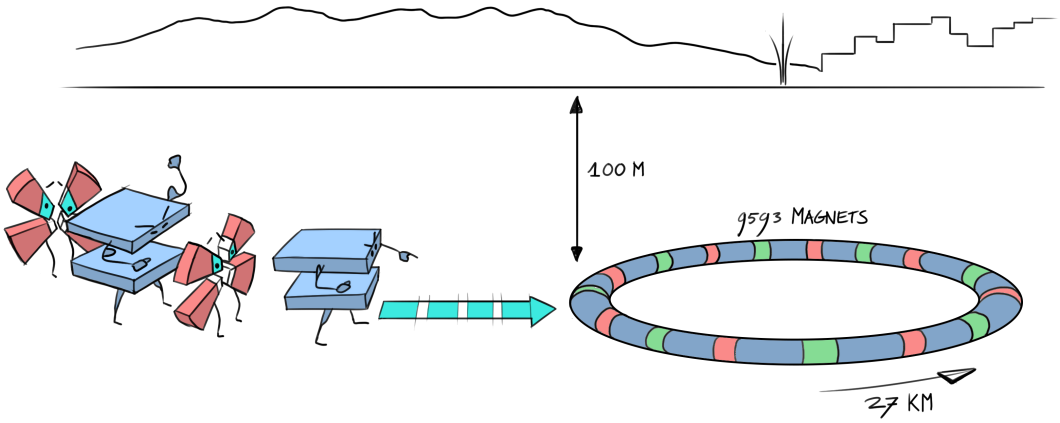

The magnets are aligned in a specific order and powered to very precise strengths to successfully guide the protons on a circular trajectory through the collider. Because the LHC is a circular machine, the protons will travel through the same machine over, and over and over. Scientists like to call this a periodic system, a system that repeats itself after a specific period, which in this case is a full turn. The series of alternating quadrupoles in the LHC will cause the protons to oscillate in the plane that is perpendicular to the direction in which they are travelling, which is referred to as the transverse plane.

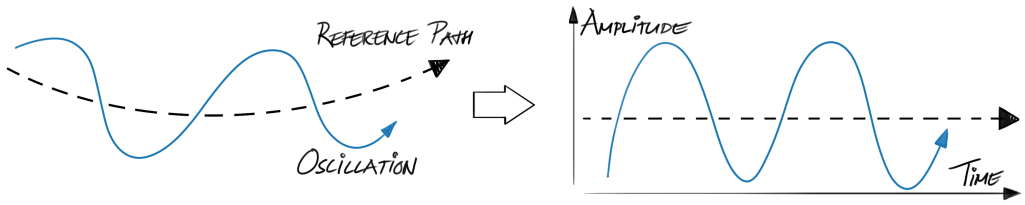

This thesis is purely focused on how the particles oscillate in this transverse plane, and the behaviour in the direction of travel is ignored. The oscillation is described with respect to the ideal particle on the reference orbit. In principle this oscillation is well behaved and controlled. However, when magnetic errors are present, it is possible that this oscillation is distorted and that the protons become unstable and get ejected from the LHC. This means that there will be less protons available for the collisions, and thus less statistical data for the experiments. Not to forget, if all the protons are lost at once it can severely damage the LHC. The energy stored in the proton beam is equivalent to the kinetic energy of a TGV (high speed train) at 150 km/h. One can easily imagine the damage that it could cause

the LHC if not well controlled. It is thus very important to understand these oscillations and understand how each magnet family and magnetic errors act on this oscillation. The aim of this thesis is to develop and validate methods with which these magnetic errors can be measured and with which corrections and compensation schemes can be found. In fact, the current performance of the LHC depends on these corrections of nonlinear errors, and the future machines such as the High Luminosity LHC or the Future Circular Collider (FCC) cannot operate without such corrections.

Since the interest lies only in this oscillation, a useful analogy is to describe it as a simple playground swing. A proton oscillating with a high transverse amplitude is comparable to being on a swing and swinging to a high height. The proton in this case embodies the behaviour of a bunch of protons in the LHC.

As the LHC is already constructed, it is not possible to open it to measure specific magnets anymore. However, the proton can be used as a spy to look for hidden magnetic errors in the LHC. The proton can travel in the accelerator and look and feel for these errors. It can then hand in its investigative report at several locations in the accelerator. The concept of using the proton beam to measure the state of the accelerator is called beam-based measurements.

However, the proton will not do all this by itself, it needs a little push so to speak. It is commonly known that there are two ways to push your little sister on a swing. Either you give her one large kick and go back to play football, or you stand by patiently and give her a gentle nudge each time she passes by. This is not different for a proton. One big kick can be used of course, using the kicker magnet, but this is hardly the nicest way. Indeed, this is not even allowed in the LHC. A single kick that is too powerful can kick the beam out of the LHC in a single turn, which is too fast for any safety feedback system. Such risks are rightfully considered too high for the LHC.

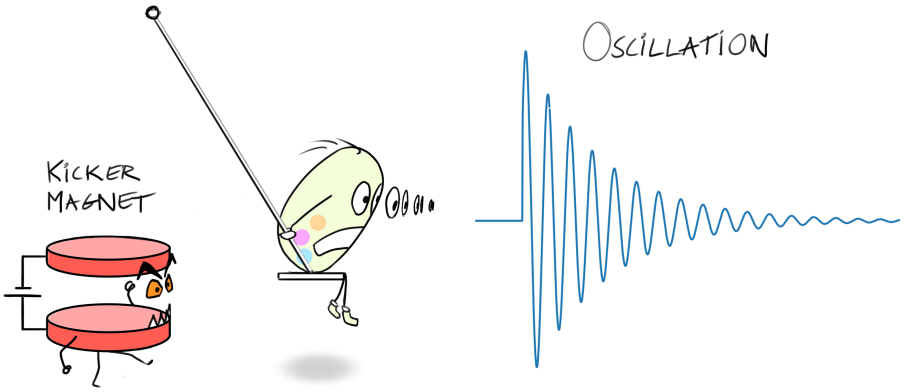

Instead, in the LHC the gentle approach is used. An ac dipole is used that gives

a nudge exactly at the right time to increase the amplitude of oscillation, or height of the swing. At some point the ac dipole adapts its strength so that the amplitude stays constant for a while, before gently guiding the proton back to standstill. These oscillations are referred to in this thesis as forced oscillations.

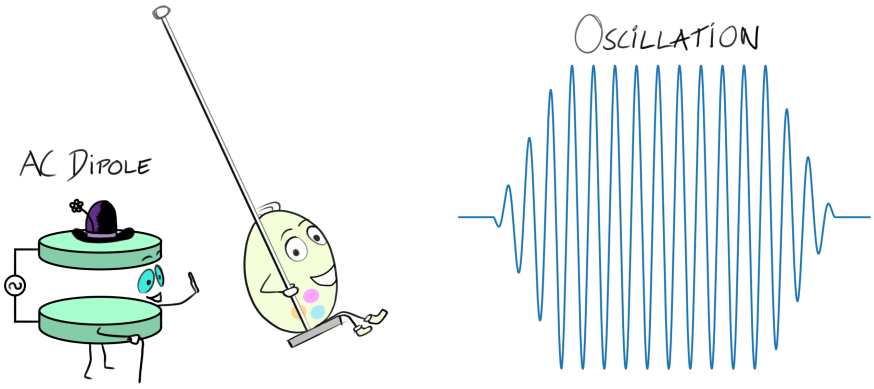

At its largest height, the proton can see the most of course. As it gets higher, the proton will be able to see more nonlinear magnets and errors with an increasing number of poles. Of course this is not the most pleasant for the proton, as it will be shaken around by the sextupoles, octupoles, and the higher order magnetic fields. But it is a necessary evil.

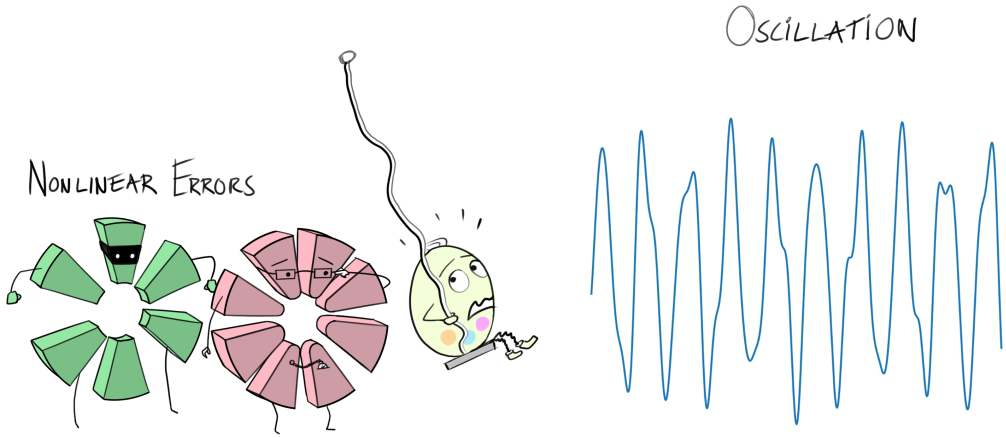

As the proton travels through the LHC, it dutifully reports its findings to the Beam Position Monitors (BPMs), that in turn translate this into readable information. More exactly, the BPMs measure the transverse position of the beam, which contains all the information about the magnetic fields the proton interacted with along the way. There are 550 BPMs around the accelerator to get a detailed view of the particle dynamics.

The BPMs provide a measurement of the transverse position of the bunch at each turn. This forms a discrete time signal of an oscillation that can be analysed

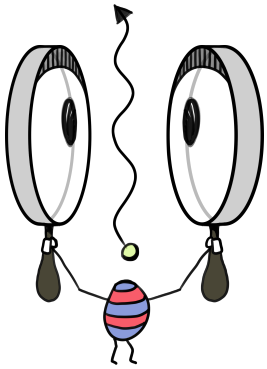

through spectral analysis. This spectral analysis reveals all the secondary modes, or oscillations, that are generated by the nonlinear sources. From these secondary modes, the resonance driving terms can be calculated. Resonance driving terms are a measure of how strong specific nonlinear sources are, and how the sum of all these sources behave at a specific location. By measuring these resonance driving terms, it is possible to locate magnetic errors and devise strategies to compensate for nonlinear errors. After lots of gatherings, meetings, coffees, lunch breaks, and sleepless nights a solution is finally found. By powering specific magnets that are well controlled, the effect of the measured errors can be countered and compensated. The resulting machine is a machine where the effect of nonlinear errors on the protons is minimized. In other words, the nonlinear errors and sources in the machine have been corrected. The particle oscillations are well understood in this situation, and any manipulation of the beams has a well predictable effect.

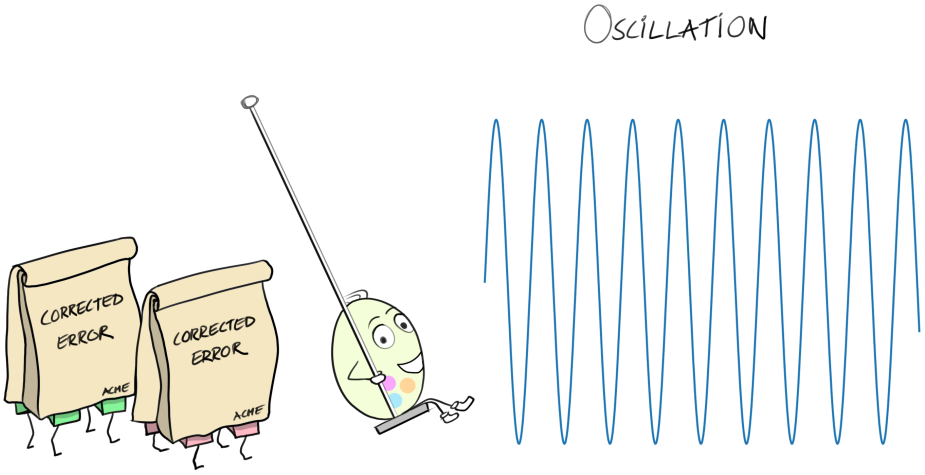

The work presented in this thesis focuses entirely on this process of measurement and correction of nonlinear errors. Chapter 4 derives a new theoretical description of how particles oscillate as a result of the ac dipole in the presence of nonlinear

sources. This new description offers a simpler parametrization of resonance driving terms compared to previous works. The presented derivations are compared to simulations and show an excellent agreement, and the results offer a novel approach to describe and study resonance driving terms of forced oscillations. It also shows for the first time that the ac dipole has a second order effect on resonance driving terms that may play a significant role in future studies. It is a truly exciting study that significantly improved the understanding of the ac dipole driven motion and invites further research to unravel all the intricacies of forced oscillations.

After these theoretical explorations, Chapter 5 presents the experiments performed in the LHC to specifically identify and correct nonlinear sources by measuring resonance driving terms. The development of the methods and an overview of all the measurements of resonance driving terms in Run II of the LHC are presented. The very first measurement of resonance driving terms of decapolar sources, with 10 poles, is achieved. This validates the use of this method to measure and correct higher order errors that other methods struggle to address. Furthermore, magnetic errors of skew octupolar order, with 8 poles, are corrected for the first time using the measurements of resonance driving terms. This is a milestone achievement, and validates the use of this method for future machines.

Chapter 6 present the first experimental demonstrations of forced dynamic aperture performed in the LHC. The forced dynamic aperture is a measure of the maximum amplitude of oscillation that particles can achieve with the ac dipole while remaining stable. The instability of particles is mainly determined by nonlinear magnetic fields. If the particles become unstable at lower amplitudes it suggests that stronger nonlinear fields are present in the machine, i.e. stronger nonlinear errors. The forced dynamic aperture can be used as a new observable to measure how nonlinear the accelerator is on average. These chapters present an analytical definition for this new observable, and present experimental evidence that this observable is sensitive to changes in the nonlinear content of the LHC.

Finally, Chapter 7 applies the concepts and methods of Chapters 4 and 5 to the case where the beams are now in collision. During collisions, the opposing beam forms a large source of nonlinearity and will affect the way particles propagate through the LHC. This interaction is called the beam-beam interaction. Chapter 7 presents theoretical derivations to describe this effect on resonance driving terms. The derivations are validated with simulations and show a good agreement. It also presents the first ever measurements of resonance driving terms resulting from the beam-beam interaction. This now opens the doors for new ways to study the beam-beam effect and possible compensation schemes.

In all, the achievements presented in this thesis significantly improve the understanding of the nonlinear motion under the influence of ac dipoles both theoretically as well as experimentally. This thesis offers the first demonstration of specific nonlinear correction strategies using the ac dipoles. The validation of these methods now offer new strategies to improve the control of the beams and further push the performance of the LHC as well as future machines as the High Luminosity LHC and the FCC.

In the end, the LHC can finally be used for its true purpose, proton collisions. The results are messy. Sprays of particle traces are left everywhere. A gruesome sight. It is here that the particle detectors start their investigations. *Did the proton leave any clues about the foundations of the universe?* Those questions are up to the detectors to answer.

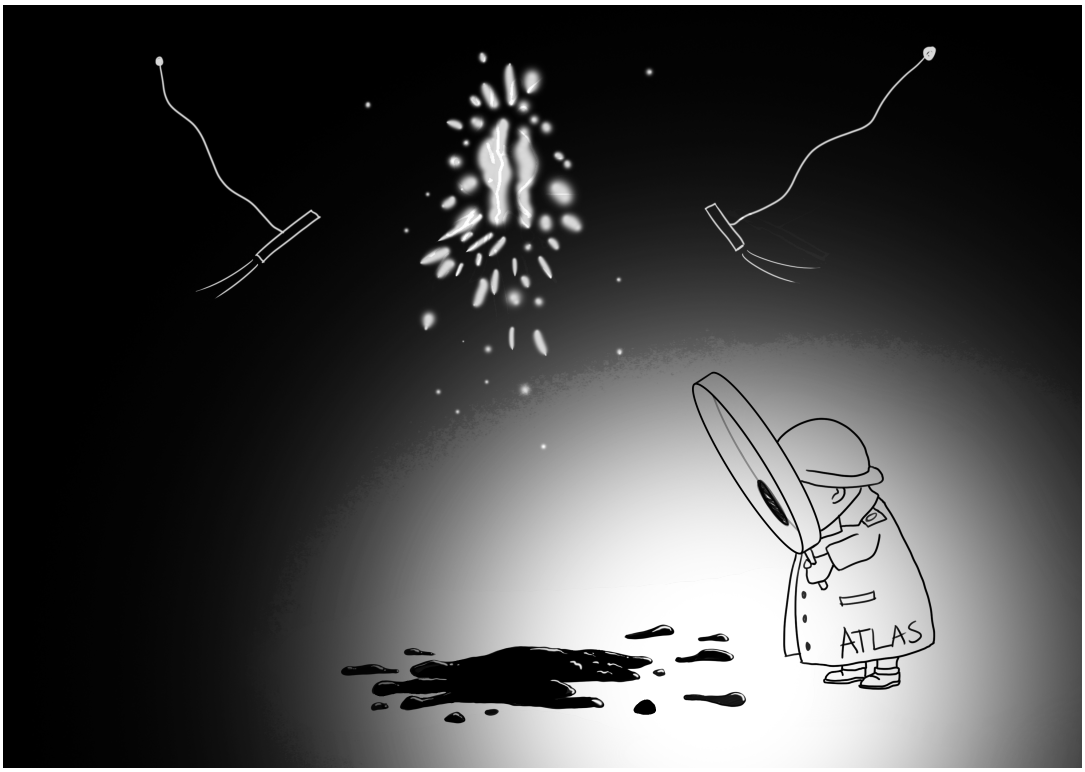

SAMENVATTING

(VAN: A NONLINEAR FUTURE)

Het is met veel plezier dat ik van de gelegenheid gebruik maak om af te wijken van de gebaande paden en een beetje creatieve vrijheid toe laat bij het samenvatten van dit proefschrift. Een waarschuwing aan de doorgewinterde fysici is op zijn plaats; er is sprake van enige oversimplicatie in deze samenvatting. Toch zal dit hopelijk helpen om een aantal van de belangrijkste elementen van dit onderzoek uit te leggen. Mocht dat niet werken hoop ik dat het in ieder geval plezierig zal zijn. Uit angst u, de lezer, te verliezen op de eerste pagina wordt er een uitgebreidere inleiding gepresenteerd. Ik hoop een beter gevoel te verschaffen over de context, uitdagingen en methoden waarop deze dissertatie is gebouwd, en pas daarna de resultaten van het onderzoek presenteren.

Voordat ik inga op de kern van dit proefschrift is het de moeite waard om de context te bespreken. Het onderzoek dat in dit proefschrift wordt gepresenteerd is uitgevoerd aan de Europese Organisatie voor Nucleair Onderzoek, beter bekend als CERN. De belangrijkste missie van CERN is het vinden van experimenteel bewijs voor de natuurkundige wetten die het universum op het meest fundamentele niveau beheersen. Tot op heden is het Standaard Model van de deeltjesfysica het meest nauwkeurige model dat de interacties van elementaire deeltjes en fundamentele krachten beschrijft. Het is uitgebreid getest en gevalideerd en is waardevol geweest bij het voorspellen van een breed scala aan verschijnselen. Er zijn echter nog veel openstaande problemen waarvoor fysici geen verklaring hebben gevonden. *Gedraagt de anti-materie zich anders dan de materie? Kan de zwaartekracht worden verenigd met de andere fundamentele krachten? Wat is die donkere materie waar mensen over praten?* Of nog exotischer, *wat is donkere energie?* Al deze onderwerpen beschrijven fysische fenomenen en waarnemingen die verder gaan dan het standaardmodel en die een nieuw begrip van de fysica vereisen. Het zijn precies dit soort vragen die CERN in haar onderzoeksprogramma probeert aan te pakken.

Om de natuurkunde op dit niveau te bestuderen, probeert CERN de condities van het vroege universum na te bootsen. De meest succesvolle manier om deze condities te benaderen is door deeltjes met zeer hoge snelheden met elkaar te laten botsen in zogenaamde deeltjesbotser (*particle collider*). In deeltjesversnellers worden

deeltjes dicht bij de lichtsnelheid versneld en met elkaar in botsing gebracht. Door protonen met grote snelheden tegen elkaar aan te botsen, d.w.z. hoge energieën, worden nieuwe deeltjes gecreëerd door de energie van de protonen om te zetten in massa. Hoe hoger de energieën van de protonen, hoe massiever de gecreëerde deeltjes zijn. Door te bestuderen welke deeltjes ontstaan en hoe deze nieuwe deeltjes zich gedragen en vervallen, proberen onderzoekers de diepere natuurkundige wetten bloot te leggen. In feite proberen onderzoekers nog steeds een antwoord te geven op de eeuwenoude vraag: Hoe worden baby's geboren? Hoewel nu op de kleinst mogelijke schaal.

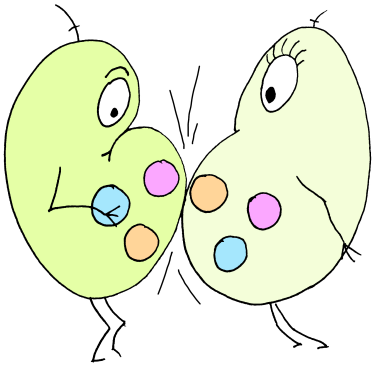

De grootste en krachtigste deeltjesbotser is de Large Hadron Collider, kortweg LHC. De LHC is een cirkelvormige versneller met een omtrek van 27 km en ligt 100 m onder de grond bij CERN, vlakbij Genève (Zwitserland). Het is het grootste wetenschappelijke experiment tot nu toe. De LHC heeft de taak om de protonen te versnellen en de botsingen op te zetten. Er zitten twee deeltjesversnellers in de LHC. Een versneller versnelt protonen met de klok mee, terwijl de andere protonen in tegengestelde richting versnelt. De twee bundels kruisen elkaar op vier verschillende locaties in de collider waar speciale detectoren zoeken naar de nieuw ontstane deeltjes. Deze detectoren zijn ATLAS, CMS LHCb en ALICE.

Het onderwerp van dit proefschrift gaat echter niet over het resultaat van de botsingen of de detectoren. Het gaat strikt om de LHC en hoe de protonen door deze deeltjesbotser reizen. De taak om de protonen te versnellen en te laten botsen is een hele uitdaging op zich.

De baan van de deeltjes door de versneller wordt volledig bepaald door magneten. Alle magneten zullen een kracht uitoefenen die loodrecht staat op de richting waarin een deeltje zich voort beweegt. [2] Een waslijst aan magneten wordt in de

2 Voor degenen die naar de Nederlandse middelbare school gingen, zou de '*BIL*'-regel een belletje kunnen doen rinkelen, terwijl anderen het misschien herkennen als de Lorentz-kracht.

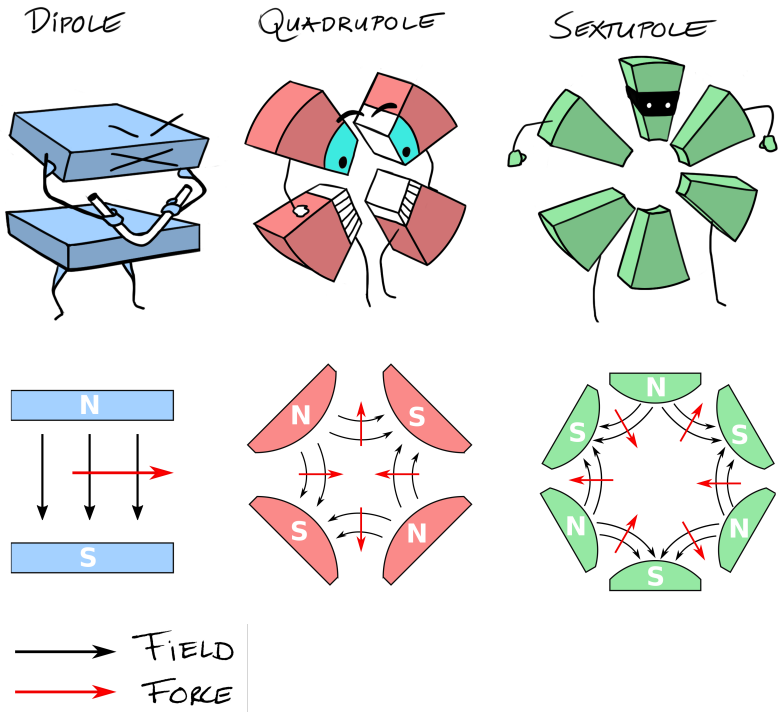

LHC gebruikt om de protonen te buigen, te verdraaien, te vormen en te duwen op de ontworpen baan. In totaal bevat de LHC ongeveer 9600 magneten. Deze worden meestal genoemd naar het aantal magnetische polen dat ze bevatten. Een dipool heeft twee polen, een quadrupool heeft vier polen, enzovoort.

De dipolen zijn de zwaarste van alle magneten in de LHC, de bodybuilders onder de magneten, en veruit de talrijkste in de LHC. Ze zijn belast met de taak om de baan van de deeltjes te buigen tot een ring. Ten tweede zijn er quadrupolen die de orde in de LHC handhaven. Quadrupolen zorgen ervoor dat de deeltjesbundels gegroepeerd en gefocust blijven. Dan zijn er ook nog sextupolen. Sextupolen zorgen ervoor dat deeltjes met energieafwijkingen op het juiste spoor blijven. Er zijn ook octupolen die bepaalde deeltjes kunnen ontstemmen. Als ze goed gecontroleerd zijn, kunnen ze nuttig zijn om enkele onstabiele deeltjes te temmen. Tot slot zijn er magneten van een hogere orde met nog meer polen. Vanaf hier wordt het rommelig. Het benoemen van magneten van een hogere orde kan een hele mond vol raken. Er zijn de decapolen met tien polen, dodecapolen met 12 polen. Het gerucht gaat dat iemand ooit heeft geprobeerd om tetradecapool te benoemen om een 14-polig magnetisch veld te beschrijven. Van al deze magneten worden de sextupolen, octupolen en meerpolige magneten van hogere orde niet-lineaire magneten genoemd.

Hoewel er veel bekend is over al deze magneten, is het onvermijdelijk dat een magneet enkele karaktereigenschappen van andere magneten kan hebben. Het is dus heel goed mogelijk dat wat wordt verondersteld een perfecte quadrupool te

zijn, in feite een aantal onbekende octupolaire kenmerken heeft. Deze worden magnetische fouten genoemd. In feite kunnen alle magneten in de LHC lichtjes afwijken van hun ontworpen magnetisch veld. Deze fouten kunnen het gevolg zijn van fabricageprocessen, maar ook van het verkeerd uitlijnen of kantelen van de magneten tijdens de installatiefase. In sommige gevallen is dit niet zo belangrijk, maar in bepaalde gevallen heeft dit ernstige gevolgen. Afwijkingen in magnetische velden kunnen de banen van de deeltjes uit het ontwerp ernstig verstoren. De deeltjes in een straal kunnen verloren gaan, geleidelijk of zelfs allemaal tegelijk. Dit verslechtert niet alleen de prestaties van de machine als er geleidelijk aan deeltjes verloren gaan, het kan ook schadelijk zijn voor de machine als alle deeltjes in één keer verloren gaan.

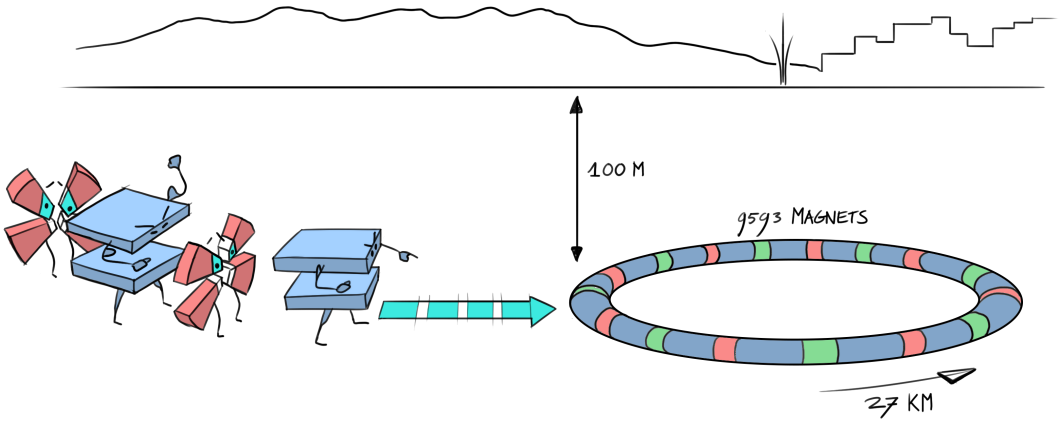

De magneten zijn in een specifieke volgorde uitgelijnd en worden tot zeer nauwkeurige sterktes aangedreven om de protonen met succes in een cirkelvormig traject door de versneller te leiden. Omdat de LHC een cirkelvormige machine is, zullen de protonen steeds weer door dezelfde machine reizen. Wetenschappers noemen dit graag een periodiek systeem, een systeem dat zich na een bepaalde periode herhaalt, wat in dit geval een volledige ronde is. De reeks van afwisselende quadrupolen in de LHC zal ervoor zorgen dat de protonen gaan oscilleren in het vlak dat loodrecht staat op de richting waarin het zich beweegt, wat het hier het transverse vlak wordt genoemd.

Dit proefschrift is puur gericht op de manier waarop de deeltjes in dit transverse vlak oscilleren. De oscillatie wordt beschreven met betrekking tot het ideale deeltje op de referentiebaan. Deze oscillatie is in principe goed gecontroleerd. Wanneer er echter magnetische fouten aanwezig zijn, is het mogelijk dat deze oscillatie vervormd is en dat de protonen onstabiel worden en uit de LHC worden geworpen. Dit betekent dat er minder protonen beschikbaar zullen zijn voor de botsingen, en

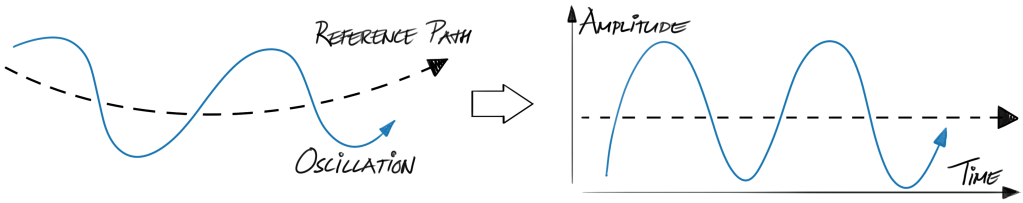

dus minder statistische gegevens voor de detectoren. Niet te vergeten, als alle protonen in één keer verloren gaan kan het de LHC ernstig beschadigen. Het is dus zeer belangrijk om deze oscillaties te begrijpen en te identificeren hoe elke magneetfamilie en magnetische fouten op deze oscillatie inwerken. Het doel van dit proefschrift is het ontwikkelen en valideren van methoden waarmee deze magnetische fouten kunnen worden gemeten en waarmee correcties en compensatie technieken kunnen worden gevonden. De huidige prestaties van de LHC zijn afhankelijk van deze correcties van niet-lineaire fouten, en de toekomstige machines zoals de High Luminosity LHC of de Future Circular Collider (FCC) kunnen niet zonder dergelijke correcties opereren.

Aangezien het belang alleen in deze oscillatie ligt, is het een nuttige analogie om het te beschrijven als een eenvoudige schommel. Een proton dat met een hoge transversale amplitude schommelt, is vergelijkbaar met een schommel die schommelt tot op grote hoogte. De proton belichaamt in dit geval het gedrag van een protonen bundel in de LHC.

Aangezien de LHC al gebouwd is, is het niet meer mogelijk om deze te openen om specifieke magneten te meten. De proton kan echter worden gebruikt als spion om te zoeken naar verborgen magnetische fouten in de LHC. De proton kan zich in versneller voortbewegen en kijken en voelen voor deze fouten. Het kan dan op verschillende plaatsen in de versneller zijn onderzoeksrapport inleveren.

Maar de proton zal dit alles niet alleen doen, het heeft als het ware een zetje in de rug nodig. Het is algemeen bekend dat er twee manieren zijn om je kleine zusje op een schommel te duwen. Of je geeft haar een grote schop en gaat weer voetballen, of je staat geduldig klaar en geeft haar een zacht duwtje elke keer dat ze langskomt. Dit is niet anders voor een proton. Eén grote schop kan natuurlijk worden gebruikt, met behulp van de kicker-magneet, maar dit is niet de beste manier. Dit is zelfs niet toegestaan in de LHC. Een krachtige schop die te sterk is kan de bundel protonen in één keer uit de LHC schoppen, wat te snel is voor elk veiligheids-systeem in de LHC. Dergelijke risico's worden terecht als te hoog beschouwd voor de LHC.

In plaats daarvan wordt in de LHC de zachte aanpak gebruikt. Een ac dipool (*alternating current*) wordt gebruikt die een duwtje precies op het juiste moment

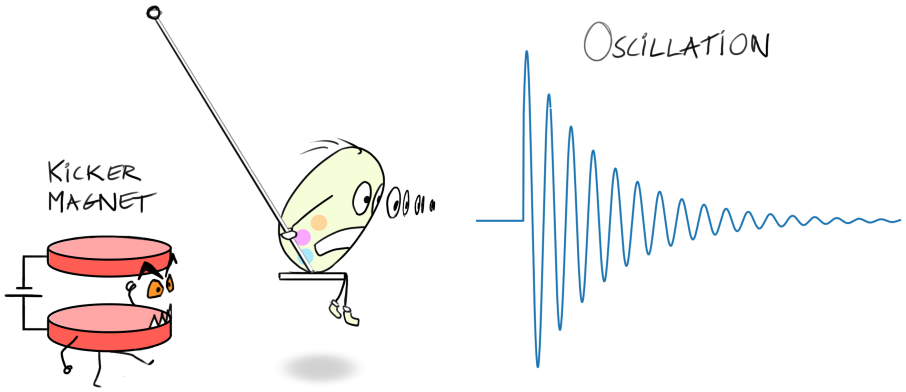

geeft om de amplitude van de oscillatie, of de hoogte van de schommel, te verhogen. Op een gegeven moment past de ac dipool zijn kracht aan, zodat de amplitude een tijd constant blijft. Vervolgens brengt de ac dipool de proton zachtjes weer tot stilstand brengt. Deze oscillaties worden in dit proefschrift geforceerde oscillaties (*forced oscillations*) genoemd.

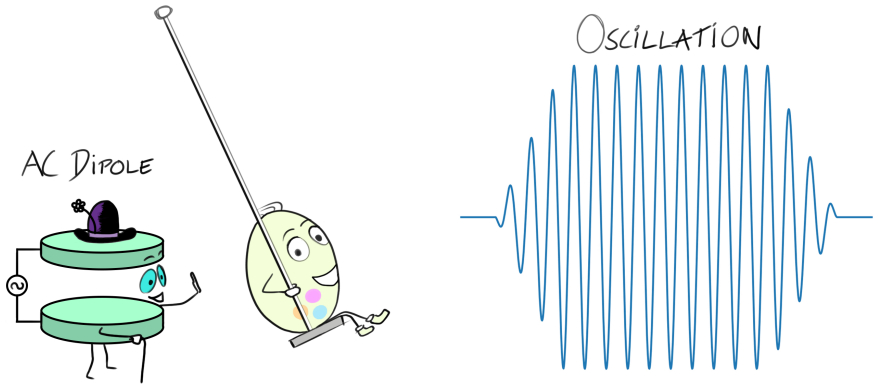

Op zijn grootste hoogte kan de proton natuurlijk het meest zien. Naarmate de proton hoger schommelt zal deze niet-lineaire magneten zien van steeds hogere orde. Dit is natuurlijk niet het prettigste voor de proton, omdat die door de sextupolen, octupolen en de hogere orde magnetische velden heen en weer geschud zal worden. Maar het is een noodzakelijk kwaad.

Terwijl de proton door de LHC reist, rapporteert het plichtsgetrouw zijn bevindingen aan de Beam Position Monitors (BPMs), die dit op hun beurt weer vertalen in leesbare informatie. Om preciezer te zijn meten de BPMs de transverse positie van de bundel. Die bevat alle informatie over de magnetische velden waarmee de proton onderweg in aanraking is gekomen. Er zijn 550 BPMs verspreid in de versneller om zo een gedetailleerd beeld te krijgen van de deeltjesdynamiek.

De BPMs geven een meting van de transverse positie van de bundel bij elke ronde. Dit vormt een discreet tijdsignaal van een oscillatie dat kan worden geanal-

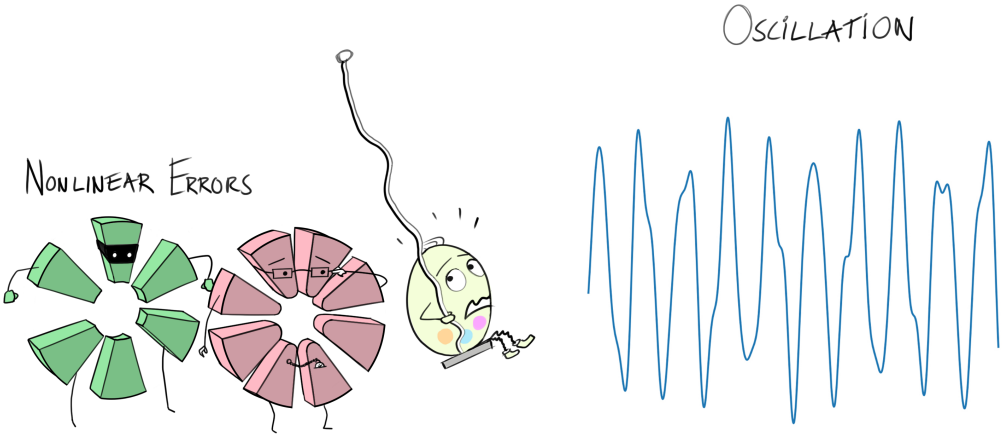

yseerd door middel van spectrale analyse. Deze spectrale analyse onthult alle secundaire modi, of oscillaties, die door de niet-lineaire bronnen worden gegenereerd. Uit deze secundaire modi kunnen de *resonance driving terms* worden berekend. Deze *resonance driving terms* zijn een maatstaf voor hoe sterk specifieke niet-lineaire bronnen zijn, en hoe de som van al deze bronnen zich op een specifieke locatie gedraagt. Door het meten van deze *resonance driving terms* is het mogelijk om magnetische fouten te lokaliseren en strategieën te bedenken om niet-lineaire fouten te compenseren. Na veel bijeenkomsten, vergaderingen, koffie, lunchpauzes en slapeloze nachten is er eindelijk een oplossing gevonden. Door specifieke magneten aan te drijven die goed gecontroleerd zijn, kan het effect van de gemeten fouten worden gecompenseerd. De resulterende machine is een machine waarbij de niet-lineaire fouten de protonen niet meer storen. Oftewel, de niet-lineaire fouten en bronnen in de machine zijn gecorrigeerd. De deeltjes oscillaties worden in deze situatie goed begrepen en elke manipulatie van de bundels heeft een goed voorspelbaar effect.

Het werk dat in dit proefschrift wordt gepresenteerd richt zich volledig op dit proces van meten en corrigeren van niet-lineaire fouten. Hoofdstuk 4 leidt een nieuwe theoretische beschrijving af van hoe deeltjes oscilleren als gevolg van de ac dipool in de aanwezigheid van niet-lineaire bronnen. Deze nieuwe beschrijving

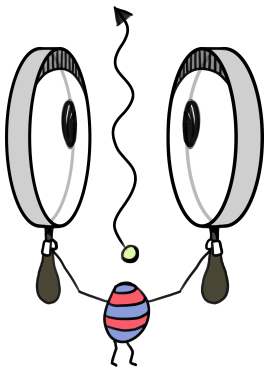

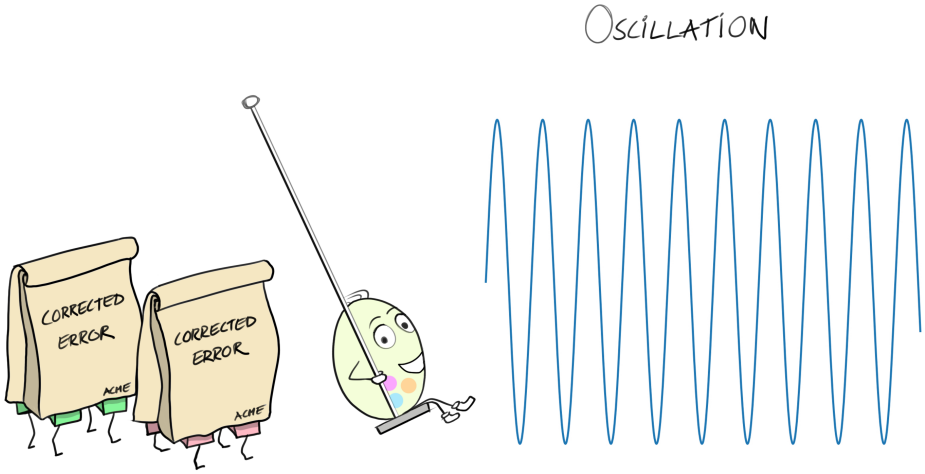

biedt een eenvoudigere parametrisering van de *resonance driving terms* in vergelijking met eerdere werken. De gepresenteerde afleidingen worden vergeleken met simulaties en laten een uitstekende overeenkomst zien, en de resultaten bieden een nieuwe benadering voor het beschrijven en bestuderen van *resonance driving terms* van geforceerde oscillaties. Het toont ook voor het eerst aan dat de ac dipool een tweede-orde-effect heeft op *resonance driving terms* die een belangrijke rol kunnen spelen in toekomstige studies. Het is een werkelijk enerverende studie die het begrip van de ac dipool gedreven oscillaties aanzienlijk heeft verbeterd. Het nodigt uit tot verder onderzoek om alle fijne kneepjes van geforceerde oscillaties te ontrafelen.

Na deze theoretische verkenningen presenteert hoofdstuk 5 de experimenten die zijn uitgevoerd in de LHC om specifiek niet-lineaire bronnen te identificeren en te corrigeren door het meten van deze *resonance driving terms*. De ontwikkeling van de methoden wordt gepresenteerd en er wordt een overzicht gegeven van alle metingen van *resonance driving terms* in Run II van de LHC. De allereerste meting van de *resonance driving terms* van decapolaire bronnen, met 10 polen, wordt bereikt. Dit valideert het gebruik van deze methode voor het meten en corrigeren van fouten van een hogere orde die door andere methoden moeilijk kunnen worden aangepakt. Bovendien worden magnetische fouten van gekantelde octupolaire orde voor het eerst gecorrigeerd met behulp van de metingen van de *resonance driving terms*. Dit is een mijlpaal en valideert het gebruik van deze methode voor toekomstige machines.

Hoofdstuk 6 presenteert de eerste experimentele demonstraties van *forced dynamic aperture*. De *forced dynamic aperture* is een maat voor de maximale amplitude van de oscillatie die deeltjes kunnen bereiken met de ac dipool terwijl ze stabiel bli-

jven. De instabiliteit van de deeltjes wordt voornamelijk bepaald door niet-lineaire magnetische velden. Als de deeltjes onstabiel worden bij lagere amplitudes suggereert dit dat er sterkere niet-lineaire velden in de machine aanwezig zijn, d.w.z. sterkere niet-lineaire fouten. De *forced dynamic aperture* kan worden gebruikt als een nieuw waarneembaar meetmethode om te meten hoe niet-lineair de versneller gemiddeld is. In deze hoofdstukken wordt een analytische definitie gegeven van deze nieuwe waarneembare kwantiteit, en wordt experimenteel bewijs geleverd dat dit waarneembare kwantiteit gevoelig is voor veranderingen in de niet-lineaire inhoud van de LHC.

Tenslotte past Hoofdstuk 7 de concepten en methoden van Hoofdstukken 4 en 5 toe op het geval dat de bundels nu in botsing zijn. Tijdens botsingen vormt de tegengestelde bundel een grote bron van niet-lineariteit en zal het de manier waarop de deeltjes zich voortbewegen door de LHC beïnvloeden. Deze interactie wordt de *beam-beam* interactie genoemd. Hoofdstuk 7 presenteert theoretische afleidingen om dit effect op de *resonance driving terms* te beschrijven. De afleidingen worden gevalideerd met simulaties en laten een goede overeenkomst zien. Het presenteert ook de allereerste metingen van de *resonance driving terms* als gevolg van de interactie tussen de twee tegenovergestelde bundels. Dit opent de deur naar nieuwe manieren om het *beam-beam* effect en mogelijke compensatiemethoden te bestuderen.

Al met al verbeteren, de in dit proefschrift gepresenteerde ondervindingen, aanzienlijk het begrip van de niet-lineaire dynamica onder invloed van ac dipolen, zowel theoretisch als experimenteel. Dit proefschrift biedt de eerste demonstratie van specifieke niet-lineaire correctiestrategieën met behulp van de ac dipolen. De validatie van deze methoden biedt nu nieuwe strategieën om de controle over de bundels te verbeteren en de prestaties van de LHC en toekomstige machines zoals de High Luminosity LHC en de FCC verder te verbeteren.

Uiteindelijk kan de LHC eindelijk worden gebruikt voor zijn ware doel, protonbotsingen. De resultaten zijn rommelig. Overal worden deeltjessporen achtergelaten. Een gruwelijk aanzicht. Het is hier dat het onderzoek van de deeltjesdetectoren begint. *Heeft de proton aanwijzingen achtergelaten over de fundamentele wetten van het universum?* Die vragen zijn aan de detectoren om te beantwoorden.

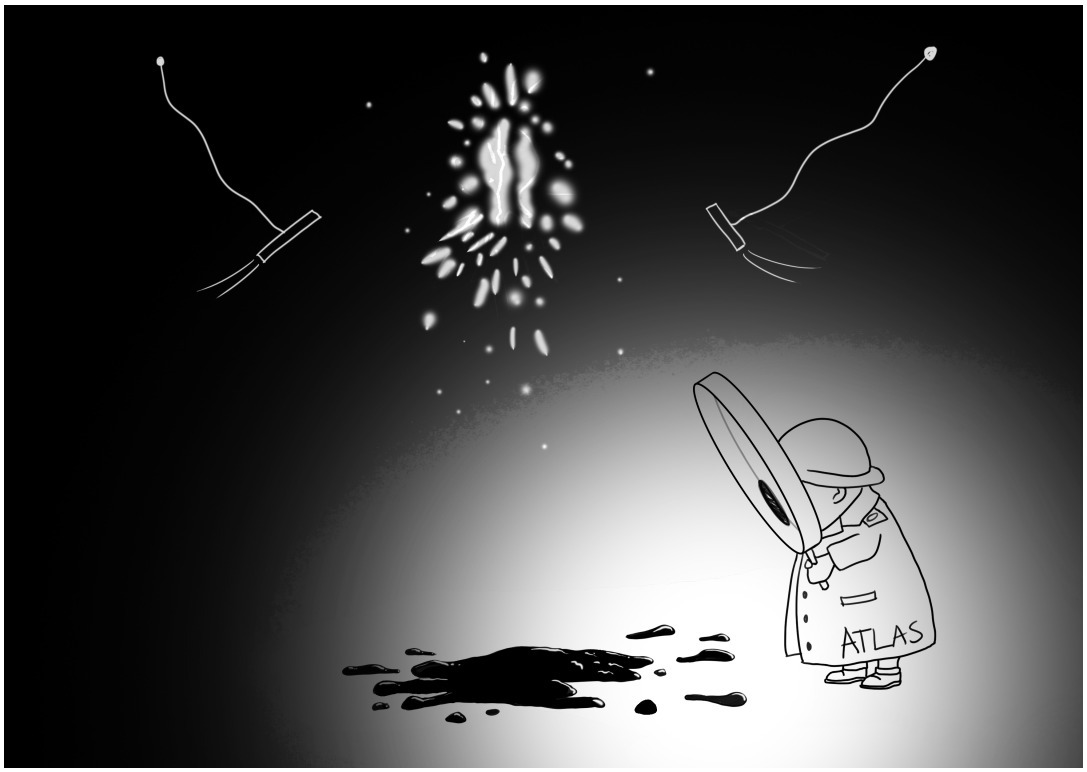
ATLAS

BIBLIOGRAPHY

[1] F. S. Carlier and R. Tomás. „Forced resonance driving terms." In: *Phys. Rev. ST Accel. Beams* (2019), Submitted.

[2] F. S. Carlier, R. Tomás, and E. H. Maclean. „Measurement and Correction of resonance driving terms in the Large Hadron Collider." In: *Phys. Rev. ST Accel. Beams* (2020), Submitted.

[3] F. S. Carlier et al. „First experimental demonstration of forced dynamic aperture measurements with LHC ac dipoles." In: *Phys. Rev. Accel. Beams* 22 (3 2019), p. 031002. DOI: 10.1103/PhysRevAccelBeams.22.031002. URL: https://link.aps.org/doi/10.1103/PhysRevAccelBeams.22.031002.

[4] F. Carlier et al. „Probing the forced dynamic aperture in the LHC at top energy using AC dipoles." In: *Proceedings, 9th International Particle Accelerator Conference (IPAC 2018): Vancouver, BC Canada, April 29-May 4, 2018*. 2018, MOPMF033. DOI: 10.18429/JACoW-IPAC2018-MOPMF033.

[5] F. S. Carlier, R. Tomás, and X. Buffat. „First measurement of resonance driving terms from head-on beam-beam interaction in the LHC." In: *Phys. Rev. Accel. Beams* (2019), Submitted.

[6] J. J. Thomson. „Cathode rays." In: *Philosophical Magazine, 44, 293-316* (1897). DOI: http://dx.doi.org/10.1080/14786449708621070.

[7] G. Danby et al. „Observation of high-energy neutrino reactions and the existence of two kinds of neutrinos." In: *Phys. Rev. Lett.* 9 (1 1962), pp. 36–44. DOI: 10.1103/PhysRevLett.9.36. URL: https://link.aps.org/doi/10.1103/PhysRevLett.9.36.

[8] M. L. Perl et al. „Evidence for anomalous lepton production in $e^+ - e^-$ annihilation." In: *Phys. Rev. Lett.* 35 (22 1975), pp. 1489–1492. DOI: 10.1103/PhysRevLett.35.1489. URL: https://link.aps.org/doi/10.1103/PhysRevLett.35.1489.

[9] K. Kodama et al. „Observation of tau neutrino interactions." In: *Physics Letters B* 504.3 (2001), pp. 218 –224. ISSN: 0370-2693. DOI: https://doi.org/10.1016/S0370-2693(01)00307-0. URL: http://www.sciencedirect.com/science/article/pii/S0370269301003070.

[10] E. D. Bloom et al. „High-energy inelastic $e - p$ scattering at 6° and 10°." In: *Phys. Rev. Lett.* 23 (16 1969), pp. 930–934. DOI: 10.1103/PhysRevLett.23.930. URL: https://link.aps.org/doi/10.1103/PhysRevLett.23.930.

[11] M. Breidenbach et al. „Observed behavior of highly inelastic electron-proton scattering." In: *Phys. Rev. Lett.* 23 (16 1969), pp. 935–939. DOI: 10.1103/PhysRevLett.23.935. URL: https://link.aps.org/doi/10.1103/PhysRevLett.23.935.

[12] F. Abe and et al. „Observation of Top Quark production in $\bar{p}p$ collisions with the Collider Detector at Fermilab." In: *Phys. Rev. Lett.* 74 (14 1995), pp. 2626–2631. DOI: 10.1103/PhysRevLett.74.2626. URL: https://link.aps.org/doi/10.1103/PhysRevLett.74.2626.

[13] S. Abachi and et al. „Observation of the Top Quark." In: *Phys. Rev. Lett.* 74 (14 1995), pp. 2632–2637. DOI: 10.1103/PhysRevLett.74.2632. URL: https://link.aps.org/doi/10.1103/PhysRevLett.74.2632.

[14] S. W. Herb et al. „Observation of a dimuon resonance at 9.5 GeV in 400-GeV proton-nucleus collisions." In: *Phys. Rev. Lett.* 39 (5 1977), pp. 252–255. DOI: 10.1103/PhysRevLett.39.252. URL: https://link.aps.org/doi/10.1103/PhysRevLett.39.252.

[15] G. Arnison and et al. „Experimental observation of isolated large transverse energy electrons with associated missing energy at s=540 GeV." In: *Physics Letters B* 122.1 (1983), pp. 103 –116. ISSN: 0370-2693. DOI: https://doi.org/10.1016/0370-2693(83)91177-2. URL: http://www.sciencedirect.com/science/article/pii/0370269383911772.

[16] G. Arnison and et al. „Experimental observation of lepton pairs of invariant mass around 95 GeVc2 at the CERN SPS collider." In: *Physics Letters B* 126.5 (1983), pp. 398 –410. ISSN: 0370-2693. DOI: https://doi.org/10.1016/0370-2693(83)90188-0. URL: http://www.sciencedirect.com/science/article/pii/0370269383901880.

[17] M. Banner and et al. „Observation of single isolated electrons of high transverse momentum in events with missing transverse energy at the CERN pp collider." In: *Physics Letters B* 122.5 (1983), pp. 476 –485. ISSN: 0370-2693. DOI: https://doi.org/10.1016/0370-2693(83)91605-2. URL: http://www.sciencedirect.com/science/article/pii/0370269383916052.

[18] P. Bagnaia and et al. „Evidence for $Z^0 \to e^+e^-$ at the CERN pp collider." In: *Physics Letters B* 129.1 (1983), pp. 130 –140. ISSN: 0370-2693. DOI: https://doi.org/10.1016/0370-2693(83)90744-X. URL: http://www.sciencedirect.com/science/article/pii/037026938390744X.

[19] G. Aad et al. „Observation of a new particle in the search for the Standard Model Higgs boson with the ATLAS detector at the LHC." In: *Phys. Lett. B* 716.1 (2012), pp. 1 –29. ISSN: 0370-2693. DOI: https://doi.org/10.1016/j.physletb.2012.08.020.

[20] S. Chatrchyan et al. „Observation of a new boson at a mass of 125 GeV with the CMS experiment at the LHC." In: *Physics Letters B* 716.1 (2012), pp. 30 –61. ISSN: 0370-2693. DOI: https://doi.org/10.1016/j.physletb.2012.08.021. URL: http://www.sciencedirect.com/science/article/pii/S0370269312008581.

[21] C. L. Cowan et al. „Detection of the free neutrino: a confirmation." In: *Science* 124.3212 (1956), pp. 103–104. ISSN: 0036-8075. DOI: 10.1126/science.124.3212.103. eprint: https://science.sciencemag.org/content/124/3212/103.full.pdf. URL: https://science.sciencemag.org/content/124/3212/103.

[22] S. H. Neddermeyer and C. D. Anderson. „Note on the nature of cosmic-ray particles." In: *Phys. Rev.* 51 (10 1937), pp. 884–886. DOI: 10.1103/PhysRev.51.884. URL: https://link.aps.org/doi/10.1103/PhysRev.51.884.

[23] O. S. Bruning et al. *LHC design report*. Geneva: CERN, 2004. URL: http://cds.cern.ch/record/782076.

[24] *ATLAS collaboration homepage*. http://atlas.web.cern.ch/Atlas/Collaboration/.

[25] *CMS collaboration homepage*. http://cms.web.cern.ch/.

[26] *LHCb collaboration homepage*. URL: http://lhcb.web.cern.ch/lhcb/.

[27] *ALICE collaboration homepage*. URL: http://aliweb.cern.ch/.

[28] A. Salam and J.C. Ward. „Weak and electromagnetic interactions." In: *Il Nuovo Cimento (1955-1965)* 11.4 (1959), pp. 568–577. ISSN: 1827-6121. DOI: 10.1007/BF02726525. URL: https://doi.org/10.1007/BF02726525.

[29] S. L. Glashow. „Partial-symmetries of weak interactions." In: *Nuclear Physics* 22.4 (1961), pp. 579 –588. ISSN: 0029-5582. DOI: https://doi.org/10.1016/0029-5582(61)90469-2. URL: http://www.sciencedirect.com/science/article/pii/0029558261904692.

[30] S. Weinberg. „A Model of Leptons." In: *Phys. Rev. Lett.* 19 (21 1967), pp. 1264–1266. DOI: 10.1103/PhysRevLett.19.1264. URL: https://link.aps.org/doi/10.1103/PhysRevLett.19.1264.

[31] M. Benedikt et al. *Future Circular Collider*. Tech. rep. CERN-ACC-2018-0057. Published in Eur. Phys. J. ST. Geneva: CERN, 2018. URL: http://cds.cern.ch/record/2651299.

[32] G. Apollinari et al. *High-Luminosity Large Hadron Collider (HL-LHC): Technical design report V. 0.1*. CERN Yellow Reports: Monographs. Geneva: CERN, 2017. DOI: 10.23731/CYRM-2017-004. URL: https://cds.cern.ch/record/2284929.

[33] A. Wolski. *Beam dynamics in high energy particle accelerators*. London: Imperial College Press, 2014.

[34] S. Y. Lee. *Accelerator physics; 3rd ed.* Singapore: World Scientific, 2012. URL: http://cds.cern.ch/record/1425444.

[35] H. Wiedemann. *Particle accelerator physics; 3rd ed.* Berlin: Springer, 2007. URL: http://cds.cern.ch/record/1083415.

[36] R. Tomás et al. „Review of linear optics measurement and correction for charged particle accelerators." In: *Phys. Rev. Accel. Beams* 20 (5 2017), p. 054801. DOI: 10.1103/PhysRevAccelBeams.20.054801. URL: https://link.aps.org/doi/10.1103/PhysRevAccelBeams.20.054801.

[37] R. Tomás et al. „Record low β beating in the LHC." In: *Phys. Rev. ST Accel. Beams* 15 (9 2012), p. 091001. DOI: 10.1103/PhysRevSTAB.15.091001. URL: http://link.aps.org/doi/10.1103/PhysRevSTAB.15.091001.

[38] T. Persson et al. „LHC optics commissioning: A journey towards 1% optics control." In: *Phys. Rev. Accel. Beams* 20 (6 2017), p. 061002. DOI: 10.1103/PhysRevAccelBeams.20.061002. URL: https://link.aps.org/doi/10.1103/PhysRevAccelBeams.20.061002.

[39] E. H. Maclean et al. „New approach to LHC optics commissioning for the nonlinear era." In: *Phys. Rev. Accel. Beams* 22 (6 2019), p. 061004. URL: https://link.aps.org/doi/10.1103/PhysRevAccelBeams.22.061004.

[40] P. Forck, P. Kowina, and D. Liakin. *Beam position monitors*. Tech. rep. 2009. URL: http://cds.cern.ch/record/1213277.

[41] A. Nosych. *Geometrical non-linearity correction procedure of LHC beam position monitors*. Tech. rep. 2014. URL: https://edms.cern.ch/document/1342295/1.

[42] M. Bai et al. „Overcoming intrinsic spin resonances with an rf dipole." In: *Phys. Rev. Lett.* 80 (21 1998), pp. 4673–4676. DOI: 10.1103/PhysRevLett.80.4673. URL: http://link.aps.org/doi/10.1103/PhysRevLett.80.4673.

[43] R. Tomás. „Adiabaticity of the ramping process of an ac dipole." In: *Phys. Rev. ST Accel. Beams* 8 (2 2005), p. 024401. DOI: 10.1103/PhysRevSTAB.8.024401. URL: https://link.aps.org/doi/10.1103/PhysRevSTAB.8.024401.

[44] E. Mobs. *The CERN accelerator complex. Complexe des accélérateurs du CERN*. Tech. rep. General Photo. 2016. URL: https://cds.cern.ch/record/2197559.

[45] G. Vanbavinckhove et al. „Optics measurements and corrections for colliders and other storage rings." Presented 16 Jan 2013. PhD thesis. Amsterdam U., 2013. URL: https://cds.cern.ch/record/1533084.

[46] A. Chao. *Lecture notes on special topics in accelerator physics*. Tech. rep. SLAC, 2002. URL: https://www.slac.stanford.edu/~achao/lecturenotes.html.

[47] E. D. Courant and H. S. Snyder. „Theory of the Alternating-Gradient Synchrotron." In: *Ann. Phys.* 3 (1958), pp. 1–48. URL: https://cds.cern.ch/record/593259.

[48] G. W. Hill. „On the part of the motion of the lunar perigee which is a function of the mean motions of the sun and moon." In: *Acta Math.* 8 (1886), pp. 1–36. DOI: 10.1007/BF02417081. URL: https://doi.org/10.1007/BF02417081.

[49] R. Tomás. „Normal form of particle motion under the influence of an ac dipole." In: *Phys. Rev. ST Accel. Beams* 5 (5 2002), p. 054001. DOI: 10.1103/PhysRevSTAB.5.054001. URL: http://link.aps.org/doi/10.1103/PhysRevSTAB.5.054001.

[50] É. Forest. *Beam dynamics: A new attitude and framework*. Harwood Academic, 1998.

[51] A. Franchi. „Studies and measurements of linear coupling and nonlinearities in hadron circular accelerators." Presented on 07 Aug 2006. PhD thesis. Frankfurt am Main: Johann Wolfgang Goethe-University, 2006.

[52] R. A. Barlow et al. *Control of the MKQA tuning and aperture kickers of the LHC*. Tech. rep. CERN-TE-Note-2010-001. CERN, 2009. URL: http://cds.cern.ch/record/1232062.

[53] S. Peggs and C. Tang. *Nonlinear diagnostics using an ac dipole*. Tech. rep. RHIC AP 159. Upton, NY: Brookhaven National Laboratory, 1998.

[54] R. Miyamoto et al. „Parametrization of the driven betatron oscillation." In: *Phys. Rev. ST Accel. Beams* 11 (8 2008), p. 084002. DOI: 10.1103/PhysRevSTAB.11.084002. URL: http://link.aps.org/doi/10.1103/PhysRevSTAB.11.084002.

[55] M. Bai et al. „Measuring beta function and phase advance in RHIC with an ac dipole." In: *Proc. of Particle Accelerator Conference (PAC'03), Portland, Oregon, USA, May 12-16*. 2003. URL: http://accelconf.web.cern.ch/accelconf/p03/PAPERS/WPAB072.pdf.

[56] R. Miyamoto et al. „Tevatron AC dipole system." In: *Proc. of Particle Accelerator Conference (PAC'07), Albuquerque, New Mexico, USA, June 25-29*. 2007.

[57] R. Miyamoto. „Diagnostics of the Fermilab Tevatron using an AC dipole." PhD thesis. Austin: University of Texas, 2008.

[58] R. Miyamoto et al. *Measurement of coupling resonance driving terms in the LHC with AC dipoles*. Tech. rep. CERN-ATS-2011-158. CERN, 2011, 3 p. URL: https://cds.cern.ch/record/1382073.

[59] X. Shen et al. „Application of independent component analysis to ac dipole based optics measurement and correction at the Relativistic Heavy Ion Collider." In: *Phys. Rev. ST Accel. Beams* 16 (11 2013), p. 111001. DOI: 10.1103/PhysRevSTAB.16.111001. URL: http://link.aps.org/doi/10.1103/PhysRevSTAB.16.111001.

[60] N. Biancacci and R. Tomás. „Using ac dipoles to localize sources of beam coupling impedance." In: *Phys. Rev. Accel. Beams* 19 (5 2016), p. 054001. DOI: 10.1103/PhysRevAccelBeams.19.054001. URL: http://link.aps.org/doi/10.1103/PhysRevAccelBeams.19.054001.

[61] I. Agapov et al. *Linear and nonlinear optics measurements with multiturn data at PETRA III*. Tech. rep. CERN-ACC-2017-258. CERN, 2017, MOPAB040. 4 p. URL: http://cds.cern.ch/record/2289147.

[62] A. Franchi. „Recent measurements of linear and nonlinear optics at the ESRF storage ring." In: *7th Low-Emittance Rings Workshop*. 2018. URL: https://indico.cern.ch/event/671745/timetable/#20180116.detailed.

[63] N. Fuster Martinez et al. „Aperture measurements with AC dipole at the Large Hadron Collider." In: *Proc. of International Particle Accelerator Conference (IPAC'18), Vancouver, Canada, April 29 - May 4, 2018*. 2018. URL: http://ipac2018.vrws.de/papers/mopmf048.pdf.

[64] R. Tomás et al. „Measurement of global and local resonance terms." In: *Phys. Rev. ST Accel. Beams* 8 (2 2005), p. 024001. DOI: 10.1103/PhysRevSTAB.8.024001. URL: https://link.aps.org/doi/10.1103/PhysRevSTAB.8.024001.

[65] S. White, E. Maclean, and R. Tomás. „Direct amplitude detuning measurement with ac dipole." In: *Phys. Rev. ST Accel. Beams* 16 (7 2013), p. 071002. DOI: 10.1103/PhysRevSTAB.16.071002. URL: http://link.aps.org/doi/10.1103/PhysRevSTAB.16.071002.

[66] R. Tomás et al. „Beam-beam amplitude detuning with forced oscillations." In: *Phys. Rev. Accel. Beams* 20 (10 2017), p. 101002. DOI: 10.1103/PhysRevAccelBeams.20.101002. URL: https://link.aps.org/doi/10.1103/PhysRevAccelBeams.20.101002.

[67] R. Tomás, T. H. B. Persson, and E. H. Maclean. „Amplitude dependent closest tune approach." In: *Phys. Rev. Accel. Beams* 19 (7 2016), p. 071003. DOI: 10.1103/PhysRevAccelBeams.19.071003. URL: http://link.aps.org/doi/10.1103/PhysRevAccelBeams.19.071003.

[68] É. Forest. „A Hamiltonian free description of single particle dynamics for hopelessly complex periodic systems." In: *Journal of Mathematical Physics* 31 (1990). DOI: https://doi.org/10.1063/1.528795.

[69] A. Bazzani et al. *A normal form approach to the theory of nonlinear betatronic motion*. Tech. rep. European Organization for Nuclear Research, Geneva (Switzerland), 1994. URL: https://inis.iaea.org/search/search.aspx?orig_q=RN:25069915.

[70] A. Franchi et al. „First simultaneous measurement of sextupolar and octupolar resonance driving terms in a circular accelerator from turn-by-turn beam position monitor data." In: *Phys.Rev.ST Accel.Beams* 17.7 (2014), p. 074001. arXiv: 1402.1461.

[71] J. Bengtsson and J. Irwin. *Analytical calculations of smear and tune shift*. Tech. rep. SSC-232. Dallas, TX: SSC Laboratory, 1990.

[72] *MAD-X: Methodical Accelerator Design*. http://madx.web.cern.ch/madx/.

[73] R. Bartolini and F. Schmidt. *Normal form via tracking or beam data*. Tech. rep. LHC-Project-Report-132. CERN-LHC-Project-Report-132. CERN, 1997, 93–106. 10 p. URL: https://cds.cern.ch/record/333077.

[74] J. Bengtsson. „Non-linear transverse dynamics for storage rings with applications to the low-energy antiproton ring (LEAR) at CERN." Presented on 1 Aug 1988. PhD thesis. Lund U., 1988. URL: https://cds.cern.ch/record/190442.

[75] R. Bartolini et al. „Measurement of resonance driving terms from turn-by-turn data." In: CERN-SL-99-032-AP. 1999, 3 p. URL: https://cds.cern.ch/record/387272.

[76] M. Benedikt et al. „Driving term experiments at CERN." In: *Phys. Rev. ST Accel. Beams* 10 (3 2007), p. 034002. DOI: 10.1103/PhysRevSTAB.10.034002. URL: https://link.aps.org/doi/10.1103/PhysRevSTAB.10.034002.

[77] W. Fischer, F. Schmidt, and R. Tomás. „Measurement of sextupolar resonance driving terms in RHIC." In: *Proceedings of PAC 2003*. IEEE Particle Accelerator Conference 20. Portland, USA, 2003.

[78] Y. Luo et al. „Measurement and correction of third resonance driving term in the RHIC." In: *2007 IEEE Particle Accelerator Conference (PAC)*. 2007, pp. 4351–4353. DOI: 10.1109/PAC.2007.4440102.

[79] Y. Alexahin et al. *Measurement and correction of the 3rd order resonance in the Tevatron*. Tech. rep. FERMILAB-CONF-06-202-AD. FermiLab, Jan. 2006.

[80] T. Bach et al. *CERN PS optical properties measured with turn-By-turn orbit data*. Tech. rep. CERN, 2013. URL: https://cds.cern.ch/record/1595218.

[81] C. Steier. *USPAS, ASU*. 2006.

[82] P. Kuske and et al. *unpublished*. 2004.

[83] G. Vanbavinckhove et al. „Linear and non-linear optics measurements at soleil." In: *Proceedings of PAC 09*. (Vancouver, Canada). Particle Accelerator Conference. 2009.

[84] R. Tomás et al. „Measurement of resonance driving terms in the ATF damping ring." In: *European Particle Accelerator Conference (EPAC'08), Genoa, Italy, 2008*. 2008. URL: https://cds.cern.ch/record/1122247.

[85] R. Bartolini et al. „Correction of multiple nonlinear resonances in storage rings." In: *Phys. Rev. ST Accel. Beams* 11 (10 2008), p. 104002.

[86] E. H. Maclean et al. „First measurement and correction of nonlinear errors in the experimental insertions of the CERN Large Hadron Collider." In: *Phys. Rev. ST Accel. Beams* 18 (12 2015), p. 121002. DOI: 10.1103/PhysRevSTAB.18.121002. URL: http://link.aps.org/doi/10.1103/PhysRevSTAB.18.121002.

[87] G. Guignard. „Betatron coupling and related impact of radiation." In: *Phys. Rev. E* 51 (6 1995), pp. 6104–6118. DOI: 10.1103/PhysRevE.51.6104. URL: http://link.aps.org/doi/10.1103/PhysRevE.51.6104.

[88] R. Calaga and R. Tomás. „Statistical analysis of RHIC beam position monitors performance." In: *Phys. Rev. ST Accel. Beams* 7 (4 2004), p. 042801. DOI: 10.1103/PhysRevSTAB.7.042801. URL: https://link.aps.org/doi/10.1103/PhysRevSTAB.7.042801.

[89] R. Bartolini and F. Schmidt. *A computer code for frequency analysis of non-linear betatron motion*. Tech. rep. SL-Note-98-017-AP. Geneva: CERN, 1998. URL: https://cds.cern.ch/record/702438.

[90] A. Garcia-Tabares Valdivieso. „Optics-measurement-based Beam Position Monitor Calibration.. Calibración de monitores de posición del haz basado en medidas ópticas." Presented 08 Nov 2019. PhD thesis. 2019. URL: http://cds.cern.ch/record/2701414.

[91] P. Hagen et al. *WISE: An Adaptative Simulation of the LHC Optics*. Tech. rep. LHC-PROJECT-Report-971. CERN-LHC-Project-Report-971. CERN, 2006, 4 p. URL: http://cds.cern.ch/record/977794.

[92] E. H. Maclean et al. „Measurement of nonlinear observables in the Large Hadron Collider using kicked beams." In: *Phys. Rev. ST Accel. Beams* 17 (8 2014), p. 081002. DOI: 10.1103/PhysRevSTAB.17.081002. URL: http://link.aps.org/doi/10.1103/PhysRevSTAB.17.081002.

[93] E. Fol, J. Coello de Portugal, and R. Tomás. *Isolation Forest algorithm for faulty Beam Position Monitors detection*. Tech. rep. To be submitted. CERN, 2020.

[94] F. S. Carlier et al. *Optics measurements and correction challenges for the HL-LHC*. Tech. rep. CERN-ACC-2017-0088. Geneva: CERN, 2017. URL: http://cds.cern.ch/record/2290899.

[95] F.S. Carlier et al. „Nonlinear correction strategies for the LHC using resonance driving terms." In: *Proceedings of IPAC 18*. (Vancouver, Canada). International Particle Accelerator Conference 9. 2018.

[96] S. Fartoukh. „Achromatic telescopic squeezing scheme and application to the LHC and its luminosity upgrade." In: *Phys. Rev. ST Accel. Beams* 16 (11 2013), p. 111002. DOI: 10.1103/PhysRevSTAB.16.111002. URL: https://link.aps.org/doi/10.1103/PhysRevSTAB.16.111002.

[97] F. S. Carlier. *Correction of skew octupoles with resonance driving terms*. LHC Machine Committee (LMC). 2018.

[98] E. Carlier, L. Ducimetiere, and E. Vossenberg. „A kicker pulse generator for measurement of the tune and dynamic aperture in the LHC." In: *Power Modulator Symposium, 2006. Conference Record of the 2006 Twenty-Seventh International*. 2006, pp. 463–466. DOI: 10.1109/MODSYM.2006.365284. URL: http://ieeexplore.ieee.org/xpls/abs_all.jsp?arnumber=4216236&tag=1.

[99] R. Miyamoto et al. *Signal quality of the LHC AC dipoles and its impact on beam dynamics*. Tech. rep. CERN-ATS-2010-063. CERN, 2010, 3 p. URL: http://cds.cern.ch/record/1269893.

[100] J. Serrano and M. Cattin. *The LHC AC dipole system: an introduction*. Tech. rep. CERN, 2010. URL: https://cds.cern.ch/record/1263248.

[101] R. Tomás et al. „CERN Large Hadron Collider optics model, measurements, and corrections." In: *Phys. Rev. ST Accel. Beams* 13 (12 2010), p. 121004. DOI: 10.1103/PhysRevSTAB.13.121004. URL: http://link.aps.org/doi/10.1103/PhysRevSTAB.13.121004.

[102] U. Iriso. *Private Communication*.

[103] K. Hock et al. „Status of AC dipole project at RHIC injectors for polarized helions." In: *Proc. of International Particle Accelerator Conference (IPAC'18), Vancouver, Canada, April 29 - May 4, 2018*. 2018. URL: http://ipac2018.vrws.de/papers/tupaf005.pdf.

[104] S. Monig et al. *Short term dynamic aperture with AC dipoles*. Tech. rep. CERN-ACC-2016-173. CERN, 2016, THPMR044. 4 p. URL: https://cds.cern.ch/record/2207450.

[105] W. Scandale. *Dynamic aperture*. Tech. rep. CERN-SL-94-24-AP. CERN, 1994, 39 p. URL: https://cds.cern.ch/record/267125.

[106] A. Bazzani et al. *Normal forms for area preserving maps, resonances and dynamic aperture*. Tech. rep. CERN-SPS-89-24-AMS. Geneva: CERN, 1989. URL: https://cds.cern.ch/record/200033.

[107] M. Giovannozzi. „Dynamic aperture for single-particle motion: Overview of theoretical background, numerical predictions and experimental results." In: *29th ICFA Advanced Beam Dynamics Workshop on Beam-Halo Dynamics, Diagnostics and Collimation in conjunction with The Beam-Beam Workshop, Montauk, NY, USA, 19 - 23 May*. Vol. 693. 2004, pp. 26–31. URL: https://cds.cern.ch/record/872653.

[108] M. Giovannozzi. *A proposed scaling law for intensity evolution in hadron storage rings based on dynamic aperture variation with time*. Tech. rep. CERN-ATS-2012-053. 2012, 024001. 20 p. URL: https://cds.cern.ch/record/1426594.

[109] K. Ohmi et al. „Response of colliding beam-beam system to harmonic excitation due to crab-cavity rf phase modulation." In: *Phys. Rev. Spec. Top. Accel. Beams* 14.EuCARD PUB 2012-002 (2011), p. 111003. URL: http://cds.cern.ch/record/1443465.

[110] L. R. Carver et al. „Instabilities and beam induced heating in 2016." In: *Proceedings Evian Workshop 16*. 2016.

[111] V. Kiselev et al. „Dynamic aperture study at the VEPP-4M storage ring." In: *Proc. of Particle Accelerator Conference (PAC'97), Vancouver, Canada, 12-16 May, 1997*. 1997. URL: http://accelconf.web.cern.ch/accelconf/pac97/papers/pdf/2V033.PDF.

[112] F. Willeke. „Dynamic aperture, theoretical aspects and observational features." In: *Beam measurement. Proceedings, Joint US-CERN-Japan-Russia School on Particle Accelerators, Montreux and Geneva, Switzerland, May 11-20, 1998*. 1998, pp. 326–350.

[113] D. Belohrad et al. *The LHC fast BCT system: A comparison of design parameters with initial performance*. Tech. rep. CERN-BE-2010-010. Geneva: CERN, 2010. URL: http://cds.cern.ch/record/1267400.

[114] S. Monig et al. „Short term dynamic aperture with ac dipoles." In: *Proc. of International Particle Accelerator Conference (IPAC'16), Busan, Korea, May 8-13, 2016*. (Busan, Korea). International Particle Accelerator Conference 7. Geneva, Switzerland: JACoW, 2016, pp. 3496–3499. ISBN: 978-3-95450-147-2. DOI: doi:10.18429/JACoW-IPAC2016-THPMR044. URL: http://jacow.org/ipac2016/papers/thpmr044.pdf.

[115] S. Cettour Cave et al. *Non-linear beam dynamics tests in the LHC: measurement of intensity decay for probing dynamic aperture at injection*. Tech. rep. CERN, 2013. URL: https://cds.cern.ch/record/1543434.

[116] G. Trad et al. „Status of the beam profile measurements at the LHC." In: 2016, 163–170. 8 p. URL: http://cds.cern.ch/record/2294529.

[117] E. H. Maclean. „New optics correction approaches in 2017." In: *Proceedings, 8th LHC Operations Evian Workshop*. 2017.

[118] M. Lammont. *CERN Bulletin, Issue No. 38-39/2016 - Monday 19 September 2016*.

[119] K. Ohmi et al. „Beam-beam limit in e^+e^- circular colliders." In: *Phys. Rev. Lett.* 92 (21 2004), p. 214801. DOI: 10.1103/PhysRevLett.92.214801. URL: https://link.aps.org/doi/10.1103/PhysRevLett.92.214801.

[120] K. Ohmi and F. Zimmermann. „Fundamental beam-beam limit from head-on interaction in the Large Hadron Collider." In: *Phys. Rev. ST Accel. Beams* 18 (12 2015), p. 121003. DOI: 10.1103/PhysRevSTAB.18.121003. URL: https://link.aps.org/doi/10.1103/PhysRevSTAB.18.121003.

[121] X. Gu et al. „Electron lenses for head-on beam-beam compensation in RHIC." In: *Phys. Rev. Accel. Beams* 20 (2 2017), p. 023501. DOI: 10.1103/PhysRevAccelBeams.20.023501. URL: https://link.aps.org/doi/10.1103/PhysRevAccelBeams.20.023501.

[122] W. Fischer et al. „Compensation of head-on beam-beam induced resonance driving terms and tune spread in the Relativistic Heavy Ion Collider." In: *Phys. Rev. Accel. Beams* 20 (9 2017), p. 091001. DOI: 10.1103/PhysRevAccelBeams.20.091001. URL: https://link.aps.org/doi/10.1103/PhysRevAccelBeams.20.091001.

[123] Y. Luo et al. „Six-dimensional weak-strong simulation of head-on beam-beam compensation in the Relativistic Heavy Ion Collider." In: *Phys. Rev. ST Accel. Beams* 15 (5 2012), p. 051004. DOI: 10.1103/PhysRevSTAB.15.051004. URL: https://link.aps.org/doi/10.1103/PhysRevSTAB.15.051004.

[124] W. Fischer et al. „Operational head-on beam-beam compensation with electron lenses in the Relativistic Heavy Ion Collider." In: *Phys. Rev. Lett.* 115 (26 2015), p. 264801. DOI: 10.1103/PhysRevLett.115.264801. URL: https://link.aps.org/doi/10.1103/PhysRevLett.115.264801.

[125] V. Shiltsev et al. „Experimental demonstration of colliding-beam-lifetime improvement by electron lenses." In: *Phys. Rev. Lett.* 99 (24 2007), p. 244801. DOI: 10.1103/PhysRevLett.99.244801. URL: https://link.aps.org/doi/10.1103/PhysRevLett.99.244801.

[126] S. Fartoukh et al. „Compensation of the long-range beam-beam interactions as a path towards new configurations for the high luminosity LHC." In: *Phys. Rev. ST Accel. Beams* 18 (12 2015), p. 121001. DOI: 10.1103/PhysRevSTAB.18.121001. URL: https://link.aps.org/doi/10.1103/PhysRevSTAB.18.121001.

[127] R. Tomás. „Direct measurement of resonance driving terms in the Super Proton Synchrotron (SPS) of CERN using beam position monitors." Presented on 30 Mar 2003. PhD thesis. Valencia: Valencia U., 2003.

[128] A. W. Chao. *The beam-beam instability*. Tech. rep. SLAC-PUB-3179. SLAC, 1983. URL: http://www.iaea.org/inis/collection/NCLCollectionStore/_Public/15/021/15021887.pdf.

[129] P. Chao A. W. Bambade and W. T. Weng. *Nonlinear beam-beam resonances*. Tech. rep. SLAC-PUB-3545. SLAC, 1985. URL: http://www.slac.stanford.edu/cgi-wrap/getdoc/slac-pub-3545.pdf.

[130] P. Goncalves Jorge et al. *MD 979: Beta-beating measurements on colliding beams*. Tech. rep. 2017. URL: https://cds.cern.ch/record/2292102.

[131] G. Trad. *Personal communications*.